

AUTOMATIC HEIGHT EXTRACTION FROM STEREOSCOPIC SAR IMAGERY

A Thesis submitted for the degree of

Doctor of Philosophy

in the University of London by

Zway-Gen Twu

University College London

November 1996

ProQuest Number: 10046027

All rights reserved

INFORMATION TO ALL USERS

The quality of this reproduction is dependent upon the quality of the copy submitted.

In the unlikely event that the author did not send a complete manuscript and there are missing pages, these will be noted. Also, if material had to be removed, a note will indicate the deletion.



ProQuest 10046027

Published by ProQuest LLC(2016). Copyright of the Dissertation is held by the Author.

All rights reserved.

This work is protected against unauthorized copying under Title 17, United States Code.
Microform Edition © ProQuest LLC.

ProQuest LLC
789 East Eisenhower Parkway
P.O. Box 1346
Ann Arbor, MI 48106-1346

Contents

Contents	1
List of Tables	5
List of Figures	9
Acknowledgement	12
Abbreviations	13
Abstract	15
1. Introduction	17
1.1 Introduction	17
1.2 Overview	17
1.3 Aims	19
1.4 Outline of This Thesis	20
2. SAR Sensors and Data Products	22
2.1 Introduction	22
2.2 ERS-1: Overview	22
2.2.1 Introduction	22
2.2.2 ERS-1 missions	23
2.2.3 ERS-1 ground segment	24
2.3 ERS-1 Data Products	25
2.4 RADARSAT Overview	27
2.5 SEASAT, SIR-A, SIR-B and SIR-C Overview	28
2.6 SAR Fundamental Principles	29
2.7 Radar Backscattering	31
2.8 SAR Image Processing	34
2.9 SAR Geocoding	35
2.10 Summary	37
3. Stereoscopy Using SAR Imagery	38
3.1 Introduction	38
3.2 SAR Image Characteristics	38

3.3 SAR Stereoscopy	39
3.4 Speckle Reduction Filters	42
3.5 Difficulties of SAR Stereo Matching	45
3.6 Summary	46
4. Stereo Matching SAR Imagery Methodology	47
4.1 Overview	47
4.2 Pyramidal Matching	51
4.3 CASCADE Programme	52
4.4 CHEOPS Programme	54
4.5 Introduction to GRUEN	59
4.6 Introduction to GRUENS	60
4.7 Summary	62
5. Intersection	63
5.1 Overview	63
5.2 Analytic Approach Overview	63
5.3 Analytic Approach	64
5.4 Space Intersection Procedures	66
5.4.1 Read header data file	66
5.4.2 Preliminary calculation	68
5.4.3 Coordinate translation	68
5.4.4 Prediction of the orbit position and velocity	69
5.4.5 Position and velocity vectors transformation	69
5.4.6 Intersection	71
5.5 Summary	72
6. Image Data Set and Test Site Description	73
6.1 Introduction	73
6.2 Image Data Set Introduction	73
6.3 Test Area Description	74
6.4 Reference DEM Introduction	78
6.5 Evaluation of DEM Accuracy Algorithm	81

7. Assessment of Stereo Matching Results	82
7.1 Introduction	82
7.2 GRUEN and GRUENS Programme Analysis	83
7.3 Determination of Matching Strategy	86
7.4 Random Seed Points Generation	98
7.5 Random Seed Points Analysis	98
7.6 PDL File Data Testing	103
7.6.1 PDL file data testing: ORSE	103
7.6.2 PDL file data testing: GRSE	104
7.6.3 PDL file data testing: DEM accuracy for separated tier	107
7.6.4 PDL file data testing: DEM accuracy and Image tiers	108
7.6.5 PDL file data testing: comparison of two PDL files	108
7.7 Blunder-removing	112
7.7.1 Global disparity analysis	113
7.7.2 Determination of threshold of blunder-removing filter	114
7.7.3 Blunder-removing filter data testing	115
7.8 Techniques of Seed Points Selection	121
7.8.1 SEED_GRUEN programme introduction	121
7.8.2 Testing of two algorithms	123
7.8.3 Seed points selection by disparity sum	126
7.8.4 DEM accuracy of the disparity sum	126
7.9 Advantages of Pyramidal Stereo Matching Analysis	131
7.10 Performances of Matching on the Opposite-side Imagery	134
7.11 Pyramidal Matching on the Speckle Reduction Imagery	138
7.12 Running Time Consideration	142
7.13 Summary	143
8. Object Domain Approach	145
8.1 Introduction	145
8.2 Geometric Constraint Conditions	146
8.3 Height Deviation and Constraint Condition	149
8.4 Determination of Constraint Condition	151
8.5 Characteristics of Constraint Values	162
8.6 Determination of Optimum Constraint Values	167
8.7 Analysis of DEM Accuracy by Geometric Constraint Conditions	170
8.8 Intersection Error Modelling by Image Coordinates	174
8.9 Standard Height Approach	176

8.9.1 Using the coarse reference DEM	176
8.9.2 Using new derived DEM	182
8.10 Analysis of Success of Object Domain Approach	184
8.11 Intersection Using the Control Points	185
8.11.1 Control points consideration	185
8.11.2 Range time calculation	186
8.11.3 DEM accuracy analysis	188
8.12 Summary	192
9. Conclusion	194
9.1 Pyramidal Matching Algorithm	194
9.2 Intersection Algorithm	197
9.3 Overview of Achievements	199
9.4 Future Studies	201
References	203
Appendix A: Least Squares Correlation Algorithm	210
Appendix B: Original Header Data File	213
Appendix C: Control Header Data File	217
Appendix D: Terms Glossary	221

List of Tables

Table 2.1:	Summary of principal characteristics of SAR sensors	22
Table 2.2:	The period and repeat cycle duration for ERS-1 six main phase	23
Table 6.1:	4 key data for the three images respectively	73
Table 6.2:	Definitions of three stereo pairs	74
Table 6.3:	Offset of sample and line pixel for the test area	74
Table 7.1:	DEM accuracies (m) for the manual seed points under 3 different patch radius	94
Table 7.2:	Coverage (%) for the manual seed points under 3 different patch radius	94
Table 7.3:	RMS (m) for ERSP and DEM accuracy (m) for ORSE of PDL1 and PDL2 under three different grid numbers	105
Table 7.4:	RMS (m) for the growing random seed points of each tier	106
Table 7.5:	DEM (m) accuracy for growing random seed points with two PDL files	105
Table 7.6:	Coverage (%) for two PDL files without the RSE	105
Table 7.7:	DEM accuracy (m) for the total and each tier	107
Table 7.8:	Influence of image tier on DEM accuracy (m) and coverage (%)	109
Table 7.9:	The relationship of DEM accuracy (m) grand disparity sum (pixel) and height deviation (m)	111
Table 7.10:	HDSE for two PDL files on tier4~8 under grid 32	111
Table 7.11:	HDSE, mean and RMS (m) for two PDL files under three different grids	112
Table 7.12:	The range and average of X and Y disparity (pixels) for three groups	113
Table 7.13:	Range and average value of disparity sum (pixels)	114
Table 7.14:	The upper and lower boundary of threshold value (pixel) of disparity sum for different percentages	116
Table 7.15:	The comparison of the final DEM accuracy (m) between five different types of threshold value and the original one	117
Table 7.16:	The comparison of the HDSE between five different types of threshold value and the original one	117
Table 7.17:	Coverage(%) of five different types of threshold value and the original one	117

Table 7.18: DEM accuracy (m) for five two-end boundaries, fixed at the lower boundary 118

Table 7.19: DEM accuracy (m) for three two-end boundary fixed at the upper boundary 118

Table 7.20: The lower 100% threshold value (pixels)for two data sets 119

Table 7.21: Number of (-) and (+)height deviation under three grid number 126

Table 7.22: Disparity sum (pixels) for ordinary and disparity seed points on tier4 under three different grids 127

Table 7.23: Number of (-) and (+)height deviation under three grid number 127

Table 7.24 DEM accuracy (m) for ordinary and disparity seed points under three different grids 127

Table 7.25: Comparisons of HDSE for ordinary and disparity seed points under three different grid 128

Table 7.26: 100% lower boundary threshold value (pixels) for three sets of disparity seed points under three different grids 128

Table 7.27: DEM accuracy (m) for the disparity seed points before and after using blunder-removing filter 129

Table 7.28: Threshold values (pixel) computed by four different minus height deviation 130

Table 7.29: Coverage(%) and DEM accuracy (m) by the four threshold values . 131

Table 7.30: DEM accuracy (m) comparison of different tiers for the original and pyramidal image 132

Table 7.31: DEM accuracy (m) of different seed_generation for the original image 132

Table 7.32: Proportion of grand_generation seed points for the original image on each tier 133

Table 7.33: Coordinates of the growing seed points for image pyramid on each tier 134

Table 7.34: DEM accuracy (m) and coverage(%) of five data sets of OP1 135

Table 7.35: DEM accuracy (m) and coverage(%) of five data sets of OP2 136

Table 7.36: Coverage (%) for the larger eigenvalue for three sets of opposite pair 136

Table 7.37: DEM accuracy (m) and coverage (%) for four sets of OP1 data 137

Table 7.38: DEM accuracy (m) and coverage (%) for four sets of OP2 data 137

Table 7.39: DEM accuracy and coverage(%) for the original and speckle-removing image 138

Table 7.40: Comparison of CPU time (hours) for five different data sets 142

Table 8.1:	9 data sets selected for testing the relationship of constraint values and height deviation	151
Table 8.2:	9 height deviation intervals and their corresponding statistics of range error (m) of the same side stereo pair	151
Table 8.3:	9 height deviation intervals and their corresponding statistics of range error (m) of the OP1	152
Table 8.4:	9 height deviation intervals and their corresponding statistics of range error(m) of the OP2	152
Table 8.5:	9 height deviation intervals and their corresponding statistics of intersection angle (°) of the SA	153
Table 8.6:	9 height deviation intervals and their corresponding statistics of intersection angle (°) of the OP1	153
Table 8.7:	9 height deviation intervals and their corresponding statistics of intersection angle (°) of OP2	154
Table 8.8:	Mean height deviation and the difference for two intervals of extreme constraint values for SA	161
Table 8.9:	Mean height deviation and the difference for two intervals of extreme constraint values for OP1	161
Table 8.10:	Mean height deviation and the difference for two intervals of extreme constraint values for OP2	162
Table 8.11:	Range error (m) of small height deviation for the same side	168
Table 8.12:	Intersection angle (°) of small height deviation for the OP1	168
Table 8.13:	Intersection angle (°) of small height deviation for the OP2	168
Table 8.14:	DEM accuracy (m) comparison for the optimum ranges or optimum values of range error for the SA	169
Table 8.15:	DEM accuracy (m) comparison for the optimum ranges or optimum values of intersection angle (°) for the OP1	169
Table 8.16:	DEM accuracy (m) comparison for the optimum ranges or optimum values of intersection angle for the OP2	169
Table 8.17:	DEM accuracy (m) and HDSE comparison between the original and constraint condition for SA	171
Table 8.18:	DEM accuracy (m) and HDSE comparison between the original and constraint condition for OP1	171
Table 8.19:	DEM accuracy (m) and HDSE comparison between the original and constraint condition for OP2	172
Table 8.20:	Gradient of errors in intersection with respect to 3 coordinates by shifting one pixel in X direction	174

Table 8.21: Gradient of errors in intersection with respect to 3 coordinates by shifting one pixel in Y direction	174
Table 8.22: Gradient of total errors in intersection of shifting one pixel in X and Y direction	175
Table 8.23: Convergence angle (°) and intersection angle (°) for three stereo pairs	175
Table 8.24: The DEM accuracy (m) and HDSE of five data sets by the standard height approach (coarse reference DEM) for SA	177
Table 8.25: DEM accuracy (m) and HDSE of five data sets by the standard height approach (coarse reference DEM) for OP1	181
Table 8.26: DEM accuracy (m) and HDSE of five data sets by the standard height approach (coarse reference DEM) for OP2	181
Table 8.27: The DEM accuracy (m) and HDSE of five data sets by the standard height approach (new reference DEM) for SA	182
Table 8.28: The DEM accuracy (m) and HDSE of five data sets by the standard height approach (new reference DEM) for OP1	182
Table 8.29: The DEM accuracy (m) and HDSE of five data sets by the standard height approach (new reference DEM) for OP2	184
Table 8.30: Lambert Zone 3 coordinates of 3 control points	188
Table 8.31: The DEM accuracy (m) and HDSE of five data sets by using 3 control points for SA	188
Table 8.32: The DEM accuracy (m) and HDSE of five data sets by using 3 control points for OP1	189
Table 8.33: The DEM accuracy (m) and HDSE of five data sets by using 3 control points for OP2	189
Table 8.34: The ground coordinates of the intersection of control points using the original and control header data file for SA.....	190
Table 8.35: The ground coordinates of the intersection of control points using the original and control header data file for OP1	190
Table 8.36: The ground coordinates of the intersection of control points using the original and control header data file for OP2	190
Table 8.37: Statistics of height difference(m) between the DEM with and without control points for SA	191
Table 8.38: Statistics of height difference (m) between the DEM with and without control points for OP1	192
Table 8.39: Statistics of height difference (m) between the DEM with and without control points for OP2	192
Table 9.1 : Summary of actual DEM accuracy and improvement in Chapter 8...	198

List of Figures

Figure 2.1:	Locations and coverage zone of ERS-1 ground receiving stations...	26
Figure 2.2:	Dependence of the azimuth resolution (R_a) on antenna beamwidth(β) and ground range	31
Figure 2.3:	Doppler history of a point target	32
Figure 2.4:	Geometry of a synthetic aperture array	33
Figure 2.5:	Flow chart of SAR image processing using the frequency domain approach	35
Figure 3.1:	Geometric distortions due to the terrain elevation effects	39
Figure 3.2:	Definitions in object space for the vertical exaggeration of camera stereo model	41
Figure 4.1:	Random seed points distribution on SA	55
Figure 4.2:	An example of PDL file	56
Figure 4.3:	CHEOPS pyramidal matching flow chart	58
Figure 5.1:	Geocentric inertial system	66
Figure 5.2:	Intersection flow chart	67
Figure 5.3:	Relationship between inertial system and geocentric terrestrial system	70
Figure 6.1:	RTM_A raw image	75
Figure 6.2:	PRI_A raw image	76
Figure 6.3:	PRI_D raw image	77
Figure 6.4:	Location of test area in France	74
Figure 6.5:	Extracted reference DEM boundary	79
Figure 6.6:	Extracted reference DEM of Aix-en-Provence	80
Figure 7.1:	Three numerical examples of 12 values of GRUEN's output	85
Figure 7.2:	PDL1 file	88
Figure 7.3:	PDL2 file	89
Figure 7.4:	Strategy 1 execution procedures	90
Figure 7.5:	Numerical example for strategy 1	91
Figure 7.6:	Strategy 2 execution procedures	92
Figure 7.7:	Numerical example for strategy 2	93
Figure 7.8:	Perspective view of DEM from manual seed points matching (radius 15).....	95

Figure 7.9: Perspective view of DEM from manual seed points matching (radius 20)	96
Figure 7.10: Perspective view of DEM from manual seed points matching (radius 25)	97
Figure 7.11: Flow chart of GRUENS_SEED	101
Figure 7.12: Diagram for the techniques of the GRUENS_SEED	102
Figure 7.13: The comparison of DEM accuracy between the original and lower threshold for three data sets	120
Figure 7.14: The comparison of DEM accuracy between the original and lower threshold without the ERSP for three data sets	120
Figure 7.15: Flow chart of SEED_GRUEN programme	124
Figure 7.16: Flow charts for two matching scripts	125
Figure 7.17: Comparisons of DEM accuracy improvements under three grid number	129
Figure 7.18: LEE filtered image matching coverage	139
Figure 7.19: MAP filtered image matching coverage	140
Figure 7.20: Original image matching coverage	141
Figure 8.1: Geometric constraint condition the same side stereo pair	147
Figure 8.2: Geometric constraint condition the opposite side stereo pair	147
Figure 8.3: Relationship of range error (m) and height deviation for the SA ..	154
Figure 8.4: Relationship of range error (m) and height deviation for the OP1 ..	155
Figure 8.5: Relationship of range error (m) and height deviation for the OP2 ..	155
Figure 8.6: Relationship of intersection angle (°) and height deviation for the SA	156
Figure 8.7: Relationship of intersection angle (°) and height deviation for the OP1	156
Figure 8.8: Relationship of intersection angle(°) and height deviation for the OP2	157
Figure 8.9: Extent of range error (m) under different height deviation (m) for the SA	158
Figure 8.10: Extent of intersection angle(°) under different height deviation (m) for the SA	158
Figure 8.11: Extent of range error (m) under different height deviation (m) for the OP1	159
Figure 8.12: Extent of intersection angle (°) under different height deviation (m) for the OP1	159
Figure 8.13: Extent of range error (m) under different height deviation (m) for the OP2	160

Figure 8.14: Extent of intersection angle ($^{\circ}$) under different height deviation (m) for the OP2	160
Figure 8.15: Range error (m) of SA with respect to the X coordinate	164
Figure 8.16: Range error (m) of SA with respect to the Y coordinate	164
Figure 8.17: Range error (m) of SA with respect to the X+Y coordinate	165
Figure 8.18: Intersection angle ($^{\circ}$) for the opposite side with respect to X coordinate	165
Figure 8.19: Intersection angle ($^{\circ}$) for the opposite side with respect to Y coordinate	166
Figure 8.20: Intersection angle ($^{\circ}$) for the opposite side with respect to X+Y coordinate	166
Figure 8.21: Perspective view of original DEM of same side	178
Figure 8.22: Perspective view of geometric constraint DEM of same side	179
Figure 8.23: Perspective view of extracted reference Aix-en-Provence DEM.....	180
Figure 8.24: Perspective view of standard height approach DEM of same side	183
Figure 8.25: 3 control points location on RTM_A image	187

Acknowledgement

First of all, I would like to express my sincere thanks to Prof. I.J. Dowman for his supervision and instruction over these past four years. I also thank Prof. J.P. Muller for his guidance and help during this study. I also feel grateful to Mark Upton for his kind assistance in teaching me to use some helpful computer commands. My thanks also go to Chrystelle Ourzik and Jeremy Morley for they show me how to draw beautiful figures for this thesis.

English academic writing is a difficult work for me and here I appreciate Isabella's help to correct my poor English writing and Paul Dare to proof-read my thesis. I also show my gratitude to Ms. Wu and Mr. Tickell who have allowed me to use their PC for without them, this thesis would not have been completed so quickly.

I honestly thank my family in Taiwan for their encouragement and endurance of my absence during these past four years. Without their moral support, this thesis would not be finished. Special thanks must go to my wife for her looking after the whole family alone in Taiwan for such a long time.

At last, I would like to appreciate the sponsorship from the government of the Republic of China for their financial support, letting me have this opportunity to study here and complete this thesis.

Abbreviations

ALSC: Adaptive Least Squares Correlation
AMI: Active Microwave Instrument
CSA: Canadian Space Agency
EECF: Earthnet ERS-1 Central Facilities
ERS-1: European Remote Sensing satellite
ERSP: Effective Random Seed Points
ESA: European Space Agency
FFT: Fast Fourier Transform
GRSE: Growing Random Seed Effects
GMST: Greenwich Mean Sidereal Time
GAST: Greenwich Apparent Sidereal Time
GCP: Ground Control Points
HBR: High Bit Rate
HDSE: Height Deviation Shifting Effect
JD: Julian Date
JPL: Jet Propulsion Laboratory
LBR: Low Bit Rate
LFM: Linear Frequency Modulated
LSC: Least Squares Correlation
MSEC: Mean Square Error on the Contrast
MHD: Mean Height Difference
MMCC: Mission Management and Control Center
NCC: Normalised Correlation Coefficient
OIE: Original Image Effect
OP1: Opposite stereo Pair - PRI_D (left), PRI_A (right)
OP2: Opposite stereo Pair - PRI_D (left), RTM_A (right)
ORSE: Original Random Seed Effect
PAF: Processing and Archiving Facilities
PDL: Pyramidal Description Language
PRI: Precision SAR Imagery
PRI_A: PRI Ascending ERS-1 image
PRI_D: PRI Descending ERS-1 image
PRF: Pulse Repetition Frequency
RSE: Random Seed Effects
RTM: Roll-Tilt Mode SAR imagery

Abbreviations

RTM_A: RTM Ascending ERS-1 Image

SA: Same side stereo pair - RTM_A (left), PRI_A (right)

SIHE: Systematic Increasing Height Effects

SIR: Shuttle Imaging Radar

UT: Universal Time

Abstract

This research was concerned with various aspects of deriving DEM information from ERS-1 SAR imagery. Stereoscopic SAR offers the possibility to determine a DEM of large areas and is complementary to interferometric SAR (IFSAR). Compared with former SAR image data sources, ERS-1 has the advantage of providing accurate ephemeris data. In addition, it has different image modes which enables the verification of results from various research groups regarding geometric configurations. One of the aims of this study was to establish a standard model for deriving DEM accuracy, based on ERS-1 as the image data source, that would be applicable for all other new types of SAR imageries. An example of such SAR imageries worth investigating in the future is RADARSAT, which provides versatile image modes with a wide range of incident angle and resolution.

In summary, the studies carried out for this research project could be described under two subheadings, namely matching and intersection. With respect to the matching, pyramidal stereo matching techniques were used in combination with an excellent area-based region growing algorithm to achieve dense coverage. The special interest in this study is the initial seed points used for the pyramidal matching process employed were chosen randomly instead of by manual selection. To examine the function of these random seed points, the original matching algorithm was modified to have four extra values in its output, which were later found to be able to aid the determination of the advantages of using image pyramids. It was also discovered that the disparity sum was a good measure for judging the factors affecting the matching accuracy in most of the studies. As a result, this parameter was used to investigate different strategies of pyramidal matching, to pin-point the link between the upper and lower tier in the image pyramid, as well as for the removal of the blunders.

The analytic method was used in this study for the intersection procedures and based on this, two new approaches were developed. Both of these approaches were found to significantly enhance the DEM accuracy and their success was determined to be due to the linear-correspondence relationship between the image and the object space. Another important discovery was that any alteration made on the slant range of matched image pixels would only result in changes of terrain height values. Different geometric conditions for the three pairs under study were also analysed. It was concluded that the convergence angle of two given orbits would have considerable influence on the intersection accuracy, the smaller the angle the greater this influence.

It is demonstrated in this thesis that with a same side convergence angle of 2.14° , the intersection error could reach 426.95m for one Y pixel shift. The above phenomenon explains the underlying reason why the DEM accuracy could not be improved to the same accuracy as, for example, SPOT data.

To summarise, a satisfactory DEM could be obtained from ERS-1 images using the approaches developed in this study which could reach an accuracy of 20.18m for the same side and 12.23m for the opposite side with the coverage of better than 80%. However, the orbit information unique to ERS-1 was observed to play an important role in the accuracy of DEM derived using the methods developed. If this information was not provided, other rigorous alternatives are required for its determination and these were investigated.

This research project has made its contribution by establishing a general model able to determine the factors that would influence the accuracy of the pyramidal matching on the SAR imagery, as well as the development of different approaches based on the object domain to greatly increase the DEM accuracy. Altogether, the results obtained in this study should be a valuable source of information for other similar work to be carried out in the future.

CHAPTER 1

Introduction

1.1 Introduction

The use of the radar imagery can be dated back to the World War II for reconnaissance. It was later adopted for topographic mapping in the early 1970s, when the US Engineers of Army Corps initiated a series of studies that became the basis for current radargrammetry. 1:25000 maps could be generated for entire countries, for example, maps were obtained for Brazil and Venezuela in 1971 and 1979 respectively.

The development of imaging SAR has progressed rapidly, since the techniques of converting signals received from the SAR could be improved digitally. From 1978 onwards, SAR imagery data has mainly been derived from space satellites such as SEASAT, SIR-A, and SIR-B. SEASAT focused mainly on the global ocean surface. Despite the fact that it only remained operational for several months, numerous images of the Earth surface were recorded to demonstrate the possibility of using satellite imageries to monitor the Earth surface. The SIR-B is another important mission leading to many important studies, including rectification [Goodenough et al., 1979], image stereo matching [Ramapryan et al., 1986], as well as the analysis of optimum look angles for stereo viewing [Thomas et al., 1987]. The tendency of using satellite radar imagery for various applications has become apparent in recent years, as more satellites carrying SAR have been launched, including NASA's Venus radar mapping mission Magellan, ERS-1, SIR-C, RADARSAT, and JERS-1. ERS-1 is the image data source utilised in this study and this satellite, along with RADARSAT, will be introduced in the next chapter.

1.2 Overview

The ground research work on topographic mapping from radar imagery, which involved the investigation of the object model, was first carried out in late 1960s. After that, pioneering research [Dowman and Morris, 1982] on the evaluation of the topographic mapping using radar imagery was undertaken, in which the number of urban features that could be identified was compared with those on aerial photographs.

The authors made the conclusion that SAR had a potential for small scale mapping and map revision, but more work was required to validate this proposal. From then on, a spectrum of studies related to radar image mapping were carried out, from the introduction of intersection [Leberl, 1976], the derivation of error modelling [Leberl, 1979], to the investigation of algorithms used for the automatic matching [Leberl, 1994]. In UCL, a series of studies on radar image mapping has been carried out over the years, and one of the remarkable achievements was the proposition of the analytic method as a mathematical model for intersection. This method was originally proposed in Clark's Ph.D. thesis to geocode SIR-B imagery and was subsequently used in an intersection algorithm for manual check points on different stereo pairs of ERS-1 images. Valuable conclusions were drawn based on Clark's work, and one of the objectives of this study was to further evaluate her findings by testing with more matching results.

Lately, most of the studies regarding radar image mapping have incorporated another sophisticated technique named interferometry to derive a Digital Elevation Model (DEM). This technique was developed in the Jet Propulsion Laboratory (JPL) in 1974, and it uses two complex SAR image data acquired by the two passes separated by the multiple of a repeat cycle to calculate the phase difference between two corresponding image points. Based on existing knowledge regarding orbit parameters, the phase difference can be related directly to the altitude on a pixel by pixel basis to generate DEMs. Unlike stereoscopic SAR, this technique deals with pixel phase rather than its intensity. Interferometry is believed to give better DEMs, but the technique still has unresolved problems and has not been proved over a wide range of land cover and atmospheric conditions. This is evident in the latest study undertaken by Kenyi and Raggam [Kenyi and Raggam, 1996], in which the accuracy of the generated DEM could achieve a Root Mean Square Error (RMSE) of 9m by using control points.

The studies described above have illustrated that radar image mapping is a promising subject worth investigating. In addition, it offers the following advantages:

- 1) it is an active sensor and the illumination can be controlled at specified incidence angles, which may produce overlapping images suitable for mapping.
- 2) its resolution is independent of the distance to the object.
- 3) it can penetrate surface layers of snow [Leberl, 1990] and vegetation, which is important for some areas that can not be covered by other sensors, such as the polar region.
- 4) it can provide 3D information by interferometric or stereoscopic SAR.

Despite the advantages described above, some drawbacks do exist in several aspects in the application of radar image mapping. Instead of processing digital image data directly by using normal computer workstations that are more feasible and can be easily modified to suit other image types, some studies actually employed more expensive and inflexible analytic stereo plotters [Leberl, 1988] and other digital stereo workstations [Toutin, 1996]. In addition, due to the lack of the orbit information, the geometric modelling for most studies was completed by selecting ground control points followed by the employment of less reliable polynomial functions. Moreover, almost all evaluation of the final derived DEM from SAR carried out in the past were based only on a small number (<100) of selected points instead of comparing on a large scale (e.g. DEMs).

1.3 Aims

The main purpose of this study was to develop an automatic approach to establish a standard model that is able to derive DEM information with great accuracy from the stereoscopic SAR imagery, and to subsequently investigate its potential and limitations. The methods developed in this study were validated using the ERS-1 image data, but they should also be applicable to other similar new radar images e.g. RADARSAT.

Considering both the advantages and the problems yet to be solved regarding the use of radargrammetry, this study aimed to achieve the following objectives :

- (1) Assessment of an existing automatic matching algorithm, combined with a) the use of random seed points and b) the sophisticated area-based GRUENS algorithm, to determine its ability to create DEMs with dense coverage as well as greater accuracy from radar imagery automatically.

- (2) Evaluation of the analytic intersection algorithm by using the Doppler equation and range equation to obtain the terrain height. This new approach utilises the header data available without the requirement of control points. In addition, a comparison of the new approach with other imagery previously completed by other research groups would be carried out.

- (3) Further analysis of the above analytic algorithm by incorporation of control points to examine the impact of these control points on the analytic algorithm.

(4) Evaluation of the feasibility of deriving DEMs from the SAR imagery. This was achieved by comparing numerous matching points on a large scale, instead of a small number of selected points as generally done in the past.

(5) Investigation and validation of the geometric conditions for stereo pairs under different situations and for which purpose, three stereo pairs, namely the same side and the two opposite sides, were included in this study.

(6) Utilising a normal computer workstation facility to prove the feasibility of deriving a DEM from SAR imagery without any analytic stereoscopic workstations, which could provide a good example for generating reliable results at affordable cost.

1.4 Outline of This Thesis

This thesis is in total divided into 9 chapters. Chapter 1 gives a general background introduction on imaging radar, with regard to its history, development and previous studies undertaken. Also included are the objectives of the research project. Some important satellites, including ERS-1, RADARSAT and SIR-B, are introduced in Chapter 2. Some basic yet very important concepts of SAR related to this study are also mentioned. These include the fundamental theory of SAR, SAR image processing, backscattering effects and SAR geocoding techniques. Chapter 3 focuses mainly on an investigation of the special features of SAR stereoscopy, as well as its limitations when utilised for different types of stereo pairs. The latter part is subdivided into several sections, discussing for example the characteristics of SAR images and speckle reduction filters. Chapter 4 examines the pyramidal stereo matching strategy adopted in this project, for which its principles and functions are introduced along with other related programmes. The intersection algorithm used for ERS-1 image data, named the analytic approach, is studied in great detail in Chapter 5, and an overview of other intersection algorithms used previously is also included. In Chapter 6, the test site and the three ERS-1 image data stereo pairs are described and the evaluation algorithm is also stated. The pyramidal matching results carried out in this study is described in Chapter 7, which covers the majority of the stereo matching results derived from this research project. This chapter considers various factors that could influence the matching results, which include the strategies to be used by defining the parameters in the PDL file, the disparity sum and the image inherited characteristics. The underlying purpose as well as the function of random seed points are also introduced, and the advantages of pyramidal matching are listed. A proposal

for a systematic analysis to investigate various aspects of the pyramidal matching is made. In Chapter 8, the enhancement of the DEM accuracy by the object domain approach instead of the image space, used in Chapter 7, is studied. Two main strategies are utilised here, one using the geometric condition and the other requiring the initial DEM information. The impact of incorporating control points on the results of intersection are also analysed. The last chapter gives a summary of the work described in all previous chapters as well as conclusions. Future related studies that need to be carried out are also discussed. Four appendices are included in the last part of this thesis. Appendix A lists the derived formula for the Adaptive Least Squares Correlation (ALSC) algorithm in detail. Both Appendix B and C give the header information of the three ERS-1 image data used in this study. Appendix B lists the original header data that was used for intersection, while in Appendix C the information of control points is also incorporated. Appendix D is a glossary of new terms that were defined in Chapter 7 and 8, for the convenience of reading.

CHAPTER 2

SAR Sensors and Data Products

2.1 Introduction

In this chapter, background information on ERS-1 and other common sensors is introduced to provide a context for this study. The principal characteristics of these sensors are listed in Table 2.1. The image formation of SAR imagery is rather complicated compared to the traditional optical imagery. To facilitate a better understanding of SAR imagery, an overview of its image formation process is provided in this chapter. Backscattering of the radar signal is also analysed here along with some fundamental concepts on the principles of SAR images. In the last section, there is a brief outline on geocoding techniques.

	SEASAT	SIR-B	ERS-1	JERS-1	ERS-2	RADARSAT
Launch date	27-June 1978	5-Oct 1984	25-Jul 1991	11-Feb 1992	20-Apr 1995	4-Nov 1995
Band	L	L	C	L	C	C
Repeat pass	3, 17	1	3, 35 168	44	35	24
Swath width	100km	20-40km	100km	75km	100km	75-500km
Resolution	25m	15m-25m	25m	18m	25m	10m-100m
Incidence angle	20°	15°-65°	23°	35°	23°	10-60°

Table 2.1: Summary of principal characteristics of SAR sensors

2.2. ERS-1: Overview

2.2.1 Introduction

On July 17, 1991, the European Space Agency (ESA) launched the first European Remote Sensing Satellite (ERS-1) into an 780 km altitude in space to provide real-time and useful information of Earth for many fields of research. With

the antenna folded its size is approximately 12m*12m*2.5m, weighting 2400kg, which makes it the largest and most sophisticated free-flying satellite ever built in Europe. ERS-1 is a forerunner of a new generation of satellites for environmental monitoring.

Compared with other contemporary satellite systems, ERS-1 has many advantages. It has the ability to meet several operational requirements for data products requested within a few hours of observations. This ability enables ERS-1 to make significant contributions to meteorology, sea state forecasting and monitoring of sea ice distribution. In addition, the stability of the ERS-1 orbit has shown a new direction in using the interferometric technique for cartography application. Another advantage of ERS-1 is that it could gather data from remote areas such as the polar regions and the southern oceans where little information has been collected before.

2.2.2 ERS-1 missions

The ERS-1 specific mission objectives are both scientific and operational. It aims to provide users with Earth observation data for a wide variety of applications and this can be achieved by its pre-determined global coverage. The main targets of the ERS-1 mission are oceans and sea-ice zones at global scale as well as some coastal areas of interest.

In order to meet the various objectives of its missions, the ERS-1 was planned to move around the Earth in a elliptical sun-synchronous polar orbit. For different purposes, ERS-1 has 8 main phases. The fundamental data of these 8 phases are listed in Table 2.2:

Mission Phase	Period	Repeat
orbit acquisition	17.07.91-30.07.91	3-day
commissioning	26.07.91-10.12.91	3-day
first ice	28.12.91-30.03.92	3-day
roll-tilt mode	02.04.92-14.04.92	35-day
multi-disciplinary	14.04.92-15.12.93	35-day
second ice	01.01.94-31.03.94	3-day
geodetic	28.09.94-21.03.95	168-day
tandem	21.03.95-06.05.96	35-day

Table 2.2: The period and repeat cycle duration for ERS-1 eight main phase

In the above 8 phases, the last long phase was introduced primarily to support the oceanographic applications without orbit disturbance. Another important campaign that was Roll-Tilt mode imaging. In this mode, the Earth was imaged by a larger incidence angle (35° instead of 23°) for a short period (4-13 April, 1992). This Roll-Tilt mode image is crucial for stereoscopic SAR, because it provides a good opportunity to evaluate the impacts of intersection angles on the results of intersection by its larger incidence angle. Results of testing them will be shown in Chapter 8.

On the ERS-1, the payload consists of active and passive microwave sensors and a thermal infrared radiometer, of which the Active Microwave Instrument (AMI) is the most important for mapping. AMI combines the functions of SAR and a Wind Scatterometer. The SAR operates in image mode for acquisition of wide-swath, all weather images over oceans, polar regions, coastal zones and land under all-weather conditions. This is named high bit rate mission (HBR). In the HBR, as the data rate is too high for on-board storage, it is only acquired within the reception zone of suitably equipped ground receiving stations. In contrast to the high bit rate mission, the low bit rate mission (LBR) was operated globally which consists of Radar Altimeter, Along Track Scanning Radiometer, AMI Wind Scatterometer, and AMI SAR in Wave Mode. Since LBR is of a global nature, along each orbit, the LBR data are stored on board then dumped to one of the ground receiving stations before the next orbit. The high bit rate mission is in particular demand since it is driven by the request of users and is constrained by the actual operations of the ground stations around the world. Therefore, this mission requires careful planning in advance.

In this study, we only used the SAR imagery as our data source, therefore, the above mentioned SAR image acquisition should be introduced further here. SAR data can only be acquired for a maximum duration of approximately 12 minutes per orbit. The rectangular antenna of the SAR directs the narrow beam sideways and downward onto the Earth surface to obtain strips of high resolution imagery of about 100km in width. This high resolution imagery is obtained through a series of image processing techniques which will be introduced in later sections.

2.2.3 ERS-1 ground segment

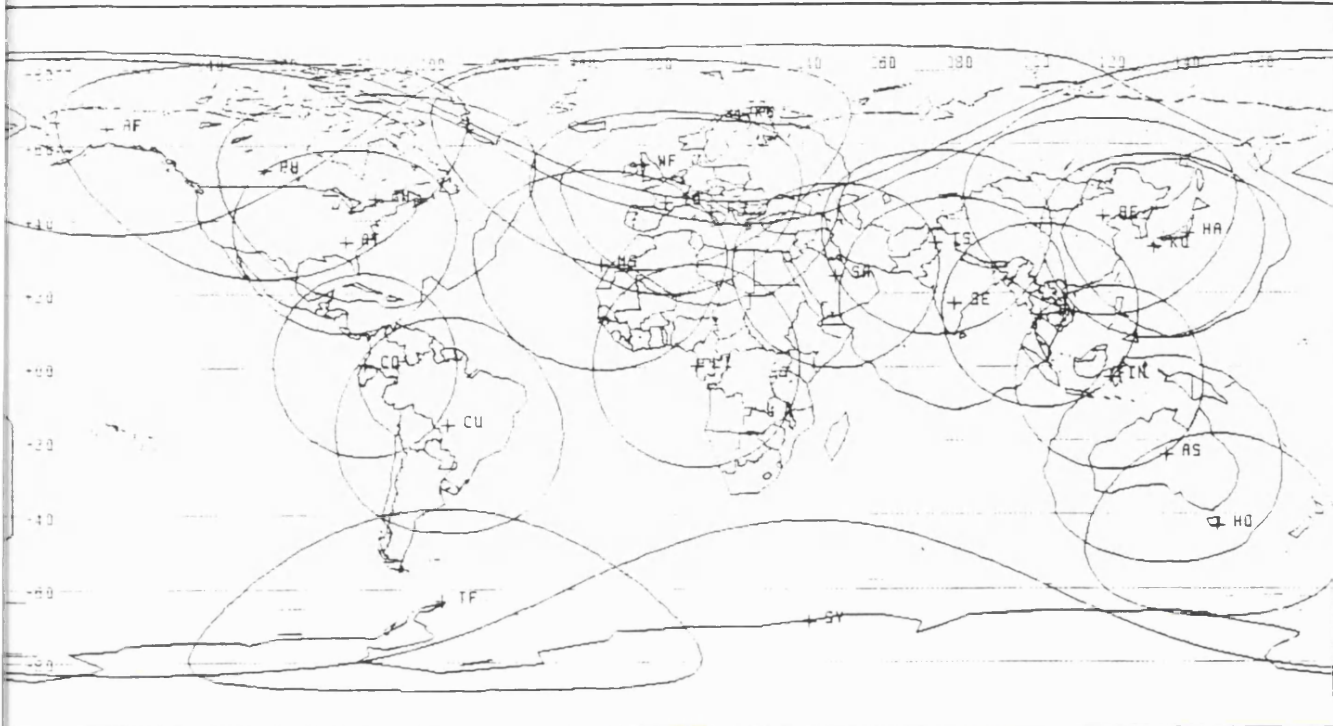
For reception, processing, and archiving the data, the ERS-1 ground segment was built as a “network”. The main components of the ground segment include the ESA monitoring center, control and services facilities, various ground stations, processing and archiving centers as well as the user interface. The monitoring center

is located in Darmstadt, Germany and named the Mission Management and Control Center (MMCC). MMCC monitors and controls the spacecraft and schedules its payload operation through the ground station in Kiruna. The Earthnet ERS-1 Central Facility (EECF) is located in Italy, which carries out all user interface functions and is also responsible for data coordination, dissemination as well as quality control. In ground stations around the world acquire the ERS-1 data almost routinely, meanwhile they also process and disseminate the fast-delivery products. The locations of these ground receiving stations (1993, September) as well as their coverage zones to are shown in Fig. 2.1. There are four Processing and Archiving Facilities (PAF), located in Germany, France, Italy and Great Britain respectively. The PAF deal mainly with off-line precision products and the archiving and distribution of ERS-1 data.

2.3 ERS-1 Data Products

There are in total 7 data products from the AMI SAR Image Mode. Each product is obtained by a series of complicated image processing procedures at PAFs (refer to [Gredel, 1993] for detailed procedures). Among these products, the Complex Image is a single-look, slant-range digital image. It is intended for ESA use in SAR quality assessment and calibration, with 2500 samples in range and 15000 samples in azimuth. The Precision Image (PRI) is a 3 non-overlapping looks, ground range digital image. The ground range is a zero-doppler coordinate system. It has been corrected for antenna elevation gain and range spreading loss and has been specified for users to perform application-oriented analysis. This product has 8000 pixels in ground range with at least 8200 pixels in azimuth, and covers 100km in ground range, 102.5 km in azimuth. Its pixel size is 12.5m for both ground range and azimuth. The Roll-Tilt image (RTM) is obtained by rotating the satellite body by 9.5° , allowing the operation of the AMI SAR at a 35° incidence angle. It is also a multiple-looked, ground range image and has the same pixel size as the PRI image.

Fig. 2.1: Locations and coverage zone of ERS-1 ground receiving stations



Key:

ESA Stations

KS Kiruna, Sweden
 MS Maspalomas, Spain
 PS Prince Albert Low Rate, Canada

FS Fucino, Italy
 GS Gatineau Low Rate, Canada

National Stations

GH Gatineau High Rate, Canada
 TO Aussaguel, France
 TS Tromsø, Norway
 LI Libreville, Gabon
 (German Transportable Station)

PH Prince Albert High Rate, Canada
 TF O'Higgins (Antarctica), Germany
 WF West Freugh, UK

Foreign Stations

AF Fairbanks, USA
 AT Atlanta Test Site, USA
 CO Cotopaxi, Equador
 HA Hatoyama, Japan
 IN Pare-pare, Indonesia
 KU Kumamoto, Japan
 SE Hyderabad, India
 TH Bangkok, Thailand

AS Alice Springs, Australia
 BE Beijing, China
 CU Cuiaba, Brazil
 HO Hobart, Australia
 IS Islamabad, Pakistan
 SA Riyadh, Saudi Arabia
 SY Syowa (Antarctica), Japan

2.4 RADARSAT Overview

RADARSAT is a sophisticated Earth observation satellite developed by Canada to support the operational needs mainly on environmental monitoring and other related fields such as agriculture, cartography and hydrology. The satellite was launched on November 4 in 1995 on a Delta II rocket and is expected to last for 5 years. RADARSAT will provide Canada as well as the world with a large amount of timely-delivered data which will meet the needs of environmental and resource professionals worldwide.

RADARSAT was developed under the management of the Canadian Space Agency (CSA) with strong support from industry (e.g. Spar Aerospace, CAL Corporation), provincial governments (e.g. Quebec, Ontario), international partnership (e.g. NASA) for the launch platform as well as other approximate 100 or so organisations in Canada. The CSA is responsible for the design and integration of the overall system for its control and operation. The data reception and processing are carried out in the ground receiving stations located in three different provinces and states in Canada and United States including, Prince Albert, Saskatchewan; Gatineau, Quebec; and Fairbanks, Alaska. .

RADARSAT carries only one SAR instrument and operates in C-band like the ERS-1. While in operation it will provide more choices in the manner for which the images are acquired. The image swath can vary from 35km to 500km giving rise to corresponding image resolution ranging from 10m to 100m. Incidence angles can be altered from less than 20° to more than 50°. RADARSAT provides global coverage with the flexibility to fulfil specific requirements. It can cover the Arctic daily regardless of the weather condition and most of Canada every 24 hours depending on the swath selected. The entire Earth would be covered every 24 days using the standard 100km wide swath. The coverage of the Arctic area is of special importance for some shipping companies and government agencies who need to deal with ice reconnaissance.

RADARSAT is in a sun-synchronous orbit and users can view a scene repeatedly at the same local time in 6 & 18 hours. This is particularly important when monitoring e.g. crops with the multi-temporal data, for which the influences of the diurnal variation needs to be minimised. Moreover, this orbit is "dawn-dusk", which means that the satellite's solar arrays will always face the sunlight. Therefore, RADARSAT primarily relies on solar rather than the battery power, and in turn it provides the users with the optimal viewing opportunities. For each orbit,

RADARSAT can capture up to 28min worth of data covering up to 1.1 million square kilometres of the Earth's surface. For convenience of users, the data can either be down-linked in real time or stored on one of the two tape recorders until the spacecraft is within the range of a receiving station. To satisfy users who require timely data, the RADARSAT processing system can deliver data to on-line users within a few hours after the satellite has passed over an area. There are three main types of imaging data acquired by RADARSAT including the quick look, georeference, and geocoded data. Quick look consists of uncorrected images, while georeferenced products are geometrically corrected to compensate for the Earth curvature. The geocoded products on the other hand are rectified on a standard map projection.

2.5 SEASAT, SIR-A, SIR-B and SIR-C Overview

In 1978, SEASAT was launched by NASA to develop global coverage with a radar imaging sensor that operated at L-band (25cm wavelength). Unfortunately, it was only operational for three months due to fatal defects on board of the satellite. Within the three months though, many coverages were obtained over land and Arctic regions and were very useful for research work on radar image mapping. This encouraged NASA to carry out another spaceborne radar imagery experiment. SIR-A (Shuttle Imaging Radar) carried by the space shuttle Columbia. It was launched in 1981 and it was also operated at L-band with primary use in exploring geological mapping. SIR-A obtained images at the selected incidence angle of 50° so that the acquired backscattering are dominated mainly by the surface roughness, which was helpful for the interpretation.

SIR-A recorded raw signals on film and subsequently converted the film to images via an optical correlator at the Jet Propulsion Laboratory (JPL). SIR-A covered ten million square kilometers of land and ocean including several previously unsurveyed area, wet tropical areas that were not acquired by the Landsat satellite due to perpetual cloud cover. The resolution of SIR-A imagery was 40m and along with the fact that it can be easily interpreted, this imagery was used for a variety of applications in geology, geomorphology and agriculture studies. One of the major accomplishment of SIR-A is that it detected the sub-surface drainage networks beneath the Sahara desert for the first time. It could also be used for topographic mapping utilising crossing orbit tracks and this subject was explored by Korbick et al., in 1986, who studied a pair of SIR-A of the Greek islands [Korbick, et al., 1986]. This pair of imagery was intersected at 34° , and the height was extracted using an analytical

photogrammetric plotter. The resulting height accuracy was $\pm 98\text{m}$, which is about ± 2.5 times of the image resolution element.

A further NASA space shuttle mission was launched in 1984 labelled SIR-B. It had many similarities to SIR-A in its system design, however, with a major difference in the image recording system. Unlike SIR-A, it could convert the signals received to images using a digital correlator. In addition, the slant range resolution of SIR-B was better than SIR-A, being 15m and 40m respectively. Another important feature of SIR-B is that it could vary the look angle. This is important with respect to radar image mapping, for it could provide image stereo pairs with different intersection angles so that different geometric conditions could be examined. This feature subsequently demonstrated how incidence angle could influence the capability of interpretation of various terrain features.

The Shuttle Imaging Radar-C (SIR-C) was the third in a series of space shuttle based Synthetic Aperture Radars sponsored by NASA designed to fly on a low Earth orbit. Unlike the SIR-A and SIR-B that operated at the single L-band and had single horizontal polarisation, SIR-C was a dual-frequency quad-polarisation radar operating at both L band and C band frequencies. The SIR-C was important for being the first instrument that could provide the multiseason coverage of a multiparameter imaging radar. The image data was collected over incidence angles from 17° to 63° .

2.6 SAR Fundamental Principles

An imaging radar works by transmitting its energy to scan the earth's surface. The transmission of energy is by means of radio microwave at the rate of pulse repetition frequency (PRF), emitted by the sensor. The bandwidths of the imaging radar determines the magnitude of range resolution. In imaging radar, two resolutions are considered with respect to two different directions. The range resolution is on the direction of the energy propagation, which is also called the range direction or across-track. The other direction is related to the flight direction of the sensor named azimuth or along-track direction.

For imaging radar, if there are two objects on the ground, then the reflected signals must be received separately by the antenna; or else the image of the two objects will be blurred altogether. The ability to discriminate between the objects is determined by their slant range and this slant range could be further calculated by the bandwidth. As a result, the bandwidth affect the range resolution as stated earlier.

Considering the azimuth resolution at a given range as shown in Fig. 2.2, it is determined by the angular beam width β of the antenna and the ground range, which is as indicated in equation (2-1).

$$R_a = R \cdot \beta \quad (2-1)$$

where:

R_a : the azimuth resolution
 β : beam width of the antenna
 R : range distance

The beam width of antenna β could be further computed by the wavelength and the physical length of the antenna as equation (2-2).

$$\beta = \lambda / L \quad (2-2)$$

where:

λ : wave length
 L : physical length of the antenna

combining (2-1) and (2-2), becomes

$$R_a = R \cdot \lambda / L \quad (2-3)$$

which indicates that, if we want to keep R_a small, then either R or λ should be decreased or L should increase. The types of radar whose beam width is controlled by the physical length of the antenna are called brute force or real antenna radar. As expressed in equation (2-3), the antenna must be very long for the antenna beam width to be narrow. The benefit of this brute force radar is its simple design but it is very restricted to short wave length for good resolutions. This restriction is rather disadvantageous, because short-range systems and short wave lengths experience greater atmospheric absorption. This problem of the brute force system can be overcome by a Synthetic Aperture Radar (SAR) system, which employs a short physical antenna but with special signal processing techniques, the effect of a very long antenna can be simulated.

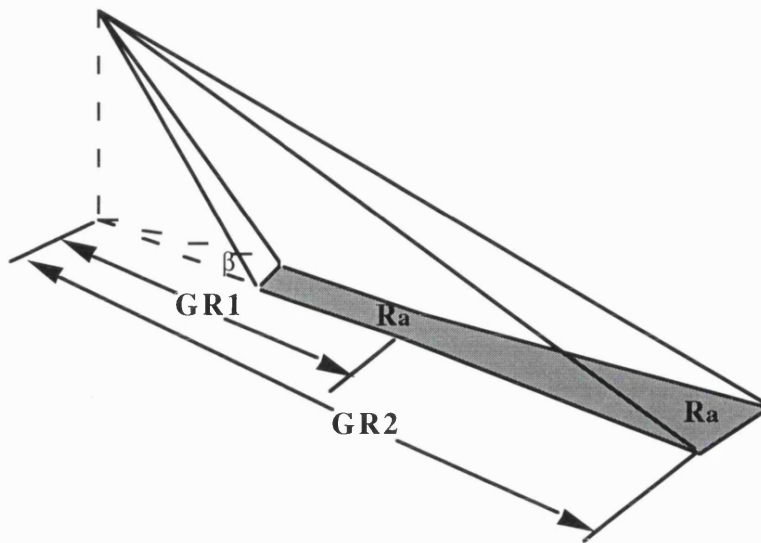


Fig. 2.2: Dependence of the azimuth resolution (R_a) on antenna beamwidth(β) and ground range (GR)

In SAR, for each object point P, the antenna transmits a pulse and records the returned echo along the flight track at each position. The Doppler shift of the echo from P will be firstly positive, then decreases to zero, then becomes increasingly negative until P exits from the beam (see Fig. 2.3). The zero Doppler will give the time at which the target is perpendicular to the azimuth. By recording the Doppler shift history and comparing with reference frequency allows many returned echoes to be focused on one single point. This function is equally used to simulate the effective length of the antenna as the distance travelled by the signals sent out from the antenna (see Fig. 2.4). As a result, the azimuth resolution is independent of the range between the sensor and the object and is only proportional to the size of the physical antenna.

2.7 Radar Backscattering

The ability to interpret features on an image is largely dependent on the degree that different targets return the signal. This signal-returning process is affected by many factors such as the wavelength transmitted by the antenna, the size, position, orientation and texture of the object, which can be estimated by the radar equation shown in equation (2-4). In this equation, the antenna gain, the transmitted power, as

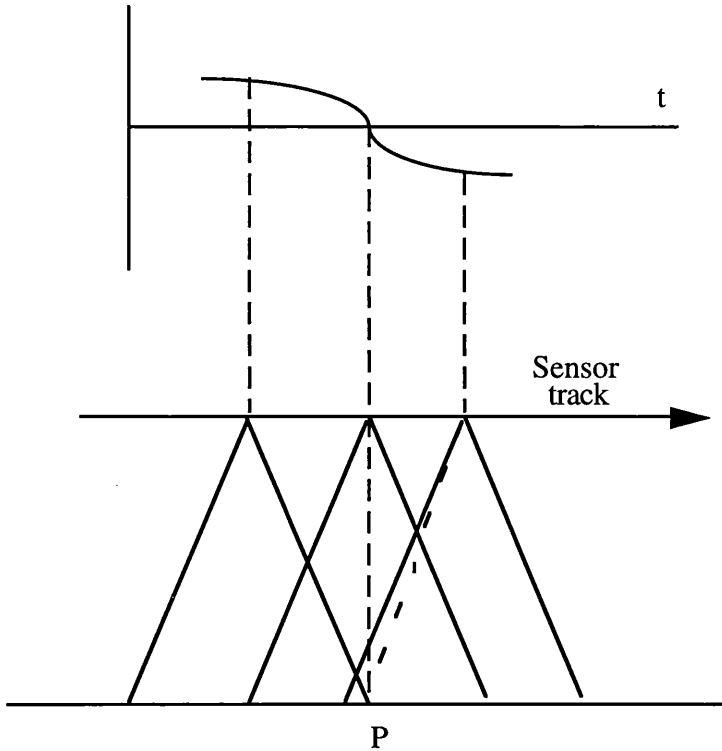


Fig. 2.3: Doppler history of a point target (after [Elachi, 1988])

well as the wavelength can all be controlled by the radar designer, all except one variable, the radar cross-section (σ). Therefore it is the factor which is of great importance in distinguishing the targets. Targets which may in all other respects be completely different can not be distinguished if they have the same backscatter.

$$S = \frac{P_t G^2 \lambda^2 \sigma}{(4\pi)^3 R^4} \quad (2-4)$$

where:

- S : returning signal
- P_t : transmitted power
- G : antenna gain
- λ : wavelength
- σ : radar cross section
- R : distance from the antenna to the target

The radar cross section of an object is partly dependent on the radar wavelength. If the target size is much larger than the wavelength, then σ will be roughly equal to the size of the real area. When the target is approximately the same as the wavelength, however, σ will be varied widely with changes in the wavelength.

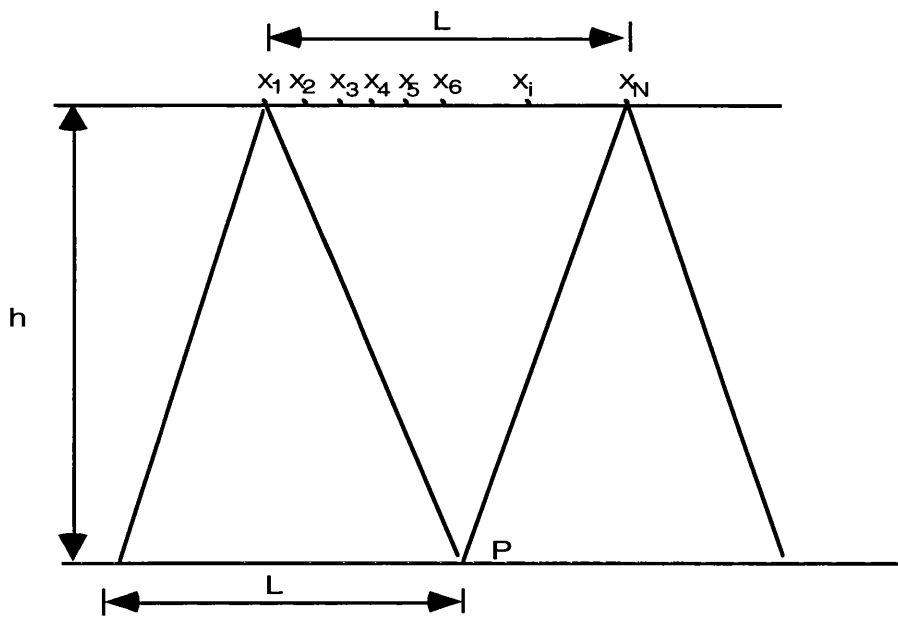


Fig. 2.4: Geometry of a synthetic aperture array. Point P is visible from locations X_1 to X_N . The length of the synthetic aperture is equal to the real antenna footprint L . (After [Elachi, 1988])

The surface of the target also has its impact on the aspect of returning energy of radar. The roughness of the surface of an object surface is a function of its relief variation with respect to the incident wavelength. With rougher surfaces, a greater proportion of energy could be reflected, and in contrast, flatter surfaces are specular reflectors from which little or no energy could be reflected back. A surface inclined towards the radar will have a stronger backscatter than a surface that is facing away from the radar. The characteristics of the objects also affect the backscattering. Vegetation is usually regarded as a moderately rough surface and appears grey in a radar image. Cities or street buildings act as corner reflector, for they have many right angles, successive specular reflections will occur and they will appear very bright (white) in radar images. Different incidence angles also cause variations in backscattering, small incidence angle will result in high backscattering, and the slope or topography of the terrain will dominate the reflection. In contrast, greater incidence angles will decrease the backscattering which becomes more sensitive to the surface texture. This relationship between the incidence angles and backscattering is affected further by surface roughness. When plotting incidence angle (Y-axis) against backscattering (X-axis), a steeper slope would be obtained from smooth surface, while almost flat when a rough surface is encountered.

2.8 SAR Image Processing

For the imaging radar, the transformation of the obtained object signal to images is rather an important aspect to be considered in this study. Overall, these transformations can be proceeded in two directions, either optical or digital, and both methods involve a series of complex procedures. In this study, only digital image processing was considered and its general concept should be introduced. Notice here that, the real situation of interaction between the sensor movement and the object has not been dealt with in this study. Rather, the start-stop approximation was adopted, which assumed that the radar platform remained stationary while transmitting and receiving the pulse. After the sensor moves to a new position, it will again remain stationary while transmitting or receiving the next pulse.

SAR digital image processing is mainly performed in the frequency domain to reduce the number of arithmetic operations. It consists of a sequence of convolution operations and a flow chart of the whole digital image process is shown in Fig. 2.5. Each step will be further introduced in the following subsections.

As seen in Fig. 2.5, the first step is to process the SAR raw data by compressing range in the frequency domain to correlate the returned signal with the transmitted chirp. The chirp is a linear frequency modulated (LFM) pulse, which consists of a long pulse, and its frequency changes linearly as a function of time. After compression, higher resolution can be obtained by a dechirping process to remove the modulated frequency from the returned echo. When the range compression is completed, another effect in the SAR imagery should be considered and corrected. It is called “range migration”. The range migration expresses the difference of the nearest range and the actual range in any given time interval, which is caused by the shifting sensor positions relative to the target points. The range migration is also affected by orbit eccentricity and earth rotation. After the range migration has been corrected, the compressed range is then input to a corner-turn memory in one row, these resulting “line-up” signals are then accumulated until the memory rows are full. Next, the data is read one column at a time and correlated with azimuth direction using an FFT (Fast Fourier Transform). The azimuth correlation process needs to utilise the azimuth chirp and it is the most complicated requiring most of the computation time. This correlation is preferably performed on the radar signal and azimuth frequency space referred to range-Doppler space with the azimuth reference function.

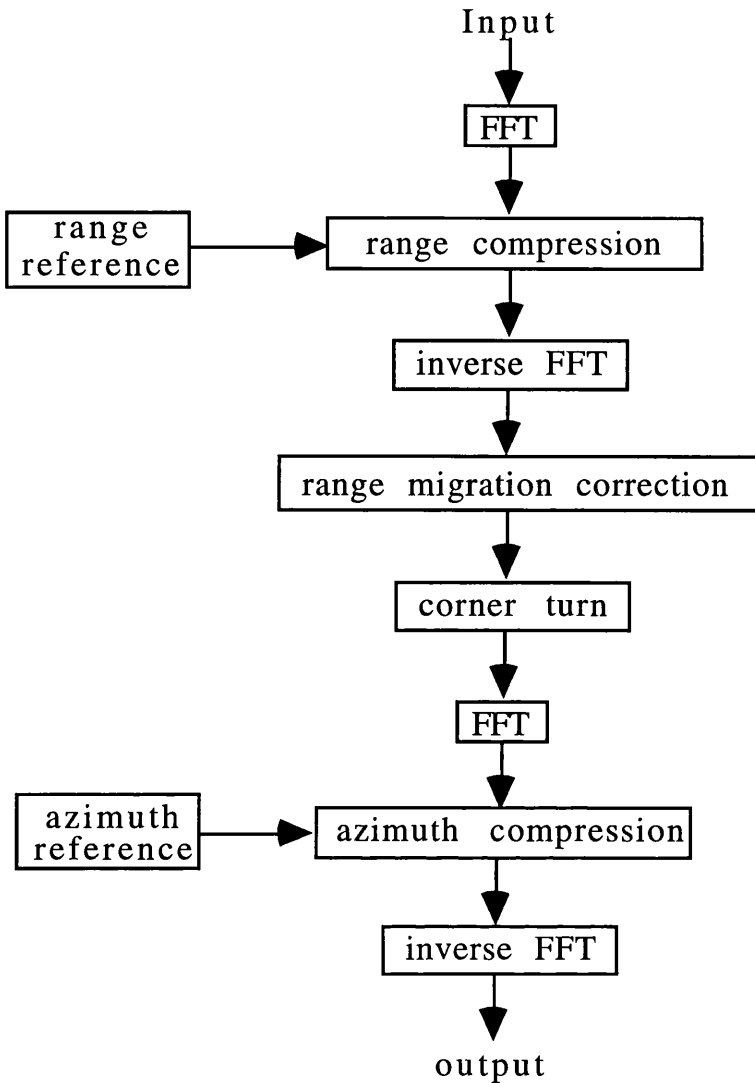


Fig. 2.5: Flow chart of SAR image processing using the frequency domain approach

2.9 SAR Geocoding

For SAR imagery, apart from layover, foreshortening, and shadow effects introduced earlier, is still affected by a number of radiometric and geometric distortions caused by the terrain relief which could prevent the effective utilisation of imagery. The elimination of these distortions is very important in many applications of remote sensing, such as multitemporal change detection. The procedure that is able to remove the distortion specifically for SAR imagery is named geocoding.

In general, three algorithms are employed to proceed geocoding, namely the polynomial, parametric and SAR range-Doppler methods. The polynomial methods

requires a large number of control points (GCP) in the image to allow the computation of polynomial coefficients of the mapping function. The outcome of this geocoded image is heavily dependent on the quality of the GCP. A general review of this method can be found [Naraghi et al., 1983]. The advantages of this method is that it does not need the ephemeris data. Noted that this method is best used for flat regions, as it is unable to deal with areas with varying terrain relief.

Parametric method attempt to model the geometry relationship of the image and object space [Meier and Nuesch, 1985]. The relationship can be described by the Doppler equation and range equation. In other words, for each image point, a set of Doppler and range equation can be constituted for derivation of the target coordinates. Similar to resection in Photogrammetry employed to calculate the exterior orientation, here, we measure the coordinates of control points in object space in order to predict the sensor position, velocity etc.. The above two equations are nonlinear, so the unknowns are solved by an iteration technique. After each iteration, the consistency of the two equations are checked by the updated parameters of sensors and when the residuals of the two equations are below a pre-determined limit, the process is terminated. Then each image point can be transformed into the map reference system by using these calculated Doppler and range equations. This method still has a disadvantage, in that it requires a large number of very good GCPs and the preliminary data of sensor must be rather accurate, otherwise, the problem of non-convergence will occur.

If orbit information is available, the SAR range-Doppler methods can be used to proceed the geocoding [Noack et al.,1987]. This method also takes advantage of the above two equations, but unlike the previous method, it will further implement the variation of Doppler frequency in the geocoding. For it will fully employ auxiliary information (e.g. orbit parameters), so a minimal number of GCPs will be required. Since for ERS-1, orbit information will be provided in the header file, this method is said to be suitable to geocode ERS-1 image data [Clark, 1991].

In this method, depending on the availability of elevation data of the test area (DEM), the geocoding could proceed in two different ways. If a DEM can be acquired, precision terrain geocoding could be adopted which rectifies the image pixels' position in a pixel-wise way. This strategy could create an ortho-image but consumes a considerable amount of computing time. On the other hand, if the DEM data is not available, we can consider the Earth as an ellipsoid, and the area covered by the sensor illumination is "flat" rather than a real undulated surface. This strategy is named standard ellipsoid geocoding. Note that even the control points are not required

for this standard ellipsoid geocoding, [Roth et al., 1993], however, the outcome will still suffer from the terrain effects.

After the geocoding procedures has been completed, the rectified image pixels may be on non-integer positions for which the grey value needs to be recalculated by the bilinear resampling function. Notice that this resampling procedures will also degrade radiometric image quality, great care therefore must be taken when analysing the geocoded products.

2.10 Summary

In this chapter, several common satellite sensors including ERS-1, RADARSAT, and SIR-B were introduced. The ERS-1 SAR image data products such as PRI and RTM were described in greater detail since they were the data sources utilised in this study. The RTM image is acquired by rotating the satellite body, its incidence angle is therefore larger compared to the PRI image. Variable incidence angles can be used as a good tool to evaluate the best geometric conditions for the different stereo pairs studied with different intersection angles. Another important subject, the techniques of geocoding, was also discussed as it gives an introduction to the relationship between the image and object space. Included also were the Doppler and range equations used in geocoding, both of which will be applied in this study to generate the DEM information.

CHAPTER 3

Stereoscopy Using SAR Imagery

3.1 Introduction

This chapter gives a general introduction to several aspects of SAR imagery, including image characteristics and stereoscopy, that are related to stereo matching. A sound understanding of these subjects is the basis for further research in this study. Three preliminary SAR image characteristics will be mentioned in the first section, followed by an illustration of the concept of stereoscopy, focusing especially on SAR imagery. The exaggeration factor would also be analysed and the elements that influence the viewing ability are summarised. A general discussion on speckle-removing filters is included here. Finally, attention will be drawn to the difficulties in stereo matching that were encountered.

3.2 SAR Image Characteristics

For an imaging radar, due to the principles of acquiring the image, terrain relief will introduce geometric as well as radiometric distortions. These distortions observed in SAR imagery, then affect the matching, interpretation as well as other applications. Therefore, the characteristics of SAR are introduced here before proceeding to practical work shown in Chapter 7 and 8.

When a vertical feature is encountered by a radar pulse, if the top of the feature is reached before the base, then layover is said to occur and the top is closer to the nadir than the base on the imagery. This situation occurs whenever the terrain slope is steeper than the depression angle. The layover effect is most severe in the near image and gradually decreases towards the far range [Lillesand and Kiefer, 1994]. If on the contrary, when the terrain slope is less steep than the depression angle, then foreshortening effects instead of the layover will take place, which will cause the slope of the surface to become compressed on the image. Its severity increases as the steepness of the slope approaches perpendicularly to the depression direction.

The layover as well as the foreshortening will appear as bright fringes on the radar imagery, while the area of shadow will appear totally black. This is because the

shadow frequently occurs on hill slopes, that are facing away from the radar antenna and as a result receiving weak signal or no signal at all. The phenomenon could also be explained by the relationship of depression angle and the back slopes, such that the shadow effect occurs when the latter is steeper than the former. The shadow length will increase with range due to the decrease in the depression angle, which in turn means the shadow is proportional to the incidence angle. The radar shadow is an important factor in interpretation, particularly for geological application. In paper [Kaupp et al., 1982], the author simulated SAR imagery with different incidence angles and concluded that large incidence angles are better for geological applications, for it not only minimises the geometric distortions but also causes large shadows that could provide enhancement of topographic relief. The distortions of layover, foreshortening and shadow are shown in Fig. 3.1.

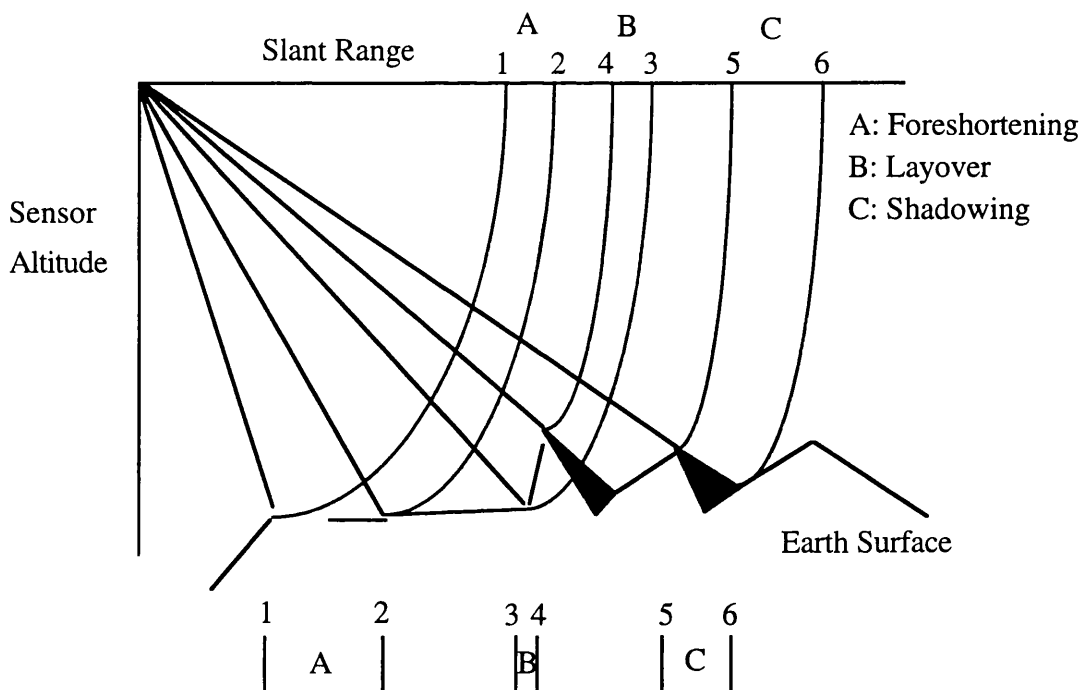


Fig. 3.1: Geometric distortions due to the terrain elevation effects (after (Schreier, 1993))

3.3 SAR Stereoscopy

An optical camera records an image in the same manner as our eyes, therefore, if two cameras are located with the same relative geometry, a satisfactory stereo model could be obtained. Unfortunately, for radar imagery, an image is recorded in a completely different manner. The radar imagery is presented by a range projection, unlike normal photography by a central projection [Rosenfield, 1967], indicating a

different geometric structure. For example, the parallax resulting from a topographic feature will be completely different from that of the airphotos by the camera. To explore this difference, various aspects of the stereoscopic condition should be discussed first. Initial work on radar stereoscopy was carried out by LaPrade. In his paper [LaPrade, 1972], determined the optimum flight configurations for airborne radar by keeping the parallax constant for all images. LaPrade also was the first one to propose the two most common stereo configurations for side-looking radar and defined these as same-side or opposite-side. There are still other arrangements such as the cross-wise which is with smaller angular separations between look directions. It is not possible to achieve the stereo with a single flight line, for the projection circles of the two images will not intersect in a distinct point.

For stereoscopic research, one important factor should be considered namely vertical exaggeration. The vertical exaggeration expresses the scale difference of the vertical scale that is greater than the horizontal scale. It is of great concern to interpreters, who must take this into account when estimating the heights of objects, rates of slopes etc.. In [LaPrade, 1972], the author stated that the vertical exaggeration is irrelevant to stereoscope type and is only dependent on the convergence angle to the eye by stereo pair separation. The vertical exaggeration factor is determined by the value of the image base to height ratio (B_n/H_n) with respect to the stereo viewing ratio (B_s/H_s). The B_n and H_n are the air base and flying height respectively as shown in the Fig. 3.2 for the camera stereo model, and this ratio determines the possibility of creating stereo models in the object space. The H_s and B_s are the eye base and the distance between the height and stereo model which is related to the ability for stereo viewing. If the vertical exaggeration factor is equal to 1, then there is no vertical exaggeration of the stereo model. From experimental work, LaPrade concluded that the optimum exaggeration factor should be 5 for the radar imagery. This exaggeration factor and the parallax could be a function of the height of a feature [Pisaruck et al., 1984], who utilise the regression method to derive their proportional relationship.

Apart from the vertical exaggeration, the stereo viewing of SAR imagery should also be considered. In [Leberl, 1979], the author summarised four factors that would affect radar stereo viewing:

- (1) The stereo arrangement
- (2) The look angles off-nadir
- (3) The stereo intersection angles
- (4) The ruggedness of the terrain

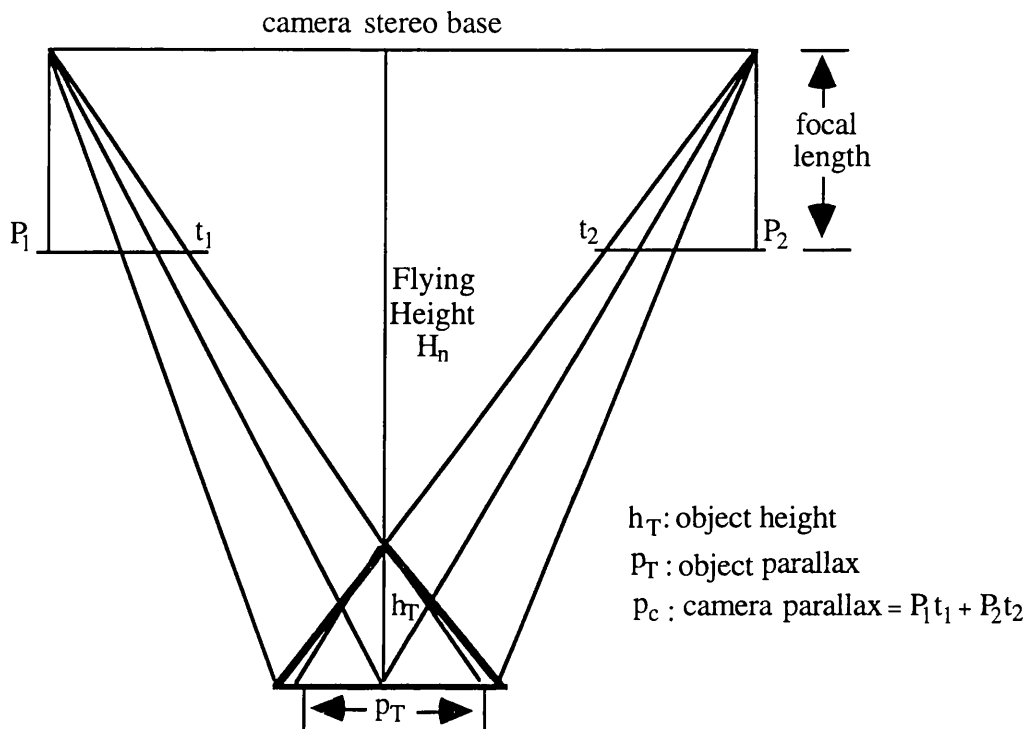


Fig. 3.2: Definition in object space for the vertical exaggeration of camera stereo model (after [LaPrade et al., 1980])

The stereo viewing is inversely related to the geometric conditions of intersection. A good geometric condition should have larger intersection angles. However, this will cause significant differences in the image contents such as tone and texture, which in turn will result in poor stereo viewing ability. An obvious example is that for the opposite side stereo pair, when the illumination direction changes, the resulting image appearance would look very different and thus hampers the viewing abilities greatly. At the same time, opposite side stereo pairs have larger intersection angles leading to greater parallax, resulting in a greater exaggeration factor and consequently giving rise to better intersection accuracy. In contrast, for good visual perception, the smaller intersection angles would be preferred which result in little difference in image tone and texture. Unfortunately, it will cause smaller parallax which is disadvantageous to the intersection. This theory, however, was under scrutiny in [Leberl et al., 1985], in which the author claimed that it is not suitable for all terrain features, as it excludes the error propagation of the base width and parallax. It was therefore one of our objectives to validate this theory by establishing the relationship between intersection angle and the accuracy of intersection and this is shown in Chapter 8.

Considering the look angles, the view ability is better for the same side when the look angles are greater [Leberl et al., 1982], and as the look angles become smaller, greater parallax will be produced creating greater vertical exaggeration. In [Kaupp et al., 1983], this statement was validated by using 18 different combinations of incidence angle on various terrain models. It was shown that the parallax to height ratio was the greatest for small incidence angle of the individual stereo pair, while resulting in the largest intersection angle. This was evident from observing three stereo pairs of (60°/20°, 75°/45°, 70°/40°), where the parallax to height to ratios were 2.17, 0.732, and 0.828 respectively. When the incidence angle became smaller, the relief displacement or image appearance would be adversely influenced to a great extent. The incidence angle was therefore said to be not less than 40° in general [Leberl, 1979]. This requirement, however, does not consider the situation of terrain ruggedness. One should notice that for the high relief terrain, the look angle should be even larger compared to any flat terrain.

In addition to the intersection angles, the viewing ability could also be influenced by several image characteristics such as layover and shadow introduced previously. Layover often leads to confusion for the observers when the image pair is viewed stereoscopically. The problems of stereoscopic viewing on some terrain features by shadow can be overcome by observing from two different directions such as the hill or mountain ridges. However, this is not applicable to the bottom of valleys, and this is the reason why rugged terrain could not be previewed stereoscopically by the opposite stereo pair [Trevett, 1986].

3.4 Speckle Reduction Filters

A single ground resolution cell of ERS-1 for 4-look is 30 meters, large enough that even within each individual cell the feature or roughness of terrain may be varied. Due to the coherent radiation during the matching process, this variation would cause the echoes of each individual surface elements to interfere with each other within the resolution cells. This interference may be constructive or destructive such that it appears as strong or weak signals in radar imagery to cause speckles. The appearance of the speckle is grainy, which reduces the capability of interpreters to discriminate the intensity of grey levels of the imagery and consequently affecting the ability in recognising different targets. In stereo matching, the speckle is also undesirable as it cause a change of textures in images. In this study, where the sheet growing algorithm was used, speckle was expected to strongly influence the accuracy as well as the resulting coverage for the matching. This assumption was indeed tested

by stereo matching the imagery that was processed by using two speckle reduction filters beforehand. The results are shown in Chapter 7.

The methods to remove speckle can be classified into two groups, namely pre-processing and post processing. The pre-processing as suggested by this name is implemented before the image product is formed. The multi-look technique is a common pre-processing technique. The post-processing on the other hand utilises image processing techniques to filter out the noise, among which the low-pass (or smoothing filter) is the most frequently used one. This low-pass filter used is in the spatial domain, some other filters could also be used in the frequency domain, such as the Wiener filter.

The multi-look processing proceeds by adding several non-coherently independent images from different portions of an aperture which will increase the true energy relative to the speckle noise. The signal to noise ratio increases in proportion to the square root of the numbers of images used, while the azimuth resolution is reduced by increasing the number of images. The disadvantage of this method is its requirement for multiple uncorrelated speckled images without considering the image statistics.

Regarding spatial filters, their function is to remove speckles usually by smoothing the imagery. The spatial filters can be grouped into two different types; simple filters or adaptive filters. Simple filters are performed utilising the same algebraic operation on all pixels, while adaptive filters change the operation depending on the local statistics of the pixels in a given window size. Commonly used smoothing filters such as the mean or median filters are classified as simple filters.

Adaptive filters consider the speckle as a multiplicative noise, that is a function of the variance of the local pixels. A low variance is indicative of the absence of feature in a particular window and a strong smoothing effect could take place. Whereas, for the higher variance, it implies that a feature exists and the smoothing effect will be very gentle. The Lee filter is a typical adaptive example [Lee, 1981]. For a flat region, this filter acts as a linear average filter, but for the higher contrast region, this filter will lose its function and therefore the noise in a smoothed area is averaged out while a high contrast object will retain its pixel value. In fact, this Lee factor can be considered as a special case of non-linear filters. In [Boucher and Hillion, 1988], these general non-linear filters were formalised by introducing a parameter α , such that if $\alpha=1$, the filter would be a Lee filter and if $\alpha =0$, this filter would take a logarithmic structure and become a loglinear filter. After these two

filters were implemented on SEASAT imagery, the loglinear filter was shown to be a better method, resulting in smaller mean square error.

Another non-linear filter, the homomorphic filter was proposed in [Boucher and Hillion, 1987]. This filter considers multiplicative noise as additive by logarithmic transformation. After the transformation, any linear filter could be used and when completing the filtering process, an inverse exponential transformation must be applied. Four homomorphic filters were evaluated on bar chart images [Jain and Christensen, 1980], they were the low-pass, Wiener, spatial and medium filters. The results showed that the Wiener filter performed best. It was named after the American mathematician, Norbert Wiener, and the filter would take into account the correlation circumstances of the noise and the signal, and must be used in the frequency domain. This filter could minimise the mean square error, but unfortunately it requires some prior knowledge of the noise and signal. Also it is only effective in the area with high signal to noise ratio, and in radar imagery, this area is generally in the high frequency region. As a result, the Wiener filter will remove the speckle as well as the high spatial frequency detail and consequently affects the resulting edges.

For non-linear filters, one important filter named the MAP filter that was used in this study should be introduced here. The advantage of this filter is its consideration of speckle correlation. This model includes the signal-dependent effects and aims at minimising the local mean square error. The MAP filter was derived from maximising a *posteriori* probability density function, which was claimed to be effective in processing multiple frames of speckle intensity images [Kuan et al., 1987].

The evaluation of these filters can be done either via visual comparison or examining statistical measures such as the Speckle Index and Mean Square Error on the Contrast (MSEC). The former is the ratio of its deviation to its mean in a given window size, as defined in [Crimmins, 1985]. This measure only describes the power of a filter to reduce the noise and does not consider the loss of information. The latter is used to see how well the contrast is preserved during the filtering process. With these two measures, 12 speckle-removing filters were tested on the ERS-1 imagery and no significant differences could be found, [Clochez, 1992]. In the same study, these filters were also used on the imagery prior to matching to investigate their performance on aiding the matching. However, the results were not very conclusive. For the above reasons, the two commonly used filters, Lee and MAP were adopted in this study and Chapter 7 assesses their effectiveness on various aspect of matching.

3.5 Difficulties of SAR Stereo Matching

The characteristics as well as the stereoscopic condition of the radar imagery have been analysed. These factors have great impact on the performance of stereo matching and are discussed in this section.

Regarding image characteristics, the grey levels are affected by geometric effects such as layover, foreshortening and shadow as described earlier. In addition, the speckle or noise could also have an influence. The radiometric difference is another concern, which mainly arise from the illumination difference. These effects or speckle will reduce the contrast of the imagery which is disadvantageous to stereo matching. The local distortions of the imagery should also to consider, which occurs most severely in the regions with rapidly changing terrain relief. Among the factors that were mentioned above, some are interrelated by the same elements, such as the terrain relief affecting the distortion and the geometric effects as well.

Considering the stereoscopy condition, its effect is more severe in the opposite side stereo as stated in the last section, for they have different illumination conditions, image quality, tones and texture [Clark,1991]. This phenomenon does not take place on conventional optical imagery, since the sun illumination angle does not change for the overlapping imagery. However, for the radar imagery, the radar uses its own energy source and the illumination depends on the sensor look direction. For the opposite stereo pair, the look directions of the two sensors are in contrast to each other and this contributes to their completely different appearance, thus increasing the difficulties in the matching process. The quantitative results of this conclusion would be presented in Chapter 7.

The above difficulties can be overcome by some image processing techniques of removing the image inherited speckle, noise, geometric as well as radiometric distortions. The filters to reduce the speckle have been introduced. For the same side, a coarse DEM can be employed to reduce geometric distortions. For the radiometric difference, especially severe on the opposite side, some techniques are introduced [Fullerton et al., 1986] to increase the stereoscopic viewing ability.

3.6 Summary

In this chapter, the overall geometric considerations for stereoscopic SAR were introduced. The inherited radar image characteristics, layover and shadow, will affect stereo viewing especially in the mountain regions. These effects are more severe for opposite side stereo pairs. These have better geometric condition due to larger intersection angles and exaggeration factors. Different speckle-removing filters were introduced and generally compared here with emphasis on their impacts on the stereo matching. The conclusion is that no particular specific filter is most beneficial, therefore, in this respect, two commonly used filters were selected for testing their effectiveness in later chapters.

CHAPTER 4

Stereo Matching SAR Imagery Methodology

4.1 Overview

In order to obtain satisfactory height extraction from the SAR imagery, the first step is to obtain good matching results. The purpose of this part of the study is to create a DEM from dense matching coverage. Therefore an examination of suitable matching on SAR imagery needs to be established. Stereo matching algorithms can generally be categorised into two types: feature-based matching and area-based matching.

Feature-based matching uses image processing techniques to extract features such as points, edges, segments or symbols from the imagery. Most studies carried out on this topic focused mainly on the first two; namely points or edges. Moravec [Moravec, 1980] and Förstner operators [Förstner and Gülch, 1987] are two common operators for point extraction. When comparing these two operators, the Förstner operator performs better since it achieves subpixel accuracy and needs more computation time. In [Allison et al., 1991], these operators were compared as mechanisms to select seed points, and the results show the seed points found by the Förstner operator could give better matching results. In [Zemerly et al., 1992] the Förstner operator was also used to select sufficient seed points for pyramidal matching on aerial imagery. The results were generated by dividing the whole image into subimages and Förstner operator was used on each one of subimages to find seed points.

Edges in images are another important feature to be considered. Some good operators can effectively extract edges, such as the DoG operator, the Roberts operator etc.. However, edges in SAR imagery may be displaced due to shadow difference or azimuth angle variation. This is especially the case when dealing with opposite side SAR imagery, since their different incidence angles give rise to a stereo pair of significantly different appearance. Another concern is the extracted edge may actually be due to the speckle noise, which would certainly affect the matching results.

Area-based matching uses two windows for the stereo image pair, one for each image separately. The one for the reference image is the target window, while the other is the search window. The similarity of the two windows is the basis for stereo

matching. Once the highest similarity is obtained, the central pixel of the search window is the conjugate point of the central point of the target window. Determination of the degree of similarity is generally done by two different algorithms, Normalised Correlation Coefficient (NCC) and Least Squares Correlation (LSC). NCC calculates the coefficient of the statistical correlation of the two windows; the location with the largest coefficient value is the matching position required. The LSC was proposed by Ackermann [Ackermann, 1984], which stated that the matching positions could be determined by minimising the sum of the square of the difference of the grey values. At UCL, LSC has been modified and developed giving two new programmes, **GRUEN** and **GRUENS**, which will be discussed in detail in the later sections (see [Otto and Chau, 1989], [Gruen, 1985]).

By comparing area-based and feature-based matching, their differences can be listed, as follows:

- (1) Area-based matching is easily affected by occlusion.
- (2) Sharp surface depth discontinuities can not be handled by area-based matching.
- (3) Area-based matching is more accurate and can reach up to subpixel level.
- (4) Area-based matching needs a very close approximation for the initial value.
- (5) Area-based matching is more sensitive to grey value noise.

For radar imagery, stereo matching techniques are mainly focused on the area-based matching approach. [Papacharalampos and Welch, 1990] implemented stereo cross-correlation to match SIR-B on the Desktop Mapping System, consisting of a DELL PC with Intel 80386 and 80387 micro processors operating at 25MHz. The correlation coefficient was used as a measure of the matching quality and the maximum correlation coefficient was determined by moving the correlation window over all the possible locations within the search window. The process was carried out in an iterative manner, starting with a large correlation window and in successive stages, performed on smaller windows around the point identified in the proceeding step. By adopting this area-based matching method, the height difference between the map and the final DEM derived was approximately $\pm 40\text{m}$ for moderate relief and $\pm 62\text{m}$ for high relief areas. It was concluded by the authors that this approach gave more accurate results when compared with that obtained by analytic plotters [Leberl et al., 1986a], consequently proving the feasibility of deriving the height by using PC based workstations.

When considering an interactive digital mapping system for SAR imagery, STARMAP should be introduced [Mercer, 1995]. The development of this system spanned nine years until it became fully operational. STARMAP used Intera's STAR-

1 image data from airborne SAR and produced a DTM, contour maps and orthorectified image maps in digital and analogue form. STARMAP was modified, renamed RMAP and primarily used to deal with satellite SAR imagery. By using STARMAP, STAR-1 image data was able to be used to successfully create DEMs for over 300,000 km square. At a grid spacing of 50m, the RMS of vertical accuracies could reach 15-30m. For this work, due to the absence of information on the aircraft track, differential GPS was used to provide such information at the level of 1-2m. ERS-1 imagery was also used with the RMAP to create DEMs, for which the vertical accuracies were determined to be 10-15m.

Another important paper regarding radar image matching was by [Ramapriyan et al.,1990]. In this paper, the Normalised Absolute Difference between the search and the template window was used as the matching score to offer initial positions for the matching candidates. The best matches were determined by a relaxation process based on the disparity continuity constraint. After the relaxation process, the disparity was computed for each point and summed up to warp the image. The whole process was then repeated with a smaller search window until the cumulative disparity was reduced below a given threshold. The matching algorithm employed was believed to be able to remove all the local distortions in the stereo pair and was therefore applied on the SIR-B imagery with incidence angle of 53.7° and 43.8°. However, the derived height for this stereo pair has considerable errors than theoretically predicted, which may be caused by insufficient information for the correct estimation of the sensor position.

When assessing the stereo matching algorithms utilised in SAR imagery, it is necessary to mention Leberl, who has made significant contributions to this field. He and his group have published a series of important papers on radargrammetry, including the early introduction of the radar geometry [Leberl,1976] and [Leberl,1979], and the recent study on incidence angle analysis [Leberl,1986b] and [Leberl,1988]. In his latest paper regarding stereo matching of SAR [Leberl et al., 1994], Leberl compared the stereo matching results obtained by experienced human stereo-operator to those derived from five often used area-based matching algorithms. Five image pairs were used for this purpose and on each pair several hundred matches were set up manually to define the location. This manual location was used as the "prediction" for the five machine stereo-matching algorithms. The deviation between the locations derived from machine and manual matching was defined as the "error" of the matching process, and a comparison was made based on the standard deviation of these errors. The results showed that the NCC performed best among the five matching algorithms used, with a deviation of only approximately ± 2 pixels. In the same paper, the DEM accuracy was also compared by choosing a basic datum point

and calculating the height difference of this point with respect to any other target terrain point. The height difference was estimated from the parallax difference between the datum point and target point by knowing the look angles of the two stereo images. After the height was obtained, a gridded DEM was produced by the manual and machine matching methods for comparison. The resulting differences in the DEM elevation determined was $\pm 100\text{m}$.

The latest research on SAR imaging was presented in paper [Raggam and Alexander, 1996], which assessed both the potential and the limitations of JERS-1 imagery. This paper used two kinds of JERS-1 imagery, optical and SAR, to discuss the aspects of the stereo matching and the geometric modelling of these two different stereo pairs. The grey-value based correlation is used to match the two stereo pairs. This algorithm could yield a coverage of 83% for optical but only 17% for the SAR image model. The low coverage of SAR image model was due to the speckle noise as well as the radiometric problems. With respect to DEM accuracy, the optical imagery could reach an RMS of 50.8m, while the SAR imagery was only 77.8m. This is due to the small intersection angles (3°) which cause serious displacement in across-track direction. This paper concludes that the cause of generating unsatisfactory DEM was due to the poor geometric condition of JERS-1, as well as the small intersection angle and base-to-height ratio. However, JERS-1 has the benefit of producing less layover which could provide more area for successful matching.

From the above review of selected papers, it is clear that area-based matching algorithms are by far the most employed method for stereo matching of SAR imagery. This is because the SAR imagery does not exhibit very clear feature information, unlike conventional optical imagery. In addition, there is the possibility that the feature could be shifted in the stereo pair, such as edge migration [Leberl, 1989] and as a consequence the usual feature detection algorithms employed in optical imagery are useless in aiding the performance of stereo matching. Compared with conventional optical imagery for which the matching accuracy could reach subpixel, the disadvantageous characteristics mentioned above, along with other difficulties in stereo matching of SAR as discussed in Chapter 3, indeed seem to hinder the performance of SAR, giving less satisfactory matching results. In order to enhance the matching accuracy of SAR imagery, another matching algorithm called **CHEOPS** was developed at UCL and is introduced in the following section.

4.2 Pyramidal Matching

For pyramidal matching, the paper [Ackermann and Hahn, 1991] should first be discussed. In this paper, various aspects of image pyramids were discussed and comparisons were made between the image pyramid and the original image. The authors stated that the image pyramid had the advantages of using less computer memory space and also it could be applied to many different areas such as image analysis and image matching. However, three conclusions regarding pyramidal image matching are of great interest to this thesis, which are: (1) its pull-in range could be increased at a coarser pyramidal level with only rough initial values required; (2) the convergence speed of the matching could be improved; (3) the reliability of searching for the correct matches would be increased. Of these three conclusions, the first one was of great importance since it suggested the feasibility of using random seed points on the first tier of image pyramid. The validation of this conclusion will be demonstrated in Chapter 7.

Due to the difficulties encountered when stereo matching ERS-1 SAR imagery, typical stereo matchers such as the Otto-Chau algorithm [Otto and Chau, 1989], which works successfully on optical imagery, [Day and Muller, 1989] could not perform as well on the SAR imagery. To overcome this problem, a new stereo matching algorithm which used a coarse to fine pyramid method was developed at UCL, which had the advantage of a higher coverage and a lower blunder rate. This sophisticated pyramidal matching is called **CHEOPS** named after the Great Pyramid of Cheops at Giza near Cairo [Denos, 1992], and is mainly utilised for dealing with SAR imagery. In this method, the Otto-Chau stereo matcher, an area-based patch correlation technique which incorporates the Gruen's Adaptive Least Squares Correlation (ALSC) and a sheet-growing technique, was employed. This matcher was applied to each tier in turn, taking the output from the previous tier as the seed points for the following tier, until the imagery was ultimately correlated to the same resolution as the input imagery. The principle of this method is to reduce the size of an image sufficiently by grey level averaging to obtain smaller discrepancies between the consecutive pixels therefore lowering the effects of discontinuities in the reduced imagery, so that the sheet growing is able to proceed.

The **CHEOPS** algorithm is capable of automatically generating the shell scripts required to match both SAR and other forms of imagery. It achieves this by first interpreting a script describing the topology of image pyramids written in a simple language called PDL (Pyramid Description Language), then converting this script to an equivalent set of executable UNIX shell scripts. **CHEOPS** can be implemented alone

from manual seed points as the input data file or can be applied in conjunction with another seed generating programme called **CASCADE**. After running the **CASCADE**, a pipeline is automatically produced which invokes the **CHEOPS** PDL file with the seed points as the input data. The remarkable characteristics of **CHEOPS** is its ability to enhance the accuracy as well as the coverage of the Otto-Chau stereo matcher by correlating at various resolutions. The advantage of **CHEOPS** is that the resulting seed points in the current tier will still be in the pull-in range of these original seed points in the next tier. Going down to the next tier, by applying the sheet growing mechanism, these seed points can once again grow many new seed points. This process is carried out until the matching has proceeded to the bottom tier of the pyramid which is the image of original resolution. As a result, addition of the seed points from all previous tiers could create a denser stereo coverage compared with that derived from stereo matching at a fixed scale imagery.

[Denos,1991a] tested the **CHEOPS** on NASA SEASAT satellite images of Death Valley, for which 9 tiers were used and a coverage of 81% of 1024 by 1024 imagery was obtained. In addition, Denos attempted the use of **CHEOPS** with SIR-B imagery after using speckle reduction. Two filters, median and local Lee statistics, were chosen, with 9 to 11 manual seed points selection and different patch sizes of 5 to 11. The best result of 61.7% was obtained by using a combination of local Lee statistics with a patch size of 11 and 9 seed points selection. [Dowman et al.,1992a] first applied **CHEOPS** on ERS-1 SAR data with different combinations of modes and angles, where the computed absolute disparity threshold was used to detect the blunders in the stereo matching. [Dowman et al.,1992b] adopted the pyramidal matching algorithm to automatically match the SAR data. It was indicated in this paper that the stereo SAR could offer sufficient accuracy of geocoding if the accuracy of the intersection in the range could achieve 10-20m level. The latest study regarding SAR matching was reported in [Clochez,1992], for which 12 different speckle reduction filters were used prior to stereo matching. It was concluded that no significant difference was observed between the 12 resulting coverages obtained.

4.3 **CASCADE** Programme

One of the most powerful aspects of the **CHEOPS** system is that it can automatically generate the seed points on the apex tier without manual intervention, hence overcoming the difficulties in recognising the seed points in SAR images. By utilising the **CASCADE** command, the user can specify whether to generate the seed points on the reference image at random or on a regular grid. There are two important

parameters in **CASCADE** to generate the seed points, namely the grid number and `uncertainty_radius`. When generating seed points on a regular grid, the seed points are generated at a grid number specified by the user. When generated at random, the default number of 50 seed points is used. It is likely that for imagery with many discontinuities or occlusions such as SAR, the seed points in a regular grid would give higher DEM accuracy if the stereo images have the same orientation.

The methods of seed point generation discussed above are all with respect to the reference image and on the first tier of the pyramidal imagery. The corresponding positions of these generated seed points on the non-reference imagery are calculated from the following formula:

$$\text{sample2}=\text{sample1}+(\text{ran1}()-0.5)*2.0*\text{uncertainty_radius}+\text{offset} \quad (4-1)$$

$$\text{line2}=\text{line1}+(\text{ran1}()-0.5)*2.0*\text{uncertainty_radius}+\text{offset} \quad (4-2)$$

where:

`line1`, `sample1` are the x (sample) and y (line) coordinates (pixel) on the reference imagery

`line2`, `sample2` are the x (sample) and y (line) coordinates (pixel) on the non-reference imagery

The `ran1()` is the linear congruential random number generator; the `uncertainty_radius` and `offset` parameters are the input parameters with default values of 3 (pixel) and 0 (pixel) respectively. As can be seen in equations (4-1) and (4-2), the seed point coordinates on the non-reference imagery are apparently most dependent on the value of the `uncertainty_radius`. As the value of the random number generator `ran1()` is between 0~1, the discrepancies of seed points coordinates on the apex tier between the two images would be in the range of $\pm \text{uncertainty_radius}$, if the offsets remain the default value. In the matching process, these discrepancies are considered as the "disparity". It is necessary to mention here that the magnitude of the `uncertainty_radius` as well as the image tier could significantly affect the number of "effective" random seed points, and the importance of this interrelation will be analysed further in Chapter 7. The function of the `offset` is to accommodate the gross shifts of all features from the reference to the non-reference image. That is, if there is a shift consistency of all the features in the stereo pair. It is possible to take this shift into account for the random seed points in advance to increase the matching accuracy. When we first investigated the **CASCADE** program, it was to our surprise that these seed points are generated randomly unlike those normal seed points selected manually. Yet, its performance is better than the typical manual seed points. The reasons for this

and the function of these random seed points will again be explained in detail in Chapter 7. For an illustration of the random seed points generation process, Fig. 4.1 shows the distribution of the random seeds on the data image RTM (left) and PRI (right).

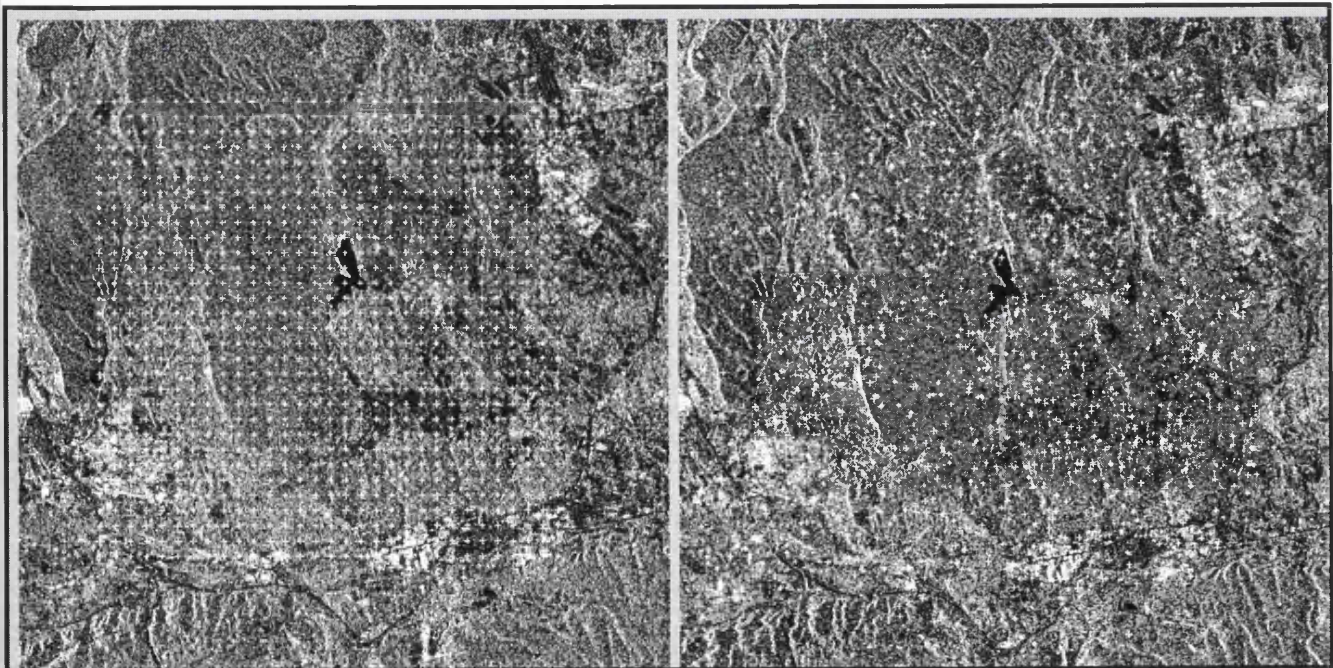
The main attribute of **CASCADE** is that it is not only a seed point generation program, but it is also able to specify **CHEOPS** stereo matching commands in the PDL file for refining and matching. These commands are utilised by **CHEOPS** in separated tiers during the matching process and if not specified by the user, the default commands for refining and matching are **GRUEN** and **GRUENS** respectively. Both **GRUEN** and **GRUENS** are area-based matching algorithms used at UCL that take advantage of the Adaptive Least Squares Correlation (ALSC) technique and will be discussed in detail in the next section. In addition, **CASCADE** offers the option to use any specified filter, designed to work with the output of the **GRUENS** programme to remove blunders. The default command, **BLUNDER**, is only suitable for detecting matching errors of SPOT imagery which uses the geometry constraint based on the difference in the look angle of the stereo pair images. The user must therefore develop his own useful filters for specific stereo imagery.

4.4 CHEOPS Programme

As stated already, **CHEOPS** is a programme which provides the harness for pyramidal matching via a PDL file. The function of the PDL file is to specify the operations carried out at each tier of the pyramid. It consists of a simple structure language developed by Mark O'Neill [Denos, 1992] which is used to describe the geometry of the pyramid. An example of a PDL file is shown in Fig. 4.2.

The PDL file always begins with an `apex` statement which specifies the number of tiers in the image pyramid to be matched. Following this are the `laplacian` statements that instruct the harness which class of pyramidal hierarchy and scale factor are required. Between `tier` and `emd` (`end matcher description`) are the stereo matching commands, which may be `matcher` or `refiner`. The first and last values of patch radius are specified by `pscale` parameters, which can be used to calculate the patch radius for the refiner and matcher of the remaining tiers accordingly. As **CHEOPS** can work with different algorithms, a list of possible refiners and matchers are passed to the **CHEOPS** harness via its command tail.

Fig. 4.1: Distribution of random seed points generated by CASCADE



stereo pair: RTM_A (left), PRI_A (right)

size: 512*512

CASCADE parameter: grid 32, uncertainty_radius 1.0

random seed points generated on the first tier (16*16) of 6 tier image pyramid

961 random seed points generated

The left hand image shows the seed points generated on the reference image and the right hand image shows the seed points generated by equation (4-1) and (4-2)

```

*-----*
* Pyramidal Description Language for ERS-1 images of South France *
* *
*      Seed points are generated at a regular grid 64*64      *
*-----*
* Reference image is 512*512
* 6tiers used-->top is 16*16
  apex 6                                6 tiers
  laplacian 2                          Laplacian image pyramid
* Autoscaling switch
  pscale 5 25 round                    patch radius specification
* Apical tier                          first tier
  tier localhost noshakeup
  gruen -patchrad $                    refining
emd
  reduce                                resolution scaling
  xtee                                  output saving
  etier
* Tier 2
  tier localhost noshakeup
  gruens -patchrad $ -pthresh 150 -grid 1    stereo matching
emd
  reduce
  xtee
  etier
* Tier 3
  tier localhost noshakeup
  gruens -patchrad $ -pthresh 150 -grid 1
emd
  reduce
  xtee
  etier
* Tier 4
  tier localhost noshakeup
  gruens -patchrad $ -pthresh 150 -grid 1
emd
  reduce
  xtee
  etier
* Tier 5
  tier localhost noshakeup
  gruens -patchrad $ -pthresh 150 -grid 1
emd
  reduce
  xtee
  etier
* Tier 6
  tier localhost noshakeup
  gruens -patchrad $ -pthresh 200 -grid 2
emd
  etier
end

```

Fig. 4.2: An example of PDL file

The commands “`reduce & xtee`” shown between the `emd` and `etier` (end of tier) are required to specify additional image processing applied within a particular tier, in order to prepare the images for stereo matching for the next tier. **REDUCE** is an image scaling command, and it must be used in all tiers in the pyramid except for the bottom tier. `Xtee` is an optional filter which saves the scaled stereo images in a compressed format along with the outputs of matching within a given tier. By using this option, it is possible to follow the coverage increasing from one tier to the next.

The tier statement may be postfixed by the following options: `localhost` instructs **CHEOPS** to run on a local station, whereas `exechost` orders the specified host you required to run across a local area via the network. The `besthost` option is for running the command on a host currently with the lowest loading.

The `shakeup` command offers an option to shakeup the seed points. It has been suggested in a previous paper [Denos,1991b] that shakeup can enhance the DEM accuracy by selecting better seed points with minimum eigenvalues under the condition that there are many seed points in the reference imagery with identical line and sample coordinates. Unfortunately, there was no data to support this theory and its validation requires further evaluation. The shakeup option might work if the seed points are chosen randomly on the reference imagery, and it is possible that the seed points created maybe satisfy the shakeup condition. For this Ph.D. project, the seed points were generated on a regular grid, so no shakeup function was used.

Simply speaking, **CHEOPS** is a programme able to produce a series of shell scripts under UNIX environment. These shell scripts are sequences of executable commands that perform stereo matching on reduced imagery. The specification of refiner and matcher as well as other parameters (e.g. image tier) are all controlled by a PDL file.

To summarise, Fig. 4.3 shows the flow chart of running **CHEOPS** with the example PDL file (shown in Fig. 4.2). In this flow chart, the scale output means the sample and line coordinate are all multiplied by a factor of 2 respectively. The first tier implements the refiner - **GRUEN**, while in other tiers the matcher **GRUENS** is implemented to sheet grow and produce many seed points. The matcher or refiner could be arranged in other ways e.g. put the refiner and matcher in every tier. The results derived from this sort PDL file is different from those obtained by previous

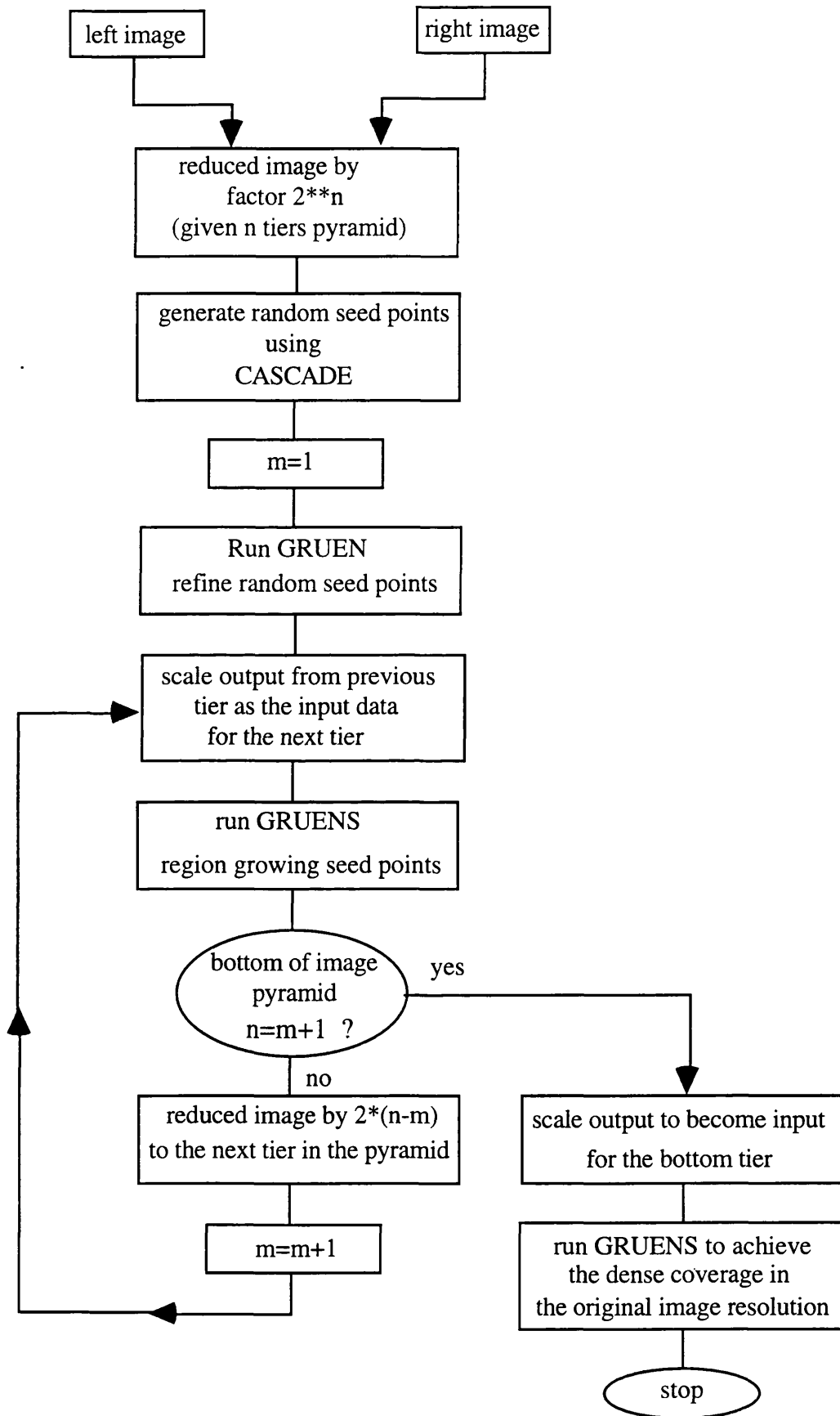


Fig. 4.3: CHEOPS pyramidal matching flow chart

PDL file. The reasons for this and more in-depth analysis of the parameters in the PDL file can be found in Chapter 7.

4.5 Introduction to GRUEN

As stated above, the refiner **GRUEN** utilises the ALSC technique to carry out the stereo matching procedures. The ALSC was developed by A.W. **GRUEN** in 1985 [Gruen,1985]. It is an area-based matching mechanism used to select the best match for a square patch surrounding the points in the left image to a patch in the right image by specifying the size of the patch radius to determine the corresponding positions of the matching points in the right image. The best match would have the minimum sum of the squares of the difference of the grey values between the two image patches. The advantage of this technique is that it allows the radiometric as well as the geometric parameters to be solved simultaneously. That is, in a pair of image patches, ALSC takes into account the image distortions from both radiometric and geometric aspects. The geometric distortions are mainly due to the difference in terrain height, position and attitude variations of the sensors which affect the pixel positions, while the radiometric distortions arise from noise and different illumination conditions caused by haze or atmospheric effects which change the pixels' grey values. Since the matching region is quite small and can be considered planar, the geometric distortions can be described well by an affine transformation between the image coordinates. The radiometric distortions on the other hand can be represented by an additive and a multiplicative factor. Since there are six parameters for affine transformation and one additive and one multiplicative parameter respectively for the radiometric distortions, a total of eight parameters are required for **GRUEN**. Note here that the number of parameters can be altered to set up the most appropriate matching model to suit any particular signal content of the images, hence it is the meaning of the term "Adaptive" comes from. In **GRUEN**, these eight parameters are solved iteratively by the least squares technique. The process starts with making initial estimate of the parameters and then linearizing the least squares equation via Taylor's series. Next, these initial values are taken as the input to determine subsequent increments of the parameters. This process is repeated until all these increments are below the specified threshold value.

The **GRUEN** approach is able to produce results with great accuracy at moderate computational cost. Moreover, the results are easily assessed by a *posterior* residual variance estimator. The disadvantage of **GRUEN** is that its pull-in range of convergence is quite small, i.e. it requires good estimate of initial values to converge

successfully. For the more detailed algorithm of the **GRUEN**, refer to Appendix A for the formulae.

In summary, **GRUEN** is a very potent and flexible technique for processing all kinds of data. It allows modification of the parameters of the affine transformation, if the matching region deviates significantly from a plane. In addition, a variety of geometric constraints can be incorporated into this algorithm to increase the matching accuracy by considering any specific conditions, for example, the collinearity condition in the multi-photo matching [Gruen and Baltsavias, 1987]. In other words, by considering the image geometry any new extra condition can be added to **GRUEN** to further enhance the performance of this **GRUEN** algorithm.

4.6 Introduction to **GRUENS**

Apart from employing the same **ALSC** technique as **GRUEN**, **GRUENS** also implements an additional region growing algorithm to produce a dense matching coverage for the stereo pairs. In principle, this region growing algorithm operates on the assumption that the local region for stereo matching is smooth, and the disparity is continuous, i.e. the disparity of any points can be predicted from that of its neighbouring points. With this predicted disparity, the initial coordinates of growing points could be determined and refined by **GRUEN** to give final results. The growing process enables the selected initial seed points to grow to reach their neighbours, and with these neighbouring points, more nearby points could be determined. This process is carried on until the cumulative number of growing points is equal to the number of all image pixels.

To start the growing process for stereo matching, the region growing algorithm requires a few good correspondence of points, called “seed points”, in advance. These seed points are normally selected manually or can be picked up by a straightforward feature detector e.g. the Moravec operator. Whatever the method adopted, the positions of these selected seed points should be accurate to about 1-2 pixels. Ideally, there should be at least one seed point for each “isolated region”, a homogeneous region where region growing algorithm has no path to follow from other well-textured areas. To ensure the growing is successful from the start, enough seed points should be selected. It is important to notice that since the characteristics of SAR imagery, e.g. noise, layover and shadow could obscure the growing process, more seed points would be required for SAR when compared to other kinds of imagery.

Once the initial seed points are selected, there are three methods commonly used for the seed growing process, including depth first, breadth first and best first. The depth first method is to initiate the growing in a single direction until the iteration exceeds the specified value before proceeding in another direction. This method is not suitable for running **GRUENS**, however, for the iteration count is not a proper measure to estimate the quality of the matches. Also, in a homogeneous region, once a mistake is made during the growing process, it will accumulate until the direction is changed. The second method, the breath first method is quite similar to the depth first, except that every direction is explored for each point. The problem of this method is the need of a very good selection of seed points to start with and the errors are also accumulated as described above. The last method, the best first, provides the answer for the region growing techniques. A unique scoring function is incorporated in this method to judge the quality of the matches and let only the best seed points to grow points, hence eliminating the accumulation of errors to obtain better results. The score used here is the largest eigenvalue of the submatrix of the X and Y disparity covariance matrix. The smaller the eigenvalue, the better the match. In implementing this best first technique, each point is stored in a priority queue according to their score and organised into a heap. Each time, a best point is retrieved from the top of the heap and used as the “mother” to grow other points in four different directions. The resulting “sons” are then inserted into the queue and this enlarged queue is reordered based on the scores. This procedure is repeated until all the image pixels are incorporated into the queue. The best first growing technique was validated in 1988 as [Otto and Chau, 1988] showed that by using this searching strategy over 99% of matched points were obtained from a 240*240 SPOT image of Aix-en-Provence.

Naturally, there is still a chance of obtaining bad matches when utilising a best first algorithm. To avoid this from happening, **GRUENS** offers several constraint parameters when running the program, and the three main types include global y disparity, calculated y disparity and eigenvalue. By setting up the maximum tolerance of these constraint parameters, the possibility of growing bad matches is greatly reduced. In theory, the global y disparity could be determined once the sensor orientation is known accurately and when the change in terrain height is small. Unfortunately, under normal circumstances, the exact location of most sensors at a given time can not be predicted with enough accuracy and therefore the use of global y disparity proved unreliable. This led to the limited use of the global y disparity and as a result, the calculated y disparity was introduced. This constraint is determined by calculating the difference of the y disparity before and after using **GRUEN**. If this difference exceeds the threshold tolerance, this seed point is considered to be a bad

match and could be rejected. Unlike the global disparity, this constraint is only related to the size of the image patch in matching, therefore being more practical to use and is now currently applied as a post-processing step. In **GRUENS**, the default value for this constraint is 3.0 pixels. The third constraint parameter, the "eigenvalue", is used as a measure to judge the best seed point from which to grow successive points as stated earlier. Thus, it is natural for this value to be used as another standard constraint.

GRUENS was developed at UCL several years ago under the Alvey project. Since then, this algorithm has been tested on many types of stereo imagery, and proved to have excellent performance with subpixel accuracy. The greatest advantage of **GRUENS** is that it only needs a few good seed points from the start to obtain a very dense stereo coverage. For other area-based matching algorithms, however, this level of coverage could not be achieved without utilising feature detectors in advance. Thus, it is worth testing **GRUENS** on ERS-1 SAR imagery to see its suitability and try to improve the algorithm if any difficulties are encountered.

4.7 Summary

This chapter has described in detail the algorithm adopted in this research to stereo match ERS-1 SAR imagery. This algorithm is executed by the **CHEOPS** programme in a pyramidal image. In each tier, the selection to use the refiner **GRUEN** or matcher **GRUENS** is dependent on the PDL file. The theory of **GRUEN** and **GRUENS** and the usage of PDL file were introduced in this chapter.

CASCADE is another programme which deals with seed points generation. These seed points are produced randomly in the first tier of the image pyramid. **CHEOPS** is linked to **CASCADE**, so once the seed points are produced, **CHEOPS** will automatically execute. Thus, without any manual intervention, plenty of matching results can be obtained. **CHEOPS** can also be executed alone from other seed data, offering the possibility to evaluate the performance of these seed points. Besides the seed points, there are other important parameters in PDL file which should be considered as well, and analysis of these will be discussed in the Chapter 7.

CHAPTER 5

Intersection

5.1 Overview

To extract the height from ERS-1 SAR stereo imagery, a relationship between image space and object space must firstly be determined. Two approaches have been employed in previous studies to define this relationship, namely (1) projection equation and (2) photogrammetric approach.

The projection equation approach is the computation of the intersection of the range sphere and Doppler cone and is used by many researchers to compute the object position from the sensor position. [Leberl,1986] used the projection equation to create a stereo pair mapping system on the Kern DSR-1/11 instrument. Thirty-two ground points were firstly identified on image and map, and these ground control points were computed via the projection equation to acquire the image coordinates. The difference of the computed image coordinates and the ones actually observed allows the resection to improve the assumed approximations of orbit positions. From these positions, the projection equation for each target is computed again to obtain its coordinate in object space.

The photogrammetric approach defines the height of a target by computing the parallax and ground range of the matching point with the available values of altitude and look angles of sensors. This method has to be used under the assumption that the two sensors have parallel flight-paths with identical attitudes at the same altitude. This ideal situation, however, rarely happens to SAR, making this heighting technique seem very impractical. [Leberl,1990] demonstrated that this photogrammetric approach caused significant errors in heighting. Also, the paper [Thomas et al.,1986], stated that consecutive small changes in elevation could not be detected by this method.

5.2 Analytic Approach Overview

[Dowman,1992] concluded that the derivation of DEMs from ERS-1 SAR image is possible with same-side or opposite-side by using the SAR analytic

approach. This analytic approach was first proposed by Clark to geocode SIR-B imagery [Clark,1991]. Although satisfactory results were obtained with SIR-B, Clark predicted that her algorithm would be more robust in ERS-1 due to a number of reasons. Firstly, ERS-1 is much better than SIR-B when considering the circumstances for intersection, as it can provide five sets of position and velocity vector in the header data file for the sensor, while SIR-B can only provide one. Secondly, the Doppler frequency is kept at zero in ERS-1, while being variable for the whole image scene in SIR-B. Unfortunately, ERS-1 had not been launched at that time for Clark to validate her theory. This proposed use of analytic approach on the ERS-1 imagery was finally tested by Chen [Chen,1993]. He firstly modified the original intersection source code in FORTRAN to suit the ERS-1 imagery, then tested the algorithm by trying to use two different combinations of image mode, namely “same side” and “opposite side”. The results were evaluated by comparing 38 manually-derived check points, and the heighting accuracy was determined to be excellent at 52m for same side, and 64m for opposite side [Chen,1994].

5.3 Analytic Approach

The analytic approach primarily solves four equations, two range equations and two Doppler equations, simultaneously with accurate orbit and Doppler information. These four equations are listed below:

$$f_{DC1} = \frac{2(\dot{S}_1 - \dot{P}) \cdot (S_1 - P)}{\lambda_1 |S_1 - P|} \quad (5-1) \quad \text{Doppler equation}$$

$$f_{DC2} = \frac{2(\dot{S}_2 - \dot{P}) \cdot (S_2 - P)}{\lambda_2 |S_2 - P|} \quad (5-2)$$

$$R1 = |S_1 - P| \quad (5-3) \quad \text{Range equation}$$

$$R2 = |S_2 - P| \quad (5-4)$$

where:

image1 and image2 are the stereo pair

f_{DC1}/f_{DC2} is the Doppler value for image1/image2

$R1/R2$ is the range distance for image1/image2

\dot{S}_1/\dot{S}_2 is the velocity vector of the sensor for image1/image2

S_1/S_2 is the position vector of the sensor for image1/image2
 λ_1 / λ_2 is the radar wavelength for image1/image2
 \dot{P} is the velocity vector of the target point on the ground
 P is the position vector of the target point on the ground
 where $\dot{P} = P * \bar{\omega}$, $\bar{\omega}$ is the Earth's rotational vector

In the above four equations, the sensor position vector (S), velocity vector (\dot{S}) and the range distance (R) are all calculated from the header data file for each image. This calculation is described in greater detail in section 5.4. The wavelength (λ) is also accessible from header data file, while the 3-D coordinates of P are unknowns to be solved by the Least Squares iteration technique.

It is important to notice that (5-1) ~ (5-4) must be carried out on a coordinate system called the geocentric inertial system, the configuration of which is shown in Fig. 5.1. As seen in this diagram, \bar{X} is the direction of vernal equinox, \bar{Y} is orthogonal to \bar{X} , and \bar{Z} is along the rotational axis of the Earth, positive towards the north. \bar{S} is the sensor position, \bar{P} is the position vector and $R_{i,j}$ is the sensor to target range distance derived from equations (5-3) and (5-4). This geocentric inertial system is fixed relative to the celestial sphere, and does not rotate with the Earth, while the data provided by the ERS-1 header data file is in the geocentric terrestrial system, which rotates with the Earth. Thus, it is necessary to convert these data prior to the intersection process. The conversion factor is related to GMST (Greenwich Mean Sidereal Time) which will be explained in section 5.4.5.

Fig. 5.1 also explains the analytic approach from a geometric view, which can be found in [Curlander,1984]. In this paper, Curlander stated that the analytic approach is determined by three planes (1) range equation (2) Doppler equation (3) Earth's shape. The range equation defines the distance of the sensor from the target which determines a sphere. The Doppler equation defines the conical surface of a zero-Doppler frequency. At a particular time, the intersection surface of a sphere and a cone will yield a circle which, when intersected with the Earth model will give the exact position of a target point.

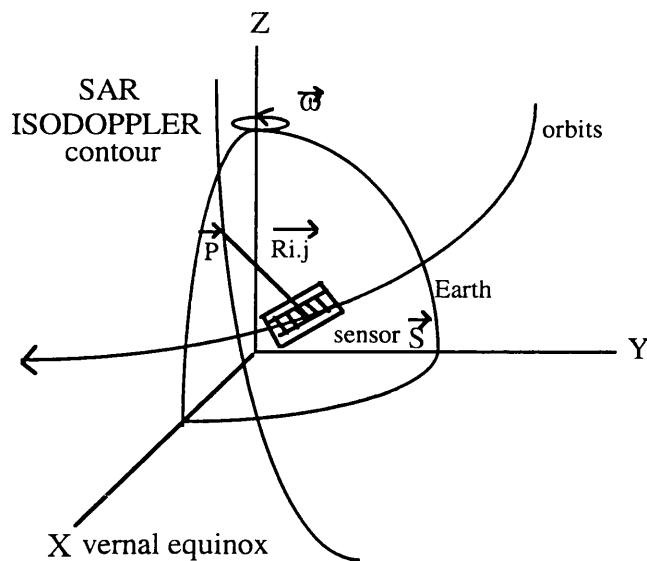


Fig. 5.1: Geocentric inertial system

5.4 Space Intersection Procedures

As previously stated, the analytic method was modified by Chen in 1993 for dealing with ERS-1 SAR data. In order to carry out the intersection, we need the matching results as well as header data to obtain the geocentric coordinates for each terrain point.

The intersection procedure includes many steps of calculation which are illustrated in the intersection flow chart (Fig. 5.2). Each step in this flow chart will be analysed further in the next few sections.

5.4.1 Read header data file

All the necessary data about ERS-1 imagery can be read out by referring to the given formats in the Computer Compatible Tape (CCT) as well as on the World Wide Web (http://gds.esrin.esa.it:80/sarpri_012095). These data contain lots of important information for intersection, of which the most useful include sensor position, sensor

velocity and scene center time, etc.. All these information are accessible from three data records:

(1). Data Set Summary Record: including the scene center geodetic latitude and longitude, ellipsoid designator and parameters, scene center line and pixel number, radar wavelength, zero-Doppler range time and azimuth time, range and azimuth time for the first, center and last pixel of the image.

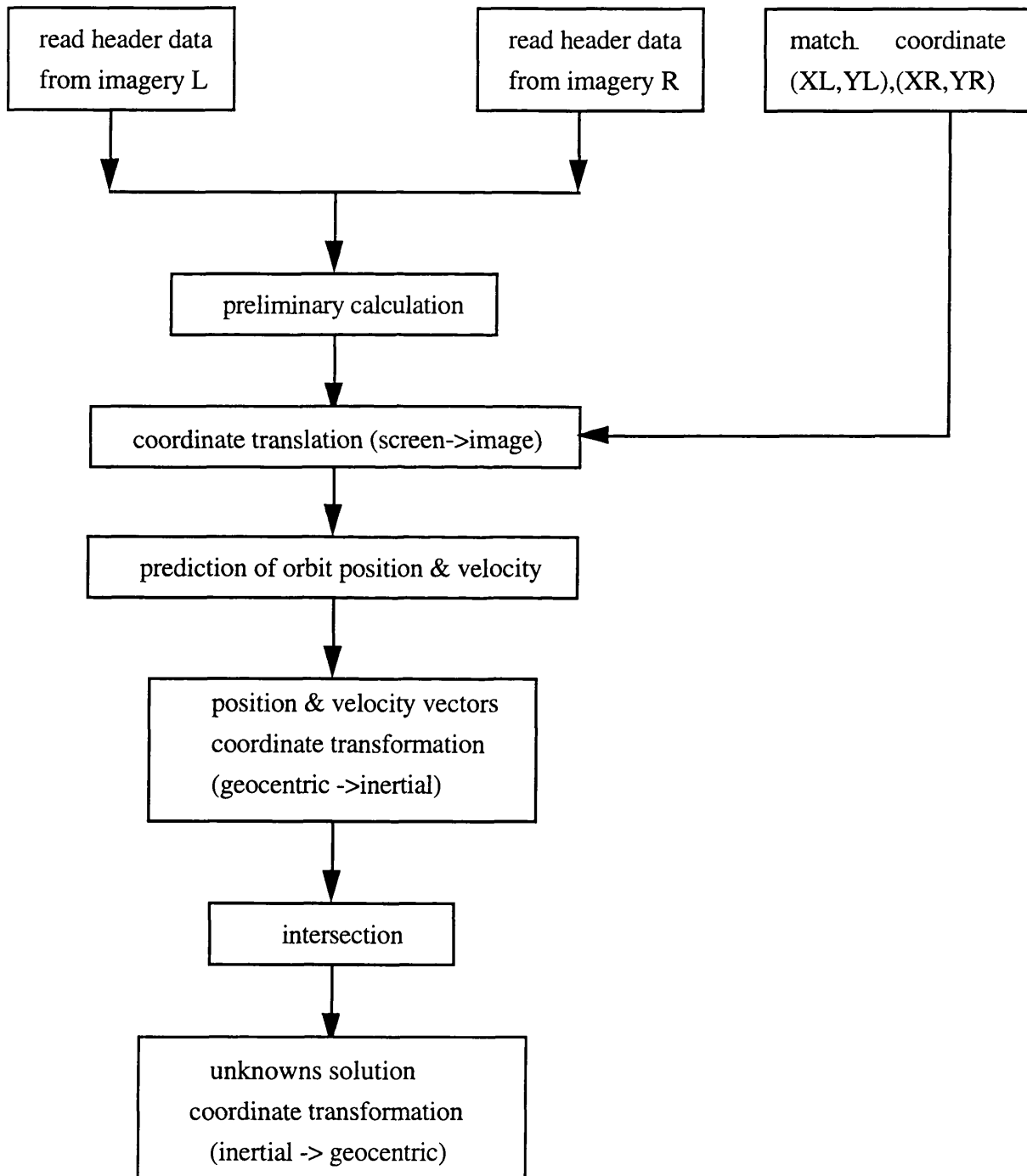


Fig. 5.2: Intersection flow chart

(2). Platform Position Data Record: including time of data point, data point position vectors, data point velocity vectors, 5 data point position vectors, 5 data point velocity vectors.

(3). Map Projection Data Record: including the map projection, general information and coordinates of the four corner points.

All the above data extracted from header file must be arranged in a certain format, so that they can be read out correctly by the programme. This format is referred in Appendix B.

5.4.2 Preliminary calculation

Prior to the intersection, it is necessary to obtain some data in advance. These data include: (1) time interval of azimuth and range for pixels (2) scene center coordinate average value. The former data is mainly used for calculating the azimuth and range time for each matching pair based on its X and Y coordinates, while the latter is the initial value for the iteration procedures.

In a given header data file, three sets of azimuth and range time intervals are provided. These include the first, center and last range time for the sample pixel as well as the first, center and last azimuth time for the line pixel. Based on these time intervals, the range and azimuth time for the pixel of each matching pair could be solved via the cubic spline interpolation [Chen, 1993]. As equations (5-1) - (5-4) are non-linear, they must firstly be linearized by Taylor's Series up to cubic and solved by Least Squares iteration. In addition, initial values of unknowns are required before the intersection can proceed. The common initial value of all the terrain points is the average coordinate of the center of the stereo pair image scene .

5.4.3 Coordinate translation

For SAR imagery, the original screen coordinate can not be input directly to the intersection procedure. This is because firstly there are two different modes, ascending and descending, for the SAR imagery and secondly the header data is given with respect to the whole scene while in many cases, only the subscene is dealt with. It is therefore necessary to translate the screen coordinate to image coordinate before proceeding to intersection.

For example, if the screen coordinate is (I,J) representing (sample, line) of the range pixel and the azimuth pixel respectively, to translate this coordinate to image coordinate (I',J') =>

For the ascending imagery

$$I'=I+I_0$$

$$J'=(J_n+1)-(J+J_0)$$

For the descending imagery

$$I'=(I_n+1)-(I+I_0)$$

$$J'=J+J_0$$

where:

I_n : line number of each pixel

J_n : pixel number of each line

I_0 ; J_0 : are the translations from the top-left corner of the screen to that of the raw imagery

5.4.4 Interpolation of the orbit position and velocity

In equations (5-1) ~ (5-4), the position (S) and velocity (\dot{S}) of sensors as well as the range distance can also be solved. This is achieved by using the azimuth and range time introduced earlier. The header file provides five sets of orbit positions and velocities at five different times separated by a constant time interval. For each matching pair, the exact location and velocity of sensor for the left and right images can now be determined by implementing the cubic spline interpolation respectively from its azimuth time. The range distance can also be calculated from the range time.

5.4.5 Position and velocity vectors transformation

The position and velocity vectors introduced above are provided by the ERS-1 header data file which is on a geocentric terrestrial system. As mentioned in section 5.3 these data must firstly be converted to the geocentric inertial system prior to intersection. The conversion between these two systems is illustrated in Fig. 5.3.

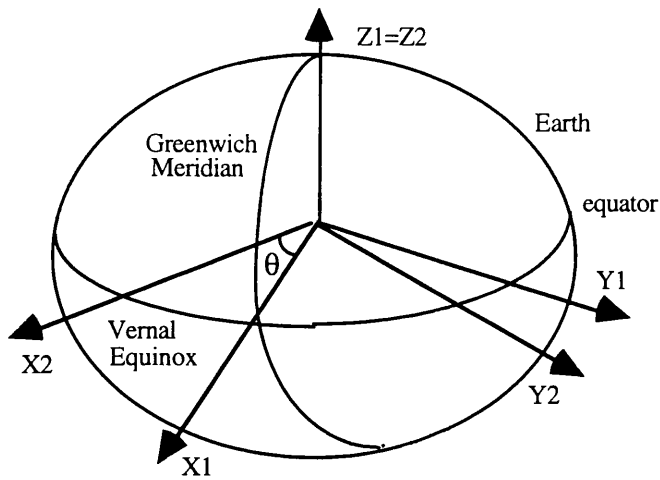


Fig. 5.3: Relationship between inertial system and geocentric terrestrial system

In Fig. 5.3, $[X_1, Y_1, Z_1]$ represents a geocentric terrestrial system, while $[X_2, Y_2, Z_2]$ is an geocentric inertial system. The intersection of X_2 with the equator is the vernal equinox.

To convert these parameters between two systems:

$$\begin{bmatrix} X_1 \\ Y_1 \\ Z_1 \end{bmatrix} = R(\theta) \begin{bmatrix} X_2 \\ Y_2 \\ Z_2 \end{bmatrix}$$

$R(\theta)$ denotes a rotation about the Z axis where θ is the hour angle of the real vernal equinox, also called the Greenwich Apparent Sidereal Time (GAST).

Since GAST is not a uniform time scale [Green,1985], we adopted GMST instead. There is only a slight difference between GMST and GAST which can be referred to as the equation of equinox, where:

$$\text{GAST} = \text{GMST} + \text{equation of equinox}$$

The equation of equinox is very small. It is proportional to θ and is very difficult to calculate. For these reasons, it is regarded as negligible [Clark,1991] and

GMST was used for this research. In ERS-1 data, the time of imaging was given with respect to Universal Time Coordinate (UTC). The UTC is the civil time, which is also broadcast by the radio stations. There is only one second difference between UTC and UT (Universal Time) for each year [Mackie, 1985] and could be ignored. Therefore, we can also take ERS-1 data as referred to the UT time reference system for the intersection. The conversion from UT to GMST requires the calculation of Julian Date (JD). For the detailed conversion, refer to [Hatcher, 1984].

For each point of a matching pair, its UT time could be derived from the previous calculation of azimuth time. After UT time has been converted to GMST, the position and velocity vectors defined in the geocentric system can be transformed to the inertial system.

Let

P_0 V_0 be the position and velocity vectors in geocentric system

P and V be the position and velocity vectors in inertial system

Then

$$P = \begin{bmatrix} \cos t & \sin t & 0 \\ -\sin t & \cos t & 0 \\ 0 & 0 & 1 \end{bmatrix} P_0$$

$$V = \begin{bmatrix} -t' \sin t & t' \cos t & 0 \\ -t' \cos t & -t' \sin t & 0 \\ 0 & 0 & 0 \end{bmatrix} P_0 + \begin{bmatrix} \cos t & \sin t & 0 \\ -\sin t & \cos t & 0 \\ 0 & 0 & 1 \end{bmatrix} V_0$$

where $t = -\text{GMST}$ and $t' = -2\pi/\text{day}$ medians in degrees

5.4.6 Intersection

After obtaining the position, velocities and range distance for each matching pair, there are only three unknown parameters left in equations (5-1) ~ (5-4). These four equations can then be solved simultaneously by using the Least Squares Method for the position vector of a common ground point. Note here that the final solution is still in the inertial coordinate system and must be converted back to geocentric coordinates again.

5.5 Summary

In this chapter, the intersection algorithm for ERS-1 SAR imagery has been analysed in detail. The main difference in the intersection procedures between ERS-1 SAR and traditional optical imagery is that ERS-1 can provide very accurate orbit information which in photogrammetric terms is the exterior orientation. This characteristic led to the possibility that no control points may be required for obtaining the DTM. Further studies could be undertaken to evaluate this assumption. It must be noted, however, that this intersection algorithm is very sensitive to the geometric conditions of the space intersection and the accuracy of the provided orbital data. Poor geometric conditions such as small intersection angle and unknown orbital accuracy may cause errors in determining the height of the target point. The influence of these causes will be discussed further in Chapter 8.

CHAPTER 6

Image Data Set and Test Site Description

6.1 Introduction

In this chapter, the three ERS-1 SAR image data sets used in this study are described in detail. The test area that is covered by one of these images is also introduced. This chapter also includes the introduction of the strategy implemented for calculating the DEM accuracy, as well as the reference DEM data provided by IGN. An overview of these topics will aid the understanding of the works presented in Chapter 7 and 8.

6.2 Image Data Set Introduction

The three types of ERS-1 images used in this study were: (1) RTM (ascending) (2) PRI (ascending) and (3) PRI (descending). The region covered by the images is in the neighbourhood of Aix-en-Provence. The header file shown in the Appendix B includes all the fundamental information for each individual image. From this, the four most important items are listed in Table 6.1.

	RTM_A	PRI_A	PRI_D
scene center time (year/month/day) (hour/min/sec)	1992 -04-10 22-00-58.51	1992-05-09 21-49-52.96	1992-05-06 10-25-49.93
scene center latitude & longitude	43.133, 5.334	43.865, 5.485	43.612, 5.485
center range incidence angle	35.962°	23.021°	23.016°
image size (sample, line)	8001.0, 7774.0	8001.0, 8203.0	8001.0, 8208.0

Table 6.1: 4 key data for the three images respectively

From the values of incidence angles (second last row of Table 6.1), it can be estimated that the intersection angles for stereo pair of SA, OP1 and OP2 as defined in Table 6.2 were approximately 13°, 46° and 59° respectively.

	stereo pair
SA	RTM_A (left), PRI_A (right)
OP1	PRI_D (left), PRI_A (right)
OP2	PRI_D (left), RTM_A(right)

Table 6.2: Definitions of three stereo pairs

6.3 Test Area Description

In order to compare the DEM derived from the three images, a common overlap region of size 1024*1024 was extracted as the test area. The offset of the line and sample pixels of this test area for the three imageries are listed in Table 6.3

	RTM_A	PRI_A	PRI_D
line	594.0	6976.0	5188.0
sample	3977.0	1695.0	2850.0

Table 6.3: Offset of sample and line pixel for the test area

The images RTM_A, PRI_A and PRI_D are shown in Fig. 6.1, 6.2 and 6.3 respectively. The range of coordinates with respect to the Lambert Zone 3 for the test area are 834950 to 850100 for the X coordinate and 3129000 to 3141750 for the Y coordinate. The test area is approximately 15km*13km, most of which is covered by the IGN 1:25000 maps of 3144est. It is located in Southern France near Aix-en-Provence, to the north-west of Marseille (Fig. 6.4). Within this area, the average height is approximately 180m and the height range is from 77m to 318m.

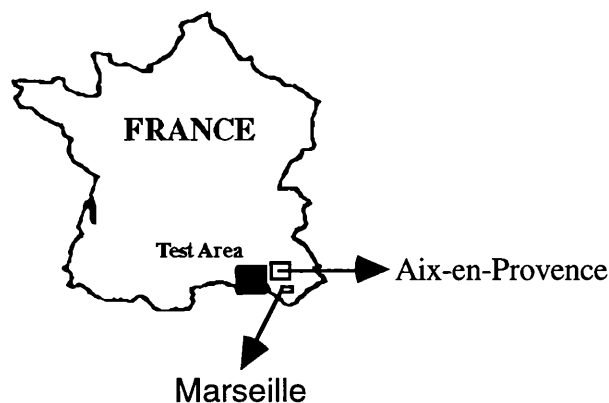


Fig. 6.4: Location of test area in France (figure not to scale)

Fig. 6.1: RTM_A raw image

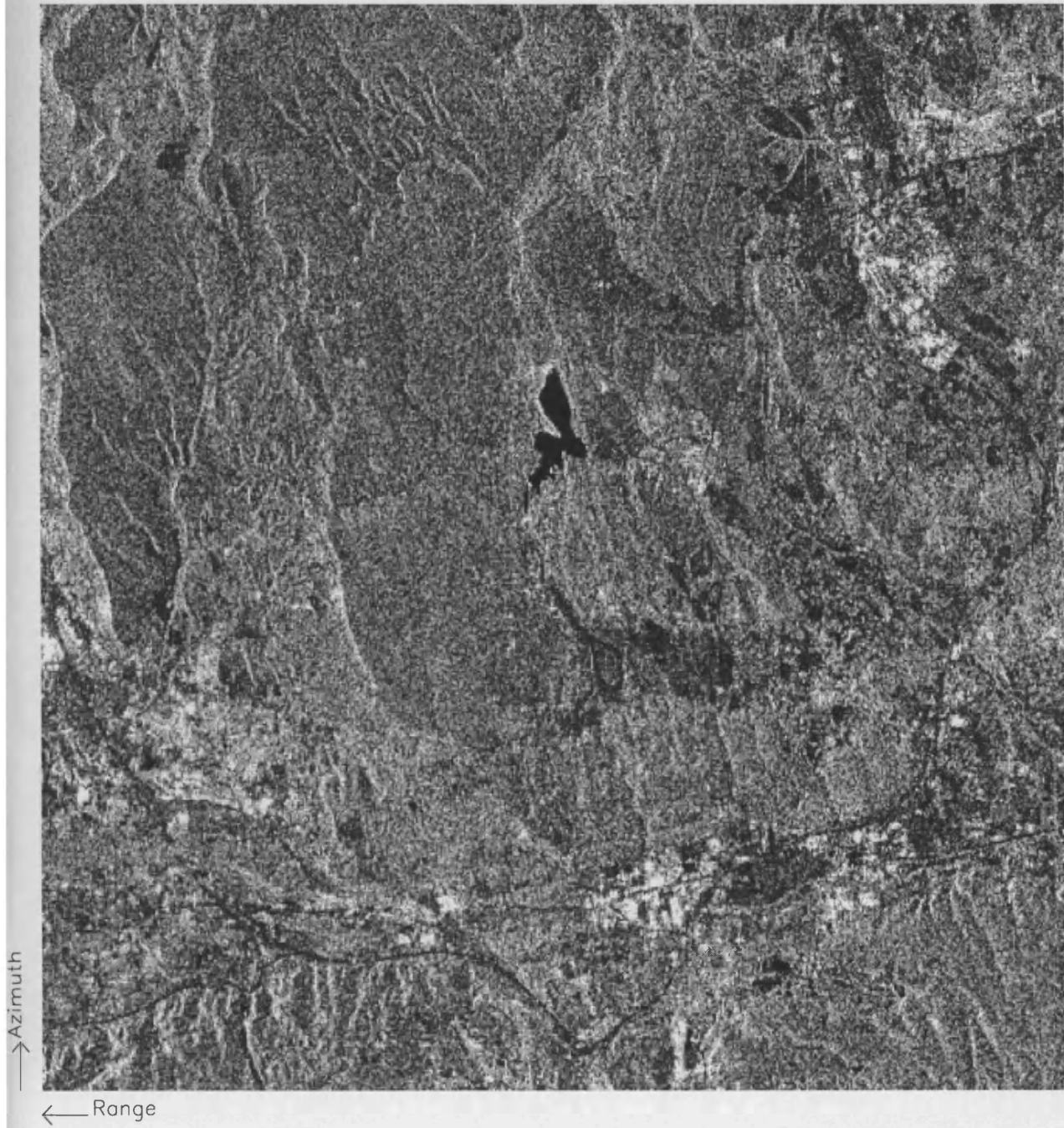


Fig.6.2: PRI_A raw image

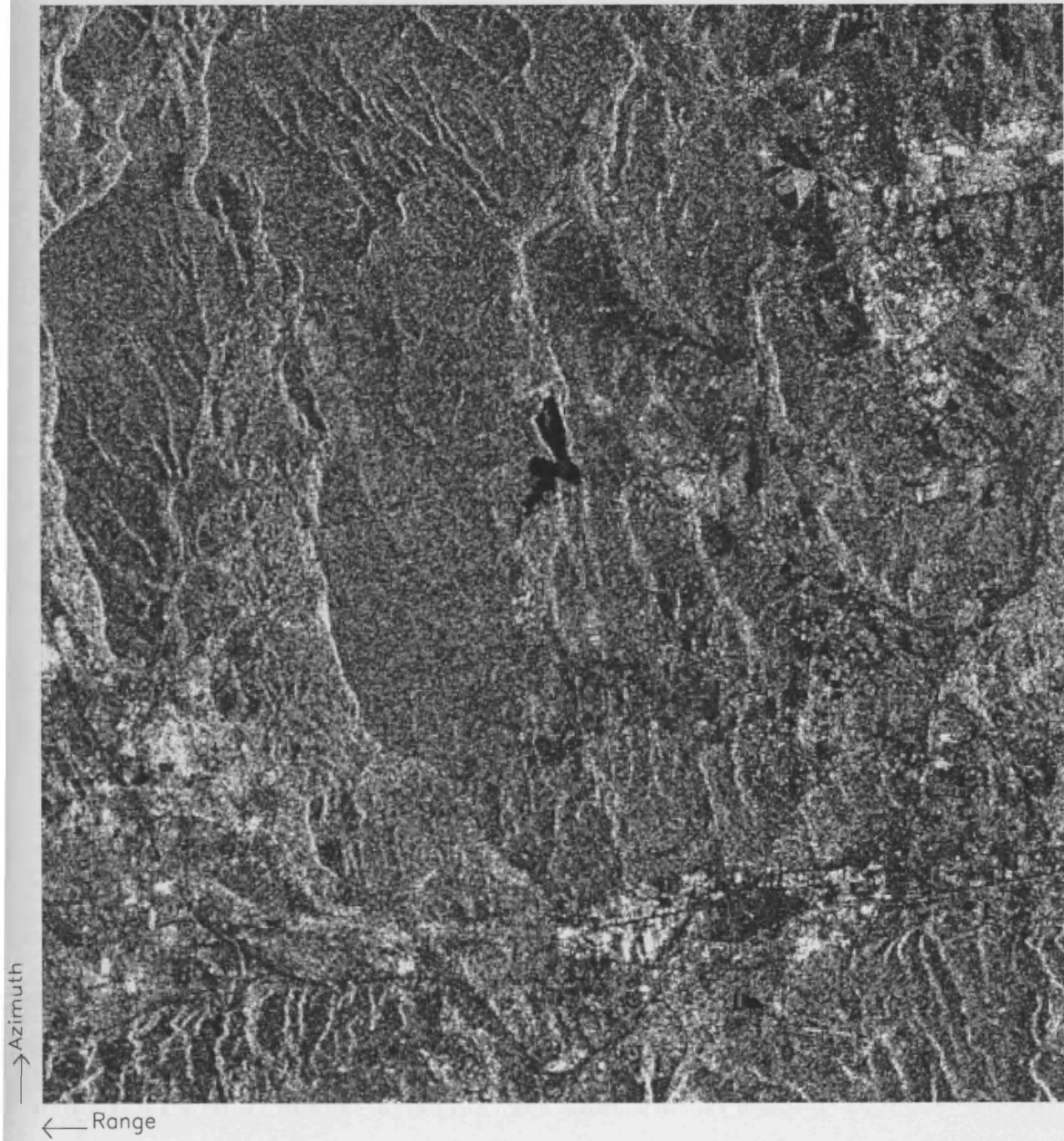
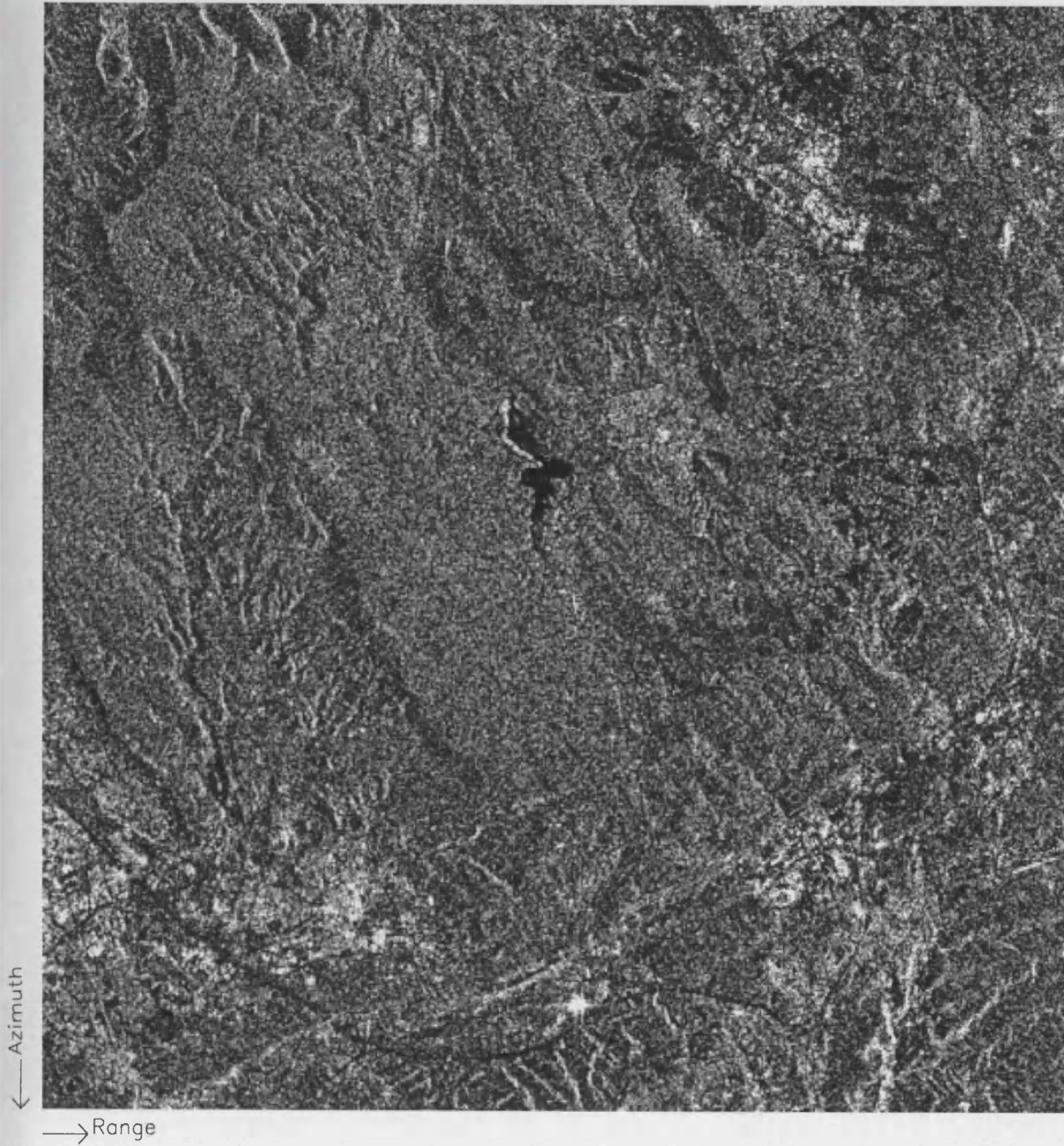


Fig.6.3: PRI_D raw image



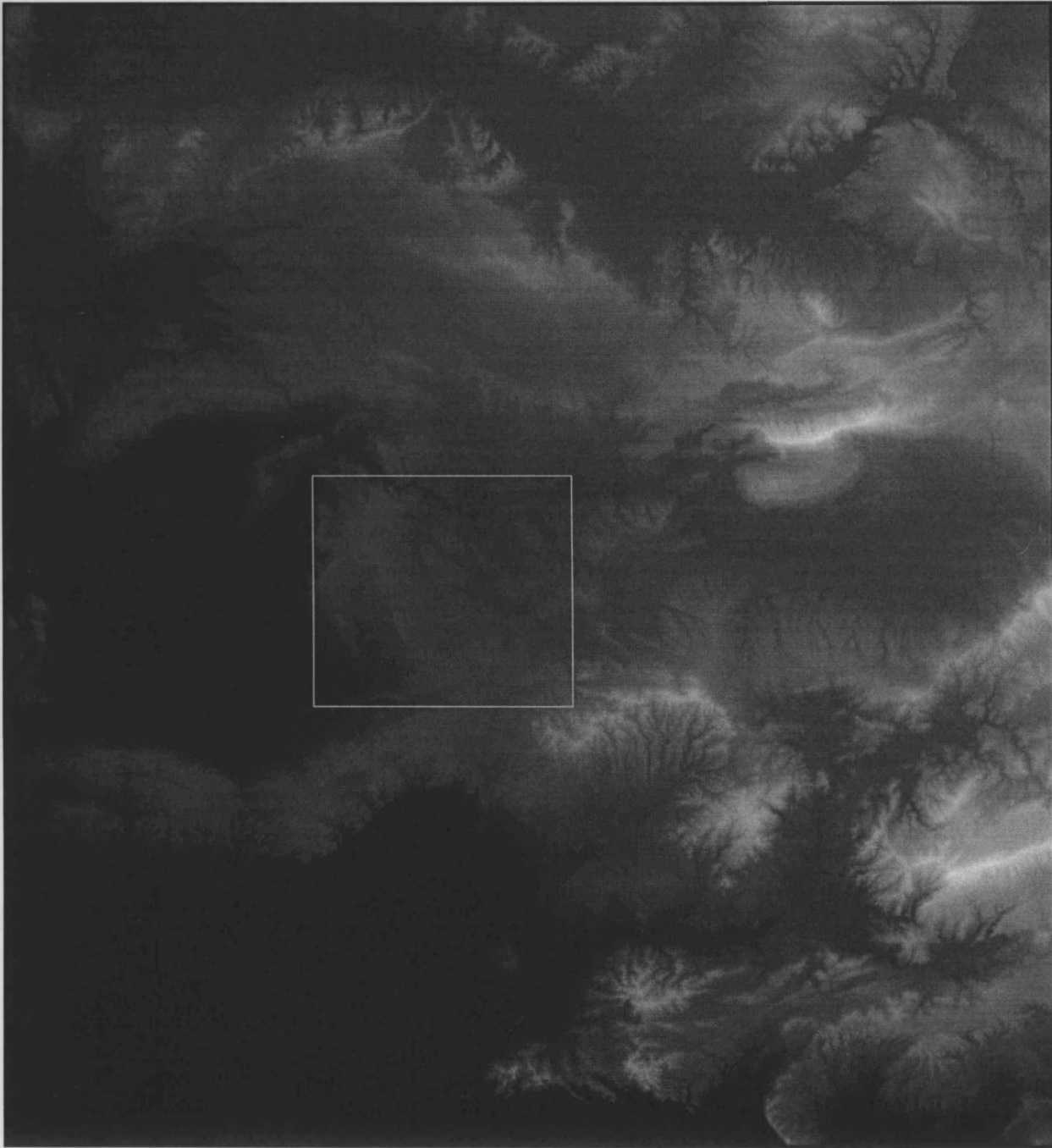
Generally, this area is without too much terrain relief. Much of the area is plain; the steepest slope region is on the west side of the area which is occupied by valleys. When observing the map more closely, it can be seen that the elevation of terrain gradually decreases from the south to north. There is a small lake in the middle of the site. Most of the railway lines pass through the south of the site. The north eastern part is the main industrial zone which can be clearly identified. When looking at the imagery, terrain features such as the valleys and hills can also be easily recognised.

Comparing the outlooks of the three images, stereo pairs SA - RTM_A and PRI_A are almost identical, while PRI_D shows many differences, the most obvious of which being the railway skewed to the right and the altered shape of the lake. This is expected since their different illuminations could hinder the ability to recognise corresponding points and features for the matching procedure, as discussed in Chapter 3. Therefore, it is rather difficult to stereo match using opposite side stereo pairs and this phenomenon will be demonstrated in the next chapter.

6.4 Reference DEM Introduction

The reference DEM data set used in this study was provided by IGN. It covers an area of 61km*63km in the south part of France, near Marseille and is with respect to the Lambert zone 3 coordinate system. This data set is stored in digital format and can be read out by using the usual **TAR** command in UNIX. The range of this data set is from 817000 to 878000 for the X coordinate and from 3103000 to 3166000 for the Y coordinate, with a grid spacing of 50m. The reference DEM is derived from 3 aerial photographs at two different scales of 1:6000 and 1:3000. Its accuracy is believed to be greater than 5 metres in the south and 2.5 metres in the north, while the overall accuracy is related to the characteristics of the local relief. In this reference DEM, a patch that corresponding to the area of interest is extracted to evaluate the matching results. The extent of this smaller extracted reference DEM is shown in Fig. 6.5. For the convenience of viewing of this extracted reference DEM, it is further shown in Fig. 6.6.

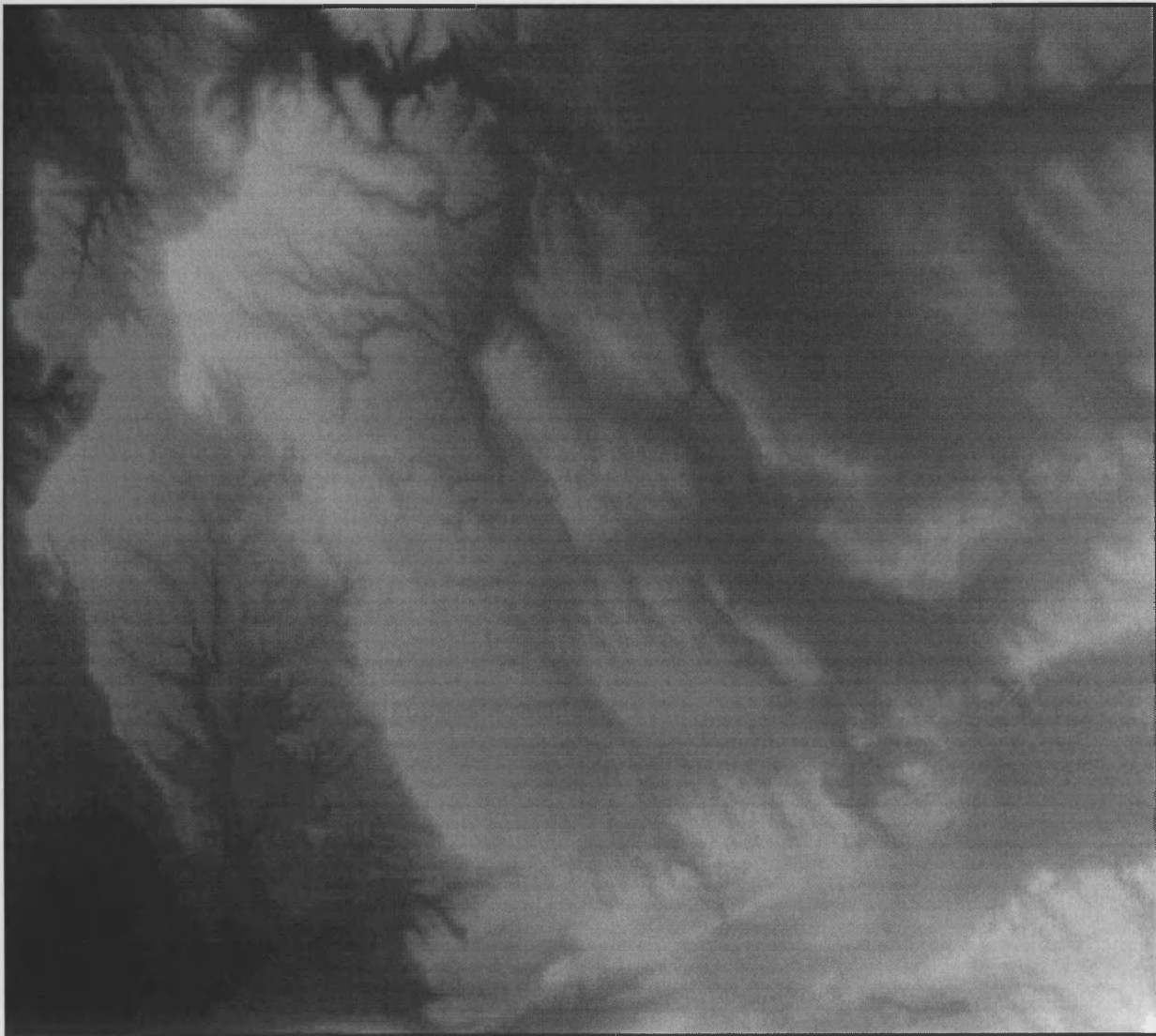
Fig. 6.5: Extracted reference DEM boundary



6.5 Evaluation of DEM Accuracy Algorithm

The method of extracting DEM accuracy used in this study is via a programme named COMPAKDEK, developed at UCL. COMPAKDEK works by comparing the input DEM by taking the reference DEM

Fig. 6.6: Extracted reference DEM of Aix-en-Provence



6.5 Evaluation of DEM Accuracy Algorithm

The method of evaluating DEM accuracy used in this study is via a programme named **COMPAREK**, developed at UCL. **COMPAREK** works by comparing the elevation of the reference point and the input DEM by kriging the reference DEM points to the same planimetric positions as that of the input DEM. The kriging is an interpolation technique which is a best linear unbiased estimator for it minimizes the estimation error variance. It estimates an unknown value of a point by using a weighed linear sum of this point neighbours. In **COMPAREK** after the kriging, the elevation of the same planimetric position of each point in the input DEM can be determined and comparisons can be made. The results generated by **COMPAREK** are the height deviation for each point, which can then also be subsequently linked to other statistical analysis commands. In this study, the DEM accuracy was defined as the standard deviation of the height deviation. To explore the characteristics of the height deviation in greater depth, its Root Mean Square (RMS) would be discussed as well.

Both values of standard deviation and RMS are used to measure the variation of height deviation. The former emphasises relative variation, while the latter the absolute variation. Their difference is related to the mean value of the height deviation. The purpose of using these two values in this study is to detect any systematic effect occurring in the matching results. For instance, if the value of RMS is larger compared to that of the standard deviation, then this systematic effect would be more obvious. In Chapter 7, the ratio of both values will be used as another measure to analyse the matching results by different strategies in pyramidal matching.

CHAPTER 7

Assessment of Stereo Matching Results

7.1 Introduction

The pyramidal stereo matching algorithm introduced in Chapter 4 is tested practically in this chapter. Various aspects of the pyramidal stereo matching technique are discussed. In general, these aspects can be approached from two different directions, seed point generation and matching procedures.

The seed point generation process is related to the **CASCADE** programme which is the method to generate seed points as well as the quantity of resulting seed points. As introduced in Chapter 4, these seed points are produced randomly in the first tier of pyramid image and the preliminary reasons for adopting these random seed points are (1) avoiding manual intervention so that the objective of automatic matching could be achieved, and (2) in paper [Ackermann, 1991], it is mentioned that the pull-in range could be increased at a coarser pyramidal level so that only rough initial values are needed. This theory proves the feasibility of using the random seed points in an image pyramid. In this chapter, the function of these random seed points and the impact of their number on the matching results will be analysed. For this purpose, the source code of **GRUENS** was modified to track down the performances of random seed points from the upper to the lower tier in the image pyramid. Moreover, this modification also exploits the advantages of utilising the image pyramid to stereo match rather than the original image. In addition, a blunder-removing filter is proposed here, which is a post-processing filter to detect the gross errors in each tiers matching results. With this filter, a technique is developed to choose the "optimum" seed points in order to enhance the matching results.

The matching procedures are influenced by the parameters of patch radius in **GRUEN** and the number of image tiers, both of which are controlled by the PDL file. The PDL file also determines the matching strategy for each image tier, whether with or without the additional refining process for each tier. The effects of this refining process will be evaluated by different numbers of seed points in section 7.6.

Simply speaking, the matching results are the combinations of the effects of the parameters mentioned above. These parameters are interrelated and are quite

complicated, and hence difficult to be analysed. For this reason, great effort has been made to find a systematic method to carry out these analyses. These analyses are based on the comparisons of the DEM accuracies which include the results of DEM on all three different SAR image pairs.

The contents of this chapter include firstly, detailed analysis of the **GRUEN** and **GRUENS** programmes. Then the same side imagery PDL file determination, and the interrelation of the seed points and image tiers are also discussed. Next, the blunder-removing filter as well as a strategy to choose the seed points are proposed. Last, the problems encountered in stereo matching the opposite side imagery are presented. For all three image pairs, the testing of speckle reduction filters to increase the coverage as well as the accuracy is incorporated.

7.2 GRUEN and GRUENS Programme Analysis

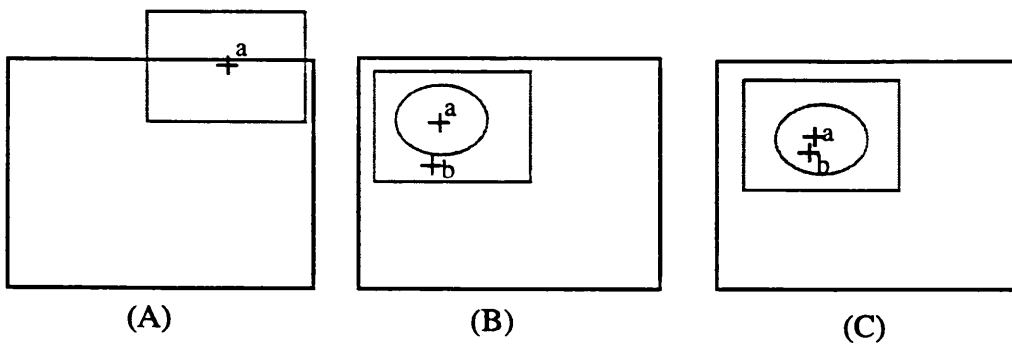
The general principle of **GRUEN** and **GRUENS** have been introduced in Chapter 5. In this section, the in-depth analysis of these two programs will be illustrated to aid the understanding of the whole process of pyramidal matching.




As mentioned previously, **GRUEN** is a refiner which only finds a pair of the matching coordinates from the given initial value. For each matching pair, the 4 coordinates of pixel location (in line and sample direction) on the left as well as the right image are taken as the input data and the coordinates on the right image are only the approximate values. The refining process is undertaken by keeping the first two columns of the input data fixed while adjusting other parameters to improve the correspondence. This procedure in turn causes column 3 ~ 4 data to be slightly altered from that of the input data. Apart from these coordinates, the output data has in addition 8 other values for each point, which can be seen in Fig. 7.1. In this figure, there are three numerical examples to show the three different situations generally encountered in matching based on the iteration value. Here, the meaning of these twelve values are introduced.

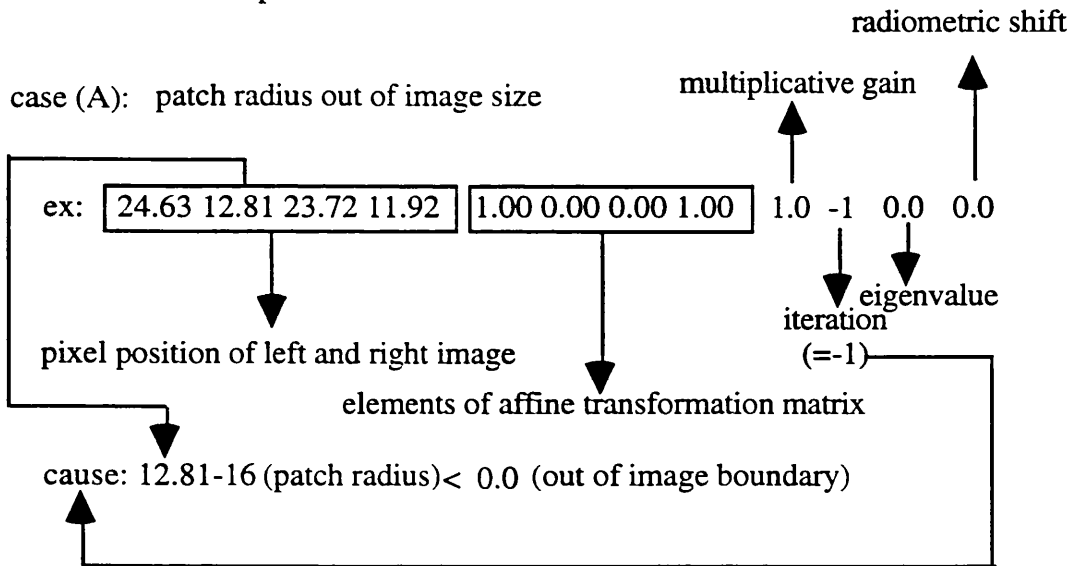
The first to fourth values are the matching results which give the correspondence of the pixel position on the left and right image. The fifth to eighth values are the 4 shaping parameters for the affine transformation matrix used to convert the coordinates of the right image to the left. Their initial values are 1, 0, 0 and 1 respectively, and if these four values appear in the output data of any point, it indicates that this point has not been subjected to any matching procedures, as in Fig.

7.1 case (A). The ninth value shows the multiplicative gain, which is the multiplicative scale factor between the coordinates of the two images, with an initial value of 1.0. The tenth is an integer field to denote the number of iterations used by **GRUEN** to search for the matched positions. This iteration value is the most important among all the other 8 output values, for it reveals the condition of the matching procedures, as illustrated in Fig. 7.1. In case (A), the iteration value is set to -1 which means that for this seed point, the matched patch has gone outside of the image boundary so that this point does not go into any matching process. This situation which can also be seen from observing the elements of the affine transformation as mentioned earlier. In case (B), the iteration value is set to -20 to imply that the points have not yet converged after 20 iterations, as a consequence of poor estimation of the initial values. If the iteration value is positive, the matching is going smoothly, as in case (C). Among the above three cases, case (A) should be given special attention because in the pyramidal matching employed in this project, this situation often occurs on the first tier of most matching points, where the image size is very small and the match patch radius for the seed points is more likely to be outside of the image boundary. The eleventh value gives the eigenvalue for the covariance matrix and as described in Chapter 4. It is the standard figure used to judge the quality of the matching points. It is based on this value that **GRUENS** grows other seed points. The twelfth value is an additive radiometric shift parameter with an initial value 0.0, and it is able to give an indication on the shifting quantity of the matched points between the left and right image.

Like **GRUEN**, **GRUENS** uses the same technique to refine the seed points. Furthermore, based on these refined seed points, it is able to grow many other seed points. However, this refinement is related to the number of values of the input data. If only four values are given as in the case of manual seed points, **GRUENS** will refine them and begin to grow; while in the case of the pyramidal matching in this study, 12 values are provided and as a result two circumstances could occur depending on the iteration values of the seed points. If the iteration value is equal to -20 (case(B), Fig. 7.1) or -1 (case (A), Fig. 7.1), **GRUENS** would just discard them since they do not qualify as good seed points. This process explains the reason why the number of random seed points will be greatly reduced. Only those seed points with positive values (case (C), Fig. 7.1) would be accepted and considered as good seed points by **GRUENS**, and they are not to be refined in the later successive tiers.



-  : image size(128*128)
-  : patch radius (16)
-  : pull-in range
- \oplus_a : initial position
- \oplus_b : matched position



case (B): poor initial value (not converged in pull-in range)

ex: 67.94 71.88 66.74 74.81 -0.04 0.04 1.0 0.56 0.78 -20 16.10 38.97

iteration
(=-20)

case (C) : successful matching

ex: 75.82 20.69 75.59 21.76 1.00 -0.00 0.00 1.03 0.51 4 33.92 70.51

iteration
(positive)

Fig. 7.1: Three numerical examples of 12 values of GRUEN's output (not to a scale)

7.3 Determination of Matching Strategy

The reason for investigating the utilisation of **GRUEN** and **GRUENS** in the preceding section is because there are two pyramidal matching strategies employed in this research project and the comprehension of these two programs is essential prior to the understanding of the execution procedures involved in these two strategies. For each strategy, a corresponding PDL file was established. The first and second strategy was represented by PDL1 and PDL2 respectively as shown in Fig. 7.2 and 7.3. From these two figures, it can be seen that the two strategies were used the same parameters except that strategy 2 had an extra refining process, implemented by **GRUEN**, on each tier. The reason for having an additional refining process, was that it was observed later that **GRUENS** does not refine the seed points prior to growing other new seed points, as mentioned in the last section. Therefore, it was in our interest to test the impacts of refining on the accuracy of the pyramidal matching.

To facilitate the understanding of the two strategies, the execution procedures are shown in Fig. 7.4 and 7.6 respectively; while their numerical examples are given in Fig. 7.5 and 7.7. For strategy 1, it can be seen from Fig. 7.4 that only the first tier employed the **GRUEN** matching command, while the remaining seven tiers used **GRUENS**. This is because on the first tier there were only a few growing seed points, and **GRUENS** is unexecutable without sufficient qualified seed points. This situation is of special concern when considering Random Seed Effects (RSE), which arise directly from the random seed points and are able to cause significant deterioration of the matching results. To avoid this, often only a few random seed points would be selected to initiate the matching procedures. Since **GRUENS** is not a suitable programme under these circumstances, **GRUEN** is firstly employed on the first tier to refine the random seed points. Once the random seed points are refined it is very likely that they will become qualified and are more reliable for **GRUENS**, and from the second tier to grow other seed points to proceed the pyramidal matching.

In Fig 7.5, it is shown that the number of random seeds on the first tier, NT1, was reduced from 4 to 2 as they entered the second tier. In a real situation, this reduction may be more than one thousand. This is because after the refining is completed on the first tier, the majority of the random seed points have negative values and they will be discarded by **GRUENS**, as described in the last section. Only those seed points with positive iteration values are allowed to proceed to the second tier. Thus, despite the fact that **CASCADE** generates thousands of random seed points, only a small proportion of them will remain; these seed points are defined

as the Effective Random Seed Points (ERSP). As shown in Fig. 7.5, the output of all the seed points remain the same (iteration values) except the line and sample coordinates of the stereo pair. These coordinates are the values of the first four columns which will be multiplied by a factor of 2 as they enter the second tier. Therefore, once the ERSP are created, they will not be subjected to any further refining procedures, other than the line and sample coordinates of each point is simply multiplied by a factor 2 for each tier. This process of multiplication is also carried out on the further growing seed points. As a result, the matching results for strategy 1 can be calculated from the growing points on each tier plus the ERSP. The derivation of the calculation is shown in Fig. 7.4 - the mathematical formula for the matching results.

For strategy 2, the coordinate variation of seed points is completely different from strategy 1. The difference is caused by the additional implementation of **GRUEN** on each tier. That is, prior to growing other seed points on each tier the resulting original seed points are firstly refined. For example, the ERSP obtained on the first tier will be refined on entering the second tier before growing other seed points. After growing, the resulting original seed points entering the 3rd tier will be refined again. This same process is repeated for all the tiers until the bottom tier is reached. Thus, unlike strategy 1, the matching results for strategy 2 could not be predicted from the growing seed points on all the tiers as shown in Fig. 7.7. The different performance of the two strategies introduced here offers an opportunity to exploit the impacts and the relative importance of the refining process on every tier, which is one of the objectives of this section.

The other objective of this section is to determine the values of parameters within the PDL file that is employed in this research. As mentioned earlier, two factors have to be considered in the PDL file, namely image tiers and patch radius. With respect to the image tier, enough image tier should be used to avoid the RSE. Regarding the patch radius, as mentioned in section 4.4, in the PDL file the patch radius for the first and the last tier can be specified by the user, and these two values can be used to proportionally calculate patch radius for the remaining tiers. Since the image size for the first tier is usually small, it is better to choose a small patch radius to limit the possibility of random seed points being outside of the image boundary and have more "qualified" random seed points. For this reason, a patch radius of 3 was used on the first tier for the 8*8 image in this project.

```

* Reference image is 1024*1024
* 8tiers used-->top is 8*8
  apex 8
  laplacian 2
  pscale 3 25 round
* Apical tier
  tier localhost noshakeup
  gruen -patchrad $
emd
  reduce
  xtee
  etier
* Tier 2
  tier localhost noshakeup
  gruens -patchrad $ -pthresh 150 -grid 1
  emd
  reduce
  xtee
  etier
* Tier 3
  tier localhost noshakeup
  gruens -patchrad $ -pthresh 150 -grid 1
  emd
  reduce
  xtee
  etier
* Tier 4
  tier localhost noshakeup
  gruens -patchrad $ -pthresh 150 -grid 1
  emd
  reduce
  xtee
  etier
* Tier 5
  tier localhost noshakeup
  gruens -patchrad $ -pthresh 150 -grid 1
  emd
  reduce
  xtee
  etier
* Tier 5
  tier localhost noshakeup
  gruens -patchrad $ -pthresh 150 -grid 1
  emd
  reduce
  xtee
  etier
* Tier 6
  tier localhost noshakeup
  gruens -patchrad $ -pthresh 150 -grid 1
  emd
  reduce
  xtee
  etier
* Tier 7
  tier localhost noshakeup
  gruens -patchrad $ -pthresh 200 -grid 2
  emd
  etier
end

```

Fig. 7.2: PDL1 file

```

* Reference image is 1024*1024
* 8tiers used-->top is 8*8
  apex 8
  laplacian 2
  pscale 3 25 round
* Apical tier
  tier localhost noshakeup
    gruen -patchrad $
    gruens -patchrad $ -pthresh 150 -grid 1
emd
  reduce
  xtee
  etier
* Tier 2
  tier localhost noshakeup
    gruen -patchrad $
    gruens -patchrad $ -pthresh 150 -grid 1
  emd
    reduce
    xtee
  etier
* Tier 3
  tier localhost noshakeup
    gruen -patchrad $
    gruens -patchrad $ -pthresh 150 -grid 1
  emd
    reduce
    xtee
  etier
* Tier 4
  tier localhost noshakeup
    gruen -patchrad $
    gruens -patchrad $ -pthresh 150 -grid 1
  emd
    reduce
    xtee
  etier
* Tier 5
  tier localhost noshakeup
    gruen -patchrad $
    gruens -patchrad $ -pthresh 150 -grid 1
  emd
    reduce
    xtee
  etier
* Tier 6
  tier localhost noshakeup
    gruen -patchrad $
    gruens -patchrad $ -pthresh 150 -grid 1
  emd
    reduce
    xtee
  etier
* Tier 7
  tier localhost noshakeup
    gruen -patchrad $
    gruens -patchrad $ -pthresh 150 -grid 1
  emd
    reduce
    xtee
  etier
* Tier 8
  tier localhost noshakeup
    gruen -patchrad $
    gruens -patchrad $ -pthresh 200 -grid 2
  emd
  etier
end

```

Fig. 7.3: PDL2 file

Chapter 7. Assessment of Stereo Matching Results

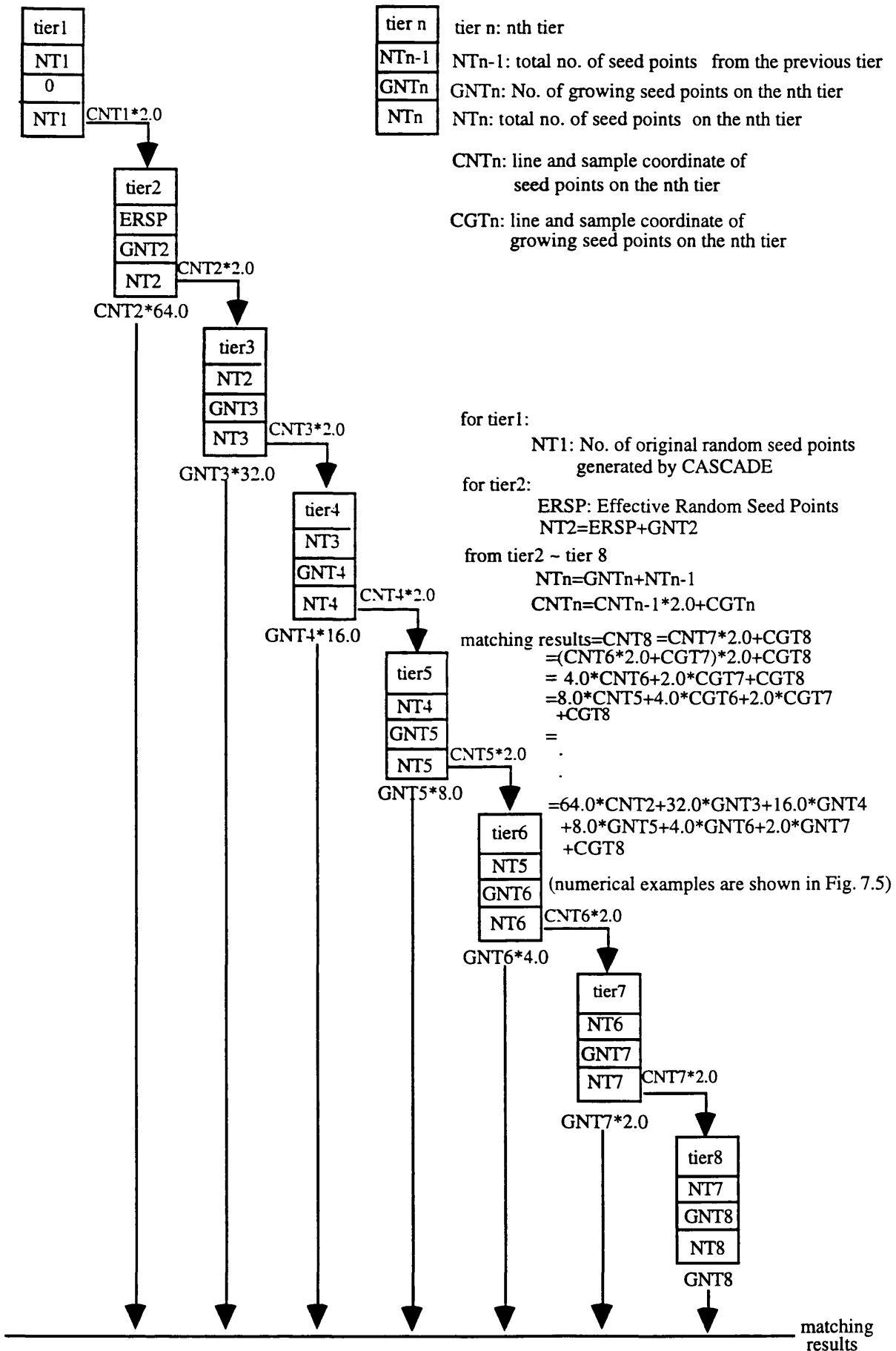


Fig. 7.4: Strategy 1 execution procedures

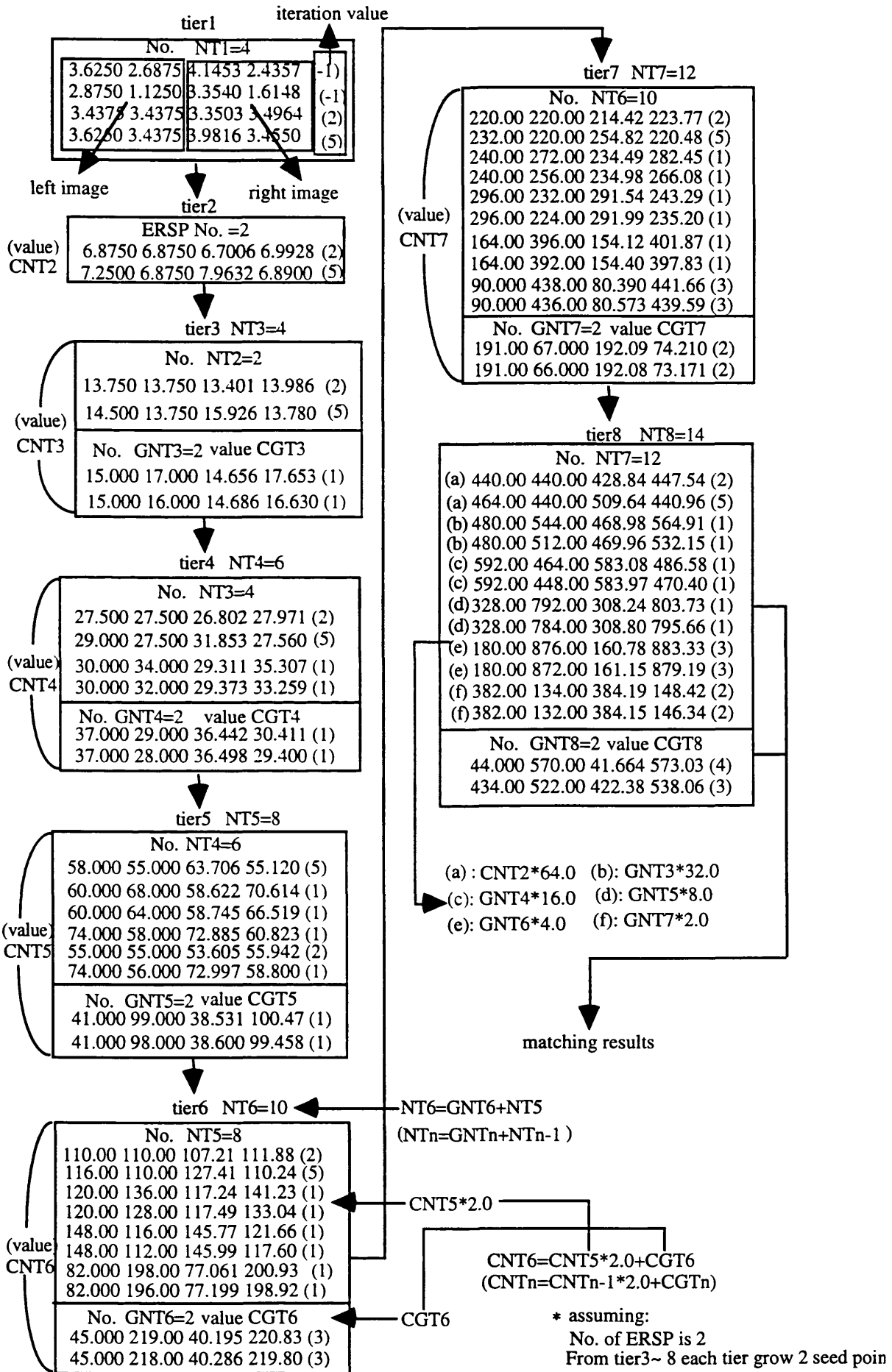


Fig. 7.5: Numerical examples for strategy 1

Chapter 7. Assessment of Stereo Matching Results

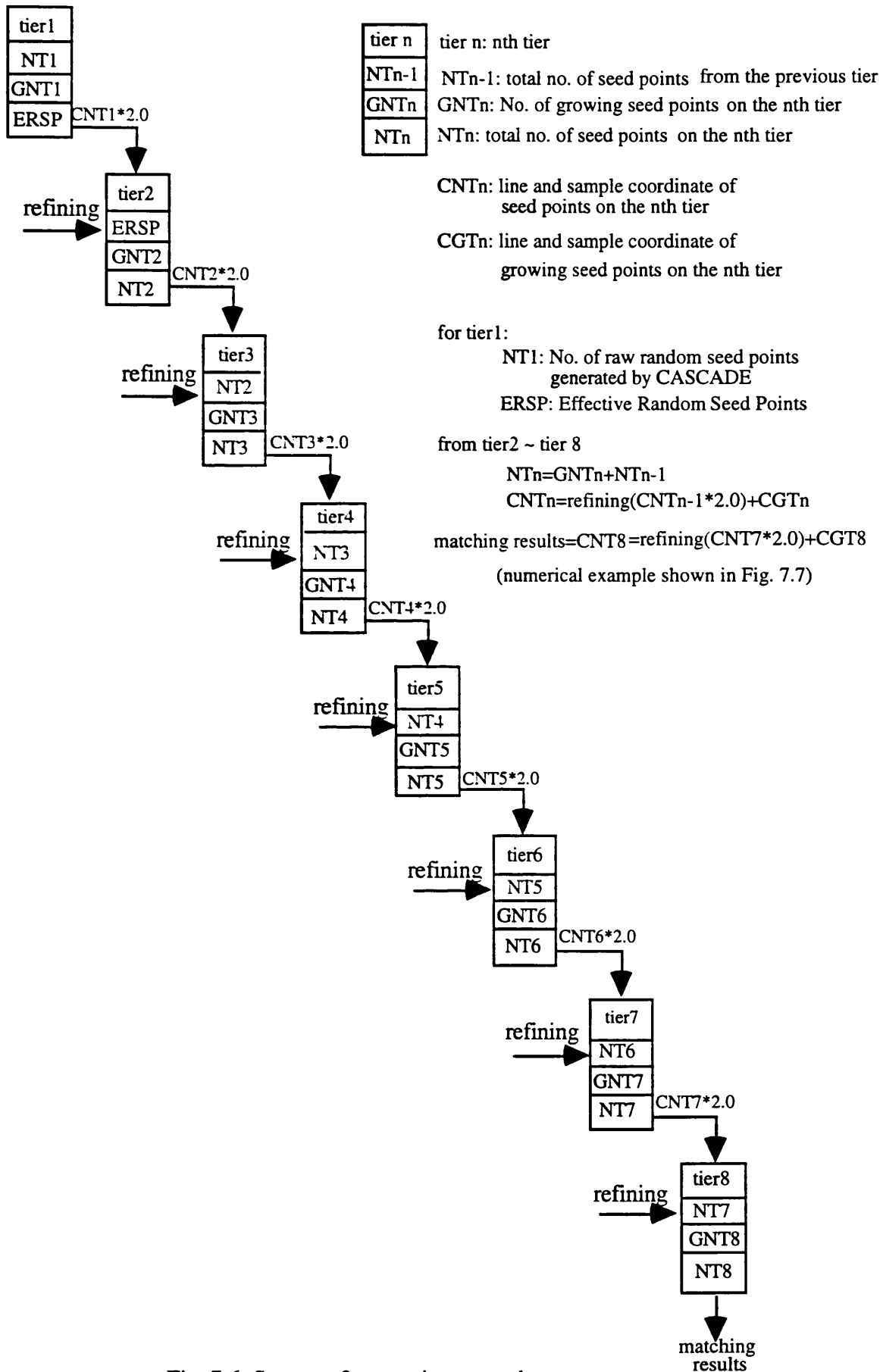


Fig. 7.6: Strategy 2 execution procedures

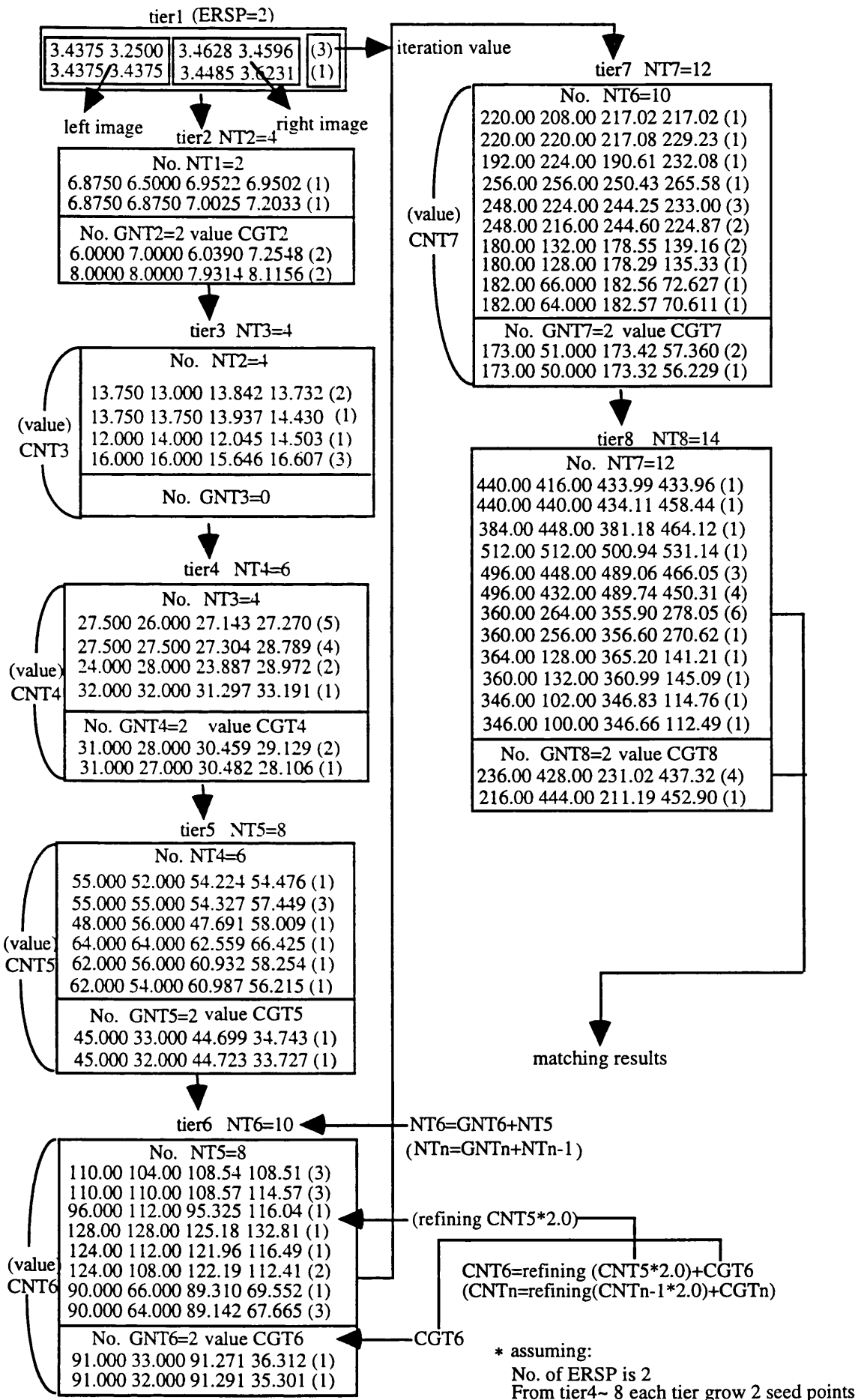


Fig. 7.7: Numerical examples for strategy 2

In contrast, a large patch radius is preferred for the last tier. This is because with small patch radius, the matching is more vulnerable to image noise. For SAR imagery, this influence could cause more severe damage, as illustrated in Table 7.1 and 7.2.

	radius 15	radius 20	radius 25
SA ^a	171.15	167.55	172.17
OP2 ^b	36.46	26.60	30.68

SA^a, OP2^b: refer to Table 6.2

Table 7.1: DEM accuracies (m) for the manual seed points under 3 different patch radii

	radius 15	radius 20	radius 25
SA	58.56	77.81	78.21
OP2	0.71	0.54	2.40

Table 7.2: Coverage (%) for the manual seed points under 3 different patch radii

Table 7.1 shows the DEM accuracy obtained using 3 different radii with the manual seed points, while Table 7.2 shows their corresponding coverage. There are 12 seed points for the same side and 9 seed points for the opposite side respectively. Considering the DEM accuracy alone, for both the same side and the opposite side, a patch radius of 20 seems to be a better value to use, though there is no significant difference compared with a patch radius of 25. When taking the coverage into account, it is observed that a patch radius of 25 performed best especially for the opposite side stereo pair, it can reach a coverage of 2.4 which is five times more than that of radius 20 at 0.54. This dense coverage could be the explanation for the less satisfactory DEM accuracy of the patch radius of 25. From these two tables, it is also demonstrated that for SAR imagery, patch radius is a crucial factor which is able to greatly affect the match results. Overall, the larger patch radius can contribute to better DEM accuracy, however, it will cause smoothing effects on the terrain height. This can be seen in Fig. 7.8, 7.9 and 7.10. These three figures give the perspective view of DEM from the radii of 15, 20 and 25 respectively. It is shown that in the central part of the image the smoothing effect is most obvious. With smaller radius (radius of 15), greater height for this area is derived, but as the patch radius becomes larger the height will gradually be reduced. In this study, deriving a satisfactory DEM is our purpose, therefore a large patch radius is adopted for the last tier. In addition, to alleviating the effects of patch radius, the patch radius is always kept fixed at 25 throughout this research, irrespective of the stereo pair type (same side or opposite side).

Fig. 7.8: Perspective view of DEM from manual seed points (radius 15)

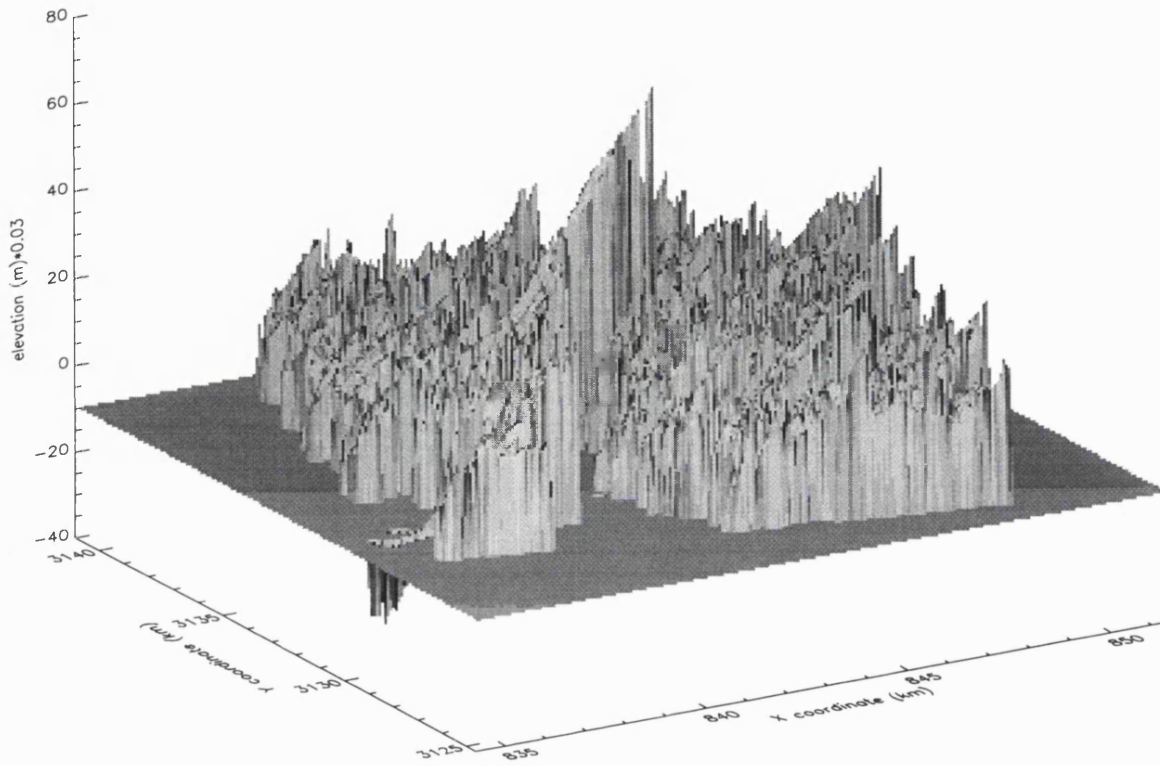


Fig. 7.9: Perspective view of DEM from manual seed points (radius 20)

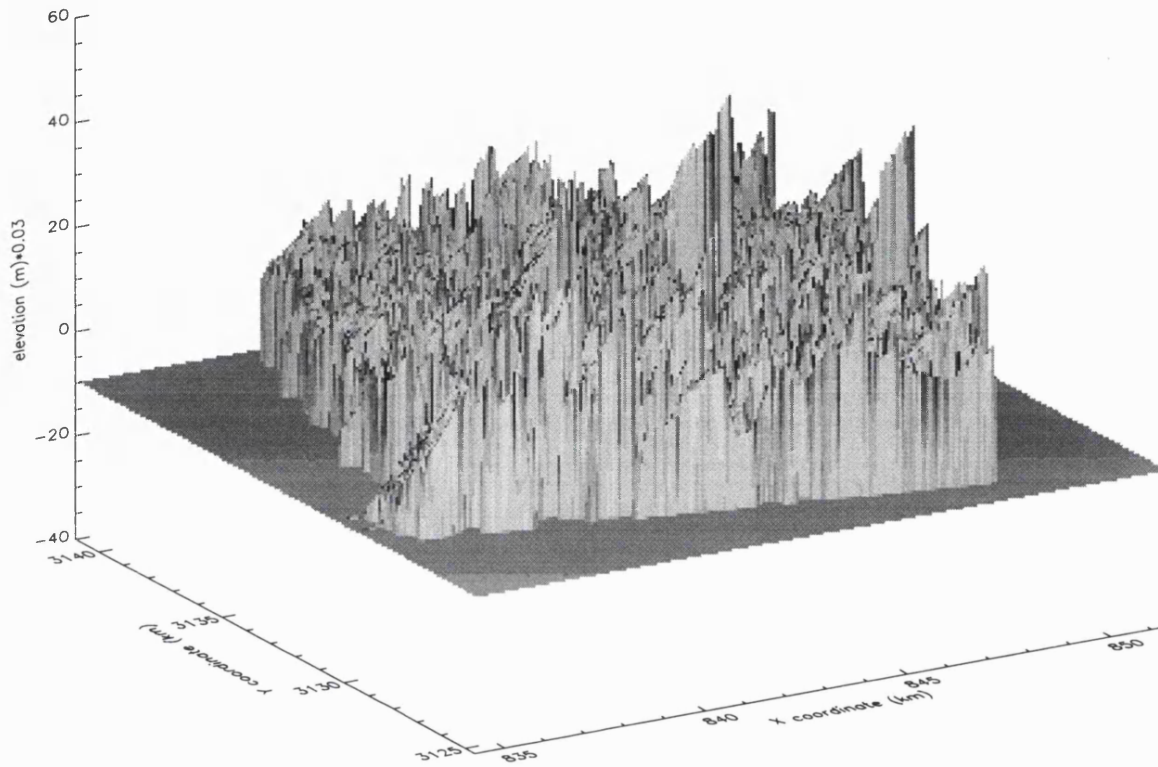
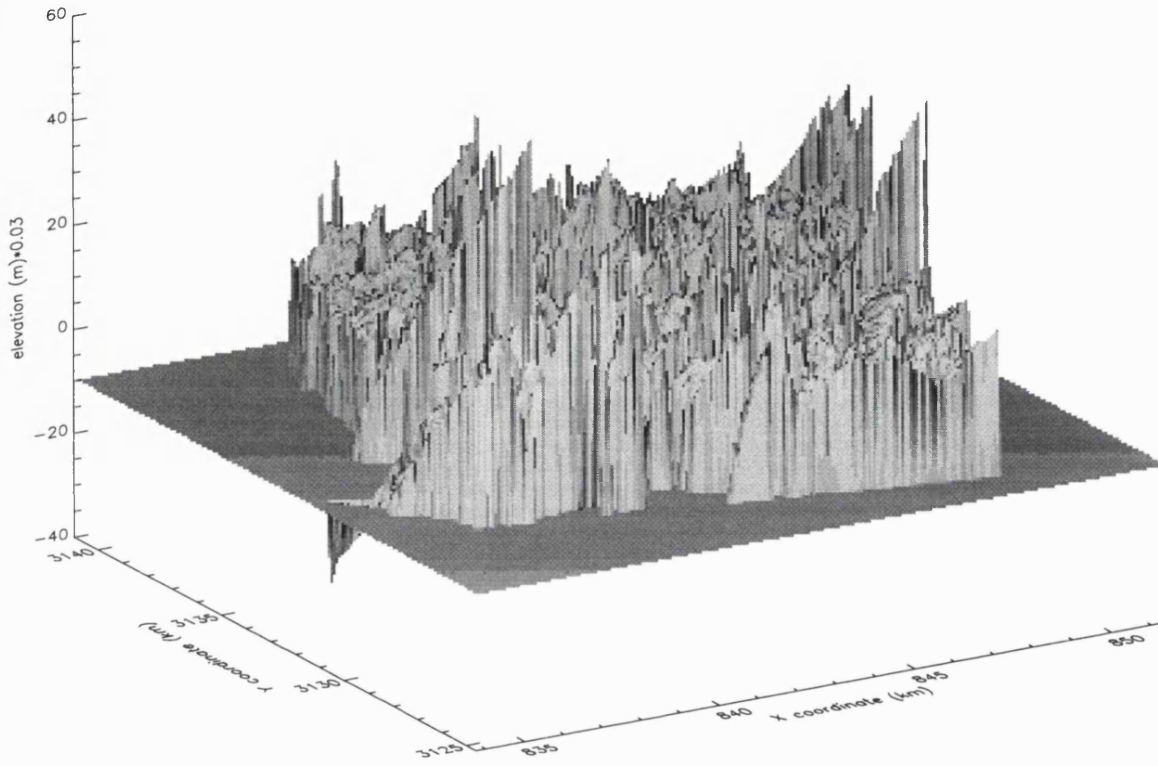


Fig. 7.10: Perspective view of DEM from manual seed points (radius 25)



Only two proceeding strategies, defined in PDL files were discussed here, yet, with various combinations of image tiers and patch radii, there are many more PDL files which could be produced. In order to simplify the influence of the PDL file on the matching results, the patch radius is fixed as described, but the image tiers vary for the evaluation of the RES.

7.4 Random Seed Point Generation

The random seed points discussed here are the “raw” random seed points which are generated by CASCADE without any refining process. The ERSP mentioned earlier is the result of inputting these random seed points to the PDL file. These random seed points, as mentioned in section 4.3, are influenced by two crucial factors: the grid number and the uncertainty_radius. The grid number is related to the interval of line and sample direction of seed points on the reference image, while the uncertainty_radius determines the disparity of these two directions. For a fixed uncertainty_radius, a greater grid number implies more random seed points, while with given grid number, a larger uncertainty_radius means fewer seed points, as many would fall outside of the image boundary of the apex tier. As a matter of fact, in an eight-tier pyramid, it is unnecessary to consider the value of uncertainty_radius greater than one. For on the apex tier if the uncertainty_radius is one, the range of disparity is between -1 to +1 pixel, corresponding to a range of disparity from -64 to +64 pixels on the original image. This range of 128 pixel is broad enough to cover the disparity of any pixel regardless of the line or the sample direction. Therefore, the value of uncertainty_radius was set at 1 for this present study.

7.5 Random Seed Point Analysis

In the initial stages of our research, difficulties were encountered when assessing the influence and the importance of the random seed points. Questions were raised regarding the function and the underlying mechanism of random seed points. The impact of the number of actual random seed points used and the different ways of processing using the PDL1 or PDL2 files have on the matching results were also under consideration. The answers to all these questions can be provided by means of a new approach introduced here which will be able to track down the random seed points on every tier. To achieve this, the source code of GRUENS was modified and named GRUENS_SEED. GRUENS_SEED utilises the same

algorithm to grow seed points but with four extra integer columns added to each line of the **GRUENS** output. One integer column was located before all the data columns and it specified *seed_number*. The other three integers were placed as the last three columns, representing the *seed_generation*, *seed_mother* and *seed_son* respectively. With these four additional columns, it was possible to trace the location of the origin of any seed point. In other words, they help to establish the regulation that could pinpoint the *initial seed points* and target the seed points subsequently created. The *initial seed points* mentioned here are the seed points prior to growing. The manual seed point is one type of initial seed point. In the case of the pyramidal matching used in this study, the *initial seed points* increased accordingly on every tier, and the number of *initial seed points* of a given tier is equal to the total number of seed points of the previous tier.

The detailed principle of **GRUENS_SEED** are described as follows. Prior to the growing process, attach a *seed_number* to each *initial seed point*. This *seed_number* ascends orderly from 1 to the total number of seed points. After the matching is completed for the initial seed points, specify the value for the *seed_generation*, *seed_mother* and *seed_son* as “1”, “0” and “1” separately for each *initial seed point*. The reason for choosing these values was that these *initial seed points* were elementary seed points that were not derived from other seed points.

There are four directions to expand for each seed point. But due to the constraint condition specified by the user (e.g. eigenvalue), not every direction would be suitable to have a new seed point. If successful growing was possible for all 4 directions, the *seed_son* would have a maximum value of 4. Therefore the *seed_son* could vary from 1 to a maximum of 4. During the growing process, first specify the *seed_mother* of any growing seed points to be equal to the *seed_son* of the seed point that it comes from. After the procedures of growing in four directions are completed, the *seed_son* is re-zeroed for reassigning the number of *seed_son* to other growing seed points. When the *seed_son* of any growing seed point was recorded as 1, it implied that this growing process had been successful, and the *seed_generation* of this given growing seed point would increase by 1. It should be noticed here that the *seed_number* did not alter for the above procedures, that is the *seed_number* of the growing seed points and that of the *initial seed point* were identical. Based on all these relationships described, it was possible to determine the growing seed points of any given seed point, and conversely the exact seed point they were derived from. Two figures are given below to aid the understanding of this **GRUENS_SEED** programme. Fig. 7.11 shows the flow chart for the method and Fig. 7.12 illustrates the use of this **GRUENS_SEED**'s technique by providing an example shown in a

diagram. In this example the growing process was said to start from the 5th *initial seed point*, and the manner by which the first four generations of seed points proceeded was demonstrated. The *seed_generation* is of great importance because it can help to explain why matching in the image pyramid is more superior than on a single tier, a concept which will be analysed in section 7.9. The *seed_number* is another parameter of great concern, for the growing seed points of ERSP could be discovered on each tier based on this number. The impact that growing seed points from ERSP has on the matching results is defined as the Growing Random Seed Effect (GRSE). It is expected that the GRSE would deteriorate the results for those seed points grown from seed points which are randomly selected, unlike the typical seed points chosen manually. As well as the GRSE, another effect called the Original Random Seed Effect (ORSE) caused only by the ERSP has an even worse influence on the matching results. The GRSE plus the ORSE would lead to the RSE which was mentioned previously in section 7.3.

For evaluating the RSE, it is necessary to firstly locate the ERSP and their growing seed points. This could be done simply by replacing **GRUENS** with **GRUENS_SEED** on each tier in the PDL file . The detailed strategy of detecting the RSE for PDL1 is as follows:

(1) On the second tier, check the *seed_number* in the output of the **GRUENS_SEED** to find out on which line the *seed_number* begins to repeat. This line number minus one will be the number of ERSP. For instance, if the ERSP is 10, the *seed_number* is from 1 to 10, which corresponds to the line 1~10 respectively. The seed number of line 11 will appear as one of the digits from 1 to 10.

(2) From the third to the bottom tier, **GRUENS_SEED** reorders the original seed points (from 1 to the number of *initial seed points*) before the growing starts on each tier. For the output of each tier, the foremost 10 lines are the matching results of ERSP. The growing seed points with *seed_number* 1 to 10 were used to calculate the GRSE. This calculation was carried out in 3 steps:

(a) From each tier, search for seed points grown from the ERSP on the output data based on their *seed_number*.

(b) The coordinates of the selected points were scaled up by a factor of $2^{*(n-m)}$ times (n is the total tier number and m is the number of current tier). e.g. on the third tier of an eight-tier image pyramid, the line and sample coordinates should be multiplied by $2^{*(8-3)}=32$.

(c) All the results were collected from step (b), which are the points growing from random seed points, and used to calculate the GRSE.

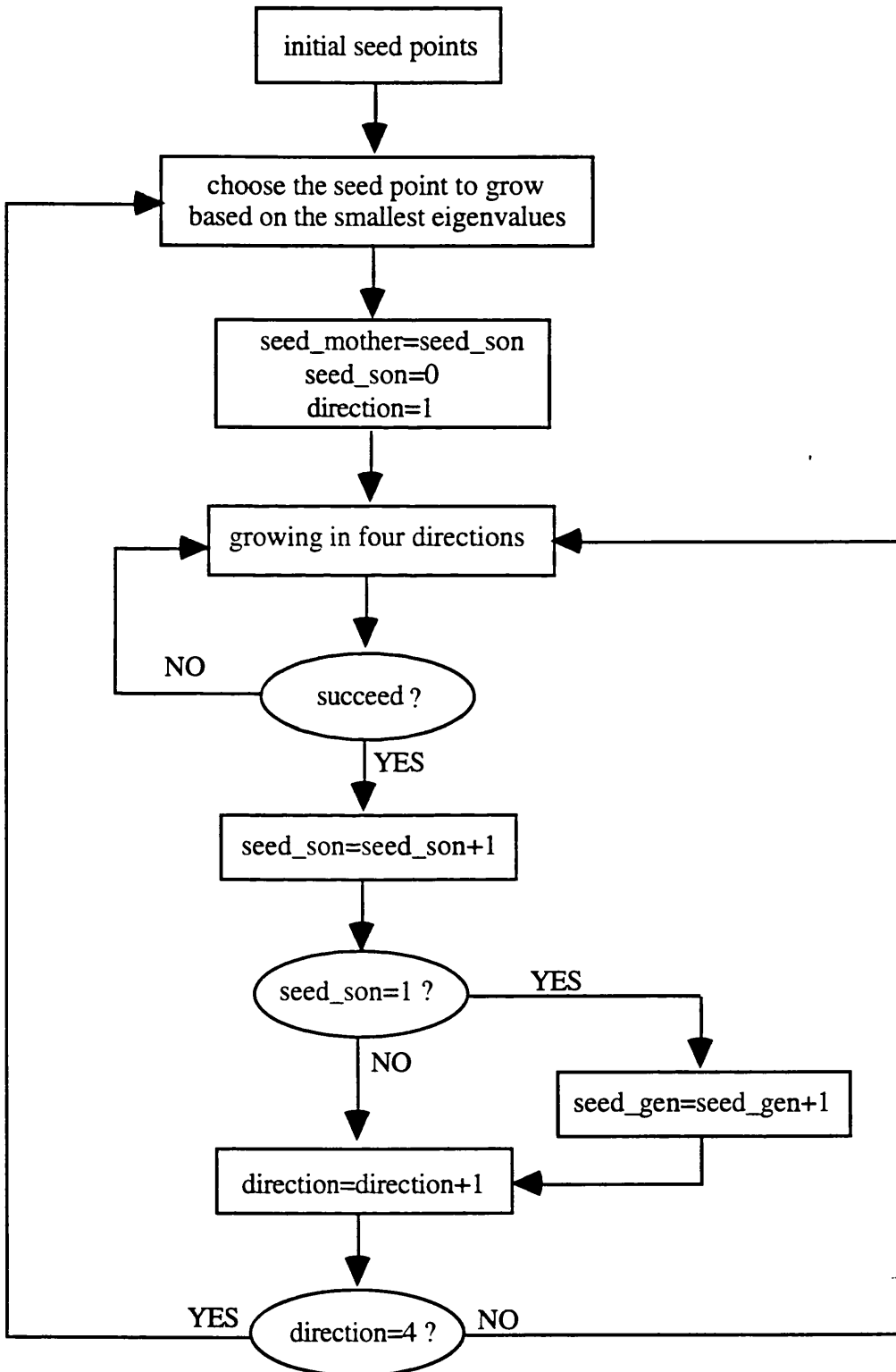
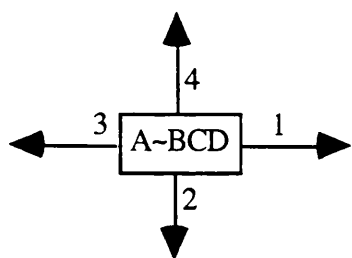
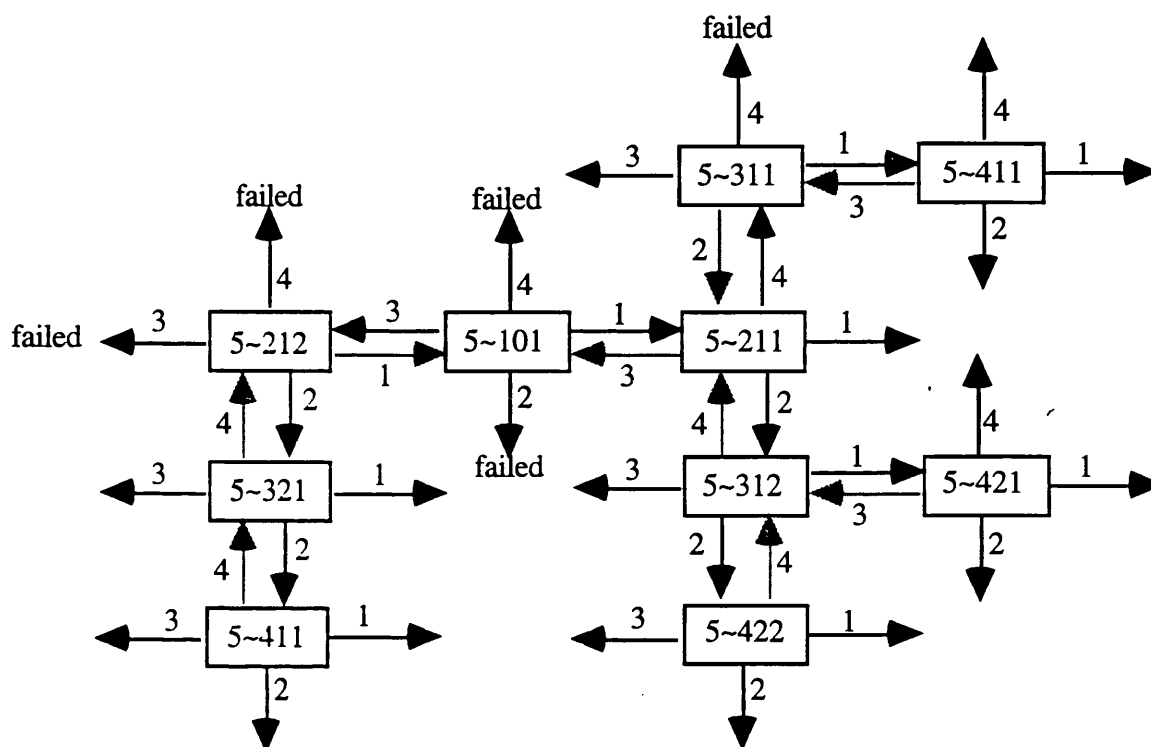


Fig. 7.11: Flow chart of GRUENS_SEED



—▶ direction to grow

—▶ direction not allowed to grow for the position has been occupied

A: seed_number

~: from 2 to 13 columns of the GRUENS_SEED output
the identical values of GRUENS from 1 to 12 column

B: seed_generation

C: seed_mother

D: seed_son

Fig. 7.12: Diagram for the techniques of the GRUENS_SEED

If the matching results were to be assessed without the GRSE , a straightforward **DELETE_LINE** programme developed could be used to get rid of all the growing random seed points obtained from step (b) based on their line and sample coordinates.

For the PDL2, the whole procedure for detecting the RSE is the same as described above, the only difference is that the ERSP is determined on the first tier instead of the second one.

From the above analyses, it was concluded that more image tiers should be used for the pyramidal matching. With more image tiers, the proportion of random seed points to total seed points becomes smaller so that the GRSE is less likely to happen. This theory will be proved by experimental results in the next section.

7.6 PDL File Data Testing

The two PDL files, PDL1 and PDL2 were tested with three different grid numbers, 32, 64 , and 128. The suffix "1" and "2" following the underscore represents the PDL1 and PDL2 file respectively e.g. grid32_1 are the seed points produced by the random seed points of grid 32 under PDL1 file. This notation will appear throughout in this thesis. Various aspects of these two PDL files affecting the DEM accuracy are discussed in this section, which include the investigation of ORSE and GRSE under three different grid numbers of random seed points as well as determination of the relationship between the image tiers and RSE. The magnitude of the influence of the above on DEM accuracy between the two PDL files was also compared. Finally, the cause of the different performances between the two stereo matching methods using PDL1 and PDL2 files was analysed.

7.6.1 PDL file data testing: ORSE

The ORSE, as mentioned in section 7.5, is simply caused by ERSP. Searching for ERSP is quite simple, since they must appear before any seed points in the matching results. Once the number of ERSP is known, it is easy to find out the ERSP and calculate its RMS which is shown in Table 7.3. In this table, it can be seen that the RMS values for PDL1 was very large, varying from 6643m to 8546m. For PDL2, the performance of ERSP was much better. This could be explained by the fact that for PDL1, once the ERSP was created on the second tier, their matching

results were not altered, except for the multiplication of the coordinates by 64 (as shown in Fig. 7.4). For PDL2, the ERSP was refined for each tier, which could give rise to better results. Now the ORSE mentioned in section 7.5 can be calculated from the difference of two DEM accuracies with and without the ERSP. For the evaluation of ORSE, Table 7.3 lists the DEM accuracy before and after removing the ERSP and the ORSE is displayed in this table as well. In PDL1, ORSE for grid 128 was quite significant, without the ORSE, the accuracy improvement could reach approximately 80m. This is due to its large number of random seed points. Table 7.3 also illustrates that the ORSE is proportional to the number of ERSP. Compared with PDL1, the ORSE of PDL2 was not so severe, as little improvement (<2m) was observed. The significant difference of ORSE between these two PDL files is thought to be consistent with the analyses of ERSP earlier.

7.6.2 PDL file data testing: GRSE

As stated in section 7.5, in addition to the ORSE, the GRSE is another important factor in RSE affecting the DEM accuracy. To analyse this GRSE, the RMS of the growing random seed points of the two PDL files for each tier is listed in Table 7.4. It is seen that for PDL1, tier7 and tier8 had no growing random seed points. This was expected since there was a large number of seed points accumulating in these two tiers with only a small proportion of ERSP and it is unlikely for the growing process to occur. But for PDL2, the growing random seed points still existed on tier7. Also, in general, the growing number of PDL2 exceeds that of PDL1 under the same grid number. The only exception was seen for grid 64. Considering the RMS of all growing seed points, PDL2 performed much better than PDL1 as the values were below 1000m. Taking into account the overall DEM accuracy, the GRSE, computed in a similar way as that for the ORSE was not significant for both PDL files as it can be seen that there was no significant difference in the sixth row in Table 7.5. Comparing the two PDL files, however, the GRSE for PDL2 seemed less effective than for the PDL1 in spite of having more growing random seed points. The reason is that for PDL2, the ERSP were refined on each tier before the growing process, so it is more likely that growing can proceed successfully and based on these refined ERSP, the growing “sons” should be more accurate.

Table 7.5 also shows that under the same grid number, the DEM accuracy for PDL1 was greater than that of PDL2. The cause for this difference maybe the discrepancies of disparity values and will be analysed in section 7.6.5.

	grid32_1	grid64_1	grid128_1	grid32_2	grid64_2	grid128_2
ERSP	9	31	121	5	9	35
RMS ^a	6643.10	8545.64	7570.34	457.83	1526.60	1156.07
DEM ^b	154.12	183.87	228.32	183.59	183.25	177.40
DEM ^c	148.34	154.54	148.65	183.58	182.98	176.79
ORSE ^d	5.78	29.33	79.67	0.01	0.27	0.61

RMS^a: RMS for the ERSP

DEM^b: DEM accuracy with the ERSP (original)

DEM^c: DEM accuracy after the ERSP is removed

ORSE^d: DEM^b - DEM^c

Table 7.3: RMS (m) for ERSP and DEM accuracy (m) for ORSE of PDL1 and PDL2 under three different grid numbers

	grid32_1	grid64_1	grid128_1	grid32_2	grid64_2	grid128_2
ERSP	9	31	121	5	9	35
Total ^a	4	148	163	36	53	188
DEM ^b	148.34	154.54	148.65	183.58	182.98	176.79
DEM ^c	148.32	153.54	145.74	183.50	182.89	176.48
GRSE ^d	0.02	1.00	2.91	0.08	0.09	0.31

Total^a: Total number of growing random seed points

DEM^b: DEM accuracy (m) without the ERSP

DEM^c: DEM accuracy (m) without the growing random seed points

GRSE^d: DEM^b - DEM^c

Table 7.5: DEM (m) accuracy for growing random seed points with two PDL files

Regarding the coverage, Table 7.6 listed the coverage without the RSE for both PDL files. The results shows that no significant difference was obtained using the two PDL files, indicating that the coverage unexpectedly did not benefit from the refining process.

	grid32_1	grid64_1	grid128_1	grid32_2	grid64_2	grid128_2
Coverage	85.80	85.74	85.77	85.72	85.68	85.37

Table 7.6: Coverage (%) for two PDL files without the RSE

Chapter 7. Assessment of Stereo Matching Results

		grid32_1	grid64_1	grid128_1	grid32_2	grid64_2	grid128_2
tier2	No.	4	3	5	None	None	None
	Min.	152.39	1223.97	328.85	N/A	N/A	N/A
	Max.	1479.27	1405.98	9192.86	N/A	N/A	N/A
	RMS	886.87	1310.52	4218.83	N/A	N/A	N/A
tier3	No.	None	139	135	7	5	6
	Min.	N/A	608.96	478.74	82.61	-623.76	-824.64
	Max.	N/A	1665.90	1443.99	1448.32	1121.94	1496.50
	RMS	N/A	960.01	793.05	897.45	768.24	855.81
tier4	No.	None	1	1	7	9	21
	Min.	N/A	1170.38	965.93	-62.41	277.35	-597.90
	Max.	N/A	1170.38	965.93	162.83	744.33	595.92
	RMS	N/A	1170.38	965.93	122.27	481.27	377.78
tier5	No.	None	3	14	5	8	45
	Min.	N/A	1241.81	413.34	-474.56	-67.47	-639.69
	Max.	N/A	1327.55	4330.30	849.23	601.87	876.28
	RMS	N/A	1409.35	1820.82	761.21	493.47	483.99
tier6	No.	None	2	8	8	15	67
	Min.	N/A	1257.54	766.09	-613.25	-1052.63	-769.37
	Max.	N/A	1293.35	4379.79	552.38	630.76	1162.32
	RMS	N/A	1275.57	2169.61	463.34	635.96	529.20
tier7	No.	None	None	None	9	16	49
	Min.	N/A	N/A	N/A	-656.70	-845.96	-1434.52
	Max.	N/A	N/A	N/A	687.76	665.22	1031.70
	RMS	N/A	N/A	N/A	605.27	538.98	488.23
tier8	No.	None	None	None	None	None	None
	Min.	N/A	N/A	N/A	N/A	N/A	N/A
	Max.	N/A	N/A	N/A	N/A	N/A	N/A
	RMS	N/A	N/A	N/A	N/A	N/A	N/A
Total	No.	4	148	163	36	53	188

Table 7.4 :RMS (m) for the growing random seed points of each tier

7.6.3 PDL file data testing: DEM accuracy for separated tier

From Fig. 7.5, it can be seen that for PDL1, the ultimate matching results could be calculated from growing seed points on each tier. Table 7.7 lists the total DEM accuracy as well as the DEM accuracy of each tier, so that the impact of the DEM accuracy of each tier on the total one could be evaluated. Here, the ERSP for PDL1 under the three grid number as well as the growing seed points were removed, so that the RSE is not considered.

		grid32_1	grid64_1	grid128_1
tier 3	growing No.	144	0	0
	DEM	172.50	N/A	N/A
tier 4	growing No.	1281	1265	1246
	DEM	330.36	309.55	323.86
tier 5	growing No.	7262	7253	7189
	DEM	185.32	185.41	182.41
tier 6	growing No.	36988	36995	36976
	DEM	155.43	160.48	153.18
tier 7	growing No.	163665	163608	163611
	DEM	141.84	146.21	139.65
tier 8	growing No.	15584	15718	15296
	DEM	133.16	166.92	139.42
Total	No.	224924	224840	224618
	DEM	148.32	153.34	145.74

Table 7.7: DEM accuracy (m) for the total and each tier

From this table, it is clear that the final DEM accuracy was predominantly controlled by that of tier7, since it contributes approximately 73% of the matching points. It was also observed that the DEM accuracy of tier7 was the best, regardless of the grid number. In general, there was a tendency for DEM accuracy to improve as matching proceeded from the upper to the lower tier, except the last one. It is also noted that, despite the fact that grid 128 had the best DEM accuracy among the three grids, it has the lowest coverage due to the removal of many growing seed points. Taking this observation into account, therefore, grid 32 gave the best values which indicates that under a certain PDL file, fewer random seed points are preferred.

It is very important to consider the DEM accuracy on each tier, as this parameter also implies the accuracy of matching on reduced imagery. For instance, an accuracy

of 133m on tier7 under grid 32 means that matching was actually carried out on the "reduced 2" imagery. As shown in Fig. 7.5, multiplying the outcome by 2 would yield part of the final result. Likewise, for the other tiers, as carried out only with varied factor values. Therefore the final results are constituted of the combination of the intermediate matching results. This is a very striking characteristic of pyramidal matching, which gives rise to higher DEM accuracy compared with traditional matching on a single tier. The experimental data which supports this conclusion will be presented in section 7.9.

7.6.4 PDL file data testing: DEM accuracy and image tiers

As mentioned in section 7.3, the RSE could be reduced by increasing number of image tiers to enhance the matching accuracy. The purpose of this section was to validate this statement. Table 7.8 shows the DEM accuracy for three different tiers (8, 6 and 4) under the same grid number 32 for PDL1. It should be expected that with more image tiers, the DEM accuracy value of DEM^c will be greater. However, a contradiction to this theory was observed between the image tier8 and tier6, which may be explained by image tier6 having a lower coverage. Table 7.8 gives evidence that the RSE is inversely proportional to the number of image tiers. This is because image size of the first tier in a pyramid with more image tiers is by comparison smaller than those with less tiers, and therefore a smaller number of ERSP could be produced. In addition, with more image tiers, there are more accumulated seed points and it is less likely that the random seed points would grow other seed points. Therefore, by using more image tiers, it is possible to minimise the ORSE as well as the GRSE to obtain greater DEM accuracy.

7.6.5 PDL file data testing: comparison of two PDL files

In section 7.6.2, it was seen that for the PDL1 the DEM accuracy was better than that of PDL2 with almost the same number of random seed points. To understand the underlying reasons for the different DEM accuracies observed, a technique based on the *disparity sum* was employed. The *disparity sum* is defined as the absolute sum of disparity of X and Y coordinate for each point. When checking the matching results, it was discovered that for each tier of two PDL files, most of the X and Y coordinates of the growing seed points were identical on the left image.

	tier 8	tier 6	tier 4
DEM ^a	154.12	199.50	250.70
ERSP No.	9	192	571
DEM ^b	148.34	148.78	189.15
growing No.	4	1552	45404
DEM ^c	148.32	143.35	151.61
Coverage ^d	85.80	84.94	67.91

DEM^a : original DEM accuracy

DEM^b: DEM accuracy after the ERSP has been removed

DEM^c: DEM accuracy after the growing random seed points has been removed

Coverage^d: Coverage (%) for the matching points without ERSP and growing random seed points

Table 7.8: Influence of image tier on DEM accuracy (m) and coverage (%)

Based on this observation, it was possible to compare the DEM accuracies according to their disparity sum. The comparisons were made on the final matching results for the growing seed points on each tier. For PDL1, this final matching could be easily calculated as illustrated in Fig. 7.5. For example, from the growing random seed points on tier4, their final matching results for both the X and Y coordinates on the left as well as right image could be easily obtained simply by multiplying of 16. This applies to the coordinates on the left image for PDL2, however, the X and Y coordinates on the right image could not be predicted due to the extra refining process for the successive tiers which altered the coordinates. Thus, a program called **COUNT_LINE** was developed to extract the growing seed points separately for the two PDL files on every tier with the same coordinates on the left image. With these two identical pairs of coordinates on the left image, the DEM accuracy as well as the total *disparity sum* on each tier, named *grand disparity sum*, could be calculated on the same basis for the comparison and are listed in Table 7.9.

Table 7.9 reveals that from tier5 ~ 7 the *grand disparity sum* for PDL2 was smaller than that of PDL1, however, the reverse was observed for tier4 and tier8. Regarding the DEM accuracy, on tier 4, PDL2 was better than that of PDL1, for tier5 ~ 7, the performance of PDL2 was in contrast worse than that of PDL1. It was also discovered that the *grand disparity sum* was proportional to the height deviation between the terrain height and the reference data height of the same point. For a smaller *grand disparity sum*, a negative height deviation is more likely to occur. The evaluation of the variation of height deviation is carried out by looking at the number

of height deviations below -250m and above +250m. For the simplification of representation, the above height deviations are denoted as (-) height deviation and (+) height deviations respectively in this thesis and the number of (-) and (+) height deviation are shown in parenthesis on the third row for each tier in Table 7.9. It is anticipated that the *grand disparity sum* will be altered as the number of (-) and (+) height deviations vary, and it was indeed the result presented in Table 7.9. When the *grand disparity sum* was small, the value of the (-)height deviation number increased, while the value of (+)height deviation number decreased, and vice versa. It was also noticed that the PDL2 always corresponded to a smaller *grand disparity sum* and the effect of decreasing the value of (+)height deviation number was not so obvious as increasing the value of (-)height deviation number. This is the reason for the decreased DEM accuracy on the tier5, 6, and 7 of PDL2. For the tier4, it is to the contrary that most of the PDL2 files created better DEM results. From the above discussions, it is concluded that additional refining processes would only be effective in improving the matching accuracy on tier4, as it reduced the *grand disparity sum* on remaining tiers, and this reduction lowered the derived height and eventually deteriorate the overall DEM accuracy.

To analyse the performances of the two PDL files, apart from the height deviation and DEM accuracy discussed above, one important criterion should be introduced, named Height Deviation Shifting Effects (HDSE). The HDSE is defined as the ratio of the RMS to the DEM accuracy of the height deviation. Taking into account the HDSE, the characteristic of height deviation can be further investigated. When the HDSE is greater than 1, it implies that the distribution of height deviation is systematically shifting to the right or left direction. The direction that the height deviation shifts determines the elevation of the majority points systematically becomes higher or lower than the reference point which would lead their mean values of height deviation to be diverged from 0. When the HDSE approaches 1, the difference of the RMS and DEM accuracy becomes smaller and the systematic effects of the height deviation shifting is reduced, which also indicates the mean value of the height deviation will be closer to 0.

Table 7.10 lists the HDSE for two PDL files under the grid 32. It shows that the HDSE for PDL2 is generally smaller than PDL1 and this contribute to the overall smaller HDSE for PDL2, which is listed in Table 7.11. In this table, HDSE for two other two grids, RMS, and the mean of the height deviation are also given for these two PDL files.

Chapter 7. Assessment of Stereo Matching Results

		grid32_1	grid32_2	grid64_1	grid64_2	grid128_1	grid128_2
tier 4	No.	1268	1268	1252	1252	1231	1231
	DPY ^a	28.87	28.88	28.98	28.94	28.95	29.00
	HD ^b	(129, 398)	(86, 561)	(87, 421)	(82, 556)	(111, 397)	(86, 536)
	DEM	331.19	276.23	310.56	266.54	323.96	264.27
tier 5	No.	7244	7244	7216	7216	7130	7130
	DPY	29.96	29.31	29.98	29.36	30.04	29.39
	HD	(82, 4186)	(487, 3265)	(56, 4114)	(458, 3348)	(58, 4120)	(440, 3144)
	DEM	185.39	276.23	184.59	253.33	182.45	223.66
tier 6	No.	36925	36925	36924	36924	36819	36819
	DPY	30.34	30.08	30.39	30.11	30.41	30.11
	HD	(230,18273)	(1634,16964)	(223,18250)	(1557,17256)	(230,18637)	(1552,16577)
	DEM	155.43	201.53	160.36	197.89	152.93	195.52
tier 7	No.	163386	163386	163354	163354	163200	163200
	DPY	30.81	30.68	30.82	30.69	30.86	30.71
	HD	(1241,76521)	(4873,75427)	(1309,78624)	(4873,75427)	(1132,79301)	(4655,73380)
	DEM	141.80	174.29	146.18	174.29	139.39	171.13
tier 8	No.	15048	15048	15172	15172	14419	14419
	DPY	37.74	37.80	37.66	37.61	39.44	39.52
	HD	(114, 5284)	(424, 5506)	(262, 5970)	(406, 6309)	(121, 5289)	(123, 5791)
	DEM	125.93	163.71	158.15	171.84	127.34	125.85

DPY^a: disparity sum

HD^b (1,2): height deviation , 1 - value below -250m 2 - value above +250m

Table 7.9: The relationship of DEM accuracy (m) grand disparity sum (pixel) and height deviation (m)

	grid32_1	grid32_2
tier4	1.06	1.15
tier5	1.74	1.26
tier6	1.81	1.39
tier7	1.89	1.52
tier8	1.89	1.57

Table 7.10: HDSE for two PDL files on tier4~8 under grid 32

	grid32_1	grid32_2	grid64_1	grid64_2	grid128_1	grid128_2
HDSE	1.83	1.48	1.78	1.51	1.88	1.56
Mean	227.42	183.59	229.46	201.18	228.32	199.12
RMS	271.47	270.82	275.34	276.40	274.14	266.11

Table 7.11: HDSE, mean and RMS (m) for two PDL files under three different grids

The two tables reveal that due to the refining process on each tier, PDL2 has a smaller HDSE than PDL1, which can also be observed from the smaller mean value of the height deviation of PDL2 file. When considering only the RMS, the performance of the two PDL files do not seem significantly different.

From the above discussions, it is concluded that PDL1 is a better choice than PDL2 with respect to DEM accuracy alone. The HDSE of PDL2 is smaller than that of PDL1 for the refining process, but unfortunately its RMS is not very superior to that of PDL1, therefore, for subsequent sections in this chapter, the matching results using the PDL1 are adopted for various tests.

In section 7.2, it is mentioned that the two PDL files represent two matching strategies respectively. It would be interesting to know if still other strategies could increase the DEM accuracy. Therefore, this study tested other two PDL files which have the same parameters as grid32_1 except there is an additional refining process for the upper (1~4) 4 and 6 (1~6) tiers. The DEM accuracy and for the former is 148.12m. while for the latter is 167.93m respectively. From this, it can be seen that the previous conclusion is consistent here. For more refining processes, the DEM accuracy will become worse.

7.7 Blunder-removing

Limited work has been carried out in recent years, to detect the blunders in the ERS-1 SAR stereo matching. In [Dowman et al., 1992a], it was mentioned that for the same side ERS-1 pair, the absolute sum of disparity value could be used as one of the measures for searching for blunders since the same side stereo pair should have similar orientation. Thus if the *disparity sum* of a given match point exceeds a certain limit, this point could be considered as a blunder. However, there was no further data to support this assumption. According to our findings from the previous section, it has been proven that the DEM accuracy was affected by the *disparity sum*. In this

section the impacts of the *disparity sum* value on the DEM accuracy as well as its possible use as a blunder-removing filter would be examined in detail. The effectiveness of this filter is also evaluated.

7.7.1 Global disparity analysis

The objective of the global disparity analysis was to determine the variation of the *disparity sum* for all of the matching results, and to investigate the relationship between the (-) and (+) height deviation and the extreme values of the *disparity sum*. With this analysis, the characteristics of the *disparity sum* could be understood, so that the techniques to remove the blunders based on the *disparity sum* could be more effectively developed.

To study the effects of *disparity sum* on DEM accuracy, the most direct and efficient way was to extract the matching points from the final results which corresponded to the greatest and smallest height deviations, and to check if their *disparity sum* could be discriminated. Next, the previously obtained grid32_1 data was selected as the experimental data in this section, for it has less random seed points, and its RSE could be a minimum. With the minimum RSE, more accurate assessment of the impacts of *disparity sum* on the DEM accuracy would be achieved. This assessment was proceeded by a selection of matching results of three groups that correspond to (-)height deviation, height deviation of -10m ~ 10m, and (+)height deviation. Then the disparity value of X and Y coordinates of the three groups were calculated and listed in Table 7.12.

It is seen that in Table 7.12, group 1 was more easily distinguished from the other two groups as its Y disparity was quite small and the average was only half of that calculated for group2. In contrast, the x and y disparity values for the majority of points were overlapped between group2 and group3, therefore making it more difficult to differentiate between these two groups.

	No.	X (range)	X (average)	Y (range)	Y (average)
group1	1830	-40.86 ~ 4.63	-5.07	-2.69 ~ 30.99	8.89
group2	2275	-39.62 ~ 11.32	-7.53	1.98 ~ 33.61	15.21
group3	5397	-35.73 ~ 15.17	-7.02	4.54 ~ 36.63	18.00

group1: matching points with height deviation below -250m
 group2: matching points with height deviation between -10 ~ 10m
 group3: matching points with height deviation above +250m

Table 7.12: The range and average of X and Y disparity (pixels) for three groups

When considering the *disparity sum*, a similar pattern was observed (Table 7.13). There was still no significant difference in the average value of *disparity sum* between group2 and 3, while group1 had a much smaller average value . Table 7.12 and 7.13 illustrated that the *disparity sum* may not be totally effective, as group3 was not easily separated from the satisfactory matching results of group2 according to their *disparity sum*. This suggests that the matching points with large *disparity sum* would not be likely correspond to the points that cause the (+)height deviation. It also indicates that the threshold of the upper boundary for *disparity sum* will not be as useful to remove blunders in contrast to our expectation, rather the lower boundary was more effective. In the next section, more data is tested to substantiate these conclusions.

	X+Y (range)	X+Y (average)
group1	0.11 ~ 71.34	14.39
group2	5.84 ~ 72.86	23.85
group3	7.39 ~ 71.85	27.05

Table 7.13: Range and average value of disparity sum (pixels)

7.7.2 Determination of the threshold of the blunder-removing filter

The blunder-removing filter was applied on each tier after the matching had been completed. As stated in the last section, the *disparity sum* was chosen as the discriminating criterion, but the threshold of which for the upper and lower boundary was yet to be determined. In this research, a progressive approach was adopted to analyse the *disparity sum* for each tier to examine their effects in a systematic manner. This approach is described in detail in the following steps:

- (1) Calculate the *disparity sum* for each tier and list the histograms.
- (2) Compute the DEM accuracy for each tier and also list their histograms.
- (3) The *disparity sum* of each point corresponds to one height deviation.
- (4) Based on the assumption that the (-) and (+) height deviations were caused by the extreme values of the *disparity sum*, remove all points with the extreme *disparity sum* outside the pre-set threshold values to check whether the points which lead to the significant height deviation can be removed as well.
- (5) The above process was carried out in an progressive manner by determining the

number of points with height deviation. This determination is proceeded by using gradually increased histogram percentages of the total number points with (-) and (+) height deviations.

To clearly illustrate the above five steps, an example is shown here to investigate the effects of large *disparity sum* on DEM accuracy. For step (5), we chose 20%,40% and 60% as the increased percentage and according to these percentages, the number of points with (+)height deviation that we intend to remove could be calculated from the histogram in step(2). This computed number is defined as the *objective number*. Next, we count the same *objective number* in a descending order from the maximum value of *disparity sum* by examining the histogram in step (1) to determine the value of *disparity sum* . and the accumulated number above this value would be equal to the *objective number*. This value could then be used as the threshold value required. For evaluation of the effects of a small *disparity sum*, the same procedures could be implemented, altering only the direction of counting the *objective number* from the minimum value of *disparity sum* to a maximum.

7.7.3 Blunder-removing filter data testing

The above proposed method of determination of the threshold of the *disparity sum* was practically tested. The threshold value was placed after the matching procedures, i.e. a post-processing filter was incorporated which eliminated the points whose *disparity sum* were outside the threshold value. In this study, the filter was applied on the lower 4 tiers (tier5 ~ 8) in the image pyramid. This is because it was observed that the number of accumulated seed points was approximately 1200 ~1400 down to the tier4, and with this small number of seed points, the evaluation of this filter seems meaningless.

In this section, only an approximate threshold value was calculated as described above. This is because the aim of the progressive approach was to look at the tendency of the influence due to the *disparity sum* value; it was not necessary to compute the threshold value to the exact *object number*. Moreover, for the disparity sum, a tiny interval in the step (1) histogram may contain a few thousands points (e.g. on tier7, there are usually more than three thousand points in a 0.6 pixel interval), and the exact location of the *object number* may correspond to five or six decimal places of the disparity sum. Since the units of *disparity sum* are pixels, which are already quite minute, this calculation would be rather worthless. For this reason, the

threshold value of the adopting blunder-removing filter was estimated to only one decimal place.

The data used for the following tests was still the grid32_1 data, and when analysing the final matching results, it was discovered that the number of (+)height deviations was more than 100,000, while the number of (-)height deviation was only ~2000. With this vast number of points, it should be tested by more varied step(2) histogram percentages. In addition, based on the global analysis, the large value of *disparity sum* may not be as efficient to remove blunders as the small value of *disparity sum*. Therefore, the percentages of (-)height deviation chosen were greater than the (+)height deviation, and there were three percentages (20%,40%, 60%) for the (+)height deviation, but only two percentages (60%, 100%) for the (-)height deviation. The computed threshold value of the upper and lower boundary for every tier is listed in Table 7.14.

	upper 20%	upper 40%	upper 60%	lower 60%	lower 100%
tier5	5.6	5.0	4.4	1.1	1.3
tier6	12.0	10.4	9.6	1.7	1.8
tier7	25.2	22.2	19.8	3.4	3.5
tier8	51.0	45.0	40.0	5.4	6.5

Table 7.14: The upper and lower boundary of threshold value (pixel) of disparity sum for different percentages for grid32_1

Table 7.15 illustrates the final DEM accuracy for six sets of data. It is seen that the accuracy was inversely proportional to the percentages of the upper boundary, but on the contrary for the lower boundary: the higher the percentage, the better the accuracy became. Comparing the DEM accuracies with the original one of 154.12, it was also found that the accuracies for all three upper boundaries and the lower boundary at 60% were all worse. Only the lower boundary at 100% had a greater accuracy at 151.15. The possible explanation for this finding is that the extensive range of *disparity sum* values used as the discriminating criterion may result in the elimination of the points that yield (+)height deviation as intended, as well as some good matching points with small disparities unexpectedly, consequently reducing the DEM accuracy.

	grid32_1	upper 20%	upper 40%	upper 60%	lower 60%	lower 100%
DEM	154.12	162.91	166.40	175.76	157.41	151.15

Table 7.15: The comparison of the final DEM accuracy (m) between five different types of threshold value and the original one

Considering the HDSE, it can be seen in Table 7.16, the upper boundary has a greater influence than the lower boundary. This is expected since from Table 7.11, it is revealed that the elevation of the PDL1 data is systematically shifting to a higher value and with the threshold value of upper boundary, it will significantly reduce the RMS. This reduction is greater than that of lower boundary, and results in a smaller HDSE. Meanwhile, when looking at the different percentages in the lower or upper boundary, however, there does not seem to be much variation in the HDSE.

	grid32_1	upper 20%	upper 40%	upper 60%	lower 60%	lower 100%
HDSE	1.81	1.01	1.01	1.01	1.03	1.03

Table 7.16: The comparison of the HDSE between five different types of threshold value and the original one

This consequence of the results shown in Table 7.15 is fairly consistent with the previous global analysis. It is also observed that the decrease in DEM accuracy was directly proportional to the number of seed points removed from the filter. Hence, the worst matching result was obtained when the upper boundary was at 60% (175.76m), a decline of approximately 20m when compared with the original DEM value (154.12m). Table 7.17 shows the coverage for grid 32 as well as the above 5 sets of data. It is found that the magnitude of the coverage decreased as both the lower and upper boundaries increased, and this decrease was much more prominent for the upper boundary. A drop of ~20% of the coverage was observed for the 60% upper boundary (63.83%) when compared with the original value (85.81%), while a difference of <2% was obtained for 100% lower boundary. This outcome was expected as the lower boundary removed only a small portion of matching points, while the upper boundary filtered out good matching points as well, which was evident from the sharp decrease in the coverage.

	grid32_1	upper 20%	upper 40%	upper 60%	lower 60%	lower 100%
coverage	85.81	79.45	72.03	63.83	85.01	84.37

Table 7.17: Coverage(%) of five different types of threshold value and the original one

For the complete analysis of setting the threshold value for the *disparity sum*, the DEM accuracy with the two-end boundary was also compared. There were three kinds of two-end boundaries tested: (1) lower boundary 60%, upper boundary 60%; (2) lower boundary 100%, upper boundary 60% and (3) lower boundary 100%, upper boundary 100%. Combining the results of the three two-end boundaries with data obtained (Table 7.15) previously enabled an in-depth investigation on the effects of the boundary on *disparity sum*. To achieve this goal, two kinds of tables were displayed here depending on which the percentage of boundary was fixed. Table 7.18 shows the DEM accuracy for the percentage of the lower boundary fixed at 60% and 100%, while Table 7.19 display the DEM accuracy for the percentage of upper boundary fixed at 60%.

	60%_0% ^a	60%_60%	100%_0%	100%_60%	100%_100%
DEM	157.41	160.76	152.43	157.25	166.48

60%_0%^a: lower boundary 60% and upper boundary 0%

Table 7.18: DEM accuracy (m) for five two-end boundaries, fixed at the lower boundary

Table 7.18 reveals that if the percentage of the lower boundary was kept constant, the DEM accuracy became poorer, as seen for both 60% or 100% lower boundary. On the contrary, when the percentage of the upper boundary was fixed, the DEM accuracy became better as the percentage of the lower boundary increased. This is shown in Table 7.19.

	0%_60%	60%_60%	100%_60%
DEM	175.76	160.76	157.25

Table 7.19: DEM accuracy (m) for three two-end boundary fixed at the upper boundary

From Table 7.18 and 7.19, it was concluded that the lower or upper boundary for the *disparity sum* had “multiple” effects. The DEM accuracy could be enhanced by the incorporation of the lower boundary, but suffered the adverse influence from the upper boundary. It was also indicated that if DEM accuracy for a particular combination of certain percentages of upper and lower boundary was known, then the impacts of changing the percentage of either upper or lower boundary on the DEM accuracy could also be predictable.

All of the above analysis was based on only one data set. Would the lower boundary still effectively to remove blunders for other data sets? Two more data sets, grid64_1 and grid128_1, were further tested here. The threshold value of the 100% lower boundary of these two data sets for four tiers are shown in Table 7.20. The DEM accuracy obtained after employing the listed threshold values are shown in Fig. 7.13. For a clear comparison, this figure also includes the original DEM accuracy for the two data sets and grid32_1. In this figure, it can easily be seen that the threshold of the lower boundary was capable of enhancing the DEM accuracies on a small scale for all three data sets, proving its effectiveness.

	grid64_1	grid128_1
tier5	1.1	1.2
tier6	1.7	1.8
tier7	3.5	3.5
tier8	6.7	6.5

Table 7.20: The lower 100% threshold value (pixels) for two data sets

So far in this section, the RSE has not yet been considered. Was the effective blunder-removing filter capable of removing the ERSP? The answer can be easily found using the *disparity sum* directly. For instance, the threshold values of 20% for the upper boundary and 100% boundary of grid32_1 are 5.6 and 1.3 respectively. The minimum, maximum and average value of *disparity sum* of ERSP on tier5 were 2.0, 12.0 and 6.1 respectively. Based on these values, the ERSP could be removed with the upper boundary but not with the lower boundary. Only 20% upper boundary was considered here, for if the *disparity sum* of any point exceeded the threshold value of 20%, it must also exceed 40% and 60%. This was also applied to the 100% lower boundary. This fact also illustrated that normally the *disparity sum* of ERSP was quite large. This characteristic resulted in the huge height deviation as shown in Table 7.3. These observations lead to the conclusion that the statistics in Fig. 7.13 included the ERSP. After removing the ERSP, the DEM accuracy was computed again and an obvious improvement was obtained (Fig. 7.14). From this figure, it was conclusive that the blunder-removing method developed in this section could enhance the DEM accuracy irrespective of the existence of ERSP.

Contributions have been made in this section in discovering the relationship between the *disparity sum* and height deviation, and the introduction to the concept of proposing a blunder-removing filter. The determination of the threshold value of this

filter depended on the distribution of *disparity sum*. In other words, it was dynamically determined and not fixed to a specified value as we used to do. This idea is of great importance, as it showed us that the threshold value could be altered for different data sets. In the next section, this conclusion will be utilised again and more superior results could be obtained.

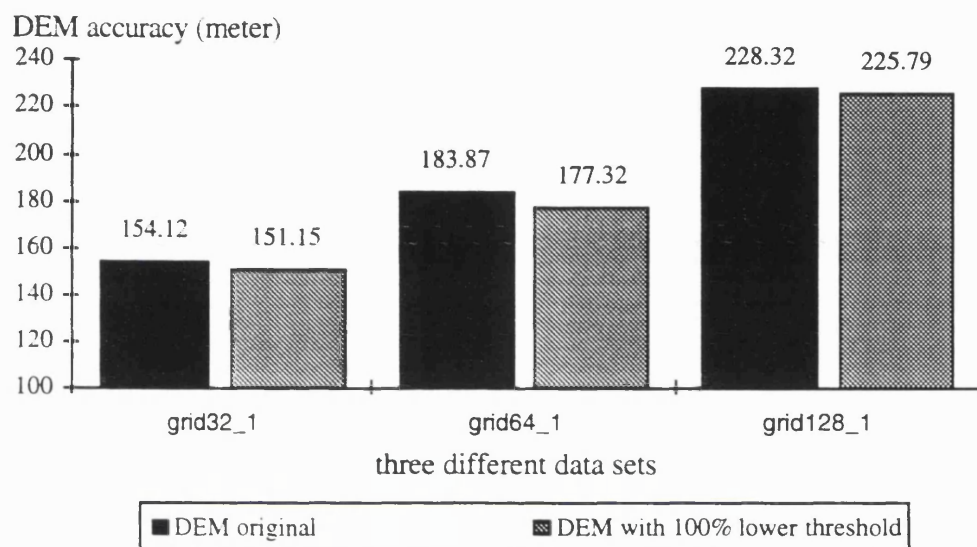


Fig. 7.13: The comparison of DEM accuracy between the original and lower threshold for three data sets

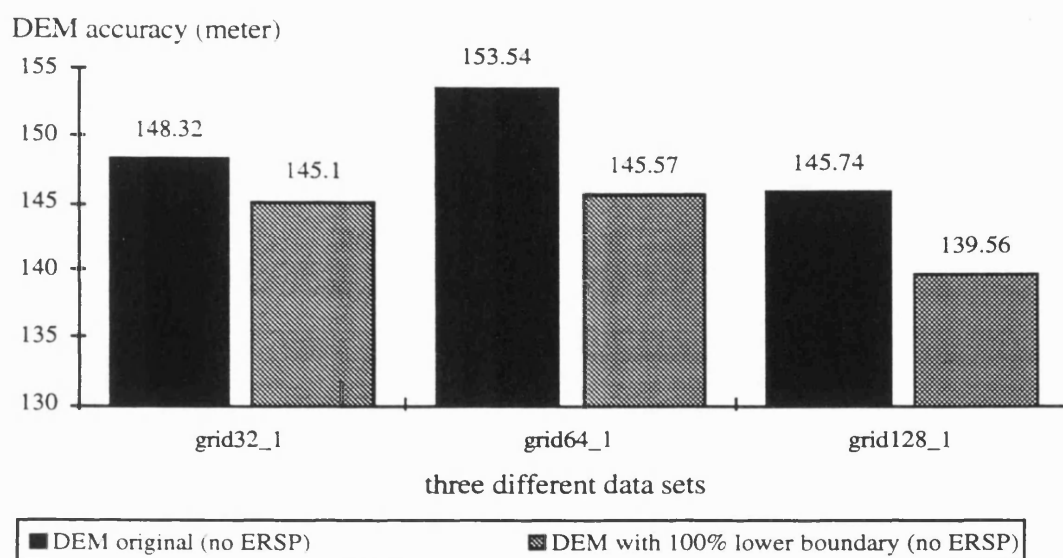


Fig. 7.14: The comparison of DEM accuracy between the original and lower threshold without the ERSP for three data sets

7.8 Techniques of Seed Points Selection

CASCADE was introduced in Chapter 5 and its function is to produce the random seed points on the first tier of an image pyramid. These seed points are generated randomly, no manual intervention is needed, and the aim of “automatic stereo matching” could be achieved. The interest of this section is to determine if any relationship existed between these random seed points and the final DEM accuracy. If this relationship could be established, it would be possible to find an unique object function for these random seed points which could yield better DEM accuracy. To achieve this, different algorithms must be tested and the process can be rather difficult.

According to the experience, under the same PDL file with the same grid, there are lots of similarities for different sets of ERSP on the tier2. For instance, the number of ERSP was almost the same, and the average of eigenvalue did not exhibit any significant differences. Moreover, fewer ERSPs would cause smaller RSE and result in better DEM accuracy. Since the number was small, it would be very hard to find any link between these seed points and the final DEM accuracy. Therefore, the determination of the object function depending on the ERSP alone would not be investigated in this study. So, instead of examining the ERSP on tier2, the seed points on tier4 were studied directly. On this tier, excluding the random seed points, there were more than 1000 seed points produced which was 10~100 times the number of ERSP. With so many seed points, it is more simple and reliable to find the object function of our interest. The other reason for choosing tier4 in the image pyramid as the place for calculating the objection function value is because down to this tier, the calculation time required for running so many times of matching procedures would still be acceptable. Instead, if on tier5, probably more than 20 times of the calculation time would be required. In addition, the purpose of the object function is to find the relationship between the seed points on the upper tiers and the final DEM accuracy. If the calculation of the matching proceeded on the lower tiers, the object function would lose its importance and meaning.

7.8.1 SEED_GRUEN programme introduction

The purpose of the **SEED_GRUEN** program is to search for the optimum random seed points that have the matching results on the tier4 conforming to the criterion of the object function. The program firstly simulates **CASCADE** to generate random seed points, thus the input data would include parameters for the

CASCADE such as grid number and uncertainty_radius. Then identical matching procedures are carried out for each set of random seed points as performed by the **CHEOPS**. Once the matching on tier4 has completed, the program automatically produces another set of random seed points again and repeats the above matching procedures. The number of this repetition can be specified by the user. In the end, one set of random seed points whose matching results on tier4 best satisfy the conditions of the object function is retained.

To ensure that the outcome of random seed points of the **SEED_GRUEN** program is more suitable to the conditions of the object function than the original random seed points, the program is designed to have the original random seed points as another set of input data. After the original random seed points have been given, this program will calculate its object function value as the initial value, by compared the initial value with many other sets of random seed points that subsequently produced by the program, the goal of finding one set of optimum random seed points could be achieved.

For a better understanding of the program, the following text introduces the detailed procedures. Let us suppose the criterion of the object function is to find the maximum value of a parameter. Once the object function value of a certain set of random seed points was found to be greater than the initial value, this set of seed points would be recorded in a file called result_good_seed_son, or else, this set would be discarded. Therefore, the result_good_seed_son file always keeps the best set of random seed points that we require. **SEED_GRUEN** also provides the option to specify the “difference limit” between the objection function value of any random seed points set and the initial value. For any random seed point set, if the difference of its objection function value and the initial value exceeds the limit, the program would be terminated. Otherwise, the program will iteratively produce as many sets of the random seed points as assigned by the user. The flow chart of this programme is shown in Fig. 7.15 and 7.16.

In Fig.7.15, there are two scripts for the matching, match_tier1_2_spt indicates that the matching is proceeding from tier1 to tier2, while match_tier2_4_spt describe the matching from tier2 to tier4. This means in the **SEED_GRUEN** program, the whole matching procedure from tier1 to 4 is divided into two steps. The reason for this two-step execution is that the ERSP is not of interest for calculating the object function value. From the results of the match_tier1_2_spt, by the techniques introduced in section 7.5, the number of ERSP can be determined. Then after employing the match_tier2_4_spt, the ERSP can be removed from the matching

results on tier4, thus the seed points calculated for the object function value would exclude the ERSP.

7.8.2 Testing of two algorithms

The impacts of selected seed points on the DEM accuracy was firstly examined by two objection functions. These two object functions were evaluated by comparing the initial value with the objection function value of 300 sets of random seed points. Each set of random seed points was produced under the conditions when the grid number was 32 and the uncertainty_radius equalled to 1.

The first function was the smallest average of eigenvalue, and this value was selected because it is related the **GRUENS** command. In **GRUENS**, the eigenvalue is the criterion that dominate the direction in which the seed points should grow. As described in Chapter 4, the principle of **GRUENS** growing process is based on the “best-first” scheme and the seed points with smaller eigenvalue are classified as good seed points. Thus, the average eigenvalue was chosen as one of the two object function values to be examined. After running the **SEED_GRUEN**, the initial value of the objection function 11.33 was decreased down to the 11.20. Unfortunately, the matching result was not quite satisfactory as the DEM accuracy was 166.48m which is poorer than the value of 148.32 by the grid32_1. With respect to the coverage, approximately 85.43% could be achieved.

The other objection function utilised the Normalised Correlation Coefficient (NCC) to calculate the objection function value. In Chapter 4, it was mentioned that this scheme is adopted to stereo match the SAR imagery in the previous researches, and for this reason, this value was regarded as an appropriate algorithm to be tested. The object function was to maximise the average NCC based on the window size of 3. The output of **SEED_GRUEN** showed an increase in average NCC from its initial value 0.299 to 0.302. The DEM accuracy still did not show any improvement, being 162.45m and the coverage was 85.44%.

The first two algorithms were not successful in enhancing the DEM accuracy, which clearly demonstrates the difficulties in selecting the optimum seed points even on the tier4 with more than 1000 seed points. Therefore, another indirect scheme instead of a direct one was proposed in this study which is introduced in the next section.

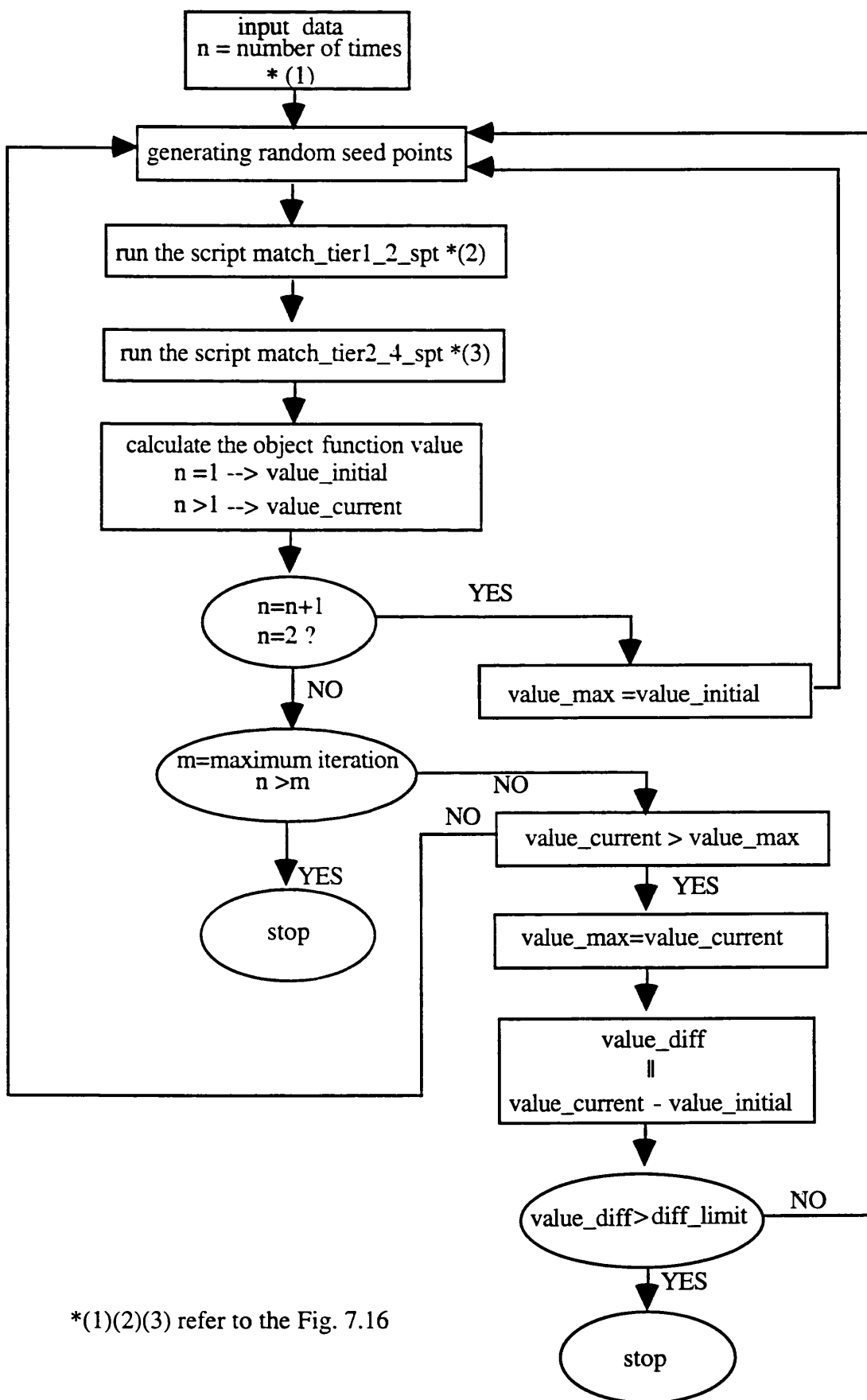


Fig. 7.15: Flow chart of SEED_GRUEN programme

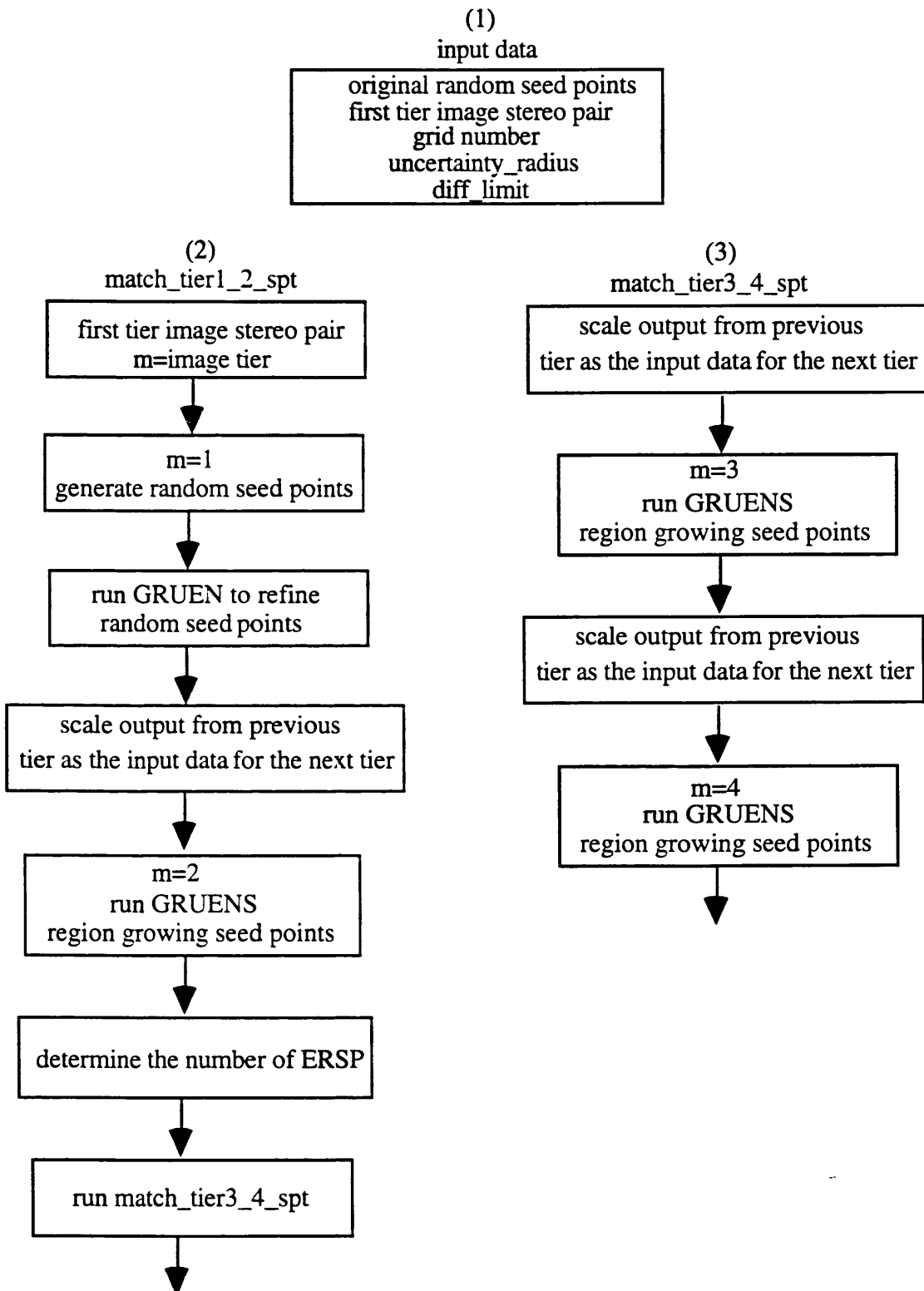


Fig. 7.16: Flow charts for two matching scripts

7.8.3 Seed points selection by disparity sum

In section 7.6, it was demonstrated that the *disparity sum* is proportional to the number of (-)height deviation. also it was discovered that for all three grids under the PDL1, the matching results had greater number of (+)height deviation seed points compared with the number of those with (-)height deviation (Table 7.21). Moreover, in section 7.7, it was concluded that the DEM accuracy could be enhanced by employing the lower boundary of *disparity sum* as the threshold which could effectively remove some points with (-)height deviation. Therefore, an assumption was made such that, if only those seed points with the smallest *disparity sum* were selected. there would be a greater number of points with (-)height deviation. If the lower boundary was then used to remove any seed points with (-)height deviation, a greater DEM accuracy could be obtained. The validation of this assumption would be described in the following subsections.

	grid32_1	grid64_1	grid128_1
No. of (-)height deviation	1834	2019	1720
No. of (+)height deviation	108750	107637	108750

Table 7.21: Number of (-) and (+)height deviation under three grid number

7.8.4 DEM accuracy of the disparity sum

The **SEED_GRUEN** program was implemented here to find the set of seed points which had the smallest *disparity sum*. Hence, the objection function was defined to have the minimum average value of *disparity sum* of seed points. For simpler representation, these seed points were named *disparity seed points* and was quoted as *grid_dpy*. As in section 7.6, the grid number was written in front of the underscore and therefore *grid32_dpy* would indicate the seed points that have the smallest average value of *disparity sum* on tier4 produced by the original random seed points of grid 32. To distinguish from the disparity seed points, those points derived from section 7.6 were denoted as the ordinary seed points.

In this study, the iteration for producing the random seed points was specified as 300 times for all three different grids. Table 7.22 gives the value of *disparity sum* on the tier4 for both the ordinary and disparity seed points.

		grid32_1	grid64_1	grid128_1
ordinary seed points	disparity sum	1.81	1.81	1.81
		grid32_dpy	grid64_dpy	grid128_dpy
disparity seed points	disparity sum	1.74	1.75	1.75

Table 7.22: disparity sum (pixels) for ordinary and disparity seed points on tier4 under three different grids

In this table, it is revealed that under the same grid, the *disparity seed points* had lower *disparity sum* compared with the ordinary seed points. Table 7.23 gives the corresponding number of matching points with (-) and (+) height deviation and supports the assumption that when the disparity decreases, the number of (+)height deviation also decreased, and instead the number of (-)height deviation would increase.

In terms of the DEM accuracy, it is shown in Table 7.24. From this table, it is seen that in general the *disparity seed points* did not improve DEM accuracy. This may be due to the smaller *disparity sum* which is similar to the situation for the PDL2 as discussed in section 7.6.5. It also illustrates that the *disparity sum* of other lower tiers (from tier4) were related, in that if the *disparity sum* on tier4 was small, it would contribute to the small *disparity sum* of the final results.

Considering the HDSE, for the *disparity seed points* under three different grids, they all equal to 1, this is much better than the ordinary seed points. The comparisons are shown in Table 7.25. From this table, it is realised that although the *disparity seed points* could lead to worse DEM accuracy, but their results would not be subjected to any systematic shifts.

	grid32_dpy	grid64_dpy	grid128_dpy
No. of (-)height deviation	14083	14047	13538
No. of (+)height deviation	6704	8188	5184

Table 7.23: Number of (-) and (+)height deviation under three grid number

		grid32_1	grid64_1	grid128_1
ordinary seed points	DEM	148.32	153.54	148.65
		grid32_dpy	grid64_dpy	grid128_dpy
disparity seed points	DEM	156.21	150.70	166.84

Table 7.24 DEM accuracy (m) for ordinary and disparity seed points under three different grids

	grid32_1	grid32_dpy	grid64_1	grid64_dpy	grid128_1	grid128_dpy
HDSE	1.81	1.00	1.78	1.00	1.88	1.00

Table 7.25: Comparisons of HDSE for ordinary and disparity seed points under three different grid

The results shown in Table 7.24 were further investigated by employing the blunder-removing filter introduced in section 7.7, which was the threshold of *disparity sum* value. This value was determined by 100% lower boundary. The threshold of *disparity sum* for the *disparity seed points* on tier4~8 under three different grids are presented in Table 7.26.

	grid32_dpy	grid64_dpy	grid128_dpy
tier5	1.7	1.7	1.6
tier6	2.6	2.5	2.4
tier7	4.3	4.1	4.1
tier8	8.5	8.0	8.0

Table 7.26: 100% lower boundary threshold value (pixels) for three sets of disparity seed points under three different grids

Compare the statistics in Table 7.26 with that in Table 7.14 and 7.20, it can be seen that under the same grid, the threshold value for the *disparity seed points* were larger than the ordinary seed points (e.g. tier7 under grid 32:4.3 vs. 3.5 Table 7.14, grid 64:4.1 vs. 3.5 Table 7.20, grid 128:4.1 vs. 3.5 Table 7.20). This observation was expected as the *disparity seed points* could cause greater number of (-)height deviation, and as a consequence, the threshold of 100% lower boundary of the *disparity sum* should increase. This also implies that the threshold could remove more blunders than the ordinary seed point which conforms the objectives stated in the section 7.8.3.

Table 7.27 shows the DEM accuracy without the RSE for the three *disparity seed points* using the threshold value listed in Table 7.26. For a clear comparison, the DEM accuracies without the threshold value constraint are also listed in this table.

Table 7.27 shows that the 100% lower boundary sum could enhance the DEM accuracy just like the ordinary seed points. This table not only proves the effectiveness of the blunder-removing filter, more importantly, it provides the evidence that this filter could result in better improvement in the DEM accuracy than

the ordinary seed points, which is the purpose of finding the *disparity seed points* in this section. The validation is demonstrated in Fig. 7.17. In this figure, with the disparity seed points, the DEM accuracy can be increased by about 15 meter for both grid 32 and grid 64, for the grid 128 even reaching 26 meter. For the ordinary seed points, the DEM accuracy could only increase by about 3 meter to a maximum value of 8. From all these facts, it was confirmed that the combination of *disparity seed points* and the blunder-removing filter could effectively enhance the DEM accuracy, as proposed by the assumption made at the beginning of section 7.8.3.

	grid32_dpy	grid64_dpy	grid128_dpy
no threshold value	156.21	150.70	166.84
with threshold value	141.94	134.41	140.89

Table 7.27: DEM accuracy (m) for the disparity seed points before and after using blunder-removing filter

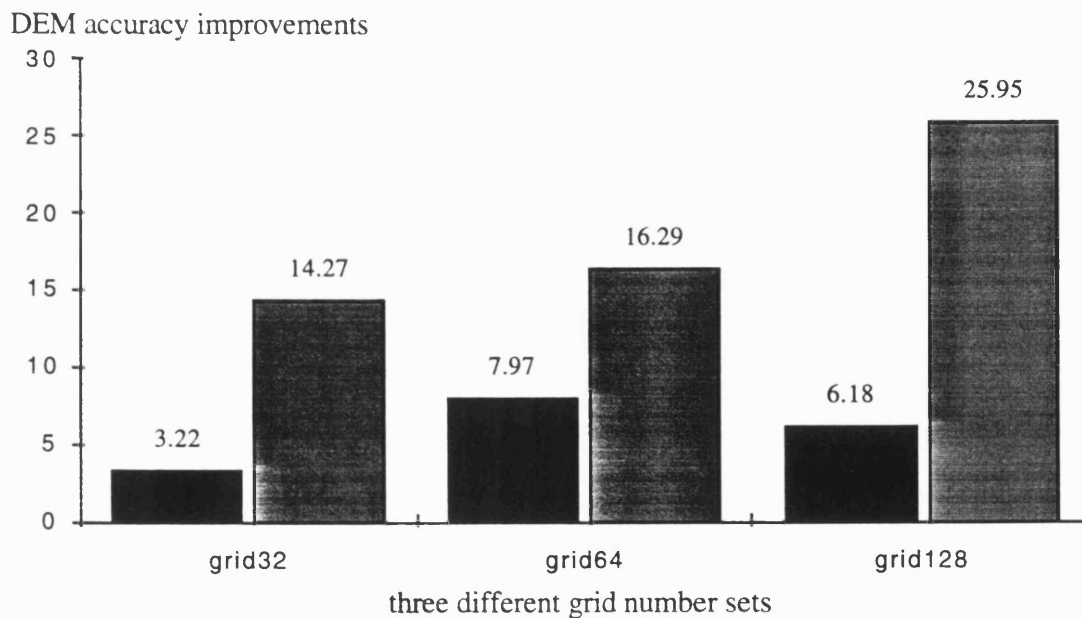


Fig. 7.17: Comparisons of DEM accuracy improvements under three grid numbers

So far, the threshold value for the blunder-removing filter was determined by the height deviation of -250m. It is of great interest to know to what degree a more stringent filter acquired by setting a higher threshold value, would affect the DEM accuracy. For the *disparity seed points* has a greater tendency to produce a large number of minus height deviation, the employment of the strict threshold value should be more successful on the *disparity seed points* than the ordinary one.

The hypothesis was tested by increasing threshold values which were determined by the height deviation of minus 200m, 150m 100m and 50m respectively. Each set of threshold value was implemented on the ordinary and *disparity seed points* of grid32. These threshold values are listed in Table 7.28, in which the br_1 means these matching points were produced by the threshold value computed by the height deviation of minus 200m. Likewise, the values for the br_2 br_3 and br_4 were obtained by using the minus 150m, 100m and 50m height deviation respectively.

The individual DEM accuracy for these four sets of threshold value as well as the coverage are displayed in Table 7.29.

In this table, it is manifested that the DEM accuracy could be improved by 11 meter (from 141.94m to 130.30m) by the br_1 points, while the higher threshold value of br_2, br_3 and br_4 points did not aid to increase the DEM accuracy. Considering the coverage for the four data sets, as the threshold value increased, the coverage decreased accordingly. Taking into account both the coverage and DEM accuracy discussed above, the threshold value for these *disparity seed points* was most appropriate to be determined by the height deviation of minus 200m.

	br_1	br_2	br_3	br_4
tier5	1.9	2.1	2.5	2.8
tier6	2.9	3.4	4.2	4.9
tier7	4.7	5.6	6.9	8.9
tier8	9.5	11.0	13.5	18.5

Table 7.28: Threshold values (pixel) computed by four different minus height deviation (200, 150, 100, 50)

	br_1	br_2	br_3	br_4
DEM	130.30	127.24	127.00	126.08
coverage	79.04	76.08	72.43	64.76

Table 7.29: Coverage(%) and DEM accuracy (m) by the four threshold values

For the ordinary seed points, the DEM accuracy for the br_1 and br_2 were 148.07 and 146.24 respectively. Compared with the value of 148.32 in Table 7.24, not much improvement was made. Therefore, this study will not investigate further with br_3 and br_4. The above discussions lead to the conclusion supporting the previous statements that the DEM accuracy for the *disparity seed points* but not the ordinary seed points could be enhanced further by more strict threshold value.

The major content of this section is to introduce techniques of selecting the seed points. With small disparity sum, these seed points can give greater DEM accuracy by filtering out blunders with higher threshold values, and the meaning of this observation is of 2 fold: (1) the final *disparity sum* is predictable from that on the upper tier, (2) the effectiveness of dynamic determination of threshold value had been validated.

7.9 Advantages of Pyramidal Stereo Matching Analysis

In section 7.5, the modified program **GRUENS_SEED** was proposed to discover the relationship of the *initial seed points* and the growing seed points. The amount of ERSP could be determined by the *seed_number* of the **GRUENS_SEED** output. Except the *seed_number*, the output had three other additional columns. In this section, one of these columns *seed_generation* was used to investigate the reasons for the superior performance of pyramidal matching compared to that of the original image under the same patch radius.

To proceed with the investigation, two matching results were chosen. One is on an eight-tier image pyramid under grid number 32, while the other was on an original image by 12 manual seed points. The DEM accuracy for the former and the latter is 148.32m and 172.17m respectively. The techniques used here was identical as described in section 7.6.5. The command **COUNT_LINE** was utilised to extract the same line and sample coordinate of the left imagery separately for the pyramid and original image. The extractions were implemented for the growing seed points on the lower 5 tiers (tier4~ 8) of the image pyramid. These extractions were used to further

calculate the DEM accuracy for these two types of images respectively and are shown in Table 7.30.

In this table, the fourth column of the table lists the difference of DEM accuracy. It is interesting to notice that the difference reduced gradually as the tier of image pyramid approached to the bottom one. The *seed_generation* of the growing seed points could be applied to explain this phenomenon. To check the results of the original image, the *seed_generation* of the growing seed points were from 2 to 712. This wide range of the *seed_generation* could be expected since there were only 12 manual seed points. It was also observed that on the original image, the DEM accuracy was inversely proportional to the *seed_generation* of the seed point, in other words, seed points with larger *seed_generation* would lead to poor DEM accuracy. This can be found evident in Table 7.31, which displays the DEM accuracy of three ranges of *seed_generation* on the original image. For comparison purpose, the ranges were divided into three groups which were the small *seed_generation* (2~101), the middle *seed_generation* (300~400) and the large *seed_generation* (>600).

	grid32_1	original image	DEM difference ^a
tier4	343.32	178.20	165.15
No.	1084	1084	1084
tier5	176.47	170.37	6.1
No.	6407	6407	6407
tier6	148.25	171.29	-23.04
No.	32964	32964	32964
tier7	136.14	168.39	-32.25
No.	147965	147965	147965
tier8	129.01	195.73	-66.72
No.	15309	15309	15309

DEM difference^a : DEM(grid32_1)-DEM(original image)

Table 7.30: DEM accuracy (m) comparison of different tiers for the original and pyramidal image

No.	seed_generation	DEM
30843	2~101	121.52
31643	300~ 400	172.05
8800	>600	190.32

Table 7.31: DEM accuracy (m) of different seed_generation for the original image

From this table, it is seen that there were only 8800 seed points with *seed_generation* larger than 600, and their resulting DEM accuracy was 190.32m worse than that of *seed_generation* 300~400 (172.05m) and 2~101 (121.52m). It is also noticed that having approximately the same value of number, the seed points with small *seed_generation* (2~101) gave rise to better DEM accuracy (121.52) when compared to that of the seed point (172.05) with *seed_generation* 300~400. Here, the seed points with *seed_generation* larger than 600 was defined as the *grand_generation* seed points. The proportion of these *grand_generation* seed points that correspond to the total number of seed points extracted earlier on each tier (listed as the number for each row in Table 7.30) could be calculated (Table 7.32).

	tier4	tier5	tier6	tier7	tier8
proportion	0.0572	0.0398	0.0410	0.0405	0.0709

Table 7.32: Proportion of *grand_generation* seed points for the original image on each tier

In general, Table 7.32 gave consistent results as our discovery in Table 7.30. With more *grand_generation* seed points, the DEM accuracy would be negatively effected. The degree of the proportion increased was corresponding to the degree that DEM accuracy decreased, and this phenomenon was most evident for the final tier (tier8). The reason for this relationship observed is that on the tier4~6 of image pyramid, most of the growing seed points would be located in the neighbourhood of the central part of image. Since in general most manual seed points are also selected in this area, and the positions of these growing seed points are relatively closer to that of manual seed points, which implies they are small *seed_generation* seed points. As the tier of the image pyramid approaches to the bottom, the positions of growing seed points expanded outward from the centre. Therefore, from the positions of manual seed points, these seed points are comparatively further away and lead to the large proportion of *grand_generation* seed points. For illustration of the above statement, Table 7.33 has the range of coordinates of the growing seed points on each tier that scaled up to the bottom tier. It shows the coordinates on each tier were gradually growing towards the margins of the image as described earlier.

	line	sample
tier4	208~ 800	192~ 784
tier5	128~ 880	128~872
tier6	76~ 940	76~ 936
tier7	44~ 976	44~ 972
tier8	26~ 996	26~ 994

Table 7.33: Coordinates of the growing seed points for image pyramid on each tier

The advantages of the pyramidal matching can therefore be concluded such that it does not exhibit the tendency of growing “bad” seed points, the *grand_generation* seed points, a phenomenon denoted here as the Original Image Effect (OIE) as seen for the original image matching. Due to this effect, the **GRUENS** running on the SAR imagery is expected to have the drawback that the quality of matching would gradually deteriorate as the growing process progresses to the end. But for the pyramidal image, despite the fact that the seed points are originated in a random manner, they would have accumulated to an approximate number greater than 200000 before entering the final tier (original image resolution). With such a large number of seed points, the *seed_generation* of the growing seed points would in contrast decrease tremendously. In addition, recall the conclusion made in section 7.6.3 that the final DEM accuracy of the pyramid image was mainly determined by the growing seed points of the tier7 (since it has the greatest number of seed points) and the OIE would not occur here but on the last tier the effective of OIE could be eliminated. On the other hand, only ~ 5000 seed points are produced on the last tier where OIE occurred, and with such low number of seed points, the possibility of having the *grand_generation* seed points could be decreased and the OIE could be minimised as well.

The discovery of the advantages of pyramidal matching using **GRUENS** on the SAR imagery in this section is believed to be a significant contribution. Whether the OIE still occur on other types of imagery and whether other matching algorithms used in the pyramidal matching have any benefits over the original image are worth investigating in the related studies in the future.

7.10 Performances of Matching on the Opposite-side Imagery

Two opposite-side stereo pairs were used for pyramidal matching in this section. In Chapter 6, the appearances of these two stereo pairs were examined, and

it was said that owing to their different appearance, the coverage as well as the matching results would be greatly affected. In this section, this statement was practically tested by means of employing the same PDL file as in the same side image. For a simple representation of the matching of different tiers along with the discrimination of the two opposite stereo pairs, there are also some notations introduced here. The pair of PRI_D (left) and PRI_A (right) is defined as the OP1, while the other pair PRI_D (left) and RTM_A (right) the OP2. For the OP1, if the original random seed points produced by grid number 32 on the apex tier of an eight-tier image pyramid were applied with PDL1, the resulting seed points are named OP1_grid32_tier8_1. Likewise for other notations.

As the expected coverage would be low, it was intended to produce as many random seed points as possible so that there is a greater possibility to grow other new seed points and eventually give rise to the increased coverage. Unfortunately, there is a limitation in producing random seed points which is related to the image size, in that the maximum number of random seed points can be produced could not exceed the image size. For instance, if the upper tier is 32*32 of image size, the maximum number of random seed points are 1024 (32*32). This explains the reasons for the unexecutable random seed points for OP1_grid512_tier4_1 (maximum number of seed points 512*512, exceeding the upper tier image size 128*128) and OP1_grid256_tier6_1. Therefore, for an image tier pyramid with greater number of tiers, the image size of the upper tier would be smaller, and as a result limit the number of random seed points could be generated. For the RSE, it is better to have more image tiers as analysed in section 7.5. However, for the opposite side pair, this would pose as a dilemma since with more image tier, the image size of the upper tier becomes smaller, and the random seed points could not be produced in great number. The only way of producing the more random seed points is to reduce the number of image tier, but this would cause severe damage to the matching results due to the RSE. The following two tables Table 7.34 and 7.35 illustrates the above statement.

	OP1 set1 ^a	OP1 set2 ^b	OP1 set3 ^c	OP1 set4 ^d	OP1 set5 ^e
DEM	338.38	338.54	313.62	291.37	119.01
coverage	83.61	83.61	73.26	9.26	2.89

- OP1 set1^a: OP1_grid512_tier2_1
- OP1 set2^b: OP1_grid512_tier2_2
- OP1 set3^c: OP1_grid512_tier3_1
- OP1 set4^d: OP1_grid128_tier4_1
- OP1 set5^e: OP1_grid128_tier6_1

Table 7.34: DEM accuracy (m) and coverage(%) of five data sets of OP1

	OP2 set1 ^a	OP2 set2 ^b	OP2 set3 ^c	OP2 set4 ^d	OP2 set5 ^e
DEM	482.35	482.29	446.78	326.34	151.57
coverage	83.58	83.52	73.01	6.54	4.03

OP2 set1^a: OP2_grid512_tier2_1

OP2 set2^b: OP2_grid512_tier2_2

OP2 set3^c: OP2_grid512_tier3_1

OP2 set4^d: OP2_grid128_tier4_1

OP2 set5^e: OP2_grid128_tier6_1

Table 7.35: DEM accuracy (m) and coverage(%) of five data sets of OP2

It is seen from the above two tables that for the same number of the tiers, the coverage as well as the DEM accuracy were not significantly different between OP1 and OP2. However, the DEM accuracy increased as the number of tiers increased irrespectively of the OP1 or OP2, unfortunately the coverage decreased accordingly. This pattern of change was found irrespectively of the opposite side stereo pair under study. In addition, looking at the values obtained from the two and three-tier image pyramid, it was also observed that the two types of PDL files utilised did not lead to any significant difference in the DEM accuracy as well as the coverage when the matching was processed on the lower number of image tiers of the pyramid. The accuracies were rather poor, for they all suffered from the RSE. In contrast, as there were more image tiers, the DEM accuracy was greatly enhanced. To attempt to increase the coverage as well for these two stereo pairs, here the two PDL files were modified to have loose constraints on each tier for the growing process. This was achieved by increasing the eigenvalue from 100 to 500. The results were however still disappointing. Table 7.36 lists the coverage of three data sets with larger eigenvalue.

	OP2 set1 ^a	OP2 set2 ^b	OP1 set3 ^c
coverage	7.83	28.00	10.38

OP2 set1^a: OP2_grid128_tier4_2

OP2 set2^b: OP2_grid128_tier8_2

OP1 set3^c: OP1_grid128_tier4_2

Table 7.36: Coverage (%) for the larger eigenvalue for three sets of opposite pair

Apart from increasing the eigenvalue, another effort was made to improve the matching coverage by removing the speckle when stereo matching the image pair. Two speckle removing filters were selected to process the image - LEE and MAP. The resulting were not satisfactory, being coverage 1.48% and 3.85% for LEE and

MAP filtered image respectively. The above finding suggests that prior to the matching procedures, more sophisticated image processing techniques are required for the opposite side imagery.

The cause of poor DEM accuracy with less image tiers was analysed earlier and it was then of our interest to determine the DEM accuracy when there were more image tiers. To obtain the answer, this study used an eight-tier image pyramid to run a number of times by the PDL1 file under grid 128. It was found that the coverage for these two pairs ranged from 0.65% to 6.9% without any significant difference. For comparison, among these results, the foremost four sets with dense coverage were selected and their DEM accuracies without the ERSP were calculated and displayed in Table 7.37 and 7.38 respectively.

	set1	set2	set3	set4
DEM	49.25	53.83	52.10	51.61
coverage	4.07	4.03	2.56	2.46

Table 7.37: DEM accuracy (m) and coverage (%) for four sets of OP1 data

	set1	set2	set3	set4
DEM	43.07	51.94	70.71	68.91
coverage	6.85	6.33	6.02	5.89

Table 7.38: DEM accuracy (m) and coverage (%) for four sets of OP2 data

These two tables exhibit that for the opposite stereo pair, the DEM accuracy could not be significantly different when using the same PDL files with the identical tier number and grid number. This is the same as observed for the same side imagery as mentioned in section 7.8. These DEM accuracies were compared further with that of manual seed points. In OP1 and OP2, 9 and 7 seed points were chosen manually to perform the stereo matching under the value of patch radius 25. Their DEM accuracy was 30.68 and 29.64 respectively, however, their coverage was rather low, being 2.4% and 1.09%. Comparing these results, it was shown that, in general, the manual seed points could achieve much higher DEM accuracy but the trade-off was that it lowered the coverage significantly.

7.11 Pyramidal Matching on the Speckle Reduction Imagery

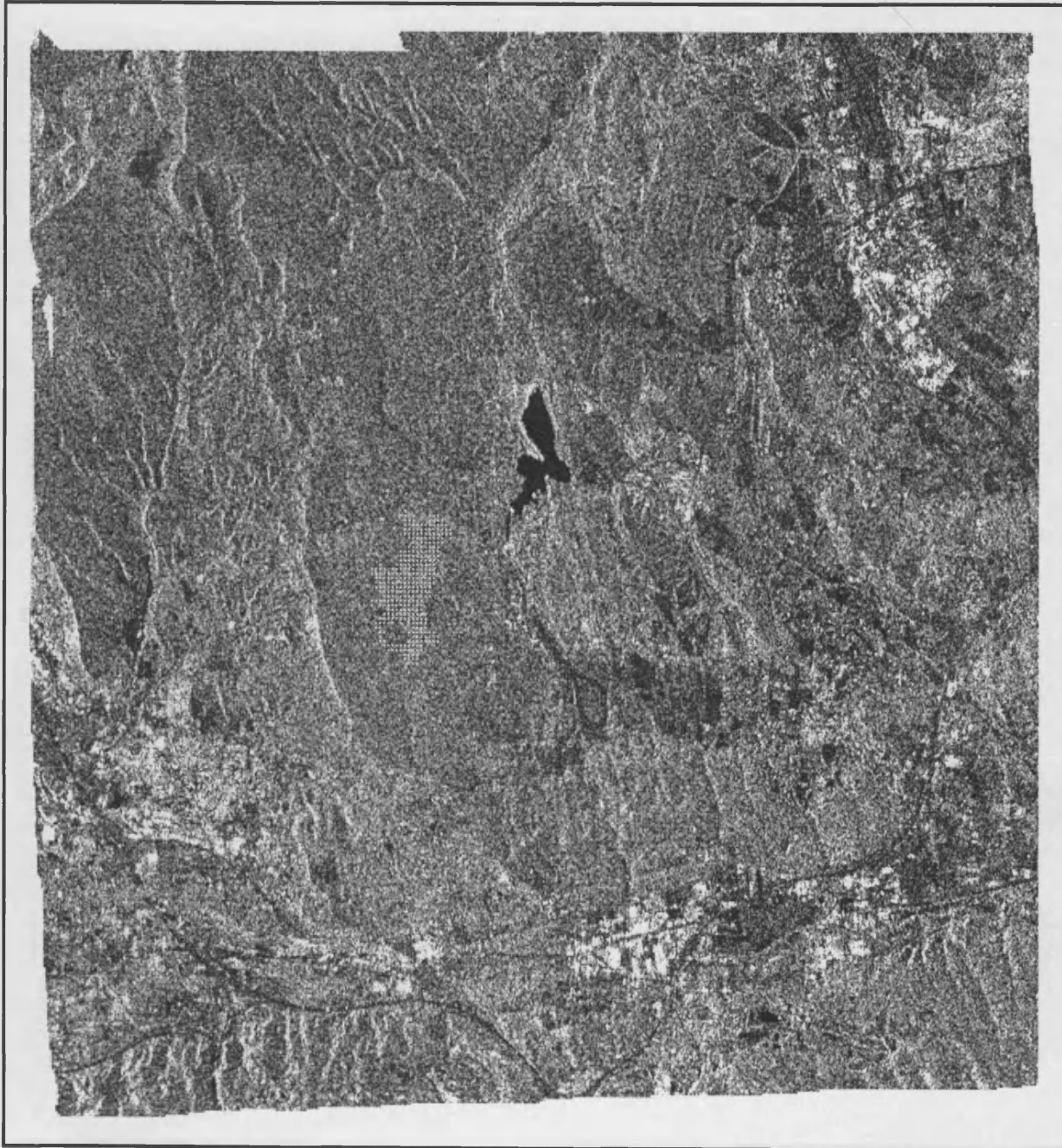
The inherited speckle in SAR imagery is believed to decrease stereo viewing and cause discontinuity, which limit the sheet growing process for the **GRUENS** algorithm. The characteristics of speckles as well as various speckle-removing filters was introduced in Chapter 3. Here, the performances of pyramidal matching for speckle-removing imagery was evaluated. Since in Clochez's report [Clochez, 1993], it was stated that there were no significant differences in terms of coverage between 12 filters tested, only two commonly used filters LEE and MAP filters were chosen to be examined in this study. These speckle-removing filters were used in a window size of 5 to remove the speckles of the same side stereo pair prior to the matching process. These speckle-removing imageries would next adopt the same parameters of grid32_1 to produce random seed points and employ the same PDL files to process the matching. The final DEM accuracies as well as the coverage of these two speckle-removing images were found encouraging, as shown in Table 7.39.

Table 7.39 list the DEM accuracy, HDSE as well as the coverage of these two speckle-removing imageries, and for comparison the results of grid32_1 is also displayed here. The preprocess of the image with the speckle removing filter indeed gave better performances of the stereo matching in terms of the coverage and DEM accuracy as well as HDSE. For a more clear illustration of the influences that these two filters have on the matching procedures, Fig. 7.18, 7.19 showed the coverage of the stereo pair of the LEE and MAP filtered image using the window size of 5, and Fig. 7.20 showed the coverage of original one. In the figures, the white dotted region represents the area that had not been matched. When inspecting these three figures, the unmatched area was the largest for the original image, which was almost twice the size of that observed for the LEE and MAP filtered image. These unmatched areas were located in the steep sloped region, which means that the usual difficult terrain features for the matching such as the hilly area could be overcome by the speckle reduction filter. The common feature observed for all 3 figures is that the margin area of imageries were not fully matched, which should be completed on the last tier of image pyramid. This could be improved if a higher eigenvalue is given for the last tier of PDL files.

	LEE filtered image	MAP filtered image	grid32_1
DEM	133.92	130.80	148.32
Coverage	86.77	86.86	85.81
HDSE	1.05	1.03	1.81

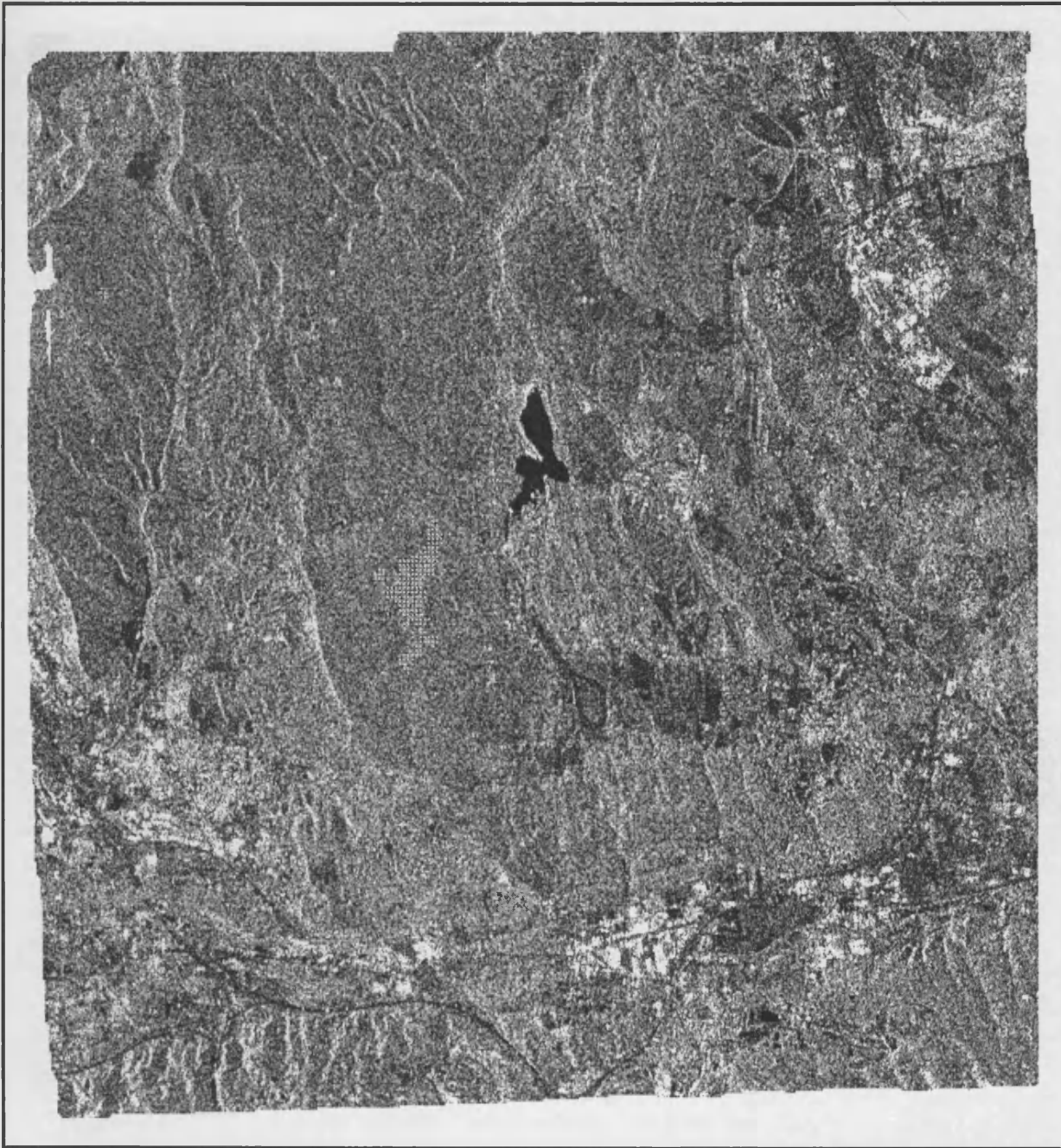
Table 7.39: DEM accuracy and coverage(%) for the original and speckle-removing image

Fig. 7.18: LEE filtered image matching coverage



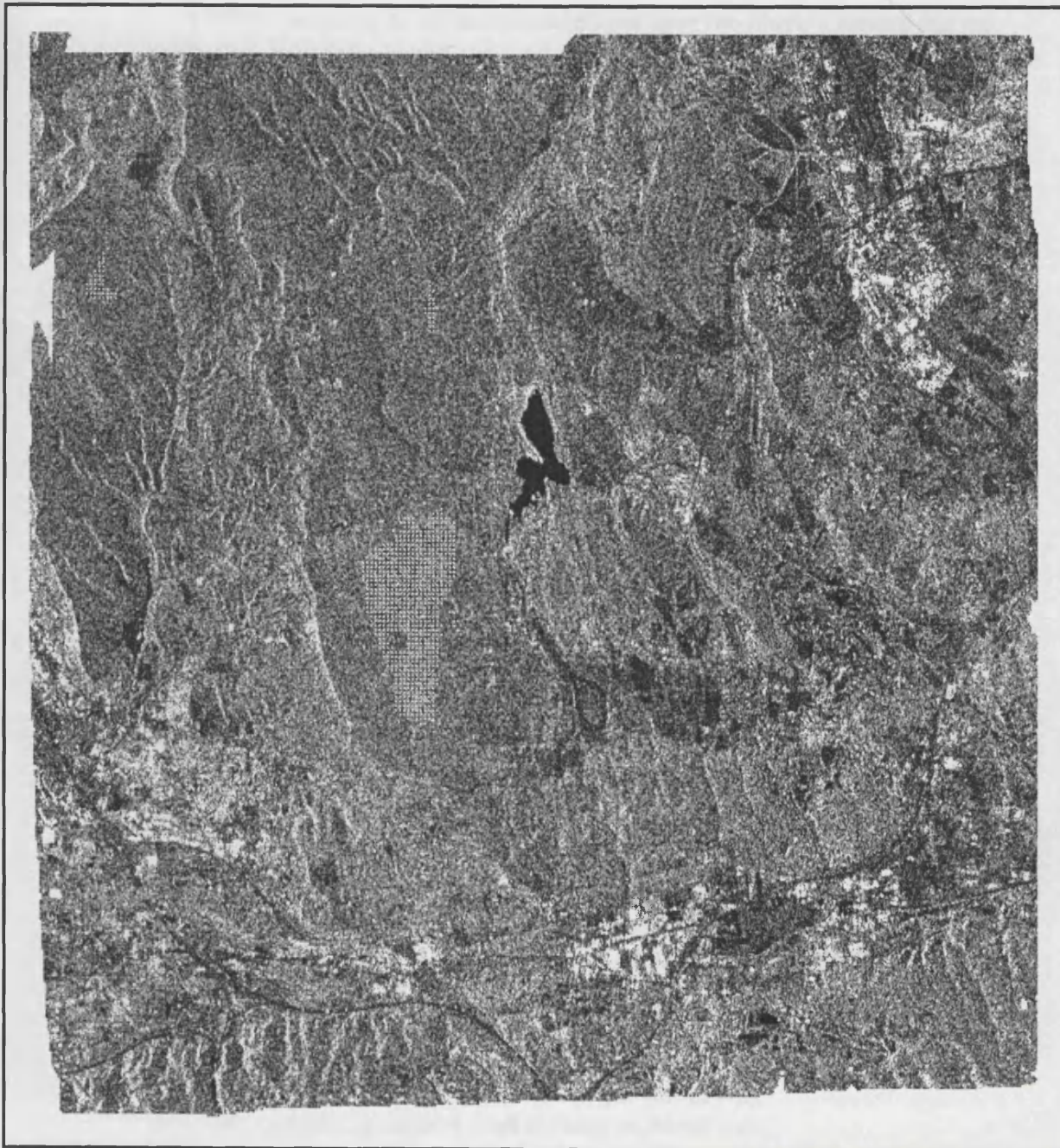
227480 points matched (87%)

Fig. 7.19: MAP filtered image matching coverage



227698 points matched (87%)

Fig. 7.20: Original image matching coverage



224937 points matched (86%)

When comparing the performances between these two filters, it seemed that the MAP filter was a better choice however without any significant difference. The experimental results in this section was more encouraging and in contrast to the previous researches [Clochez, 1993] [Twu, 1994] in that the DEM accuracy as well as the coverage were not expected to be improved. This is because the SAR imagery shows very complicated characteristics as described in Chapter 3, and the speckle is only one of many factors that influence the matching. So, based on the speckle alone, impacts on the stereo matching could not be easily evaluated.

7.12 Run Time Consideration

In this chapter, many studies were carried out to evaluate the effects of various parameters in the pyramidal matching that may have on the DEM accuracy. Some work required longer computation time, e.g. the generation of the for grid32_2 took approximately one week on a different SUN workstation. Apart from the DEM accuracy, computation time is therefore also an important consideration with respect to different values of parameters, so that we can speculate on the trade-off between DEM accuracy and computation time to determine whether the time is worth spending. The CPU time for five different data set running on a single SUN workstation is listed in Table 7.40.

data set	1 ^a	2 ^b	3 ^c	4 ^d	5 ^e
CPU time (h)	85.32	71.31	65.52	93.36	86.78

1^a: sa_grid32_tier8_1

2^b: sa_grid32_tier6_1

3^c: sa_grid32_tier4_1

4^d: sa_grid32_gruentier6_tier8 (refining on the tier1~6)

5^e: sa_grid32_gruentier4_tier8 (refining on the tier1~4)

Table 7.40: Comparison of CPU time (hours) for five different data sets

From Table 7.40, it is clearly illustrated obviously that the CPU time required is directly proportional to the image tiers of the pyramid. In addition, the refining process certainly needs extra time for computation, which can be seen by comparing the CPU time required for three data sets of the same number of tiers, such as data set 1,4, and 5. Apart from the number of image tiers and the refining process, the patch radius is another important factor to affect the computation time, with a quadratic relationship. The accumulated number of matching results on each tier also has its

influence, especially for lower tiers with greater number of seed points. This is because for each new growing seed point, the **GRUENS** has to reorder the priority queue from these accumulated seed points based on their eigenvalue as described in Chapter 4. The longer the queue, the more lengthy the reordering process would become.

7.13 Summary

Various aspects of the techniques utilised for pyramidal matching were presented and analysed in this chapter, covering issues of generating the random seed points, usage of PDL file, development of the blunder-removing filter, as well as the strategy of selecting optimum seed points. With respect to the effects of random seed points, **GRUENS** was modified to give additional output displayed in an extra four columns. With these four columns, the tracking of the performance of random seed points on each tier was possible and the number of ERSP could be calculated. By knowing the number of ERSP, the RSE could be evaluated as well. The RSE deteriorated the matching results demonstrated in this chapter is of special concern when considering the opposite stereo pair. Further analysis of RSE showed it was related to the PDL files employed. If the PDL2 rather than PDL1 was used, the RSE could be effectively reduced. Under a fixed PDL file, the RSE could be further reduced by increasing the image tiers. Unfortunately it was not applicable to the opposite stereo pair, for it caused the coverage to decline dramatically. Another function of the extra four columns mentioned above was to offer a good insight into excellence of the pyramidal matching. The OIE was introduced here to demonstrate the disadvantage of **GRUENS**.

The *disparity sum* was proposed in section 7.6.5 to find out the cause of the DEM accuracy difference between the two PDL files based on its relationship with the number of (-) and (+)height deviation. This *disparity sum* was further used to remove the blunders in section 7.7. In this section it was concluded that the threshold of lower boundary rather than the upper boundary could effectively enhance the DEM accuracy. This was proved by the progressive approach of testing three different percentages of the lower and upper boundaries respectively. The multiple effects of these two boundaries were also displayed in this section. This *disparity sum* was implemented again in section 7.8 to find out the set of seed points that could lead to greater DEM accuracy after removing the blunders with small *disparity sum*. In this section, two preliminary points were proposed. The first one was when removing the blunders, the threshold value should be given in a dynamic manner, and the second

Chapter 7. Assessment of Stereo Matching Results

one being the validation of the connection of *disparity sum* between the upper and lower tiers.

Most of the above conclusions were tested with three different grid number in this chapter to check the effects of the number of random seed points. The result was determined to be the same with all three different grid numbers which means that the conclusions made above are reliable and the number of random seed points does not need to be considered.

CHAPTER 8

Object Domain Approach

8.1 Introduction

Chapter 7 described how DEM accuracy would be enhanced by applying an algorithm in the image domain, using , for example the threshold value of disparity sum. This algorithm did effectively improve the DEM accuracy by a maximum of 16% (166.84m to 140.89m, Table 7.27 grid128_dpy), however, at the same time it resulted in reduced coverage. In addition, these improvements were only made on the same side stereo pair. For the opposite stereo, the final DEM accuracy obtained varied from “excellent” to “poor” depending on the image tiers. Those poor DEM accuracies with denser coverage were worth testing by other algorithms to reach a better DEM accuracy. For the above reason, two new approaches are proposed in this chapter. The first method utilises the intersection condition mentioned in Chapter 5, while the second one requires approximate height values. Both approaches are based in the object domain and the coverage would not be affected.

In the first approach, two geometric *constraint conditions* were introduced - *range error* and intersection angle . The *range error* is derived from equations 5-3 ~ 5-4 in Chapter 5 while the intersection angle come from the general observations of matching points. These two conditions were tested with all the stereo pairs, and the condition best suited for a particular stereo pair would be selected based on analyses presented in later sections. After the condition is determined, it can be used to shift the coordinates of the matching points to obtain superior DEM accuracy without decreasing its coverage.

The techniques of shifting the coordinates were used in the second approach, however, this shifting only occurs in the range direction. This method requires an initial DEM information to give an initial value and from this the magnitude of shifting of the range direction could be determined. This approach was expected to give rise to better DEM accuracy than the first one, but it is strongly dependent on the quality of DEM data provided.

The function of the control points was also examined by giving 3 extra range times in the header data file calculated from the control points. It was found that these

control points could increase the intersection height systematically. In theory, the extent of this was related to the intersection angle .

The contents of this chapter is to firstly introduce the definitions of the *range error* and intersection angle and the formula they were derived from. The techniques by which the applicable constraint condition was determined for three pairs as well as the strategy of choosing the optimum value for the *constraint conditions* are proposed. This value was subsequently tested with various data for all three pairs which brought about a general discussions on the effectiveness and limitations of the *constraint conditions* to increase the DEM accuracy for these three pairs. By shifting the X and Y coordinate of the matching results on the stereo pair, the sensitivity and influence of the intersection formula on the target's ground coordinate as well as heighting accuracy were examined. Next, the results derived from the second approach are presented, and the reasons for adopting this object domain approach are also analysed. Finally, control points are used to help generate the DEM and the impact of these control points will also be discussed in this chapter.

8.2 Geometric Constraint Condition

In this section, two important *constraint conditions* named *range error* and intersection angle are introduced. These two conditions were subsequently used to shift the coordinates for greater DEM accuracy. The *range error* and intersection angle are shown in Fig. 8.1 and Fig. 8.2 for the same side and opposite side respectively. The *range error* is the sum of the difference of the slant range and range distance for the left and right image respectively. The slant range is the distance of the sensor point to the terrain point, while the range distance could be determined by calculating the range time provided by the header data file. The orbit position S1L and S1R as well as the range distance R1L and R1R were estimated by the image matching coordinates and the header data file. These calculations were the same as for the intersection detailed in Chapter 5. The intersection angle was calculated by the formula as described in the figure (Fig. 8.1 & 8.2). From these two figures, it can be seen that the *range error* is virtually the sum of residuals of the two range equations defined in equation (5-3) and (5-4), and the intersection angle is related to the incidence angle of the stereo pair. It can be seen clearly that the intersection angle is greater for the opposite stereo pair compared to the same side. Here, the intersection angle was calculated for each single terrain point, unlike the one provided in Chapter 6 which was the general value estimated by the incidence angle of the image centre. It should be noticed here that for either *range error* or intersection angle , the

calculations must be carried out on geocentric inertial coordinate system, the same reference coordinate system mentioned in Chapter 5 for intersection.

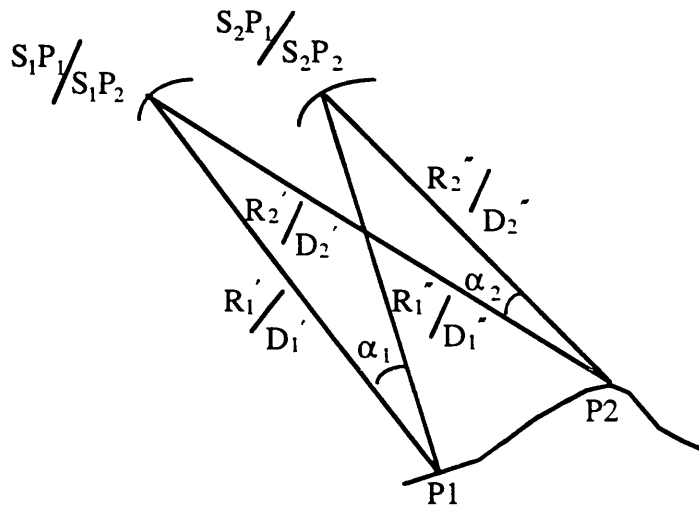


Fig. 8.1: Geometric constraint condition the same side stereo pair

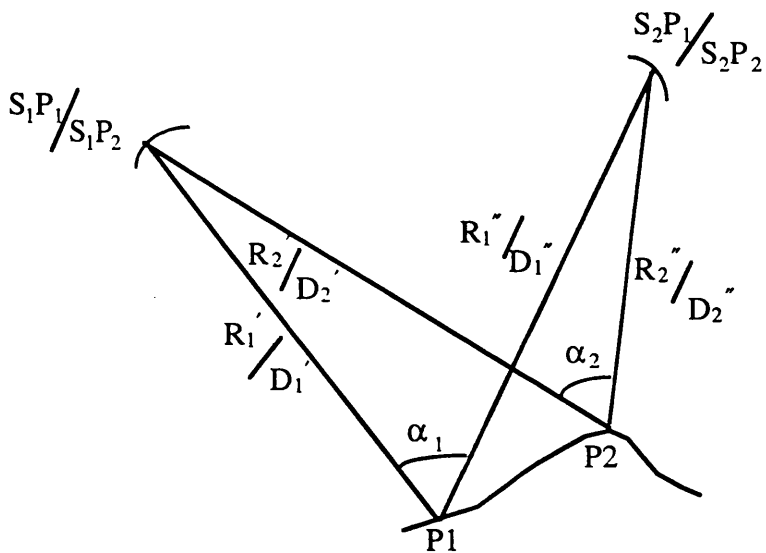


Fig. 8.2: Geometric constraint condition the opposite side stereo pair

In Fig. 8.1 and 8.2:

Considering P1 and P2 are any two terrain points from intersection

let S_1 and S_2 are two orbits respectively

S_1P_1 : the orbit position for point P1 (left image)

S_2P_1 : the orbit position for point P1 (right image)

D_1' : the range distance for point P1 (left image)

D_1'' : the range distance for point P1 (right image)

R_1' : slant range for P1 (left image)

R_1'' : slant range for P1(right image)

S_1P_2 : the orbit position for point P2 (left image)

S_2P_2 : the orbit position for point P2 (right image)

D_2' : the range distance for point P2 (left image)

D_2'' : the range distance for point P2 (right image)

R_2' : slant range for P2 (left image)

R_2'' : slant range for P2 (right image)

α_1 : the intersection angle for P1

α_2 : the intersection angle for P2

Then:

P1 is the intersection terrain point of R_1' and R_1''

P2 is the intersection terrain point of R_2' and R_2''

$R_1' = |S_1P_1 - P_1|$; $R_1'' = |S_2P_1 - P_1|$; $R_2' = |S_1P_2 - P_2|$; $R_2'' = |S_2P_2 - P_2|$

D_1' : range distance for P1 calculated from range time (left image)

D_1'' : range distance for P1 calculated from range time (right image)

D_2' : range distance for P2 calculated from range time (left image)

D_2'' : range distance for P2 calculated from range time (right image)

P1 (range_error) = $(R_1' - D_1') + (R_1'' - D_1'')$

P2 (range_error) = $(R_2' - D_2') + (R_2'' - D_2'')$

$$\alpha_1 = \cos^{-1} \left(\frac{(\vec{R}_1') \cdot (\vec{R}_1'')}{|\vec{R}_1'| * |\vec{R}_1''|} \right)$$

$$\alpha_2 = \cos^{-1} \left(\frac{(\vec{R}_2') \cdot (\vec{R}_2'')}{|\vec{R}_2'| * |\vec{R}_2''|} \right)$$

8.3 Height Deviation and Constraint Condition

In the last section, the definitions of the two *constraint conditions*, *range error* and *intersection angle* was introduced. For simplicity the values of these two *constraint conditions* are named *constraint values*. Here, it is of interest to know if any relationship exists between the *constraint values* and height deviation. If it was the case, it is important to test whether this relationship is common for all data sets and therefore could be described by an unique function named *constraint_height function*. The ideal case for this *constraint_height function* is a one-to-one correspondence, in other words, a certain given constraint value would lead to a particular height deviation. If the value is altered, the height deviation would also be influenced. Therefore, once a constraint value that could result in small height deviation is determined, say v , techniques could be employed to make the *constraint values* of all matching points equal to v , consequently obtaining greater DEM accuracy. Unfortunately, this is not possible in real practice as the relationship of the height deviation and constraint value is not unique. The above mentioned constraint value of v may only appear as an interval rather than a single value, and as a result, the strategy described earlier will not be so effective as expected. Instead, the effectiveness would be influenced by the width of the interval, such that the narrower the interval, the better the matching result would be obtained using the proposed method.

To facilitate the search for a relationship between the constraint value and height deviation, three sets of matching results were chosen from Chapter 7 for each stereo pair. These three sets included different types of data, including different PDL files and various number of image tiers, to check if the relationship is general, so that it is reliable and can be utilised. It should be noted here that for the same side stereo pair, the selection of three stereo pairs was not difficult since their matching results had no significant difference with respect to the DEM accuracy and coverage. For the opposite stereo pairs, in contrast, the selected data would have to cover varied height deviation in order to investigate the relationship more accurately. Thus, less number of image tiers were chosen for this opposite stereo pair and in total 9 data sets were selected as listed in Table 8.1.

SA	OP1	OP2
sa_grid32_tier8_1	OP1_grid512_tier2_1	OP2_grid512_tier2_1
sa_grid32_tier8_2	OP1_grid512_tier2_2	OP2_grid512_tier2_2
sa_grid32_tier6_1	OP1_grid512_tier3_1	OP2_grid512_tier3_1

Table 8.1: 9 data sets selected for testing the relationship of constraint values and height deviation

After the selection had been completed, the matching points of different height deviation were appointed. In order to facilitate the establishment of this relationship, the whole range of height deviation (-1000m ~ 1000m) was divided into 9 intervals. These 9 intervals of height deviation and their corresponding *constraint values* for all nine data sets are listed in Table 8.2 ~ 8.7, where Table 8.2 ~ 8.4 shows the *range error*, while Table 8.5 ~ 8.7 specify the intersection angle. The parameters listed include the minimum, average and maximum *constraint values*.

It is observed that in Table 8.2 ~ 8.4 the average values of *range error* did not show any significant difference under a given height deviation for all three pairs. Even the largest difference did not exceed 6 m (-239.57m compared to -245.34m at height deviation 500m ~ 1000m, Table 8.4). Similarly, although variations did occur, the minimum and maximum values of *range error* in general, were very consistent. Comparing among these three pairs listed, OP2 had the most variations. The same similarity in the intersection angle was obtained when comparing Table 8.5 ~ 8.7, such that for the opposite-side stereo pair, the average value were almost identical and the largest difference of minimum and maximum value did not exceed 0.02°. From Table 8.2 ~ 8.7, therefore, it was concluded that the two *constraint values* for a given interval of height deviation were almost identical. This finding encourages us to further investigate the possibility to use them to obtain greater DEM accuracy as suggested earlier.

For this purpose, one data set was chosen for each stereo pair, which were the sa_grid32_tier8_1 for SA, OP1_grid512_tier2_1 for OP1 and OP2_grid512_tier2_1 for OP2 respectively. In Fig. 8.3 ~ 8.5, the relationship between the average values of *range error* and height deviation was represented in three pairs. For the same side stereo pair, it is seen in Fig. 8.3 that *range error* decreased gradually from 13.54m to -31.47m as the height deviation increased from -1000m ~ -500m to 500m ~ 1000m. This trend was not observed for the OP1 and OP2 as can be seen in the Fig. 8.4 and 8.5. When plotting the intersection angle against DEM deviation, no significant

difference was observed under different height deviation (Fig. 8.6). In contrast, for OP1 and OP2, the intersection angle is regularly increased as the height deviation increased from -1000 ~ -500 to 500 ~ 1000 (Fig. 8.7 & 8.8). These observations made from the above six figures provided preliminary evidence that the *range error* seemed a more suitable constraint condition for the same side, while the intersection angle was more for the opposite side. However, it would not be reliable to just consider the average values. Therefore, two other analyses were adopted to aid the finalisation of this study.

8.4 Determination of Constraint Condition

In this section, two other analyses were used to facilitate the determination of the constraint condition best suitable for each stereo pair. The first method was to inspect the extent of *range error* covered by the minimum and maximum *constraint values* under 9 different height deviations by plotting these deviations against *constraint values* extent. If there was no overlapping region of *constraint values* under different height deviations, then the relationship could be described as an one-to-one function as stated in section 8.3. The greater degree of the overlap means the function deviated from the ideal correspondence.

	sa_grid32_tier8_1	sa_grid32_tier8_2	sa_grid32_tier6_1
-1000 ~ -500	(8.78 ^a , 16.59 ^b , 35.53 ^c)	(10.08, 17.08, 30.41)	(10.20, 13.54, 32.04)
-500 ~ -250	(-1.21, 5.86, 16.09)	(-2.84, 4.36, 15.77)	(-2.80, 5.40, 15.82)
-250 ~ -100	(-7.22, -1.58, 6.32)	(-7.90, -1.67, 6.20)	(-8.31, -2.23, 6.19)
-100 ~ -50	(-9.38, -5.18, -0.06)	(-9.70, -5.04, 0.12)	(-9.56, -5.68, -0.08)
-50 ~ 50	(-14.34, -8.49, -2.05)	(-15.02, -8.24, -2.11)	(-15.24, -8.55, -1.74)
50 ~ 100	(-16.46, -11.70, -6.29)	(-16.24, -11.21, -5.73)	(-18.07, -11.17, -6.15)
100 ~ 250	(-22.83, -15.64, -7.43)	(-23.07, -15.76, -7.55)	(-23.22, -15.58, -7.38)
250 ~ 500	(-33.42, -19.39, 48.72)	(-32.69, -19.72, -12.94)	(-31.87, -19.62, -13.26)
500 ~ 1000	(-90.05, -32.34, -24.34)	(-92.13, -31.90, -25.56)	(-91.09, -31.47, -23.36)

(a,b,c): a- minimum range error ; b- mean range error ; c-maximum range error

Table 8.2: 9 height deviation intervals and their corresponding statistics of range error (m) of SA

	OP1_grid512_tier2_2	OP1_grid512_tier2_1	OP1_grid512_tier3_1
-1000 ~ -500	(-35.97, 8.58, 34.33)	(-35.39, 8.42, 34.52)	(-33.71, 8.96, 32.25)
-500 ~ -250	(-36.32, -3.31, 34.18)	(-39.87, -3.32, 34.15)	(-34.32, 32.04, -3.15)
-250 ~ -100	(-36.48, -0.67, 33.98)	(-36.57, -0.67, 34.01)	(-34.52, -0.70, 31.85)
-100 ~ -50	(-36.54, 1.02, 33.88)	(-36.60, 1.15, 33.96)	(-34.58, 0.75, 31.78)
-50 ~ 50	(-38.35, -0.76, 33.91)	(-37.85, -0.84, 33.94)	(-34.79, -0.30, 31.80)
50 ~ 100	(-37.96, -6.38, 33.87)	(-36.67, -6.27, 33.90)	(-34.62, -0.30, 31.80)
100 ~ 250	(-36.92, -0.97, 33.85)	(-36.93, -0.94, 33.86)	(-35.85, -1.02, 31.69)
250 ~ 500	(-37.20, -7.17, 33.75)	(-37.13, -7.19, 34.02)	(-35.20, -8.79, 31.46)
500 ~ 1000	(-37.17, -28.61, -13.97)	(-37.19, -28.64, 12.34)	(-34.80, -28.56, -6.67)

Table 8.3: 9 height deviation intervals and their corresponding statistics of range error (m) of OP1

	OP2_grid512_tier2_1	OP2_grid512_tier2_2	OP2_grid512_tier3_1
-1000 ~ -500	(-208.49, 141.47, 363.80)	(-280.06, 141.41, 362.70)	(-230.15, 146.31, 340.51)
-500 ~ -250	(-392.49, -1.14, 349.68)	(-393.51, -1.86, 349.69)	(-372.61, 1.92, 332.74)
-250 ~ -100	(-397.92, -34.60, 343.46)	(-399.34, -34.88, 342.62)	(-377.22, -29.54, 321.01)
-100 ~ -50	(-399.62, -6.70, 339.63)	(-399.54, -5.90, 339.87)	(-379.53, -18.67, 318.58)
-50 ~ 50	(-401.83, -19.23, 337.29)	(-401.49, -19.26, 337.37)	(-382.34, -18.76, 316.29)
50 ~ 100	(-403.38, -36.78, 335.06)	(-403.49, -35.93, 335.08)	(-381.40, -38.77, 314.08)
100 ~ 250	(-406.58, -49.85, 333.32)	(-407.86, -50.0, 334.67)	(-386.91, -50.17, 310.35)
250 ~ 500	(-414.18, -102.63, 329.55)	(-414.23, -102.55, 330.83)	(-386.91, -50.17, 310.35)
500 ~ 1000	(-430.35, -239.57, 130.70)	(-430.08, -245.34, 131.80)	(-410.17, -242.52, 63.84)

Table 8.4: 9 height deviation intervals and their corresponding statistics of range error (m) of OP2

	sa_grid32_tier8_1	sa_grid32_tier8_2	sa_grid32_tier6_1
-1000 ~ -500	(14.82 ^a , 14.95 ^b , 14.98 ^c)	(14.85, 14.94, 14.98)	(14.82, 14.93, 14.97)
-500 ~ -250	(14.82, 14.94, 14.98)	(14.82, 14.93, 14.98)	(14.82, 14.92, 14.97)
-250 ~ -100	(14.82, 14.92, 14.97)	(14.80, 14.90, 14.97)	(14.81, 14.92, 14.97)
-100 ~ -50	(14.81, 14.91, 14.97)	(14.80, 14.90, 14.97)	(14.80, 14.92, 14.97)
-50 ~ 50	(14.80, 14.91, 14.98)	(14.79, 14.90, 14.98)	(14.79, 14.90, 14.98)
50 ~ 100	(14.79, 14.91, 14.98)	(14.79, 14.90, 14.98)	(14.78, 14.89, 14.98)
100 ~ 250	(14.78, 14.89, 14.98)	(14.78, 14.90, 14.98)	(14.78, 14.89, 14.98)
250 ~ 500	(14.78, 14.86, 14.98)	(14.78, 14.86, 14.98)	(14.78, 14.86, 14.98)
500 ~ 1000	(14.78, 14.90, 14.96)	(14.78, 14.90, 14.96)	(14.78, 14.90, 14.96)

(a,b,c): a- minimum intersection angle ; b-mean intersection angle ;

c- maximum intersection angle

Table 8.5: 9 height deviation intervals and their corresponding statistics of intersection angle (°) of SA

	OPI_grid512_tier2_2	OPI_grid512_tier2_1	OPI_grid512_tier3_1
-1000 ~ -500	(43.84, 43.89, 43.96)	(43.84, 43.89, 43.98)	(43.84, 43.89, 43.96)
-500 ~ -250	(43.88, 43.95, 44.04)	(43.88, 43.95, 44.04)	(43.88, 43.95, 44.04)
-250 ~ -100	(43.97, 44.02, 44.10)	(43.96, 44.02, 44.10)	(43.98, 44.02, 44.10)
-100 ~ -50	(44.02, 44.07, 44.12)	(43.95, 44.07, 44.18)	(44.02, 44.07, 44.12)
-50 ~ 50	(44.04, 44.09, 44.15)	(44.04, 44.09, 44.15)	(44.04, 44.09, 44.15)
50 ~ 100	(44.07, 44.11, 44.16)	(44.07, 44.11, 44.16)	(44.07, 44.12, 44.16)
100 ~ 250	(44.09, 44.15, 44.22)	(44.09, 44.15, 44.21)	(44.09, 44.15, 44.21)
250 ~ 500	(44.15, 44.20, 44.25)	(44.15, 44.20, 44.25)	(44.15, 44.19, 44.24)
500 ~ 1000	(44.23, 44.24, 44.25)	(44.23, 44.24, 44.25)	(44.18, 44.24, 44.24)

Table 8.6: 9 height deviation intervals and their corresponding statistics of intersection angle (°) of OPI

	OP2_grid512_tier2_1	OP2_grid512_tier2_2	OP2_tier3_grid512_1
-1000 ~ -500	(58.58, 58.63, 58.75)	(58.58, 58.63, 58.75)	(58.58, 58.65, 58.75)
-500 ~ -250	(58.61, 58.69, 58.81)	(58.60, 58.69, 58.82)	(58.61, 58.69, 58.81)
-250 ~ -100	(58.64, 58.74, 58.85)	(58.64, 58.74, 58.85)	(58.64, 58.74, 58.84)
-100 ~ -50	(58.69, 58.77, 58.87)	(58.69, 58.77, 58.87)	(58.70, 58.77, 58.86)
-50 ~ 50	(58.70, 58.79, 58.89)	(58.70, 58.79, 58.89)	(58.70, 58.79, 58.89)
50 ~ 100	(58.72, 58.81, 58.90)	(58.72, 58.81, 58.90)	(58.72, 58.81, 58.90)
100 ~ 250	(58.73, 58.83, 58.93)	(58.73, 58.83, 58.93)	(58.73, 58.83, 58.92)
250 ~ 500	(58.77, 58.88, 58.95)	(58.77, 58.88, 58.95)	(58.77, 58.88, 58.94)
500 ~ 1000	(58.83, 58.92, 58.98)	(58.83, 58.92, 58.98)	(58.84, 58.92, 58.97)

Table 8.7: 9 height deviation intervals and their corresponding statistics of intersection angle (°) of OP2

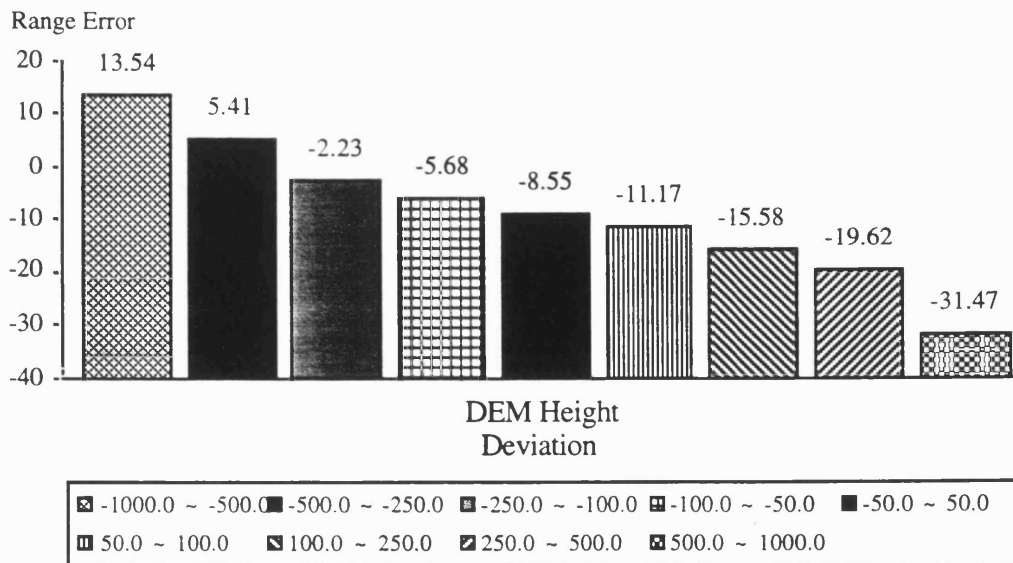


Fig. 8.3: Relationship of range error (m) and height deviation for the SA

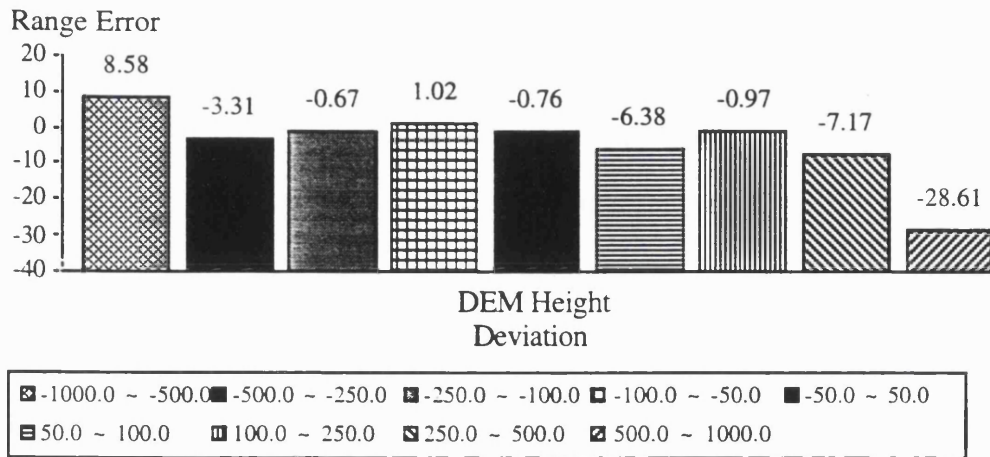


Fig. 8.4: Relationship of range error (m) and height deviation for the OP1

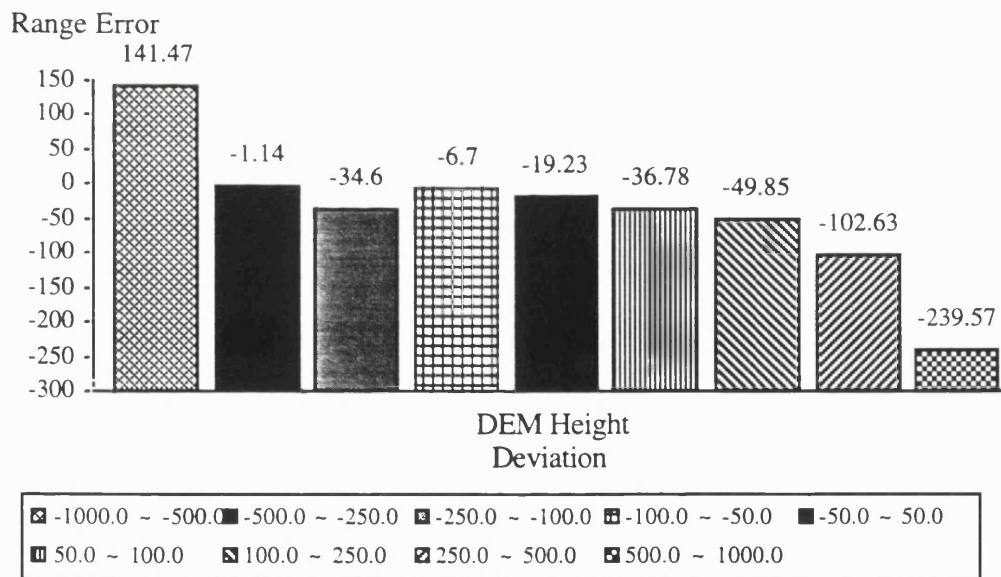


Fig. 8.5: Relationship of range error (m) and height deviation for the OP2

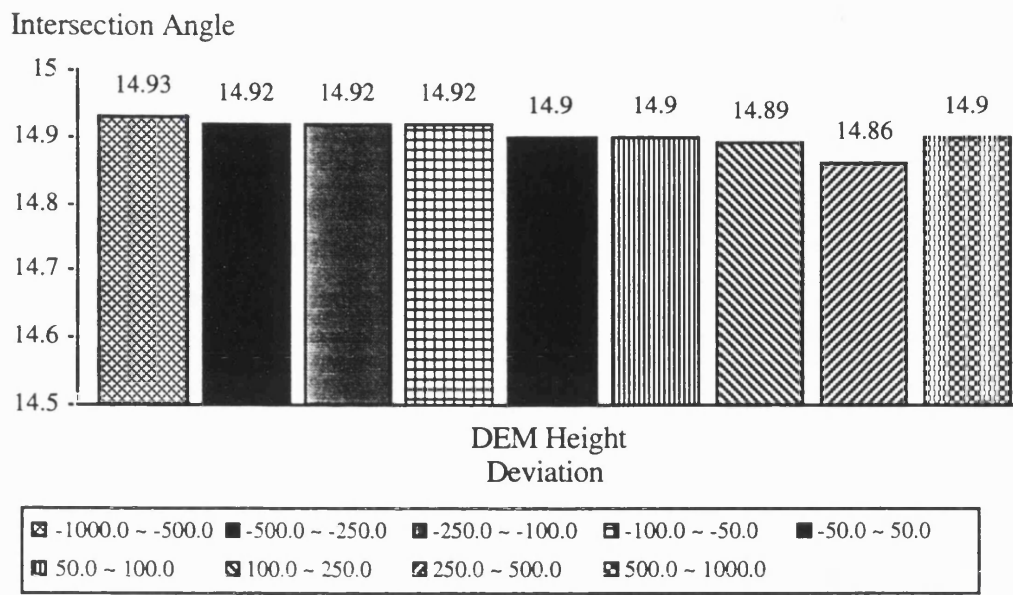


Fig. 8.6: Relationship of intersection angle (°) and height deviation for the SA

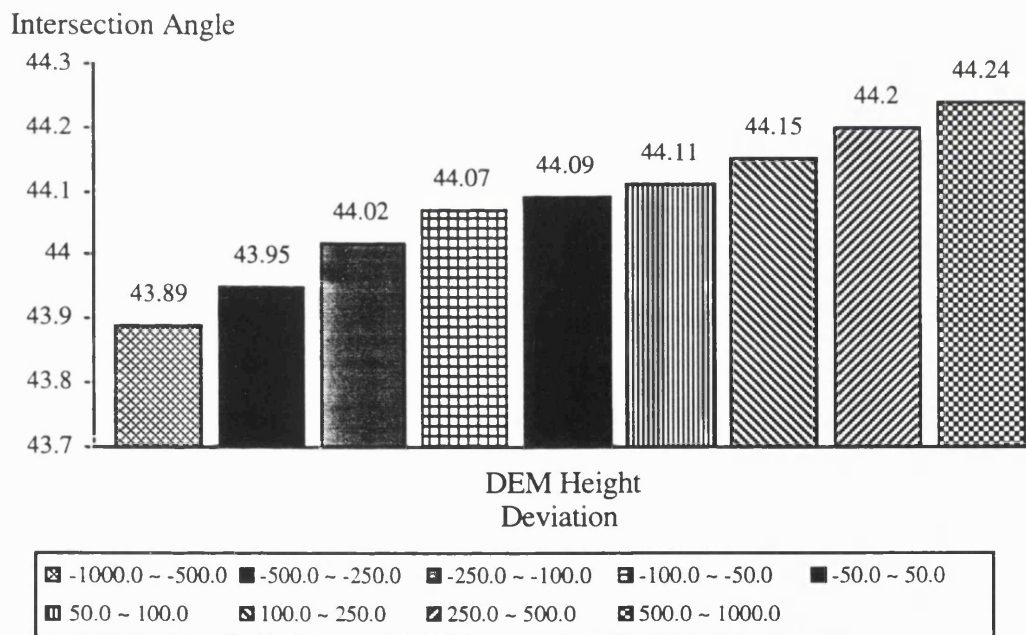


Fig. 8.7: Relationship of intersection angle and height deviation for the OP1

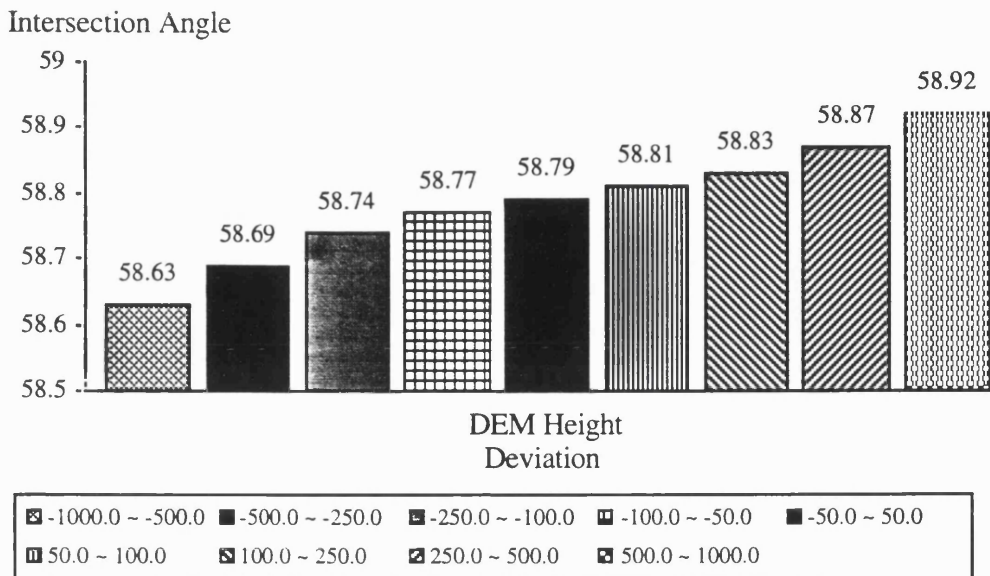


Fig. 8.8: Relationship of intersection angle(°) and height deviation for the OP2

Fig. 8.9 and 8.10 show the extent of overlap of the *range error* and intersection angle plotted against height deviations of the same side. It is seen that the *range error* was obviously a better constraint condition than the intersection angle for the same side stereo pair since little overlap was obtained. This finding was in accordance with the statement made earlier in section 8.3. Notice that the whole extent of the *range error* (X coordinate) gradually shifts towards the left as indicated in the Fig. 8.9 as the value of height deviation increased. This phenomenon however did not occur in Fig. 8.10 for the intersection angle. For the opposite stereo pair, the situation was on the contrary as seen in Fig. 8.11~ 8.14 such that the extent of intersection angle moved towards the right as the value of height deviation increased.

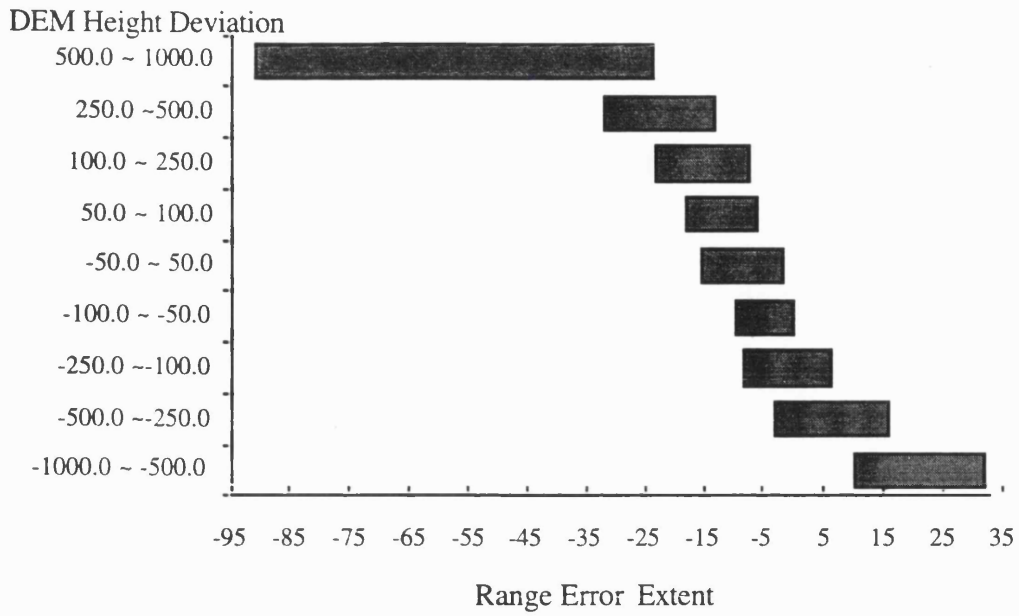


Fig. 8.9: Extent of range error (m) under different height deviation (m) for the SA

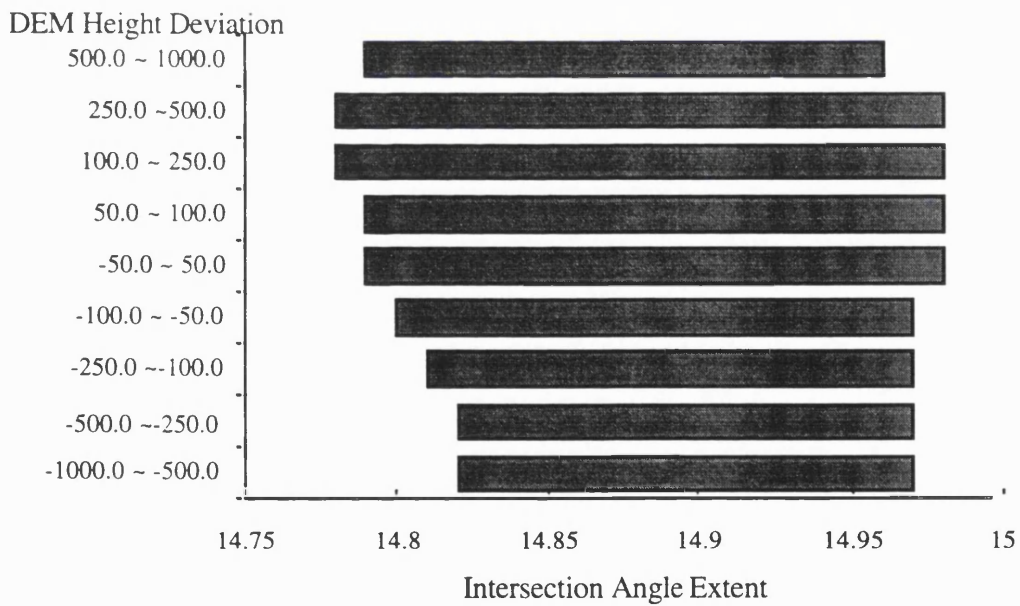


Fig. 8.10: Extent of intersection angle(°) under different height deviation (m) for the SA

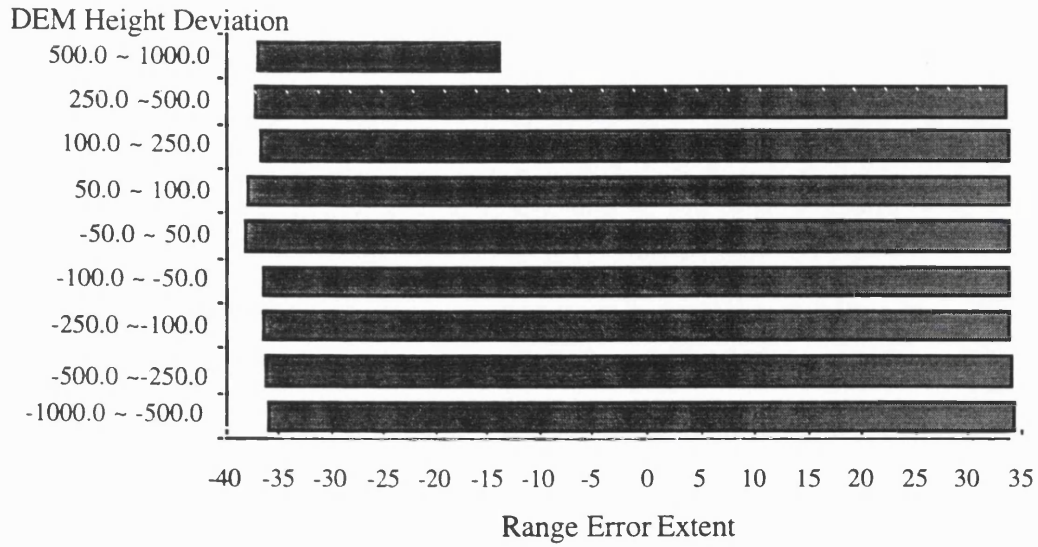


Fig. 8.11: Extent of range error (m) under different height deviation (m) for the OP1

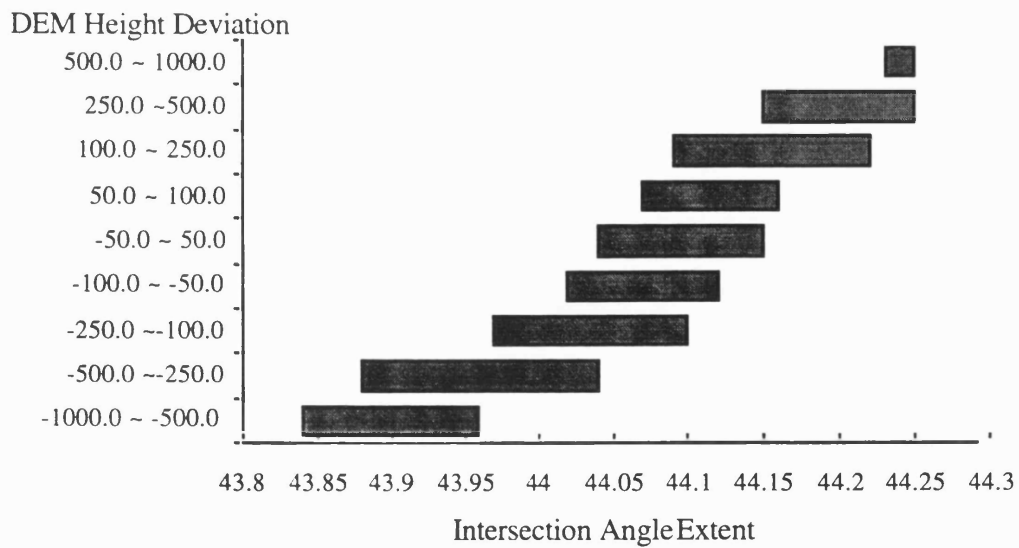


Fig. 8.12: Extent of intersection angle (°) under different height deviation (m) for the OP1

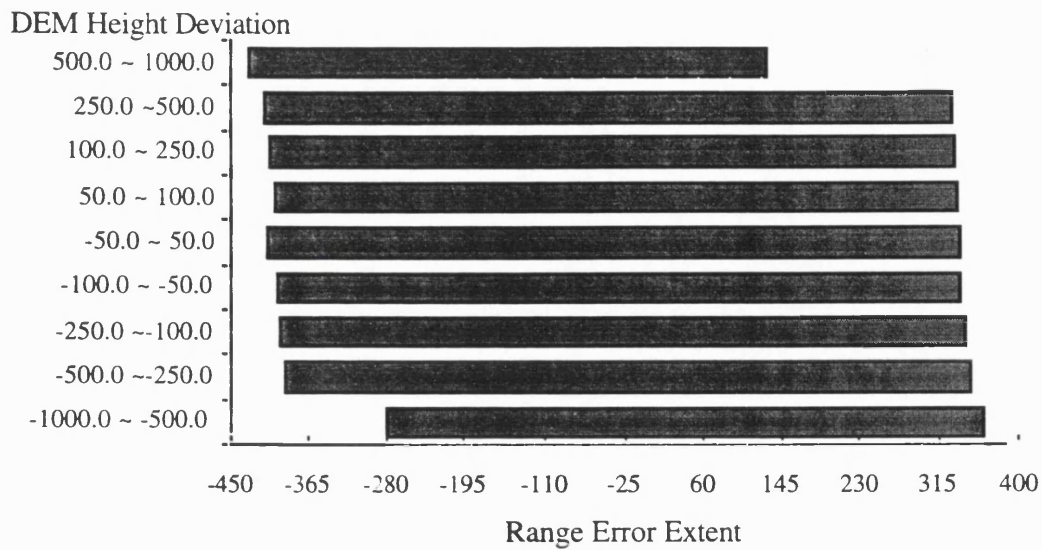


Fig. 8.13: Extent of range error (m) under different height deviation (m) for the OP2

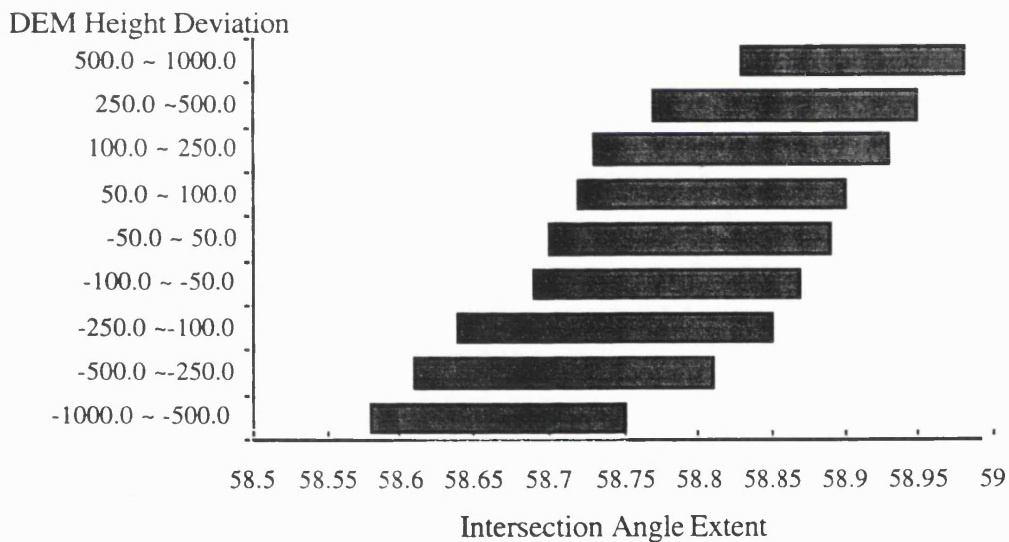


Fig. 8.14: Extent of intersection angle (°) under different height deviation (m) for the OP2

Except for checking the extent of *constraint values*, a second strategy was used to aid the determination of constraint condition by looking at the variations of height deviation under a specified constraint value interval. If the height deviation corresponding to the extreme intervals of constraint value was well-concentrated at two ends, then this given constraint condition could be suitably adopted. The two most extreme intervals of *constraint values* were chosen by giving the upper and lower threshold limits. These two threshold limits could be obtained by firstly calculating all the *constraint values* of all the matching results. We then focused on

the two mean height deviation corresponding to the two extreme intervals of *constraint values* . If the height deviation was strongly affected by the *constraint values* , then these extreme intervals of *constraint values* would lead to the two extreme well-concentrated height deviations and their mean values must be significantly different. Under a given constraint condition, if the difference of mean height deviation (MHD) obtained was tremendous, then this constraint condition was said to be suitable for that particular stereo pair.

From the MHD listed in Table 8.8 ~ 8.10, the same conclusion could be made such that the *range error* was indeed a better constraint condition for the same side, while intersection angle for the opposite side. This conclusion was obtained by all three methods adopted for defining the relationship between the height deviations and the two *constraint conditions* . It is therefore said to be undoubtedly correct for a particular stereo pair.

range error (m)	extent	>0.0	intersection angle (°)	extent	>14.95
	No.	3013		No.	29232
	MHD ^a	-294.73		MHD	163.69
range error (m)	extent	<-25.0	intersection angle (°)	extent	<14.80
	No.	10781		No.	8842
	MHD	530.82		MHD	262.15
MHD difference		825.55	MHD difference		98.56

MHD^a - mean height deviation (m)

MHD difference: (larger-smaller) mean height deviation

Table 8.8: Mean height deviation and the difference for two intervals of extreme constraint values for SA

range error (m)	extent	>300.0	intersection angle (°)	extent	>44.20
	No.	12040		No.	26563
	MHD	-261.49		MHD	389.66
range error (m)	extent	<-300.0	intersection angle (°)	extent	<43.90
	No.	19636		No.	30079
	MHD	-14.73		MHD	-610.94
MHD difference		246.76	MHD difference		1000.60

Table 8.9: Mean height deviation and the difference for two intervals of extreme constraint values for OPI

range error (m)	extent	<-350.0	intersection angle (°)	extent	>58.90
	No.	16890		No.	34744
	MHD	402.88		MHD	782.37
range error (m)	extent	>300.0	intersection angle (°)	extent	<58.60
	No.	13876		No.	8079
	MHD	-398.24		MHD	-799.33
MHD difference		801.12	MHD difference		1582.70

Table 8.10: Mean height deviation and the difference for two intervals of extreme constraint values for OP2

8.5 Characteristics of Constraint Values

After the constraint condition had been determined for each stereo pair, it was necessary to investigate the characteristics of the *range error* and intersection angle. In section 8.3, it was mentioned that the technique of improving the DEM accuracy would be by making the *constraint values* of all the matching points to be equal to that with the smallest height deviation. The effectiveness of this technique is based on how well the *range error* or intersection angle could be estimated by a function. To find out this function, the gradient of *range error* and intersection angle have to be first evaluated by considering the correlation of gradient and image coordinates. If the gradient is constant for all the image coordinates, then all the *constraint values* could be estimated by a linear function and computed by using this constant, hence, any alteration of the *constraint values* to the specified value would be possible. On the contrary, if the gradients are variant between different image coordinates, then the constraint value should be described by a nonlinear function. As a result, the constraint value could not be predicted easily and so the alteration to a specified value would not be accurate. To discover the gradient of *range error* and intersection angle with respect to the image coordinates, three groups of different image coordinates, which were the small, central and large group, were selected based on their coordinates on the left imagery. For the small and large group, all their coordinates were below 50 and above 900 respectively and for the central group, the coordinates concentrated on the interval of 510 ~ 520. In each group, average gradients of all the points were calculated. This average gradient was computed five times, each time with 10 increments on the coordinates of the right imagery. Three sets of the five average gradients were plotted on a graph to show the variation of gradient by different image coordinates. From examining the influence on the gradient with

respect to each X and Y coordinate as well as both of them, three figures are shown for each stereo pair. The *range error* was used for the same side, while the intersection angle for the opposite side.

In Fig. 8.15, it is shown that the gradients of *range error* were almost identical (from -0.295 to -0.31) with respect to the increased X coordinate (different group), and at a given X coordinate (same group) the gradient was fixed at a constant. This situation became more complicated as seen in Fig. 8.16 for the Y coordinate variation. In the same group as well as the different group, the gradient regularly decreased. Fig. 8.17 shows the gradient change with simultaneous variation of X and Y coordinate, represented as (X+Y). It is discovered that the (X+Y) gradient was approximately the sum of X and Y coordinate, which means these gradient of *range error* could be additive. From Fig. 8.18~ 8.20 are three figures for the gradients of intersection angle of the opposite side. They show that the change of gradient was very minute and all gradients could be considered identical irrespective of the group type. The additive effect was observed here for the intersection angle as seen in Fig. 8.20. From the analyses of Fig. 8.15 ~ 8.20, evidence indicate that the gradient of *range error* and the intersection angle were almost fixed constant in spite of the different image coordinates. Therefore, in this study, the gradient of central group was taken as the gradient constant. Among the chosen central group gradients, there were other choices which were gradients with respect to the X, Y, and X+Y coordinates. For the same side, the gradient of Y direction (-8.1) was much greater than that of X direction (-0.294), this value was therefore used in subsequent calculations for matching pixel shifting in Y direction to alter their *range error*. For the opposite stereo pair, both gradients with respect to the X and Y coordinate were quite minute. To use a greater gradient, we could employ the gradient of X +Y coordinate (Fig. 8.20), which was -0.000323 for OP1 and -0.00067 for OP2 respectively.

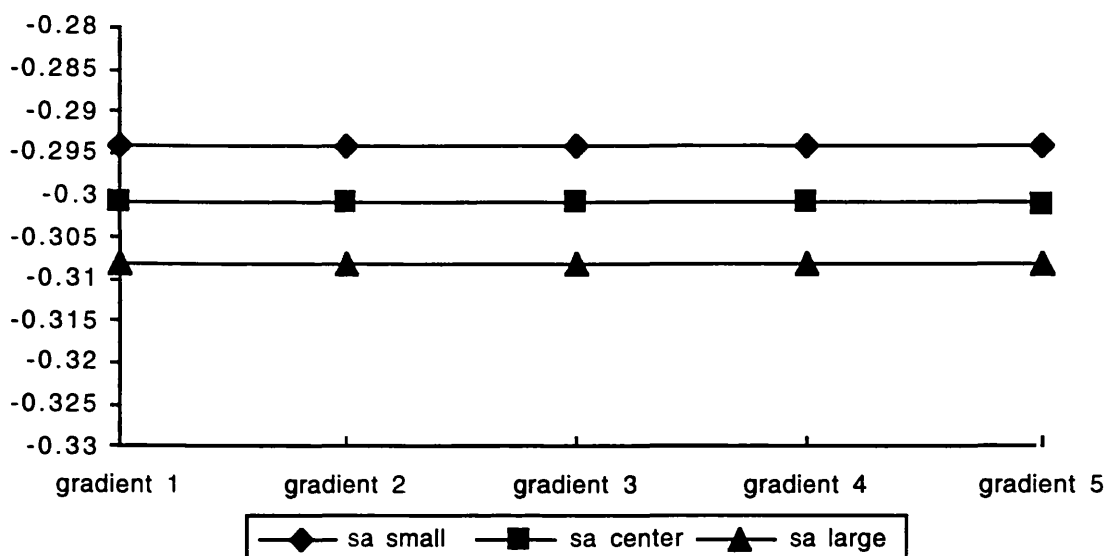


Fig. 8.15: Range error (m) of SA with respect to the X coordinate

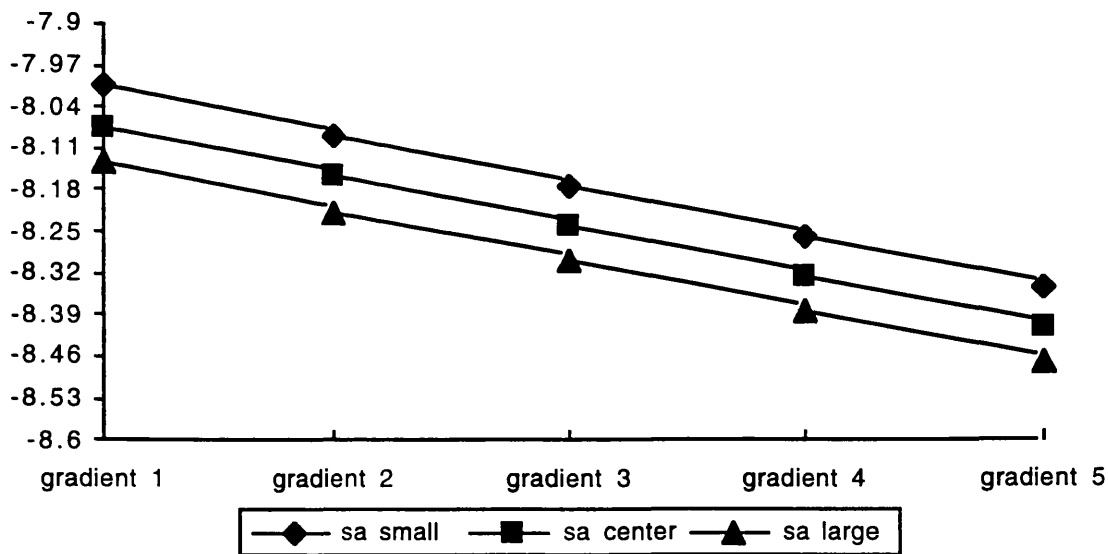


Fig. 8.16: Range error (m) of SA with respect to the Y coordinate

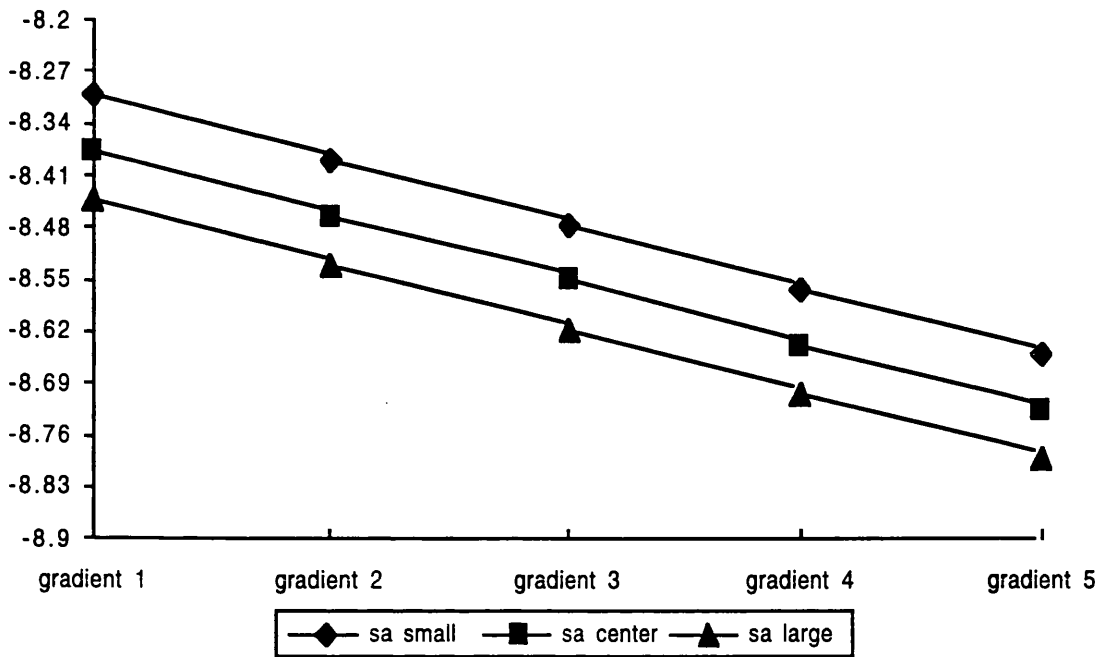


Fig. 8.17: Range error (m) of SA with respect to the X+Y coordinate

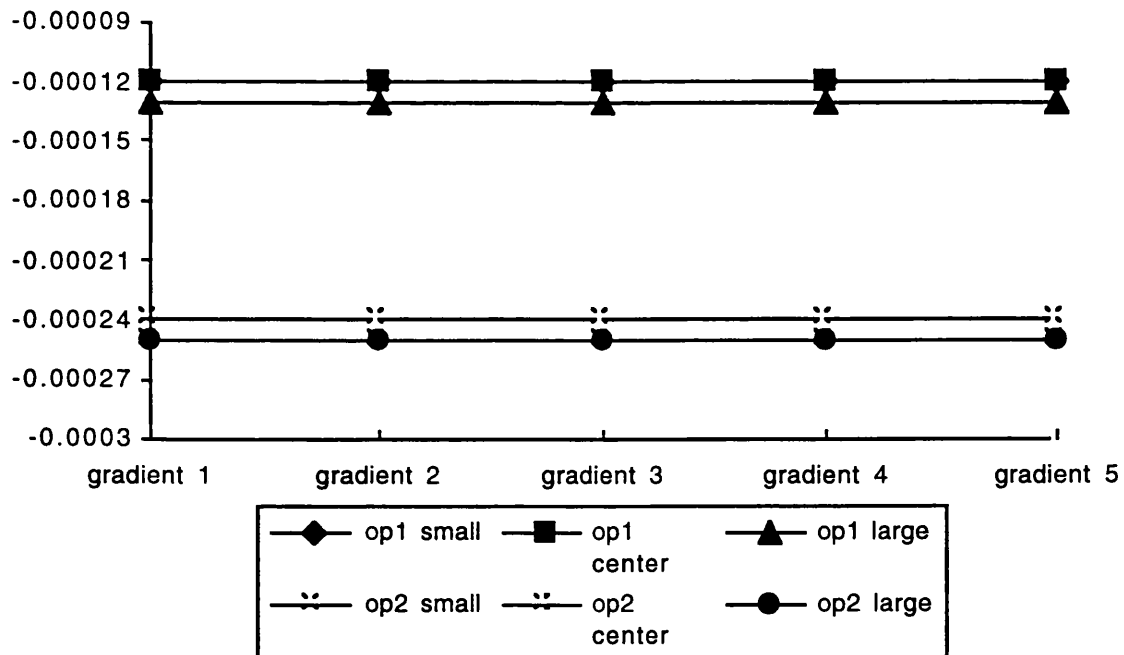


Fig. 8.18: Intersection angle (°) for the opposite side with respect to X coordinate

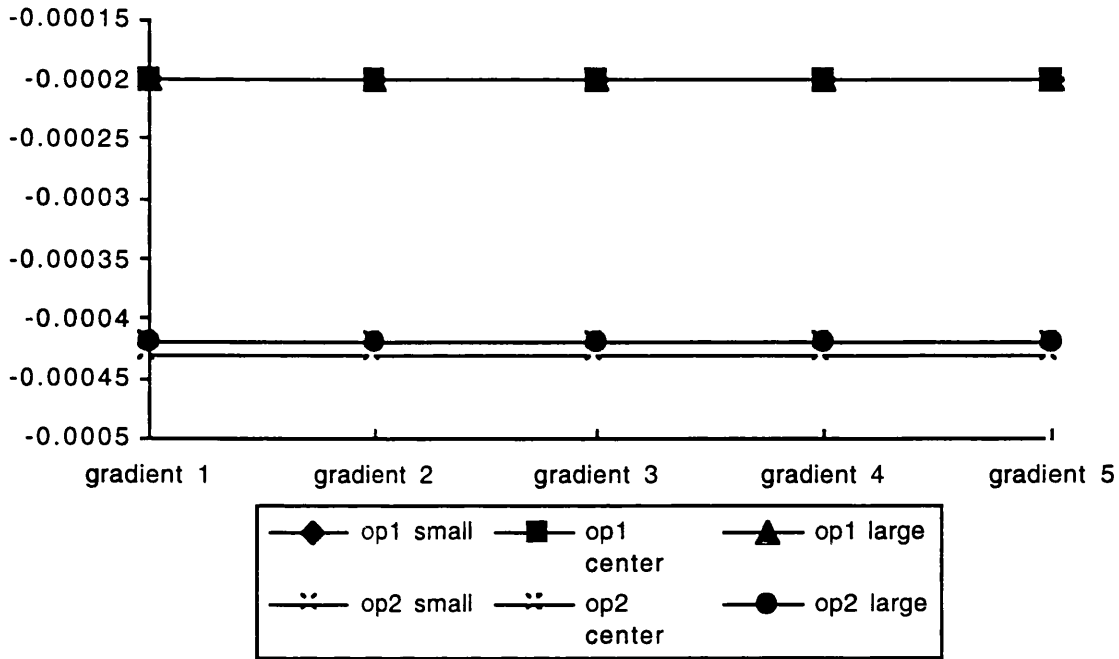


Fig. 8.19: Intersection angle (°) for the opposite side with respect to Y coordinate

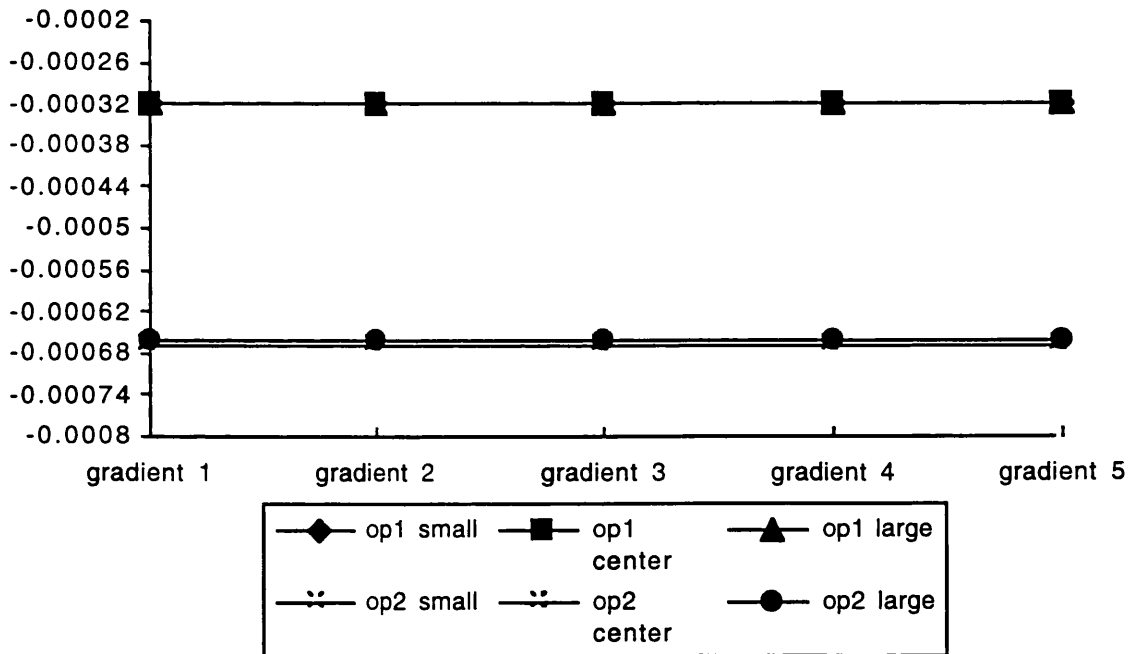


Fig. 8.20: Intersection angle (°) for the opposite side with respect to X+Y coordinate

8.6 Determination of Optimum Constraint Values

The gradient of *range error* and intersection angle for three stereo pairs has been determined. Two programs were developed - **SAR_ANGLE_CHANGE** and **SAR_RANGE_CHANGE** to shift every pixel coordinate as described in the last section. The gradient constant would have been assigned by the program so that no specification of the gradient by the user is required. There are three types of input data; two of which are the data files of the matching coordinate of the stereo pair and their corresponding DEM coordinates. Notice that these DEM coordinates are derived with respect to the inertial coordinate system. The remaining inputting data is the optimum minimum and maximum *constraint values*. The program only deals with points whose *constraint values* are outside the optimum range. For those points whose *constraint values* are smaller than the minimum threshold, this minimum value is used to subtract their *constraint values* and the difference is subsequently divided by the gradient constant to calculate the shifting magnitude individually for each point. The same technique would be implemented for those points whose *constraint values* are larger than the optimum maximum *constraint values*, only that the subtraction difference is calculated in a reversed order. After the shifting magnitude has been obtained, the Y coordinate would shift based on this value directly for the same side, while for the opposite side, the shifting magnitude should be calculated by the X+Y coordinate. Thanks to the additive effect, this shifting magnitude could be applied on X and Y simultaneously by the same value.

The purpose of the above two programs introduced is to enable the resulting *constraint values* of each point to fall in the optimum range specified by the user. Another underlying meaning of the optimum range of *constraint values* is that when the range is approaching zero, it implies the constraint value of all the points will be altered to approach a single value. For instance, if the optimum range of *constraint values* is $v-\gamma$ and $v+\gamma$ when the interval of γ is very small, then the resulting *constraint values* calculated by the program will be very close to v . The objective of this optimum range is to offer the feasibility to deal with various *constraint_height* functions that describe the relationship of the *constraint values* and height deviation. If the nature of this function becomes more close to the one-to-one correspondence, a narrower range width would be required. The determination of optimum range is very important, such that if a given optimum range is too broad then the shifting magnitude is comparatively small, and as a consequence the DEM accuracy could only be marginally improved. In contrast, if the optimum range is very small, it is very crucial to decide the v correctly for the resulting values of all the points approaching to the

value of v . This value of v as well as the optimum range was therefore what we decided next for these three stereo pairs respectively.

From the results obtained according to Table 8.2 ~ 8.7, the relationship was established for *constraint_height* function, such that their correspondence are almost identical for the *constraint_height function* for the same stereo pair. Therefore, the *constraint values* of the small height deviation (-10m ~ 10m) of three data sets were discovered for three pairs separately and listed in Table 8.11 ~ 8.13. The values of intersection angle for the OP1 and OP2 in Table 8.12 and 8.13 were identical among the three data sets. These common ranges or values were next considered as the optimum quantity. Some variations was observed for the same side in Table 8.11 for individual optimum range without significant difference. A broader extent say -14.0 ~ -12.0 could cover these three individual optimum range as a whole. Depending on how closely the *constraint_height function* resembles the one-to-one correspondence, either the optimum range or the optimum value was adopted. As stated earlier, the optimum range would be for the function that was far away from the one-to-one correspondence.

	sa_grid32_tier8_1	sa_grid32_tier8_2	sa_grid32_tier6_1
minimum	-12.01	-12.18	-13.36
maximum	-3.73	-3.48	-3.69
mean	-8.1	-8.0	-8.1

Table 8.11: Range error (m) of small height deviation for the same side

	OP1_grid512_tier2_1	OP1_grid512_tier2_2	OP1_grid512_tier3_1
minimum	44.06	44.06	44.06
maximum	44.14	44.14	44.14
mean	44.09	44.09	44.09

Table 8.12: Intersection angle (°) of small height deviation for the OP1

	OP2_grid512_tier2_1	OP2_grid512_tier2_2	OP2_grid512_tier3_1
minimum	58.71	58.71	58.71
maximum	58.88	58.88	58.88
mean	58.79	58.79	58.79

Table 8.13: Intersection angle (°) of small height deviation for the OP2

Another three smaller data sets were selected in each stereo pair to test both the optimum range and optimum values to check their DEM performances. The reason for implementing both of them was because the *constraint_height function* may not have the characteristics of one-to-one correspondence, and the optimum value probably would not be very effective. Then the DEM accuracy for the optimum range or value were calculated, they were then listed along with the original one in Table 8.14~ 8.16 for three pairs separately.

original (without any constraint)	155.63m
optimum range (-14.0m ~-12.0m)	48.30m
optimum value (-8.0m)	42.27m

Table 8.14: DEM accuracy (m) comparison for the optimum ranges or optimum values of range error for the SA

original (without any constraint)	289.29m
optimum range (44.06° ~44.14°)	665.81m
optimum value (44.09°)	950.76m

Table 8.15: DEM accuracy (m) comparison for the optimum ranges or optimum values of intersection angle (°) for the OP1

original (without any constraint)	444.82m
optimum range (58.71° ~ 58.88°)	314.74m
optimum value (58.79°)	177.78m

Table 8.16: DEM accuracy (m) comparison for the optimum ranges or optimum values of intersection angle for the OP2

From the above three tables, it is obvious that the optimum value was more effective in improving the DEM accuracy for the OP2 and same side than the optimum range, e.g. the DEM accuracy increased from 48.30m to 42.27m for the same side (Table 8.14) and 314.74m to 177.78m for the OP2 (Table 8.16). In contrast, the use of both optimum range and value deteriorated the DEM accuracy for the OP1, with the latter to a greater extent (950.75m compared to 665.81m, Table 8.15). These results illustrate that for OP2 and same side, the *constraint_height function* was comparatively

close to the one-to-one correspondence, for which the use of the optimum value could effectively enhance the DEM accuracy. For this reason, the optimum value of (-8.0m) of *range error* and (58.79°) of intersection angle will be adopted for both the same side and OP2 in the subsequent experiments to enhance the DEM accuracy. For the OP1, neither the optimum range or optimum value was helpful in obtaining greater DEM accuracy, on the contrary, they caused the decrease in accuracy to a greater extent. This is probably due to the relationship between the *constraint values* and height deviation being more complicated and could not be fully described by a simple *constraint_height function*. This is also the reason why the optimum value should give rise to much worse DEM accuracy than the optimum range. As a consequence, the optimum range should be wider to account for the complexity of the *constraint_height function*. This would lead to the question as to which lower or upper *constraint values* would be best suitable for this optimum range. It was decided that an important data set of the manual seed points which had rather good DEM accuracy (30.68m), however, very low coverage (2.4%) could be used. Next, the *constraint values* of the height deviation (-10m ~ 10m) was also found from this data set (43.94° ~ 44.17°). This optimum range was wider than the original one used being 44.06° ~ 44.14° and could be tested. With this new optimum range, the DEM accuracy was found to be increased to 119.01m, better than the original DEM accuracy 289.29m by about 170m. This improvement was satisfactory and therefore this range (43.94°~44.17°) was considered as the optimum range for the OP1.

8.7 Analysis of DEM Accuracy by Geometric Constraint Conditions

The optimum value (-8.0m) for the *range error* was implemented on five data sets of four different types of data (different PDL file, tiers, and speckle-removing imagery) and their DEM accuracies are listed in Table 8.17. This table shows that by employing constraints on the *range error*, the DEM accuracy could be improved tremendously by 85.70m (sa_grid512_tier8_1_MAP) to 138.99m (sa_grid512_tier8_2). It was interesting to see that all the resulting accuracy due to the use of this constraint condition increased to approximately 45m irrespective of the data set is used. For the OP1, the optimum range (43.94°~ 44.17°) of intersection angle was implemented as well on five data sets and their results are shown in Table 8.18. The DEM accuracy improved from 0 (OP1_grid128_tier6_1) to 99.49m (OP1_grid512_tier3_2) and it seemed that the improvement was affected by the coverage. For the lower coverage, the *constraint conditions* was not so effective on DEM accuracy improvement, and this situation was seen most obvious in Table 8.19 for the OP2, where the DEM accuracy improvement at coverage 1.77% and 83.52%

was -2.4m and 288.35m respectively. The cause of this inverse relationship may be because the *constraint_height function* was not originally with property of one-to-one correspondence. Meanwhile, the optimum range or optimum value determined was based on the general observation of different data sets. This constraint condition could be applied to the large coverage because there were comparatively many matching points which satisfied the *constraint_height function* as expected. If the number of matched points decreased significantly, the matched points that would satisfy the function would also proportionally decrease and ultimately lead to worse DEM accuracy.

	DEM ^a	DEM ^b	DEM ^c	coverage	HDSE
sa_grid512_tier8_1	148.32	44.72	103.60	85.80	1.04
sa_grid512_tier8_2	183.50	44.51	138.99	85.74	1.04
sa_grid512_tier6_1	143.35	44.63	98.72	84.94	1.04
sa_grid512_tier8_1_MAP ^d	130.80	45.10	85.70	86.86	1.02
sa_grid512_tier8_1_LEE ^e	133.92	45.14	88.78	84.87	1.02

DEM^a : original DEM accuracy

DEM^b: DEM accuracy with constraint condition

DEM^c: DEM accuracy improvement (DEM^a- DEM^b)

sa_grid512_tier8_1_MAP^d: MAP filtered image instead of the original one

sa_grid512_tier8_1_LEE^e: LEE filtered image instead of the original one

Table 8.17: DEM accuracy (m) and HDSE comparison between the original and constraint condition for the SA

	DEM ^a	DEM ^b	DEM ^c	coverage	HDSE
OP1_grid512_tier2_1	338.54	243.76	94.78	83.61	1.02
OP1_grid512_tier2_2	338.39	246.62	91.77	83.61	1.02
OP1_grid256_tier3_2	315.49	216.00	99.49	20.06	1.03
OP1_grid512_tier3_1	313.62	216.58	97.04	73.26	1.06
OP1_grid128_tier6_1	119.01	119.01	0.0	2.9	1.11

Table 8.18: DEM accuracy (m) and HDSE comparison between the original and constraint condition for the OP1

	DEM ^a	DEM ^b	DEM ^c	coverage	HDSE
OP2_grid512_tier2_1	482.35	194.09	288.26	83.58	1.04
OP2_grid512_tier2_2	482.28	193.93	288.35	83.52	1.04
OP2_grid512_tier3_1	446.78	195.27	251.51	73.01	1.05
OP2_grid128_tier6_1	47.71	50.11	-2.4	1.77	1.70
OP2_grid512_tier4_1	60.28	62.04	-1.76	1.46	1.06

Table 8.19: DEM accuracy (m) and HDSE comparison between the original and constraint condition for the OP2

As well as the DEM accuracy improvement, Tables 8.17 ~ 8.19 also list the individual HDSE for each data set. The relationship between HDSE and the coverage was very similar to that of DEM accuracy and the coverage. The HDSE approached to 1 at higher coverage and when the coverage decreased, the HDSE also gradually deviated from 1 (Table 8.18 and 8.19). This phenomenon illustrates that the constraint condition had the same impact on DEM accuracy improvement and HDSE, which was dependent on the coverage.

From the above three tables, it is seen that the *range error* of the same side was more effective than the intersection angle of the opposite side. For the opposite side, the intersection angle seemed more useful for OP2 since the DEM accuracy could be improved by a maximum of approximately 290m. Although it may lead to negative DEM accuracy improvement in Table 8.19, this could be easily improved according to our analysis by using the optimum range rather than the optimum value.

It is interesting that the above conclusion is quite similar to the geometric condition for intersection. Larger intersection angles would result in better geometric condition for the intersection and lead to greater DEM accuracy and vice versa. It has been determined here that with larger intersection angle for the opposite stereo pair, the constraint condition of using intersection angle would be more effective. As shown in the above three tables, this angle was best for the OP2 and worst for the same side as the constraint condition. For the same side with small intersection angle, this constraint condition could not even be applied to obtain greater DEM accuracy, in conclusion, the larger intersection angle of a stereo pair could provide another advantage of using this intersection angle as a constraint condition would be very effective.

In conclusion, the geometric constraint condition has been applied successfully to significantly improve the DEM accuracy. The optimum value in this chapter was

determined from the relationship of the constraint value and height deviation. It was then our next objective to investigate whether other methods could be used to find the optimum range and value directly. The solution to this task is considered to be related to the header data files of each pair.

For the *range error*, there are two quantities to be considered; the slant range and range distance as shown in Fig. 8.1 and Fig. 8.2. When considering the range distance, it is found that the range time of the RTM_A has longer time interval than that of PRI_A and PRI_D as seen in Appendix B. In addition, the range time of PRI_D and PRI_A are equal, and the difference of range distance is caused only by varied image coordinates. For the stereo pair used, in this study, the offset of X coordinate was larger in PRI_D than in PRI_A (2850 compared to 1695, as seen in Chapter 6), and as a result, the range distance for PRI_D was bigger than that in PRI_A.

The slant range is dependent on the sensor position. For the 5 position vectors provided in the header data file for three stereo pairs, the calculated slant range for RTM_A was the largest one, then the PRI_D and PRI_A was the smallest one. It was interesting to see that the order from the largest to smallest slant range coincided with that of range distance. The two larger slant range and range distance contributed to extensive *range error* for the OP2 as seen in Fig. 8.13. This explanation can also be applied to the small *range error* extent seen in Fig. 8.11 for the OP1. The above discussion illustrates the cause for the different *range error* obtained for these three pairs. From this, it can be concluded that the optimum *range error* was constant for a given same side stereo pair since they were derived from a fixed header data file. For this reason, the chosen optimum *range error* -8.0 used in this study was applicable for the subscene of the stereo pair as well as other areas in this pair of imagery. When considering different other same side stereo pairs, the optimum *range error* would be varied. This variation would be dependent on the header files and could be investigated further by different image pairs.

For the optimum intersection angle, it is harder to define an usual approach, as it is related to 5 sensor positions of the header file. The only solution is by a trial-and-error method, gradually increasing the range until a satisfactory result is obtained. Based on the above discussions, it is concluded that for a given stereo pair with the fixed header data file, the relative relationship between range time as well as the sensor positions would not be altered. As a result, the optimum value of *range error* and intersection angle should be applicable to the whole imagery.

8.8 Intersection Error Modelling by Image Coordinates

In this chapter, another important analysis should be included, which is the evaluation of the intersection errors caused by the image coordinates. In paper [Dowman and Chen, 1996], it has been demonstrated that the errors resulting from the shifting image pixels in X and Y directions are related to the intersection angle and convergence angle. The former is the angle determined by the incidence angle of the stereo pairs, while the latter is the difference between the two orbit track angles of the sensors. In this paper, it was shown that the errors that result from shifting image pixels in the X direction is inversely proportional to the sine value of the intersection angle. The errors that are caused by shifting pixels in the Y direction is inversely proportional to the cosine value of half convergence angle.

In this section, the above relationships of the image coordinates and intersection angle were tested to validate the conclusion that was introduced in the previous paper. To serve this purpose, the techniques mentioned in section 8.5 for evaluating the gradient of *range error* and intersection angle were utilised here. After three groups of different image locations had been extracted for each stereo pair, it was found that the gradients of the errors were almost identical, irrespective of the group type (same group or in the different group) in the three stereo pairs, and the direction in which the pixel was shifting. These gradients of errors with respect to 3 coordinates are listed in Table 8.20 for shifting one pixel in the X direction, and in Table 8.21 for shifting one pixel in the Y direction.

	SA	OP1	OP2
gradient of errors in X	-0.00045	-0.00014	-0.000214
gradient of errors in Y	0.0052	0.0046	0.0076
gradient of errors in Z	-2.78	-2.46	-4.02

Table 8.20: Gradient of errors in intersection with respect to 3 coordinates by shifting one pixel in X direction

	SA	OP1	OP2
gradient of errors in X	366.1	32.30	29.99
gradient of errors in Y	80.50	-5.20	-5.70
gradient of errors in Z	204.40	-1.10	1.60

Table 8.21: Gradient of errors in intersection with respect to 3 coordinates by shifting one pixel in Y direction

Table 8.22 lists the total errors of 3 coordinates caused by shifting one pixel in the X and Y direction for three stereo pairs.

	SA	OP1	OP2
shifting one pixel in X direction	2.78	2.46	4.02
shifting one pixel in Y direction	426.95	30.37	32.84

Table 8.22: Gradient of total errors in intersection of shifting one pixel in X and Y direction

The values listed in the above were found to be fairly consistent with the conclusion made in the previous paper. Table 8.23 lists the convergence angle and intersection angle of all three stereo pairs. With the smaller convergence angle, the errors by shifting pixels in the Y direction should be greater, as it is inversely proportional to the cosine value of the convergence angle. For the same side, which has the smallest convergence angle (2.14°), greater errors were indeed obtained (426.95m), while on the contrary, for the OP1, with the largest convergence angle (27.16°), the intersection error was small at only 30.37m as the intersection error. For the errors caused by shifting the pixel in X direction, due to the errors are inversely proportional to the sine value of the intersection angle, the largest intersection angle would result in greater errors. This is supported by the results obtained for the OP2, for it had the largest intersection angle (58°) and the largest error in the X direction (4.02). The results for the same side and OP1, however, did not fit into the above prediction.

	SA	OP1	OP2
convergence angle	2.14	27.16	21.94
intersection angle	15	46	58

Table 8.23: Convergence angle ($^\circ$) and intersection angle ($^\circ$) for three stereo pairs (after [Chen and Dowman and, 1996])

It could also be seen from Table 8.22 that shifting one pixel in Y direction resulted in a greater influence on the DEM accuracy than in the X direction for all these three stereo pairs. This is because the Y direction is related to the azimuth time. The azimuth time will affect the sensor position, velocity and slant range and consequently the parameters in Doppler equation (5-1~5-2) as well as the range equation (5-3~5-4)

will be altered, ultimately influencing the final solution of intersection. While in the X direction, the range equation would be affected, giving less impact on the coordinates of intersection.

In Table 8.22, it is also observed that for the same side, one pixel shifting in the Y direction would cause greater errors to about 427m. It is for this tremendous deviation that the best DEM accuracy for the same side could not reach within 100m, as seen in Chapter 7. For the opposite side, however, this situation was greatly improved, as the huge errors could be reduced by approximately one fourteenth, from 427m to 30m. For these reasons, it can be found the obvious evidence that the accuracy of the intersection by the opposite stereo pair was better than that of same side stereo pair. While considering the errors by pixels shifting in X direction, the OP2 seemed to have suffered greater impact however without statistical difference (4.02 to 2.46).

8.9 Standard Height Approach

8.9.1 Using the coarse reference DEM

In section 8.7, the effectiveness of the constraint condition to enhance the DEM accuracies was demonstrated for each stereo pair. This effectiveness is achieved by smoothing greatly the height difference of the original DEM which could be easily seen in the Fig. 8.21 (original DEM) and 8.22 (geometric constraint DEM). Unfortunately, this smoothing effect will decrease the accuracy of representation of the terrain features. This could be seen if it is compared to the reference DEM of the same area shown in Fig. 8.23. By comparing Fig. 8.22 and 8.23, it can be seen that while the general tendency of the terrain relief was maintained, the height difference was smoothed out and the breaklines of the terrain was eliminated. This is because the DEM was derived using the *range error* rather than the real height value, therefore, the relationship of the relative height for all the matching points could not be fully presented. To overcome this problem, another approach name the *standard height approach* was proposed here, the concept of which was derived from the results shown in Table 8.20. This table demonstrated this effect by showing that shifting the pixels in range direction, the height (Z coordinate) was influenced to a greater extent than the X and Y coordinates. That is, when shifting the matching points in the range direction, only the height value would be altered. Therefore, the height value could be arbitrarily determined for each individual point. In this approach, the height information, the matching coordinates as well as the derived DEM are required as the

input data, and this height information could be considered as the standard height. On the other hand, the derived DEM could be termed the *initial height*. After calculating the differences between the initial and standard height, the shifting magnitude for the range direction of each single point could be determined. With this shifting magnitude, new matching results could be produced and consequently another DEM could be obtained. The X and Y coordinate of this new derived DEM would be similar to the old DEM, only the height would be very close to the standard height. A program **SAR_DEM_CHANGE** had been developed to carry out the procedures of this *standard height approach*, and the gradient of the Z coordinate in Table 8.20 was adopted to calculate the shifting magnitude, which were -2.78, -2.46 and -4.02 for same side, OP1 and OP2 respectively. The objective of this study was to create the DEM, and the evaluation of the accuracy would be based on the reference DEM of Aix-en-Provence area, which whole data set therefore could not be used as the *standard height* data. Instead, we subsampled every 20 pixels of this data set (grid 50m) to be the new reference DEM (grid 1km) and use it to kriging the *standard height* of each single point for any sets of matching results. The reason for adopting this coarse DEM was to see if this approach could work successfully on the coarse DEM. If it does, this example could be a basis for testing other worldwide available coarse DEM data set. Table 8.24 ~ 8.26 list the DEM accuracies and HDSE of the five data sets shown in Table 8.17 ~ 8.19 respectively.

	DEM ^a	DEM ^b	DEM ^c	coverage	HDSE
sa_grid512_tier8_1	148.32	20.63	127.69	85.80	1.05
sa_grid512_tier8_2	183.50	20.84	162.66	85.74	1.05
sa_grid512_tier6_1	143.35	21.07	122.28	84.94	1.05
sa_grid512_tier8_1_MAP	130.80	20.31	110.49	86.86	1.05
sa_grid512_tier8_1_LEE	133.92	20.18	113.74	84.87	1.05

DEM^a: original DEM accuracy

DEM^b: DEM accuracy with standard approach

DEM^c: DEM accuracy improvement (DEM^a- DEM^b)

Table 8.24: The DEM accuracy (m) and HDSE of five data sets by the standard height approach (coarse reference DEM) for SA

Fig. 8.21: Perspective view of original DEM of same side

DEM accuracy: 148.32m; Coverage: 85.80%
Bottom-Left Corner of DEM (X,Y) : (833.250,3122.750) km
Extent of DEM (X,Y) : (19.350,19.350) km
Height exaggeration factor : 0.2

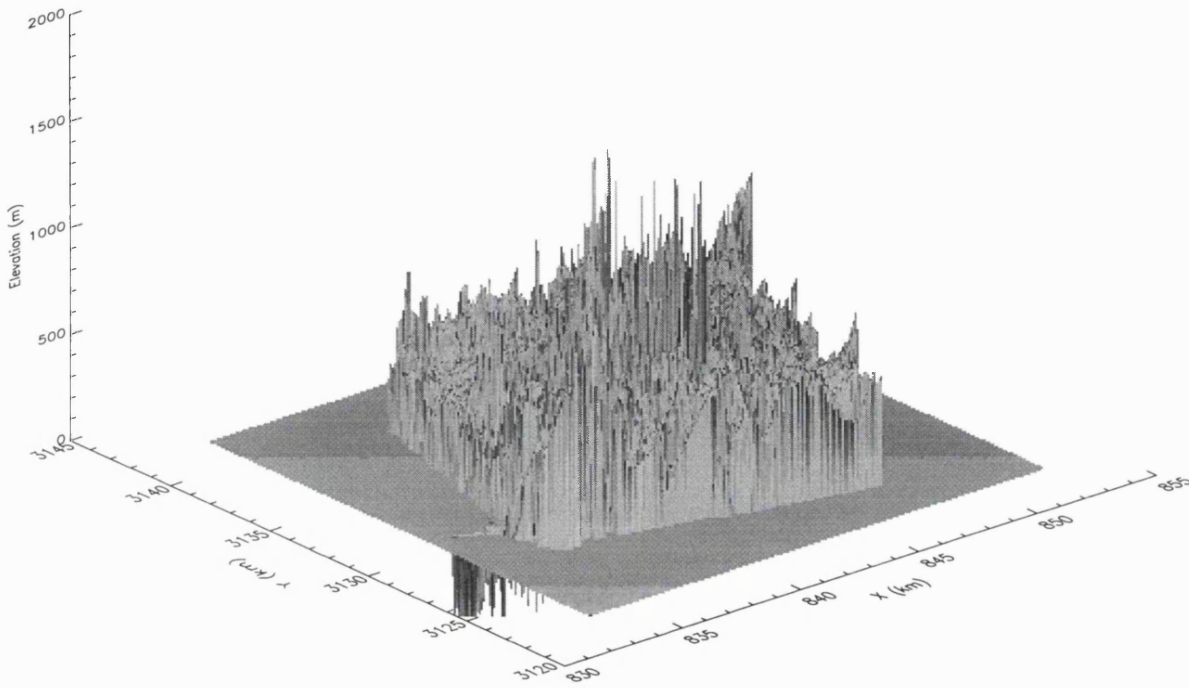


Fig. 8.22: Perspective view of geometric constraint DEM of same side

DEM accuracy:44.72m; Coverage: 85.80%
Bottom-Left Corner of DEM (X,Y) : (834.500,3124.500) km
Extent of DEM (X,Y) : (16.100,15.850) km
Height exaggeration factor : 0.2

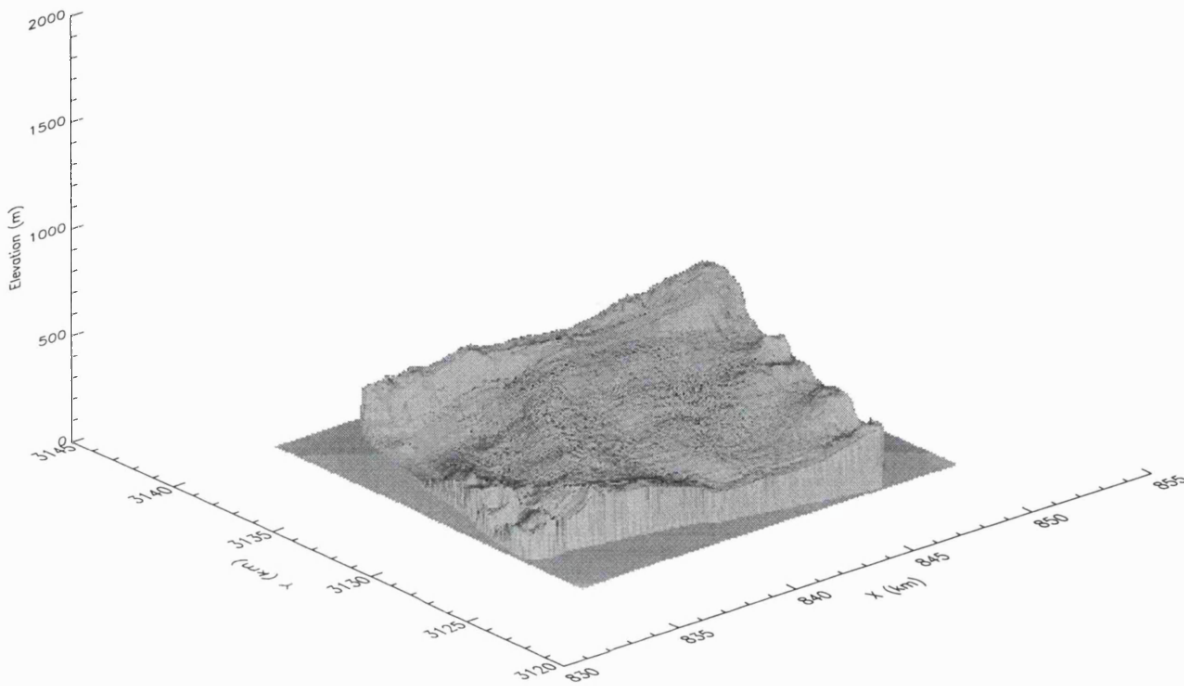


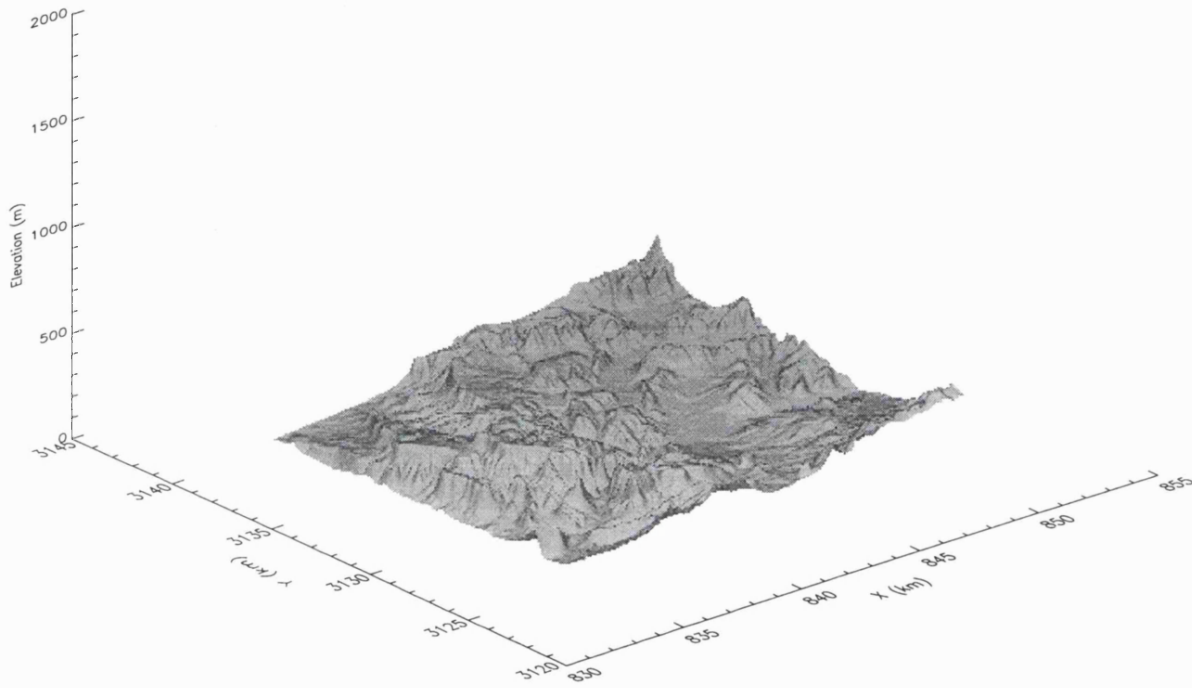
Fig. 8.23: Perspective view of extracted reference Aix-en-Provence DEM

DEM grid: 50m

Bottom-Left Corner of DEM (X,Y) : (834.500,3124.500) km

Extent of DEM (X,Y) : (16.100,15.850) km

Height exaggeration factor : 0.2



	DEM ^a	DEM ^b	DEM ^c	coverage	HDSE
OP1_grid512_tier2_1	338.54	17.89	320.65	83.61	1.06
OP1_grid512_tier2_2	338.39	17.89	320.50	83.61	1.06
OP1_grid512_tier3_1	313.62	15.68	297.94	73.26	1.04
OP1_grid256_tier3_2	315.49	16.76	298.73	20.06	1.04
OP1_grid128_tier6_1	119.01	10.03	108.98	2.9	1.00

Table 8.25: DEM accuracy (m) and HDSE of five data sets by the standard height approach (coarse reference DEM) for OP1

	DEM ^a	DEM ^b	DEM ^c	coverage	HDSE
OP2_grid512_tier2_1	482.35	16.91	465.44	83.58	1.08
OP2_grid512_tier2_2	482.28	16.92	465.36	83.52	1.08
OP2_grid512_tier3_1	446.78	16.25	430.53	73.01	1.07
OP2_grid128_tier6_1	47.71	9.87	37.84	1.77	1.07
OP2_grid512_tier4_1	60.28	8.43	51.85	1.46	1.32

Table 8.26: DEM accuracy (m) and HDSE of five data sets by the standard height approach (coarse reference DEM) for OP2

From the three tables (Table 8.24~ 8.26), it is shown that the DEM accuracies could be greatly increased to a value of approximately 20m for the same side and could reach to 17m for the OP2. The advantage of this approach being a lower coverage, the improvement of DEM accuracy was still effective in contrast to the result shown in Table 8.17 ~ 8.19 due to the use of *constraint conditions*. Considering the HDSE, no significant difference was observed when compared with those in Table 8.17 ~ 8.19; however, under lower coverage, the HDSE did not increase so greatly as seen for the *constraint conditions*. For this approach, the only special concern was the maintenance of any changes in terrain features. The 3D terrain appearances of the DEM derived of the data sa_grid32_tier8_1 by this approach is shown in Fig. 8.24. In this figure, the variation of the terrain feature resemble more closely to the reference DEM. This was expected since the *standard height approach* utilises the height value for each single point directly and as a result, the variation of terrain feature could be better maintained.

With respect to DEM accuracies, HDSE as well as the maintenance of terrain features, the *standard height approach* was determined to be a better choice. However, the performance of this approach is dependent on the accuracies of the

standard height of each point. In this study, this *standard height* was obtained by kriging the 1km grid coarse DEM, which could also be alternatively obtained by other DEM data set. With smaller interval of grid, higher DEM accuracies could be achieved.

8.9.2 Using new derived DEM

The hypothesis presented in the last section was further tested to examine the relationship between grid intervals of reference DEM and derived DEM accuracy here. The DEM of sa_grid512_tier8_2 (44.51m) obtained by using the *range error* was selected as the new reference DEM (see Table 8.17) as it was the best among all the derived DEM in this study. This new reference DEM was further subsampled at the grid 50m the same as the original Aix-en-Provence DEM. The same techniques employed in previous section were adopted, where the *standard height* of each single point was calculated by kriging this new reference DEM. The results are shown in Table 8.27~ 8.29 for the three stereo pairs respectively.

	DEM ^a	DEM ^b	DEM ^c	coverage	HDSE
sa_grid512_tier8_1	148.32	51.75	96.57	85.80	1.02
sa_grid512_tier8_2	183.50	51.57	131.93	85.74	1.02
sa_grid512_tier6_1	143.35	51.58	91.77	84.94	1.02
sa_grid512_tier8_1_MAP	130.80	46.77	84.03	86.86	1.03
sa_grid512_tier8_1_LEE	133.92	46.67	87.25	84.87	1.03

DEM^a : original DEM accuracy

DEM^b: DEM accuracy with standard approach

DEM^c: DEM accuracy improvement (DEM^a- DEM^b)

Table 8.27: The DEM accuracy (m) and HDSE of five data sets by the standard height approach (new reference DEM) for SA

	DEM ^a	DEM ^b	DEM ^c	coverage	HDSE
OP1_grid512_tier2_1	338.54	12.79	325.75	83.61	1.00
OP1_grid512_tier2_2	338.39	12.77	325.62	83.61	1.00
OP1_grid512_tier3_2	315.49	12.23	303.26	73.26	1.00
OP1_grid256_tier3_2	313.62	12.68	300.94	20.06	1.00
OP1_grid128_tier6_1	119.01	10.41	108.60	2.9	1.00

Table 8.28: The DEM accuracy (m) and HDSE of five data sets by the standard height approach (new reference DEM) for OP1

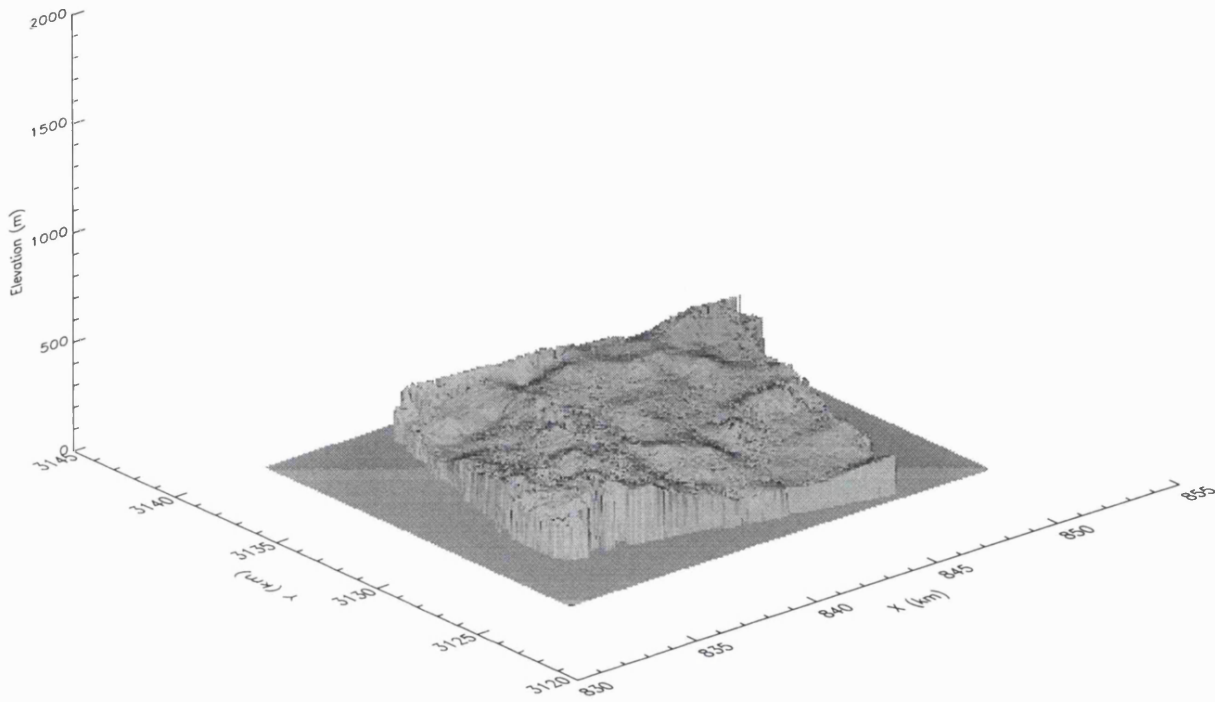
Fig. 8.24: Perspective view of standard height approach DEM of same side

DEM accuracy: 20.63m

Bottom-Left Corner of DEM (X,Y) : (833.700,3124.900) km

Extent of DEM (X,Y) : (17.550,15.250) km

Height exaggeration factor 0.2



	DEM ^a	DEM ^b	DEM ^c	coverage	HDSE
OP2_grid512_tier2_1	482.35	16.79	465.56	83.58	1.17
OP2_grid512_tier2_2	482.28	16.46	465.82	83.52	1.18
OP2_grid512_tier3_1	446.78	15.06	431.72	73.01	1.20
OP2_grid128_tier6_1	47.71	12.49	35.22	1.77	1.28
OP2_grid512_tier4_1	60.28	7.70	52.58	1.46	1.17

Table 8.29: The DEM accuracy (m) and HDSE of five data sets by the standard height approach (new reference DEM) for OP2

When observing the results shown in the above three tables, it was found that the DEM accuracy could also be greatly improved as previously noticed when using the coarse reference DEM (Table 8.24~ 8.26). Comparing these results with those listed in Table 8.24~ 8.26, the DEM accuracy for same side was reduced by approximately 30m (from about 20m to 50m), but it was increased by about 5m (from about 18m to 13m) in the case of OP1. In contrast, OP2 did not show any significant difference. Although the DEM accuracy in general did not increase as previously seen (Table 8.24~ 8.26), overall, better DEM was obtained when compared with the original DEM. The exceptional feature illustrated in this section is that the reference DEM used was derived in this study so that no external DEM was required. This is rather important since it demonstrates that it is possible to obtain the satisfactory DEM, especially for the opposite side, by using both algorithms introduced in this chapter.

8.10 Analysis of Success of Object Domain Approach

The improvement of DEM accuracies achieved in this chapter was significantly greater than in Chapter 7 by adopting the object domain approach. The underlying reasons is that the two approaches tested in this chapter utilise the relationship of the target coordinates in the object space and the matching coordinates in the image space.

In this study, the satellite orbit positions was determined by the cubic spline interpolation from the five sensor positions offered by the header data file as described in Chapter 5. The size of the subscene used in this study was relatively small compared to the whole scene, hence the cubic spline can be approximated by a straight line, and consequently the sensor positions could be regulated by the linear variation. In other words, the relationship of the coordinates of the object space and image space was established on a linear basis. From this basis, the *range error*, intersection angle

as well as the *standard height* could be well estimated from the image coordinates. Once the optimum value of *range error*, intersection angle and *standard height* were determined, the shifting magnitude for the matching coordinates in the image could also be easily calculated. From this corrected matching coordinates, the optimum value of *range error*, intersection angle and *standard height* could be produced and consequently a better DEM could be achieved.

8.11 Intersection Using Control Points

So far in this chapter, all the intersection results were obtained using the ephemeris data from the original header file of ERS-1 which does not include information on control points. ERS-1 is special in this respect that it could offer these information utilised in this research, however, the ephemeris data of the latest satellite such as RADARSAT or JERS-1 in contrast may not be able to provide. Therefore, it is of great interest to know whether control points maybe required for intersection to supplement the insufficient ephemeris data and subsequently their possible impact on the DEM accuracy.

8.11.1 Control points consideration

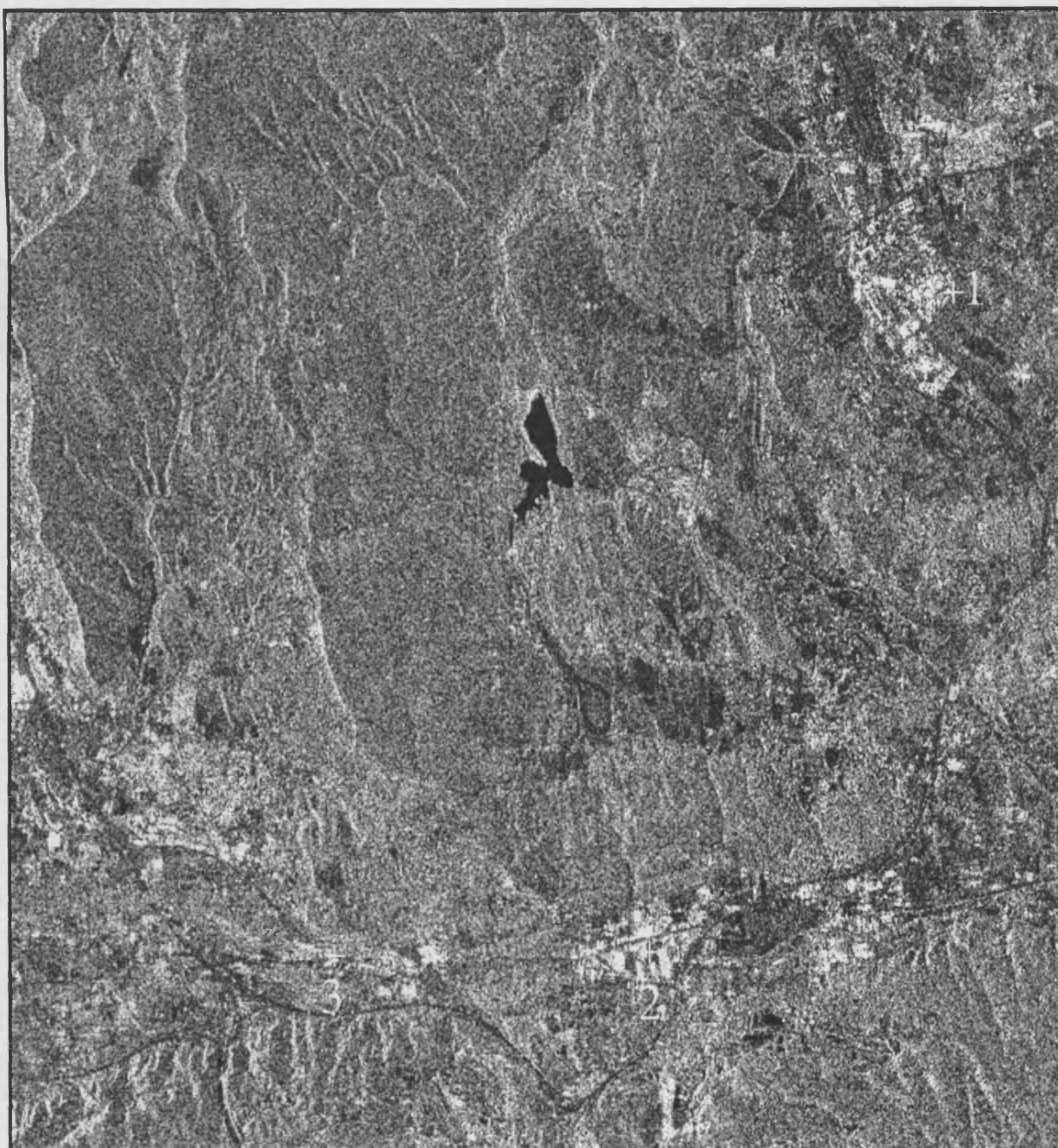
In the intersection process, the determination of the azimuth or range time is rather crucial, as azimuth time will give the sensor position, velocity and the range time will give the value of slant range which will be subsequently used to constitute the Doppler and range equation. With these two equations, the unknowns of the terrain height could be obtained as described in Chapter 5. There are three sets of azimuth and range time provided by ERS-1. The individual azimuth and range time of matching points would be obtained from the cubic spline interpolation of these original azimuth and range time. The purpose of the control points is to give extra azimuth or range times apart from the original 3 sets provided. In addition, the range shift introduced in [Chen and Dowman, 1996] could also be decreased by using the control points. When considering the azimuth time, which is related to the Y coordinate, based on the results shown in Table 8.21 as well as the conclusion made in section 8.8, it was said to significantly influence the results of the intersection. Unfortunately, the control points with respect to this azimuth direction could not be easily utilised since the azimuth time of these control points are difficult to determine. The Doppler equation is the condition that could be used to solve the azimuth time which specifies that the slant range vectors must be perpendicular to the sensor

velocity vectors as shown in Fig. 8.1 and 8.2. From this perpendicular condition, however, the correct sensor position and velocity for each control point still could not be calculated for there are 6 unknowns (3 sensor position and 3 sensor velocity respectively), while only three equations. Without these sensor positions and velocity, the azimuth time for the control points could not be obtained. In contrast, the range time is only related to the slant range and if the slant range of the control points is known, the range time could be subsequently calculated. Therefore, in this section the positions of control points were only used to constrain the range direction.

8.11.2 Range time calculation

As decided in the above section, the control points would be selected in the range direction. These control points should be identified clearly on the images and on the map. In addition, the range position of the control points should be evenly distributed in the imagery so that the range constraint could be effective on the whole imagery. However, this is the ideal situation and can't be easily achieved. To try to satisfy both the above two conditions, three identical control points were manually selected on the RTM_A, PRI_A, and PRI_D respectively. Fig. 8.25 shows these the locations of three control points on the RTM_A imagery and Table 8.30 gives the map coordinates of Lambert Zone 3 of these three control points. The pixel position on the range and azimuth direction were then recorded. The recorded position of the azimuth direction was further computed to obtain the sensor position, while the ground coordinates of the control points could be read out from the map. With the ground coordinate and sensor position, the slant range of each control point could be calculated. With these slant ranges, the corresponding range time could also be estimated for each control point. The range positions of control points in the image along with their corresponding range times were then input into the original header data file (Appendix B). Appendix C shows these new header data files for each of the three images respectively. From the comparison of Appendix B and C on a specified imagery, it can be easily recognised that the information of the two header files were identical, except that the number of range time increased from 3 (Appendix B) to 6 (Appendix C). That is, 3 extra range time was given by the 3 control points. To distinguish these, the header data files in Appendix C were named *control header data files*, while those in Appendix B were named *original header data files* for the remainder of this study.

Fig. 8.25: 3 control points locations on RTM_A image



	No.	X	Y	Z
control points	1	844800.0	3128630.0	216.0
	2	856750.0	3136630.0	134.0
	3	839700.0	3128100.0	97.0

Table 8.30: Lambert Zone 3 coordinates of 3 control points

8.11.3 DEM accuracy analysis

With these *control header data files*, the five data sets of these three stereo pairs that were used in this chapter are tested to obtain the 3D information of the matching points. The results are shown in Table 8.31~ 8.33 for same side, OP1 and OP2 respectively. From these three tables, it could be seen that the use of control points caused decreased DEM accuracies. The amount of reduction was most severe for OP2 (approximately 130m) and was slightest for OP1 (approximately 5m). Considering the HDSE, its value for the same side was dramatically increased. As the resulting DEM accuracies did not improve as expected, this study investigated further the cause of deteriorating DEM accuracy by these control points. This was carried out for the benefits for other fellow researchers who use the same model without the ephemeris data, in that the disadvantages of utilising control points observed could be avoided and substituted by other methods of incorporation of the control points.

	DEM ^a	DEM ^b	DEM ^c	coverage	HDSE
sa_grid512_tier8_1	148.32	182.59	-34.27	85.80	1.98
sa_grid512_tier8_2	183.50	202.40	-18.90	85.74	1.79
sa_grid512_tier6_1	143.35	170.40	-27.05	84.94	2.13
sa_grid512_tier8_1_MAP	130.80	157.69	-26.89	86.86	1.33
sa_grid512_tier8_1_LEE	133.92	167.04	-33.12	84.87	1.32

DEM^a : original DEM accuracy

DEM^b: DEM accuracy with control header data file

DEM^c: DEM accuracy improvement (DEM^a- DEM^b)

Table 8.31: The DEM accuracy (m) and HDSE of five data sets by using 3 control points for SA

	DEM ^a	DEM ^b	DEM ^c	coverage	HDSE
OP1_grid512_tier2_1	338.54	342.94	-4.4	83.61	1.04
OP1_grid512_tier2_2	338.39	345.05	-6.6	83.61	1.04
OP1_grid512_tier3_2	315.49	317.74	-2.25	73.26	1.05
OP1_grid256_tier3_2	313.62	319.00	-5.38	20.06	1.05
OP1_grid128_tier6_1	119.01	111.70	7.31	2.9	1.36

Table 8.32: The DEM accuracy (m) and HDSE of five data sets by using 3 control points for OP1

	DEM ^a	DEM ^b	DEM ^c	coverage	HDSE
OP2_grid512_tier2_1	482.35	609.67	-127.32	83.58	1.01
OP2_grid512_tier2_2	482.28	609.67	-127.39	83.52	1.01
OP2_grid512_tier3_1	446.78	583.59	-136.81	73.01	1.01
OP2_grid128_tier6_1	47.71	148.28	-100.57	1.77	1.02
OP2_grid512_tier4_1	60.28	60.28	0.0	1.46	1.05

Table 8.33: The DEM accuracy (m) and HDSE of five data sets by using 3 control points for OP2

The impact of these control points on the intersection were further examined for three stereo pairs respectively (Table 8.34–8.36). It is worth noticing from these tables, that the X and Y ground coordinates of 3 control points using *control header data file* were almost identical as those using the *original header data files* and only Z values were altered. This situation was the same as in the *standard height approach* (section 8.9) for which the pixels were only shifted only in the range direction, compared to the control points studied here which were used to constraint only in the range direction as well. The height deviation obtained by the use of the control header data file was improved as easily seen in these three tables. From this discovery, in addition, it can be concluded that any procedures that merely change the slant range values of the matching points would not alter the resulting X and Y coordinates of the intersection, since only height information would be affected.

		X	Y	Z	height deviation
control point 1	File 1 ^a	842734.84	3128122.66	-981.05	-1157.55
	File 2 ^b	842734.85	3128122.57	-933.83	-1110.33
control point 2	File 1	843309.61	3135837.66	-1797.56	-1974.25
	File 2	843309.61	3135837.64	-1789.61	-1966.30
control point 3	File 1	837985.32	3127021.61	-1165.53	-1242.50
	File 2	837985.36	3127021.17	-926.82	-1003.81

File 1^a: original header data file

File 2^b: control header data file

Table 8.34: The ground coordinates of the intersection of control points using the original and control header data file for SA.

		X	Y	Z	height deviation
control point 1	File 1 ^a	844773.97	3128643.23	186.20	-33.8
	File 2 ^b	844773.97	3128643.17	217.59	-2.41
control point 2	File 1	846621.09	3136682.48	105.68	-30.74
	File 2	846622.00	3136682.41	140.47	4.05
control point 3	File 1	841625.46	3127952.45	82.30	-77.01
	File 2	841625.46	3127952.52	43.85	-115.48

Table 8.35: The ground coordinates of the intersection of control points using the original and control header data file for OP1.

		X	Y	Z	height deviation
control point 1	File 1 ^a	844955.15	3128611.32	243.65	24.34
	File 2 ^b	844955.15	3128611.35	225.10	5.79
control point 2	File 1	846915.99	3136630.68	153.04	6.75
	File 2	846915.99	3136630.70	146.22	-0.07
control point 3	File 1	841948.83	3127896.15	-172.56	-322.51
	File 2	841948.85	3127895.40	228.01	78.07

Table 8.36: The ground coordinates of the intersection of control points using the original and control header data file for OP2

Observing the DEM value derived from using *the control header data file*, other important discoveries were made. It was found that the height value of most points were increased. This increasing magnitude was defined here as the Systematic

Increasing Height Effects (SIHE), which is proportional to the gradient introduced in Table 8.20. This table lists the gradient of three stereo pairs with respect to shifting one pixel in the range direction. From this table, it can be deduced that the SIHE should be more severe in the OP2 but slightest in the OP1. These could be found evident in the results shown in Table 8.37~ 8.39. In each of these three tables, three data sets were computed for the three stereo pairs respectively for the height difference when using the *control* and *original header data file*. The average value of SIHE for the OP2 was approximately 159m, which was greater than that of OP1 at ~34m. This observation was consistent with the amount of DEM accuracy deterioration observed earlier. Remember it was previously stated that the gradient in theory is also related to the intersection angle of the orbits, so that for larger intersection angle, the gradient would be larger since OP2 had the greatest intersection angle (58°), its SIHE would be expected to be the greatest.

It can be concluded that control data points are unable to improve the DEM accuracy. Rather, DEM accuracy was decreased because these control points could cause the SIHE. However, for areas with greater terrain relief, the control points may be advantageous for the final intersection results. Regarding the SIHE, it is determined to be dependent on the intersection angle of the stereo pairs, which variable is further linked to their incidence angle and the orbit variation. The establishment of the relationship between the SIHE and the intersection angle of the stereo pair, as well as their individual incidence angle waited to be further investigated in future studies.

The initial requirements for this method of incorporating the control points information to succeed is that the azimuth time must be correct. The correct timing of azimuth is dependent on the header data offered from ERS-1. However, this method can't be used on other satellite images without orbital information. Therefore, other alternative methods of utilising the control points information should be developed by other researchers in future.

	No.	mean	min.	max.
sa_grid512_tier8_1	224924	101.65	-138.39	306.14
sa_grid512_tier8_2	224754	101.76	-138.40	306.14
sa_grid512_tier6_1	222673	102.01	-138.35	306.15

Table 8.37: Statistics of height difference(m) between the DEM with and without control points for SA

	No.	mean	min.	max.
OP1_grid512_tier2_1	219181	34.56	-75.66	151.77
OP1_grid512_tier2_2	219177	34.57	-75.80	164.34
OP1_grid512_tier3_1	192048	27.34	-75.93	140.75

Table 8.38: Statistics of height difference (m) between the DEM with and without control points for OP1

	No.	mean	min.	max.
OP2_grid512_tier2_1	219096	158.87	-169.94	476.04
OP2_grid512_tier2_2	218953	158.79	-170.00	476.60
OP2_grid512_tier3_1	191398	152.45	-172.09	477.32

Table 8.39: Statistics of height difference (m) between the DEM with and without control points for OP2

8.12 Summary

In this chapter, two approaches based on the object domain utilised the constraint condition and *standard height* to enhance the DEM accuracy. For the geometric *constraint conditions*, the *range error* were suitable for the same side while intersection angle was for the opposite side. The decision was based on the analysis of the results after testing with three different methods. By determining the optimum value of *range error* and intersection angle, the image coordinate could be shifted to give rise to better DEMs. The results showed that the improvement could be made by approximately 288m (OP2_grid512_tier2_1). Unfortunately, under lower coverage, it was not so effective and any variation of the terrain features could not be followed and shown with accuracy.

The *standard height approach* made use of the direct relationship of height values and image coordinates to shift the X coordinate. The two reference data sets were tested here. With the coarse DEM of grid 1km that was subsampled from the original Aix-en-Provence reference DEM, it was found to be better than that obtained when using the geometric constraint method for not only was a greater improvement in DEM accuracies observed, but also it would still maintain the terrain features. With the second reference data that derived from this study, the DEM accuracy was also improved. It was demonstrated that without an external DEM, greater DEM accuracy

could also be obtained by the *standard height approach*. Notice here that the performance of this approach was related to the input reference DEM data. The reasons for the success of the object domain approach were analysed and it was concluded that it was due to the linear relationship of the coordinates of the image space and object space.

The last section evaluated the impacts of the control points on the intersection coordinates. It was concluded that control points would cause SIHE which was responsible for the deterioration of the DEM accuracy for the three stereo pairs. It also illustrated that this SIHE was linked to the intersection angle, such that with greater intersection angle, the SIHE would become more pronounced.

CHAPTER 9

Conclusion

The ultimate aim of this study was to derive DEMs with greater accuracy from SAR imagery in an automatic manner. This was approached by two methods, namely the pyramidal matching algorithm (Chapter 7) and the intersection algorithm (Chapter 8). For the pyramidal matching, an area-based region growing algorithm was employed in an image pyramid to obtain images with dense coverage, while deriving higher accuracy automatically. Several fundamental factors of this matching method that may affect the resulting DEM were investigated. Notice that for this method, the random seed points were utilised, unlike the normal adoption of manual seed points. The function of these random seed points as well as their possible influence were also discussed in Chapter 7. The analytic method, which utilises the Doppler and range equations to obtain the terrain ground coordinates, was adopted as part of an intersection strategy. This method requires the header data files and from this readily available information, DEM accuracy could be increased significantly (Chapter 8). Apart from experimental details, the background and theories regarding the matching algorithm (Chapter 4) and the intersection algorithm (Chapter 5) were also covered in this study.

9.1 Pyramidal Matching Algorithm

In Chapter 7, various aspects related to the pyramidal stereo matching were analysed and discussed, based on the following four main issues : (1) determination of matching strategy, (2) development of the blunder-removing filter, (3) analysis of the techniques of seed points selection, as well as (4) examination of the advantages of using the multi-resolution image. These four issues were interrelated and could be investigated by studying several common parameters. The main purpose of this chapter was to establish a systematic approach by which these parameters could be selected and ultimately answer the questions regarding the four issues.

Two strategies were introduced which corresponded to two individual PDL files. These two PDL files were given the same parameters with the only difference that strategy 2 employed both **GRUEN** and **GRUENS** on each tier, while for strategy 1, only **GRUENS** was used as the matching mechanism. It was observed

that for strategy 1, the seed points were not subjected to any further refining process prior to growing other new seed points. Extra refining process could be accomplished if desired by running additional **GRUEN** on each tier. Next, a modified **GRUENS** programme named **GRUENS_SEED** was developed. The function of this new programme was identical to the original one except that four extra columns were added in the output. These four extra values aided the tracking of each seed point on each tier, so that the number of ERSP (Effective Random Seed Points), ORSE (Original Random Seed Effects) and GRSE (Growing Random Seed Effects) could be determined. The examination of both ORSE and GRSE was important, since they both could deteriorate the matching results. The former results directly from the original random seed points, while the latter comes from their growing seed points. The value of ERSP is affected by both the grid number and the number of image tiers, and itself in turn influences both ORSE and GRSE with a positive linear relationship. When ERSP increases with decreasing number of image tiers under the same grid number, GRSE would increase to affect the matching results. It was due to this relationship that more image tiers should be used in the pyramidal matching to decrease the negative GRSE, as illustrated in Table 7.8. With respect to the strategy, as a result of the extra refining process employed, the ORSE was greatly reduced for strategy 2. This could be seen in Table 7.3, such that the greatest ORSE could reach 79.67m for strategy 1 under grid number of 128, compared to 0.61m for strategy 2. With respect to the GRSE, strategy 2 was more likely to grow other seed points from the original random seed points with less impact on the final DEM accuracy (Table 7.4 and 7.5). The comparison of the DEM accuracy of these two strategies was made by means of the values of the grand disparity sum. It was discovered that because the refining process would reduce the grand disparity sum, strategy 2 gave rise to a less accurate DEM. However, when comparing HDSE, strategy 2 performed better since it produced less HDSE, and it was concluded that strategy 1 increased the terrain height systematically by its larger grand disparity sum.

The *disparity sum* was further employed to remove the blunders on each tier in the matching (section 7.7). It was discovered that the *disparity sum* was related to the number of (+) or (-) height deviation. By dynamic determination of the threshold values for each data set on each tier, the DEM accuracy could be enhanced. It was also observed that the lower threshold of *disparity sum* was more effective in removing the blunders compared to the upper boundary, and this was validated by using the progressive approach to test on different percentages of lower and upper boundaries. The multiple effects of a combination of lower and upper boundaries on the DEM accuracy were also investigated here. The enhancement of DEM accuracy was approximately 5m on average for the three data sets (Fig. 7.14).

The relationship between the *disparity sum* and the height deviation, as well as the effectiveness of the lower boundary to remove blunders, encouraged further research to choose the optimum seed points. Since the region-growing process proceeded in a non-deterministic manner, even under the same parameters with the same number of seed points, the results obtained would not be identical. Due to this problem, the use of the smallest average eigenvalue or NCC to select the optimum seed points was not successful. However, it was found that the *disparity sum* was linked between each tier and it was thought that this property could be utilised to select the seed points, such that the points with the smallest average *disparity sum* were named disparity seed points. With these seed points, and the application of the lower threshold value of the disparity sum, greater DEM accuracy was achieved. In section 7.8, a new **SEED_GRUEN** programme was developed to simulate the **CHEOPS** and repetitively tested on 300 sets of random seed points to obtain the disparity seed points. Following that, the lower boundary was implemented again, and the resulting DEM accuracy showed an improvement of 16m on average for all three data sets (Fig. 7.17), significantly better than the 5m DEM mentioned earlier. This result was consistent to the conclusion made in section 7.7, which stated that the threshold value should be dynamically determined. In section 7.9, the advantages of the pyramidal stereo matching was analysed. This was achieved by comparing the results of the original and multi-resolution images, for which the manual and random seed points were used respectively. The comparisons were made by taking the advantage of one of the **GRUEN_SEED** extra four outputs, the *seed_generation*, as a measure quantity. It was found that the results on the original image were related to the *seed_generation* of the seed points with an inverse proportional relationship named OIE. Whether this effect is specific for SAR images waits further investigations. The evaluation of matching performance on the opposite-side image was shown in section 7.10. The results showed that the matching coverage was greatly decreased due to the different image characteristics as described in Chapter 3. Despite the fact that the coverage could be increased to the standard level by employing fewer image tiers, the DEM accuracy actually decreased tremendously as the number of image tiers decreased, therefore suggesting that other sophisticated image processing techniques should be applied prior to the matching. The use of a speckle-reduction filter on the pyramidal matching was examined in section 7.11. Two common filters, the LEE and MAP filter, were used and the results showed that the coverage as well as the DEM accuracy were both improved.

9.2 Intersection Algorithm

In this study, in addition to utilising the algorithm applied on the image space, another approach was developed based on the object space to enhance the DEM accuracy without decreasing the matching coverage. This work was presented in Chapter 8 and involved the employment of two methods, namely the geometric constraint condition approach and the *standard height approach*.

The range error and intersection angle were the two geometric constraint conditions applied for the geometric constraint condition approach. The range errors were derived from the range equations (Equation 5-3 and 5-4) for intersection, while the intersection angles were determined by general observations of the matching points. However, not both conditions were found suitable for each stereo pair. It was observed based on analysing the results obtained by testing with three different methods that, for the same side pair the range error was preferred, while for the opposite side the intersection angle should be adopted. Also discovered was the fact that the DEM accuracy could be greatly increased by specifying the optimum range or optimum value for the range error or intersection angle. This finding was supported by results shown in Table 8.18~20, for which five different sets of coverage data were obtained for each of the three stereo pairs. The improvement was up to 138.99m (Table 8.17, sa_grid512_tier8_2) for the same side, 99.49m (Table 8.18, OP1_grid256_tier3_2) for OP1 and 288.35m for OP2 (Table 8.19, OP2_grid512_tier2_2). It was also observed that these improvements were dependent on the coverage as well, such that the increase became more obvious for larger coverages.

When comparing the constraints-derived DEM to the original DEM, although greater accuracy could be achieved for the former, it was discovered that the constraint conditions effectively smoothed the terrain heights (Fig. 8.21 and 8.22). This smoothing effects unfortunately would eliminate many terrain features, as seen by comparing Fig. 8.22 and 8.23. For this reason, another *standard height approach*, which required the initial DEM information, was proposed to maintain the terrain features. Its effectiveness was subsequently tested on two different reference DEM in this study. The first reference DEM was the coarse one (grid 1km) derived from subsampling every 20 pixels of the original reference DEM (Aix-en-Provence). The second one was created in this study by using constraint conditions on data set sa_grid512_tier8_2 and was subsampled at a grid of 50m, for which the DEM accuracy was 44.51m (Table 8.17). The results for the coarse DEM are shown in Table 8.24~26, where its improvement was seen greater than that obtained using the

constraint conditions, reaching for the same side a maximum of 162.66m (Table 8.24, sa_grid512_tier8_2), for OP1 320.65m (Table 8.25, OP1_grid512_tier2_1) and for OP2 465.44m (Table 8.26, OP2_grid512_tier2_1). In addition, the terrain features could be better maintained when using the coarse DEM (Fig. 8.24) . The results obtained using the second reference DEM were shown in Table 8.27~29. Compared with the first coarse reference DEM, the same side stereo pair performed worse with a maximum DEM reaching only 131.93m (Table 8.27, sa_grid512_tier8_2). In contrast, or both opposite side pairs, the second DEM could give rise to better results, for OP1 at 325.75m (Table 8.28, OP1_grid512_tier2_1) and OP2 at 465.82m (Table 8.29, OP2_grid512_tier2_2). The remarkable feature of this *standard height approach* utilising the second reference DEM was that as long as the SAR image was available, no external reference DEM was required to derive satisfactory DEM for any region on Earth. To summarise the above mentioned DEM accuracy and improvement when using the new methods in Chapter 8 by different strategies, Table 9.1 illustate these data plus the table and page number that they appear. For the comparions, the actual DEM accuracy that can be reached by these strategies are also listed here.

strategy		Actual DEM accuracy (m)	improvement (m)	table	page No.
geometric constraint	SA	44.51	138.99	8.17	171
	OP1	216.00	99.49	8.18	171
	OP2	193.95	288.35	8.19	172
standard height (coarse DEM)	SA	20.84	162.66	8.24	177
	OP1	17.89	320.65	8.25	181
	OP2	16.91	465.44	8.26	181
standard height (grid 50m DEM)	SA	51.57	131.93	8.27	182
	OP1	12.79	325.75	8.28	182
	OP2	16.46	465.82	8.29	184

Table 9.1: Summary of actual DEM accuracy and improvement when using the new methods in Chapter 8

Compared to the improvement obtained by applying the matching algorithm on the image space introduced in Chapter 7, the improvement made using the algorithm from the object space was always greater regardless of the approach employed. This success was due to the linear relationship observed between the image pixel and the ground coordinates, so that the estimation of the impact of shifting the image pixel on the terrain height could be quite reliable. This linear variation was due to the fact that

the orbital path could be approximated by a straight line, and the sensor position and velocity could be therefore predicted accurately by altering the image pixels.

The intersection by incorporating the control point information was also investigated in this study. This was achieved by calculating the range time for each control point and providing these range times in the original header data file. These new control header data files were subsequently used for intersection. Unfortunately, the obtained DEM accuracy was not as good as expected, and this was thought to be due to the SIHE (Systematic Increasing Height Effects) that occurred. The SIHE has the effect that would increase terrain height, the magnitude of which was then in turn related to the intersection angle, such that for larger intersection angles the SIHE was more pronounced. This was seen in Table 8.37~39. Despite that the control points were not effective to obtain greater DEM accuracy, it is possible that they may be more suitable for application on other high relief areas and this still awaits further analysis. In addition, the use of these control header data files offered another opportunity to verify an important concept discovered in this study, that is, when only the slant range was varied, the terrain height would be altered. The *standard height approach* used the gradient of the range direction to shift the pixels in the X direction corresponding to changes of the slant range of matching points. Similarly, when using the control header data file, only the slant range was altered. Therefore, the consequences of using the control header data file would be the same as that of the *standard height approach*, only the intersected height value would be affected.

9.3 Overview of Achievements

Overall, the main achievements of this study could be described in two respects including the pyramidal matching and object domain approach. The examination of the pyramidal matching was rather difficult to proceed as it involved the optimisation of multiple parameters. A general strategy was developed in this study to answer several questions raised previously, such as the mechanism by which the random seed points could work. This study showed that most of the matching results were derived from the results of upper tiers in the image tier with only a minor proportion of points were related to the random seed points. The advantage of the pyramidal matching was also demonstrated here as mentioned earlier, and most importantly, it is able to increase the pull-in range for the seed points in the coarser resolution, which means that on each tier, the results generated from the previous tier would be accurate enough to offer as initial values for matching on the current tier. This could be found evidence from the refining results of strategy 2 (PDL2) prior to

the growing process where the iteration values of most seed points remained positive. The possibility of deriving a DEM from a large SAR image set using the pyramidal matching was validated. This study used an image of 1024*1024 in size, and for the same side the coverage could reach an average of 85%. With respect to its matching accuracy, its performance for the opposite side was much worse than the same side, and this was expected due to the disadvantages described in Chapter 3. For the same side, the matching accuracy should be in the subpixel level. Although its best DEM accuracy was 148.32m, since one pixel shift in Y direction could yield approximately 205m height deviation, it was still in an acceptable level.

The analytic approach was evaluated on three stereo pairs, and the impact of intersection angles on the intersection results were analysed. In general, the findings were consistent with the conclusions made in [Chen and Dowman, 1996]. For larger intersection angles, as in the case of OP2, the intersection coordinates were more liable to change by shifting the pixel in the X direction. This could be seen by comparing the data in Table 8.20. For this study, the intersection angle was crucial in determining the SIHE by control header data file as mentioned earlier. For the geometric constraint condition, the intersection angle condition was more suitable to be used for the stereo pair with the largest intersection angle, as demonstrated in Table 8.18 and 8.19. OP2 had larger intersection angle than OP1, which lead to greater DEM accuracy improvement. When considering the intersection errors caused by the image pixels, the convergence angle of two orbits was more important than the intersection angle, for it could cause more significant influence. This could be seen from the data listed in Table 8.20 and 8.21. With smaller convergence angle, the intersection error was more pronounced and this effect would vary significantly as seen in Table 8.22. For the same side, a deviation of 426.95m for the intersection coordinates with was derived, while for the OP1, reaching only 30.37m. This huge difference in the intersection error could be used to explain the reasons for poorer DEM accuracy obtained for the same side stereo pair. From this, it was also deduced that the accuracy of azimuth direction was much more important than the range direction. In other words, the orbit information would be required with great accuracy. Except the above two factors, the convergence and intersection angles, intersection errors could also be result from other sources of error. The accuracy of range and azimuth time that are given in the original header data file should be considered. Other elements with respect to the radiometric aspects, such as atmospheric effects and the scattering ambiguities of the targets, would also affect the intersection error. The evaluation of the influence of these factors need to be investigated further.

9.4 Future Studies

The objectives of this study overall have been achieved as presented in this thesis. However, many problems were encountered during this research and could be examined by subsequent researchers and they are listed as follows:

- (1) Testing of new point operators on SAR imagery - for example, as presented in [Bauer et al., 1996], the feature points were extracted and used as the seed points for the pyramidal matching instead of generating seeds in a random manner to evaluate their performance.
- (2) Region-growing method is a very powerful area-based matching algorithm for producing the dense matching points. However, the OIE (Original Image Effects) were detected on SAR imagery in this study. This OIE should be investigated further and a built-in blunder removing strategy specific for the SAR image should be developed in the growing process to improve the matching accuracy.
- (3) The possibility of deriving satisfactory DEMs for the opposite side SAR image was demonstrated and proven to yield better DEM. However, the regular grid DEM could not be obtained in this study due to difficulties encountered in the image pyramid. This should be overcome by developing more sophisticated image processing techniques.
- (4) The geometric constraint conditions used in the study was very effective in increasing the DEM accuracy, however, the reasons for the range error being more suitable for the same side and the intersection angle for the opposite side still remained unsolved. In this study, the determination was by general observation, which should also be substituted by other rigorous geometric analysis. From this, the optimum range or value could also be determined for any stereo pair by their specific header information.
- (5) SIHE should be investigated further, including the tests on areas with different terrain relief, observing its effects on the DEM accuracy and the utilisation of more control points to see its variation .
- (6) Develop other methods by which the control points information could be incorporated to check their impacts on the intersected coordinates.

(7) The importance of the orbit information was addressed earlier. The ERS-1 may be a special case to offer the orbit information, but for the RADARSAT or JERS-1, this information would probably not be available. Developing a general approach suitable to any SAR image to acquire the information used for intersection instead of the header data file should be carried out, bearing in mind that the requirement of generating satisfactory DEM accuracy should be reached.

REFERENCES

[Ackermann, 1984] Ackermann F., 1984. Digital image correlation: performance and potential applications in photogrammetry. *Photogrammetry Record* 11(64): 429-439

[Ackermann and Hahn, 1991] Ackermann F., Hahn M., 1991. Image pyramids for digital photogrammetry. *H. Ebner D. Fritsch C. Heipke (eds.) Digital Photogrammetric Systems*, Wichmann pp.43-58

[Allison et al., 1992] Allison D., Zemerly M.J., Muller J.P., 1992. Automatic seed points generation for stereo matching and multi-image registration. *17th International Archives of Photogrammetry and Remote Sensing Washington D.C., U.S.A.* 29(B2): 275-285

[Bauer et al., 1996] Bauer A., Raggam H., Hummelbrunner W., 1996. Automatic tie-pointing in overlapping images *International Archives of Photogrammetry and Remote Sensing* 31(B2): 315-320

[Boucher and Hillion, 1988] Boucher J.M., Hillion A. 1988 Non linear filtering and edge detection in speckle radar images. *IGARSS'88 Edinburgh, U.K.* pp.1267-1268

[Boucher and Hillion, 1987] Boucher J.M., Hillion A 1987. Alpha linear processing of a multiplicative noise with application to radar images. *IAESTED Symposium on control, filtering and signal processing Geneva, Switzerland* pp.42-46

[Chen, 1993] Chen P.H., 1993. Extraction of three dimensional geometric data from European ERS-1 SAR imagery. *M.Sc. Thesis, University College London* 82 pages

[Chen, 1994] Chen P.H., 1994. The evaluation of the space intersection from different radargrammetric configurations of the European ERS-1 SAR imagery. *Midterm report University College London* 24 pages

[Chen and Dowman, 1996] Chen P.H., Dowman I.J., 1996. Space intersection from ERS-1 synthetic aperture radar images. *Photogrammetry Record* 15(88): 561-573

- [Clark, 1991] Clark C., 1991. Geocoding and stereoscopy of synthetic aperture radar images. *Ph.D. Thesis University College London* 223 pages
- [Clochez, 1992] Clochez O., 1993. Speckle noise reduction and stereo matching of ERS-1 SAR imagery. *Training Period Report, University College London* 61pages
- [Crimmins, 1985] Crimmins T.R., 1985. Geometric filter for speckle reduction. *Applied optics* 24(10): 1438-1443
- [Curlander, 1984] Curlander J.C., 1984. Utilization of speceborne SAR data for mapping. *IEEE Transaction on Geoscience and Remote Sensing* GE-22 (2): 106-112
- [Day and Muller] Day T., Muller J.P., 1989. Digital elevation model production by stereo-matching SPOT image-pairs: a comparison of algorithms. *Image Vision Computing* 7(2): 95-101
- [Denos, 1991a] Denos M., 1991. An automated approach in stereo matching SEASAT imagery. *Proceedings of British Machine Vision Conference Glasgow, U.K.* pp 24-32.
- [Denos, 1991b] Denos M., 1991. Automatic height extraction from SAR imagery. *Transfer Ph.D. Report University College London*
- [Denos, 1992] Denos M., 1992. A pyramidal scheme for stereo matching SIR-B imagery. *International Journal of Remote Sensing* 13(2): 387-392
- [Dowman and Morris, 1982] Dowman I.J., Morris A.H. 1982. The use of synthetic aperture radar for mapping. *Photogrammetry Record* 10(60): 687-696
- [Dowman et al., 1992a] Dowman I.J., Upton M., Knecht J. K., Davison C., 1992. Preliminary studies on the application of the ERS-1 data to topographic mapping. *Proceedings of the First ERS-1 Symposium ESA* (3): 543-549
- [Dowman et al., 1992b] Dowman I. J., Clark C., Denos M., 1992. Three dimensional data from SAR images. *International Archives of Photogrammetry and Remote Sensing Commission IV* 27(B4): 425-426
- [Dowman, 1992] Dowman I.J., 1992. The geometry of SAR images for geocoding and stereo application. *International Journal of Remote Sensing* 13(9): 1609-1617

[Elachi, 1988] Elachi C., 1988. Spaceborne radar remote sensing: applications and techniques *IEEE Press, U.S.A.*

[Förstner and Gülch, 1987] Förstner W., Gülch E., 1987. A fast operator for detection and precise location of distinct points, corners and centers of circular features. *Proceeding of ISPRS Intercommission Workshop on Fast Processing of Photogrammetric Data, Interlaken Finland* pp. 281-305

[Fullerton et al., 1986] Fullerton J.K., Leberl F., Marquardt R.E., 1986. Opposite-side SAR image processing for stereo viewing. *Photogrammetry Engineering and Remote Sensing* 52(5): 1487-1498

[Goodenough et al., 1979] Goodenough D.G., Guindon B., Teillet P.M., 1979. Correction of synthetic aperture radar and multispectral scanner data sets. *Proceeding of 13th International Symposium on Remote Sensing of Environment Ann Arbor, U.S.A.* pp.259-270

[Gredel, 1993] Gredel J. 1993. The German processing and archiving facility for ERS-1. *SAR Geocoding Data and Systems Gunter Schreier (ed.) Wichmann* pp. 23-51

[Green, 1985] Green R.M., 1985. Spherical astronomy. *Cambridge University Press*

[Gruen, 1985] Gruen A.W., 1985. Adaptive least squares correlation: a powerful image matching technique. *South African Journal of Photogrammetry, Remote Sensing and Cartography* 14(3): 175-187

[Gruen and Baltsavias, 1987] Gruen A. W., Baltsavias E.P., 1987. Geometrically constrained multiphoto matching. *ISPRS, Intercommission Conference on Fast Processing of Photogrammetric Data. Interlaken, Switzerland* pp. 204-230

[Hatcher, 1984] Hatcher D.A., 1984 Simple formula for Julian day numbers and calendar dates. *Quarterly Journal Royal Astronomy Society* 25:53-55

[Jain and Christensen, 1980] Jain A.K., Christensen C.R. 1980 Digital processing of images in speckle noise. *SPIE* 243: 46-50

- [Kaupp et al., 1982] Kaupp V.H., Waite W.P., MacDonald H.C., 1982. Incidence angle considerations for space imaging radar. *IEEE Transaction on Geoscience and Remote Sensing* GE-20(3) : 384-389
- [Kaupp et al., 1983] Kaupp V.H., Bridges L.C., Pissaruck M.A., MacDonald H.C., Waite W.P., 1983. Simulation of spaceborne stereo radar imagery: experimental results. *IEEE Transaction of Geoscience and Remote Sensing* GE-21(3):400-405.
- [Kenyi and Raggam, 1996] Kenyi L.W., Raggam H. 1996. SAR interferometry: a comparative analysis of DTMs. *International Archives of Photogrammetry and Remote Sensing* 31(B4): 442-444
- [Korbick et al., 1986] Korbick M.F., Leberl F., Raggam J., 1986. Radar stereo mapping with crossing flight lines. *Canadian Journal of Remote Sensing* 12:132-148
- [Kuan, et al., 1987] Kuan D.T., Sawchuk A.A., Strand T.C., Chavel P., 1987. Adaptive restoration of images with speckle. *IEEE Transaction on Acoustics Speech and Signal Processing* ASSP-25(3): 373-381
- [LaPrade, 1963] LaPrade G.L. 1963. An analytical and experimental study of stereo for radar. *Photogrammetric Engineering* 29: 294-300.
- [LaPrade, 1972] LaPrade G.L. 1972. Stereoscopia-a more general theory. *Photogrammetric Engineering* pp.1177-1187
- [LaPrade et al., 1980], LaPrade G.L., Briggs S.J., Farrell R.J., Leonardo E.S. 1972. Stereoscopia. *Manual of Photogrammetry 4th edition* pp. 519-528
- [Lee 1981] Lee J.S. 1981. Speckle analysis and smoothing of synthetic aperture radar images. *Computer Graphics and Image Processing* 17:24-32
- [Leberl, 1976] Leberl F.W., 1976. Imaging radar application to mapping and charting. *Photogrammetria* 32: 75-100
- [Leberl, 1979] Leberl F.W., 1979. Accuracy analysis of stereo side-looking radar. *Photogrammetric Engineering and Remote Sensing* 45: 1083-1096
- [Leberl et al., 1982] Leberl F W ., Raggam J., Korbick M., 1982. Stereo side-looking radar experiments . *IGARSS'82 Munich, Germany* : (2)1-7.

- [Leberl et al., 1985] Leberl F.W., Raggam J., Kobrick M., 1985. On stereo viewing of SAR images. *IEEE Transaction on Geoscience and Remote Sensing* GE-23(2):110-117.
- [Leberl et al., 1986a] Leberl F.W., Domik G., Raggam J., Korbick M., 1986. Radar stereomapping techniques and application to SIR-B images of Mt. Shasta. *IEEE Transaction on Geoscience and Remote Sensing* GE-24(4): 473-481
- [Leberl et al., 1986b] Leberl F.W., Domik G., Raggam J., Cimino J., Kobrick M., 1986. Multiple incidence angle SIR-B experiment over Argentina: stereo-radargrammetric analysis. *IEEE Transaction on Geoscience and Remote Sensing* GE-24(4): 482-491
- [Leberl et al., 1988] Leberl F.W., Mayr W., Domik G., Kobrick M., 1988. SIR-B stereo-radargrammetry of Australia. *International Journal of Remote Sensing* 9(5): 997-1011
- [Leberl, 1990] Leberl F.W., 1990. Radargrammetric image procesing. *Artech House Inc., Norwood U.S.A.*
- [Leberl et al., 1994] Leberl F.W., Maurice K., Thomas J. K., Millot M., 1994. Automated radar image matching experiment. *ISPRS Journal of Photogrammetry and Remote Sensing* 49(3): 19-33
- [Lillesand and Kiefer, 1994] Lillesand T. M., Kiefer R.W., 1994. Remote sensing and image interpretation. 3rd edition, *Wiley & Sons U.S.A.*
- [Mackie, 1985] Mackie J.B., 1985. The elements of astronomy for surveyors *Charles Griffin U.S.A.*
- [Mercer, 1985] Mercer J.B., 1985. SAR technologies for topographic mapping *Photogrammetric Week'95 D. Fritsch D. Hobbie (eds) Wichmann* pp. 117-126
- [Meier and Nuesch, 1985] Meier E.H. and Nuesch D.R., 1985. Registration of spaceborne SAR data to large scale topographical maps. *19th International Symposium on Remote Sensing of Environment Ann Arbor, U.S.A.* pp. 581-594

- [Moravec, 1980] Moravec H.P. 1980. Obstacle avoidance and navigation in the real world by a seeing robot rover. *Ph. D. thesis, Stanford University*
- [Naraghi et al., 1983] Naraghi M., Stromberg W., Dailey M., 1983. Geometric rectification of radar imagery using digital elevation models. *Photogrammetry Engineering and Remote Sensing* 49(2):195-199
- [Noack et al., 1987] Noack W., Popella A., Schreier G., 1987. Knowledge-based SAR processing and geocoding in the elementary components of the German processing and archiving facility for high throughput and precision processing of ERS-1 SAR data. *IEEE Transaction on Geoscience and Remote Sensing* GE-25(6): 758-768
- [Otto and Chau, 1989] Otto G.P., Chau T.K.W., 1989. Region-growing algorithm for matching of terrain images. *Image Vision Computing* 7(2): 83-94
- [Papacharalampos and Welch, 1990] Welch R., Papacharalampos D., 1990. 3-D computation and display of terrain models from stereo imaging radar data. *IGARSS'90: Washington D.C. U.S.A.* 1967-1969
- [Pisaruck et al., 1984] Pisaruck M. A., Kaupp V.H., MacDonald H.C., Waite W.P., 1984 . Model for optimum parallax in stereo radar imagery. *IEEE Transaction on Geoscience and Remote Sensing* GE-22(6): 564-569
- [Raggam and Alkexander, 1996] Raggam H., Alexander A., 1996. Assessment of the potential of JERS-1 for relief mapping using optical and SAR data. *International Archives of Photogrammetry and Remote Sensing* 31(B4): 671-676
- [Ramapriyan et al., 1990] Ramapriyan H.K., Strong J.P., Huang Y., Murray C. W. Jr., 1986. Automated matching of pairs of SIR-B images for elevation mapping. *IEEE Transaction on Geoscience and Remote Sensing* GE-24(4): 462-472
- [Rosenfield, 1967] Rosenfield G.H. 1967. Stereo radar techniques. *Semi-Annual Convention of American Society of Photogrammetry St. Louis U.S.A.* pp 586-594.
- [Roth et al., 1993] Roth A., Craubner A., Hugel T., 1993. Standard geocoded ellipsoid corrected images. *SAR Geocoding Data and Systems Gunter Schreier (ed.) Wichmann* pp. 159-172

[Schreier, 1993] Schreier G., 1993. Geometrical properties of SAR images *SAR Geocoding Data and Systems Gunter Schreier (ed.) Wichmann* pp. 103-134

[Thomas et al., 1986] Thomas J.K., Kaupp V.H., Waite W.P., MacDonald H.C., 1986. Computer-derived height from SIR-B stereo radar images. *IGARSS'86 Zürich, Switzerland* pp. 639-654

[Thomas et al., 1987] Thomas J., Kaupp V., Waite W., MacDonald H. 1987. Considerations for optimum radar stereo. *IGARSS'87 Ann Arbor, U.S.A.* pp. 1531-1536

[Toutin, 1996] Toutin T. 1996. Opposite side ERS-1 SAR stereo mapping over rolling topography. *IEEE Transaction on Geoscience and Remote Sensing* 34(2): 543-549

[Travett, 1986] Trevett J.W., 1986. Imaging radars for resources surveys *Chapman & Hall U.K.*

[Twu 1993] Twu Z. G., 1993. Automatic height extraction from ERS-1 SAR imagery *Transfer Ph. D. Report University College London* 48 pages

[Zemerly et al., 1992] Zemerly M.J., Holden M., Muller J.P., 1992. A multi-resolution approach to parallel stereo matching of airborne imagery. *International Archives of Photogrammetry and Remote Sensing* 31(B2): 350-357

APPENDIX A*

Least Squares Correlation Algorithm

The grey values two small patches, the left and right imagery of the stereo pair, are $G_1(X_i, Y_j)$ and $G_2(X_i', Y_j')$ respectively. The relationship of these two grey functions can be described by the affine transformation shown in the equation below. (A-1).

$$\begin{bmatrix} X_i' \\ Y_j' \end{bmatrix} = \begin{bmatrix} a_1 \\ a_4 \end{bmatrix} + \begin{bmatrix} a_2 & a_3 \\ a_5 & a_6 \end{bmatrix} \begin{bmatrix} X_i \\ Y_j \end{bmatrix} = \begin{bmatrix} a_1 & a_2 & a_3 \\ a_4 & a_5 & a_6 \end{bmatrix} \begin{bmatrix} 1 \\ X_i \\ Y_j \end{bmatrix} \quad (\text{A-1})$$

In addition, another two parameters, h_1 and h_2 , are introduced for scaling and shifting the function $G_2(X_i', Y_j')$ to minimise the total sum of square difference of the two grey values of the conjugate point to give:

$$G_1(X_i, Y_j) = h_1 + h_2 G_2(X_i', Y_j') \quad (\text{A-2})$$

Substitute the $G_2(X_i', Y_j')$ with the equations of A-1 and A-2 to give:

$$G_1(X_i, Y_j) = h_1 + h_2 G_2 \left[\left(\begin{bmatrix} a_1 & a_2 & a_3 \\ a_4 & a_5 & a_6 \end{bmatrix} \begin{bmatrix} 1 \\ X_i \\ Y_j \end{bmatrix} \right)^T \right] \quad (\text{A-3})$$

Equation of A-3 can be simplified to:

$$G_1(X_i, Y_j) = h_1 + h_2 G_2(X_i, Y_j; A) \quad (\text{A-4})$$

Where $A = \begin{bmatrix} a_1 & a_2 & a_3 \\ a_4 & a_5 & a_6 \end{bmatrix}$ and $G_2(X_i, Y_j; A)$ dictate the grey values of the right image after transformation of matrix A.

Equation of A-4 is nonlinear and can be linearized by the Taylor's Series shown in A-5.

$$G_1(X_i, Y_j) = h_1^0 + h_2^0 G_2(X_i, Y_j; A^0) + \Delta h_1 + G_2(X_i, Y_j; A^0) \Delta h_2 + \sum_{n=1}^6 \left(h_2^0 \frac{\partial G_2}{\partial a_n} \Delta a_n \right)$$

(A-5)

Where h_1^0, h_2^0 and A^0 are the initial values for h_1, h_2 and A initial values, while $\Delta h_1, \Delta h_2$, and $\Delta a_n (n=1 \sim 6)$ represent the increments of h_1, h_2 and a_n that are unknowns.

The coefficients of $\frac{\partial G_2}{\partial a_n}$ are as follows:

$$\begin{aligned} \frac{\partial G_2}{\partial a_1} &= \frac{\partial G_2}{\partial X_i'} \frac{\partial X_i'}{\partial a_1} + \frac{\partial G_2}{\partial Y_j'} \frac{\partial Y_j'}{\partial a_1} = \dot{G}_{2x} \cdot 1 + \dot{G}_{2y} \cdot 0 = \dot{G}_{2x} \\ \frac{\partial G_2}{\partial a_2} &= \frac{\partial G_2}{\partial X_i'} \frac{\partial X_i'}{\partial a_2} + \frac{\partial G_2}{\partial Y_j'} \frac{\partial Y_j'}{\partial a_2} = \dot{G}_{2x} \cdot X_i + \dot{G}_{2y} \cdot 0 = X_i \dot{G}_{2x} \\ \frac{\partial G_2}{\partial a_3} &= \frac{\partial G_2}{\partial X_i'} \frac{\partial X_i'}{\partial a_3} + \frac{\partial G_2}{\partial Y_j'} \frac{\partial Y_j'}{\partial a_3} = \dot{G}_{2x} \cdot Y_j + \dot{G}_{2y} \cdot 0 = Y_j \dot{G}_{2x} \\ \frac{\partial G_2}{\partial a_4} &= \frac{\partial G_2}{\partial X_i'} \frac{\partial X_i'}{\partial a_4} + \frac{\partial G_2}{\partial Y_j'} \frac{\partial Y_j'}{\partial a_4} = \dot{G}_{2x} \cdot 0 + \dot{G}_{2y} \cdot 1 = \dot{G}_{2y} \\ \frac{\partial G_2}{\partial a_5} &= \frac{\partial G_2}{\partial X_i'} \frac{\partial X_i'}{\partial a_5} + \frac{\partial G_2}{\partial Y_j'} \frac{\partial Y_j'}{\partial a_5} = \dot{G}_{2x} \cdot 0 + \dot{G}_{2y} \cdot X_i = X_i \dot{G}_{2y} \\ \frac{\partial G_2}{\partial a_6} &= \frac{\partial G_2}{\partial X_i'} \frac{\partial X_i'}{\partial a_6} + \frac{\partial G_2}{\partial Y_j'} \frac{\partial Y_j'}{\partial a_6} = \dot{G}_{2x} \cdot 0 + \dot{G}_{2y} \cdot Y_j = Y_j \dot{G}_{2y} \end{aligned}$$

Where $\dot{G}_{2x} = \frac{\partial G_2}{\partial X_i'}$ and $\dot{G}_{2y} = \frac{\partial G_2}{\partial Y_j'}$ represent the gradient in X and Y direction of point (X_i', Y_j') on the right imagery.

Supposing the function of grey values $G_1(X_i, Y_j)$ and $G_2(X_i', Y_j')$ are equal to the digitised grey value function $g_1(X_i, Y_j)$ and $g_2(X_i', Y_j')$ plus the noise function $n_1(X_i, Y_j)$ and $n_2(X_i', Y_j')$ respectively,

Then the initial value of $(h_1^0, h_2^0, a_1^0, a_2^0, a_3^0, a_4^0, a_5^0, a_6^0) = (0, 1, 0, 1, 0, 0, 0, 1)$

$$\begin{aligned} G_1(X_i, Y_j) - G_2(X_i', Y_j') &= [g_1(X_i, Y_j) - g_2(X_i', Y_j')] + [n_1(X_i, Y_j) - n_2(X_i', Y_j')] \\ &= \Delta h_1 + G_2(X_i, Y_j) \Delta h_2 + \dot{G}_{2x}(X_i, Y_j) \Delta a_1 + X_i \dot{G}_{2x}(X_i, Y_j) \Delta a_2 + \\ &Y_j \dot{G}_{2x}(X_i, Y_j) \Delta a_3 + \dot{G}_{2y}(X_i, Y_j) \Delta a_4 + X_i \dot{G}_{2y}(X_i, Y_j) \Delta a_5 + Y_j \dot{G}_{2y}(X_i, Y_j) \Delta a_6 \end{aligned} \quad (A-6)$$

Let $L(X_i, Y_j) = g_1(X_i, Y_j) - g_2(X_i', Y_j')$ be the grey value difference of the stereo pair and $V(X_i, Y_j) = n_2(X_i', Y_j') - n_1(X_i, Y_j)$ be the residual

Then Equation B-6 can be simplified to

$$V(X_i, Y_j) = AX - L(X_i, Y_j) \quad (A-7)$$

Appendix A. Least Squares Correlation Algorithm

The X matrix in Equation A-7 are 8 unknown of parameters ($\Delta h_1, \Delta h_2, \Delta a_1, \Delta a_2, \Delta a_3, \Delta a_4, \Delta a_5, \Delta a_6$) which can be solved by the Least Squares Adjustment.

* The formula shown in this appendix were derived from:

[Ackermann F., 1984. Digital image Correlation: performance and potential application in photogrammetry. Photogrammetric Record 11(64): 429-439]

APPENDIX B

Original Header Data File

Three ERS-1 header data files for PRI_A, PRI_D and RTM_A are shown in B-1, B-2 and B-3 respectively. These files provide the essential information of each imagery for the intersection and their data are accessible from three data record files, Data Set Summary, Platform Position Data and Map Projection Data. By the given formats (field number) in the Computer Compatible Tape (CCT) as well as in the WWW NETSCAPE, these data could be read out from the record files as described in section 5.4.1. Four data columns are shown in this appendix for each file, of which the Format column lists the value of each data, while the Data Source column specifies the record file that the data is extracted from, and in the Fields column lists the field number. The last column gives the description of the data.

B-1 PRI_A original header data file

<Format>	<Data Source>	<Fields>	< Descriptions>
1992 5 9 21 49 45.213	*	12	Given time of data point
5	*	14	Given data points number
4.10	*	20	Time interval of points
5264327.100 191199.680 4846563.970	*	29	Given position vector 1
-4883.95297 -2071.44947 5327.40019	*	30	Given velocity vector 1
5244253.680 182711.460 4868545.29	*	31	Given position vector 2
-4908.44794 -2069.34942 5350.73746	*	32	Given velocity vector 2
5224080.020 174131.950 4890437.600	*	33	Given position vector 3
-4932.85232 -2067.19719 5328.97712	*	34	Given velocity vector 3
5203806.490 165761.370 4912240.50	*	35	Given position vector 4
-4957.16564 -2064.99288 5307.11958	*	36	Given velocity vector 4
5183433.460 157299.940 4933953.58	*	37	Given position vector 5
-4981.38742 -2062.73658 5285.1652	*	38	Given velocity vector 5
1992 5 9 21 49 52.960	#	11	Scene center time
43.865 5.485	#	13&14	Scene center lat. & long.
6378.144 6356.759	#	17&18	Semi-major & -minor axes
4102.0 4000.5	#	26&27	Center azimuth, range pixel
0.057	#	42	Wave length
0.0055505 0.0056714 0.0058113	#	126	Three range pixel's time
-7.674 0.0 7.673	#	127	Three azimuth pixel's time
43.320 5.019	@	68&69	Left-top corner lat. & Long.

<Note: * Platform Position Data Record >

< # Data Set Summary Record >

< @ Map Projection Data Record >

Appendix B. Original Header Data File

B-2 PRI_D original header data file

<Format>	<Data Source>	<Fields>	< Descriptions>
1992 5 6 10 25 41.813	*	12	Given time of data point
5	*	14	Given data points number
4.097	*	20	Time interval of points
5143231.03 833540.99 4908235.52	*	29	Given position vector 1
5256.57794 -1078.1531 -5311.1556	*	30	Given velocity vector 1
51640720.6 829109.55 4886429.61	*	31	Given position vector 2
5233.1339 -1084.96443 -5332.98113	*	32	Given velocity vector 2
5186113.91 824650.27 4864534.46	*	33	Given position vector 3
5209.59071 -1091.7421 -5354.70951	*	34	Given velocity vector 3
5207410.56 820163.29 4842550.5	*	35	Given position vector 4
5185.94883 -1098.48592 -5376.34034	*	36	Given velocity vector 4
5228610.14 815648.75 4820478.10	*	37	Given position vector 5
5162.2087 -1105.19571 -5397.87321	*	38	Given velocity vector 5
1992 5 6 10 25 49.931	#	11	Scene center time
43.612 5.485	#	13&14	Scene center lat. & long.
6378.144 6356.759	#	17&18	Semi-major & -minor axes
4104.5 4000.5	#	26&27	Center azimuth, range pixel
0.057	#	42	Wave length
0.0055505 0.0056714 0.0058113	#	126	Three range pixel's time
-7.678 0.0 7.678	#	127	Three azimuth pixel's time
43.966 6.231	@	68&69	Left-top corner lat. & Long.

<Note: * Platform Position Data Record >

< # Data Set Summary Record >

< @ Map Projection Data Record >

Appendix B. Original Header Data File

B-3 RTM_A original header data file

<Format>	<Data Source>	<Fields>	< Descriptions>
1992 4 10 22 00 54.202	*	12	Given time of data point
5	*	14	Given data points number
4.067	*	20	Time interval of points
5341579.700 -46194.180 4765245.050	*	29	Given position vector 1
-4891.76041 -1835.40296 5450.89988	*	30	Given velocity vector 1
5321632.62 -53653.33 4787373.61	*	31	Given position vector 2
-4916.26169 -1832.27458 5429.7672	*	32	Given velocity vector 2
5301586.07 -61099.66 4809416.02	*	33	Given position vector 3
-4940.67305 -1829.09897 5408.53701	*	34	Given velocity vector 3
5281440.410 -68532.980 4831371.87	*	35	Given position vector 4
-4964.99403 -1825.87623 5387.20971	*	36	Given velocity vector 4
5261196.00 -75953.090 4853240.77	*	37	Given position vector 5
-4989.22417 -1822.60648 5365.78567	*	38	Given velocity vector 5
1992 04 10 22 00 58.514	#	11	Scene center time
43.133 5.334	#	13&14	Scene center lat. & long.
6378.144 6356.759	#	17&18	Semi-major & -minor axes
3887.0 4000.5	#	26&27	Center azimuth, range pixel
0.057	#	42	Wave length
0.0061443 0.0063333 0.0065359	#	126	Three range pixel's time
-7.303 0.0 7.302	#	127	Three azimuth pixel's time
42.62 4.844	@	68&69	Left-top corner lat. & Long.

<Note: * Platform Position Data Record >
 < # Data Set Summary Record >
 < @ Map Projection Data Record >

APPENDIX C

Control Header Data File

Three ERS-1 header data files for PRI_A, PRI_D and RTM_A are shown in C-1, C-2 and C-3 respectively. The data values as well as the their arrangements are similar to those listed in Appendix B, however, these files in addition incorporate extra range times from the control points. The detailed calculation of the range time is shown in section 8.11.

C-1 PRI_A control header data file

<Format>	<Data Source>	<Fields>	< Descriptions>
1992 5 9 21 49 45.213	*	12	Given time of data point
5	*	14	Given data points number
4.10	*	20	Time interval of points
5264327.100 191199.680 4846563.970	*	29	Given position vector 1
-4883.95297 -2071.44947 5327.40019	*	30	Given velocity vector 1
5244253.680 182711.460 4868545.29	*	31	Given position vector 2
-4908.44794 -2069.34942 5350.73746	*	32	Given velocity vector 2
5224080.020 174131.950 4890437.600	*	33	Given position vector 3
-4932.85232 -2067.19719 5328.97712	*	34	Given velocity vector 3
5203806.490 165761.370 4912240.50	*	35	Given position vector 4
-4957.16564 -2064.99288 5307.11958	*	36	Given velocity vector 4
5183433.460 157299.940 4933953.58	*	37	Given position vector 5
-4981.38742 -2062.73658 5285.1652	*	38	Given velocity vector 5
1992 5 9 21 49 52.960	#	11	Scene center time
43.865 5.485	#	13&14	Scene center lat. & long.
6378.144 6356.759	#	17&18	Semi-major & -minor axes
4102.0 4000.5	#	26&27	Center azimuth, range pixel
0.057	#	42	Wave length
6			No. of range pixel's time
0.0055505	1.0	#	126 1st range pixel's time
0.00560574	1850.0	\$	Range pixel's time of GCP
0.005617348	2291.0	\$	Range pixel's time of GCP
0.005627508	2617.0	\$	Range pixel's time of GCP
0.0056714	4000.5	#	126 Center range pixel's time
0.0058113	8000.0	#	126 Last range pixel's time
-7.674 0.0 7.673		#	127 Three azimuth pixel's time
43.320 5.019		@	68&69 Left-top corner lat. & Long

<Note: * Platform Position Data Record >

< # Data Set Summary Record >

< @ Map Projection Data Record >

< \$ GCP's data >

C-2 PRI_D control header data file

<Format>	<Data Source>	<Fields>	< Descriptions>
1992 5 6 10 25 41.813	*	12	Given time of data point
5	*	14	Given data points number
4.097	*	20	Time interval of points
5143231.03 833540.99 4908235.52	*	29	Given position vector 1
5256.57794 -1078.1531 -5311.1556	*	30	Given velocity vector 1
51640720.6 829109.55 4886429.61	*	31	Given position vector 2
5233.1339 -1084.96443 -5332.98113	*	32	Given velocity vector 2
5186113.91 824650.27 4864534.46	*	33	Given position vector 3
5209.59071 -1091.7421 -5354.70951	*	34	Given velocity vector 3
5207410.56 820163.29 4842550.5	*	35	Given position vector 4
5185.94883 -1098.48592 -5376.34034	*	36	Given velocity vector 4
5228610.14 815648.75 4820478.10	*	37	Given position vector 5
5162.2087 -1105.19571 -5397.87321	*	38	Given velocity vector 5
1992 5 6 10 25 49.931	#	11	Scene center time
43.612 5.485	#	13&14	Scene center lat. & long.
6378.144 6356.759	#	17&18	Semi-major & -minor axes
4104.5 4000.5	#	26&27	Center azimuth, range pixel
0.057	#	42	Wave length
6			No. of range pixel's time
0.0055505 1.0	#	126	1st range pixel's time
0.0056714 4000.5	#	126	Center range pixel's time
0.005682932 4355.0	\$		Range pixel's time of GCP
0.005683764 4371.0	\$		Range pixel's time of GCP
0.005697656 4808.0	\$		Range pixel's time of GCP
0.0058113 8000.0	#	126	Last range pixel's time
-7.678 0.0 7.678	#	127	Three azimuth pixel's time
43.966 6.231	@	68&69	Left-top corner lat. & Long

<Note: * Platform Position Data Record >
 < # Data Set Summary Record >
 < @ Map Projection Data Record >
 < \$ GCP's data >

C-3 RTM_A control header data file

<Format>	<Data Source>	<Fields>	< Descriptions>
1992 4 10 22 00 54.202	*	12	Given time of data point
5	*	14	Given data points number
4.067	*	20	Time interval of points
5341579.700 -46194.180 4765245.050	*	29	Given position vector 1
-4891.76041 -1835.40296 5450.89988	*	30	Given velocity vector 1
5321632.62 -53653.33 4787373.61	*	31	Given position vector 2
-4916.26169 -1832.27458 5429.7672	*	32	Given velocity vector 2
5301586.07 -61099.66 4809416.02	*	33	Given position vector 3
-4940.67305 -1829.09897 5408.53701	*	34	Given velocity vector 3
5281440.410 -68532.980 4831371.87	*	35	Given position vector 4
-4964.99403 -1825.87623 5387.20971	*	36	Given velocity vector 4
5261196.00 -75953.090 4853240.77	*	37	Given position vector 5
-4989.22417 -1822.60648 5365.78567	*	38	Given velocity vector 5
1992 04 10 22 00 58.514	#	11	Scene center time
43.133 5.334	#	13&14	Scene center lat. & long.
6378.144 6356.759	#	17&18	Semi-major & -minor axes
3887.0 4000.5	#	26&27	Center azimuth, range pixel
0.057	#	42	Wave length
6			No. of range pixel's time
0.0061443 1.0	#	126	1st range pixel's time
0.0063333 4000.5	#	126	Center range pixel's time
0.006343284 4290.0	\$		Range pixel's time of GCP
0.006362758 4597.0	\$		Range pixel's time of GCP
0.006377702 4893.0	\$		Range pixel's time of GCP
0.0065359 8000.0	#	126	Last range pixel's time
-7.303 0.0 7.302	#	127	Three azimuth pixel's time
42.62 4.844	@	68&69	Left-top corner lat. & Long

<Note: * Platform Position Data Record >
 < # Data Set Summary Record >
 < @ Map Projection Data Record >
 < \$ GCP's data >

APPENDIX D Terms Glossary I (Chapter 7)

Terms	Definition	Defined Section
Effective Random Seed Points (ERSP)	The number of original random seed points that has the impact on the matching results	7.3
Random Seed Effects (RSE)	The effect that deteriorate the matching results due to the original random seed points and their growing seed points	7.3
initial seed points	The seed points that exist originally prior to the matching	7.5
Original Random Seed Effects (ORSE)	The effect that deteriorate the matching results derived directly from the original random seed points	7.5
Growing Random Seed Effects (GRSE)	The effect that deteriorate the matching results due to the growing seed points of the original random seed points	7.5
Height Deviation Shifting Effect (HDSE)	The ratio of RMS to the DEM accuracy of the height deviation	7.6
disparity sum	The absolute sum of the disparity of X and Y coordinate of a single point	7.6
grand disparity sum	The summation of disparity sum on each tier of the image pyramid	7.6
disparity seed points	The seed points created from the seed points on tier4 with the smallest grand disparity sum	7.8
grand generation seed points	The seed points whose seed_generation is greater than 600	7.9
Original Image Effect (OIE)	The effect that deteriorate the matching accuracy for the grand generation seed points which occur on the original resolution of SAR image	7.9

APPENDIX D Terms Glossary II (Chapter 8)

Terms	Definition	Defined Section
range error	Sum of difference of slant range and range distance for a given target point	8.2
constraint conditions	Two geometric conditions used for intersection, which are range error and intersection angle	8.3
constraint values	The value of range error or intersection angle of a given target point	8.3
constraint_height function	The function that describe the relationship of constraint values and height deviation	8.3
initial height	The height data of the DEM produced by the original matching results	8.9
standard height	The height data of the inputting DEM, which is used to calculate the shifting magnitude from the initial height	8.9
standard height approach	Using the shifting magnitude to shift pixels in the range direction such that the height of each single point could approach the standard height	8.9
original header data file	The header data file that is provided by the ERS-1 without the range time of control points	8.11
control header data file	The header data file that include extra range time calculated by the control points	8.11
Systematic Increasing Height Effects (SIHE)	The effect of increasing the elevation of targets by using the control header data file	8.11